Development and Deployment of an Inner Detector Minimum Bias Trigger and Analysis of Minimum Bias Data of the ATLAS Experiment at the Large Hadron Collider

D I S S E R T A T I O N

zur Erlangung des akademischen Grades

Doctor Rerum Naturalium (Dr. Rer. Nat.)
im Fach Physik

eingereicht an der
Mathematisch-Naturwissenschaftlichen Fakultät I
Humboldt-Universität zu Berlin

von
Dipl.-Phys. Regina Esther Kwee

Präsident der Humboldt-Universität zu Berlin:
Prof. Dr. Jan-Hendrik Olbertz

Dekan der Mathematisch-Naturwissenschaftlichen Fakultät I:
Prof. Dr. Andreas Herrmann

Gutachter:
1. Prof. Dr. Hermann Kolanoski
2. Dr. Nick Ellis
3. Dr. Klaus Mönig

eingereicht am: 9. September 2011
Tag der mündlichen Prüfung: 13. Januar 2012

Dedicated to my parents
Evy and Rudie H. S. Kwee

Abstract

Soft inelastic QCD processes are the dominant proton-proton interaction type at the LHC. More than 20 of such collisions pile up within a single bunch-crossing at ATLAS, when the LHC is operated at design luminosity of $\mathcal{L} = 10^{34}\,\mathrm{cm}^{-2}\,\mathrm{s}^{-1}$ colliding proton bunches with an energy of $\sqrt{s} = 14$ TeV. Inelastic interactions are characterised by a small transverse momemtum transfer and can only be approximated by phenomenological models that need experimental data as input. The initial phase of LHC beam operation in 2009, with luminosites ranging from $\mathcal{L} = 10^{27}$ to $10^{31}\,\mathrm{cm}^{-2}\,\mathrm{s}^{-1}$, offered an ideal period to select single proton-proton interactions and study general aspects of their properties.

As first part of this thesis, a Minimum Bias trigger was developed and used for data-taking in ATLAS. This trigger, mbSpTrk, processes signals of the silicon tracking detectors of ATLAS and was designed to fulfill efficiently reject empty events, while possible biases in the selection of proton-proton collisions is reduced to a *minimum*. The trigger is flexible enough to cope also with changing background conditions allowing to retain low-p_{T} events while machine background is highly suppressed.

As second part, measurements of inelastic charged particles were performed in two phase-space regions. Centrally produced charged particles were considered with a pseudorapidity smaller than 0.8 and a transverse momentum of at least 0.5 or 1 GeV. Four characteristic distributions were measured at two centre-of-mass energies of $\sqrt{s} = 0.9$ and 7 TeV. The results are presented with minimal model dependency to compare them to predictions of different Monte Carlo models for soft particle production.

This analysis represents also the ATLAS contribution for the first common LHC analysis to which the ATLAS, CMS and ALICE collaborations agreed. The pseudorapidity distributions for both energies and phase-space regions are compared to the respective results of ALICE and CMS.

Zusammenfassung

Weiche inelastische QCD Prozesse dominieren am LHC. Über 20 solcher Kollisionen werden innerhalb einer Strahlkreuzung bei ATLAS stattfinden, sobald der LHC die nominelle Luminosität von $\mathcal{L} = 10^{34}\,\mathrm{cm}^{-2}\,\mathrm{s}^{-1}$ und die Schwerpunktsenergie von $\sqrt{s} = 14$ TeV erreicht. Diese inelastischen Wechselwirkungen sind durch einen geringen Impulsübertrag gekennzeichnet, welche theoretisch lediglich durch phänomenologische Modelle angenähernd beschrieben werden können. Zu Beginn des Strahlbetriebs des LHC's 2009 war die Luminosität relativ niedrig mit $\mathcal{L} = 10^{27}$ bis $10^{31}\,\mathrm{cm}^{-2}\,\mathrm{s}^{-1}$, was ein sehr gutes Szenario bot, um einzelne Proton-Proton Kollisionen zu selektieren und deren allgemeine Eigenschaften experimentell zu untersuchen.

Zunächst wurde ein Minimum-Bias Trigger entwickelt, um Daten mit ATLAS aufzunehmen. Dieser Trigger, mbSpTrk, verarbeitet Signale der Silizium-Spurdetektoren und verwirft effizient Ereignisse ohne eine Proton-Wechselwirkung, wobei zugleich eine mögliche Verschiebung zu bestimmten Ereignistypen hin *minimier* wird. Um einen flexiblen Einsatz des Triggers zu gewährleisten, wurde er mit einer Sequenz ausgestattet, welche effizient Machinenuntergrund unterdrückt.

Im zweiten Teil der Arbeit wurden geladenen Teilchenmultiplizitäten im zentralen Bereich in zwei kinematisch definierten Phasenräumen gemessen. Mindestens ein geladenes Teilchen mit einer Pseudorapidität kleiner als 0.8 und einem Transversalimpuls mindestens 0.5 bzw. 1 GeV musste vorhanden sein. Vier typische Minimum-Bias Verteilungen wurden bei zwei Schwerpunktsenergien von $\sqrt{s} = 0.9$ und 7 TeV gemessen. Die Ergebnisse sind derart präsentiert, dass sie nur minimal von Monte Carlo Modellen abhängen.

Die vorgestellten Messungen stellen zudem den Beitrag der ATLAS Kollaboration dar für die erste, LHC-weit durchgeführte Analyse, der auch die CMS und ALICE Kollaborationen zustimmten. Ein Vergleich konnte mit den Pseudorapiditätsverteilungen angestellt werden.

Contents

1. Introduction

The Large Hadron Collider (LHC) at CERN has extended the frontiers of particle physics with unprecedented high centre-of-mass energy and luminosity. It was built to collide proton bunches of around 10^{11} protons every 25 ns at an energy of $\sqrt{s} = 14$ TeV. Four experiments were constructed at the LHC to shed more light on unresolved fundamental questions e.g. about the origin of mass, properties of the elementary constituents of matter or the evolution of the universe. Two of them are general purpose detectors, ATLAS and CMS, designed to cope with high luminosities of $\mathcal{L} = 10^{34}$ cm^{-2}s^{-1} and prepared to discover the Unknown, while two other experiments, LHCb and ALICE, pursue more specific purposes, by investigating matter-anti-matter asymmetry in b-meson decays and color-deconfined states in form of quark-gluon plasma, respectively.

However, the nature of proton-proton collisions comprise also one of the largest challenges for the high luminosity LHC experiments. At nominal operation every bunch-crossing that may contain a rare event with signatures of new physics will be overlapping with more than 20 inelastic proton-proton collisions. It is indispensable to characterise such event types as accurate as possible for a successful LHC physics programme. These processes however, carry typically a low momentum transfer Q^2 and perturbative QCD is no more applicable. This results in highly uncertain cross-section calculations at LHC energies. Although several theoretical approaches exist to describe these *soft* inelastic interactions, the currently best available description is delivered by phenomenological models. Despite their success, these models need experimental data as input to improve their predictions. In the new energy territory that the LHC has entered in the beginning of 2010 with proton-proton collisions at $\sqrt{s} = 7$ TeV, measurements of soft processes were the first to be performed − as a validation of existing models, as a guidance of how to improve them, but also as measure of how well the detector is understood which is a baseline for any subsequent physics analysis.

For such kind of measurements it is crucial that the selection of proton-proton interactions is as unbiased as possible, i.e. none of the different types of inelastic interactions shall be preferably selected. A random trigger would be the ideal option to select an unbiased event sample to study general characteristics of inelastic proton-proton interactions. However, in particular in the beginning of the LHC operation, the luminosity was relatively low, starting at $\mathcal{L} = 10^{27}$ to $10^{31}\,\mathrm{cm}^{-2}\,\mathrm{s}^{-1}$. Depending on the exact machine parameters, the probability of a proton-proton interaction per bunch-crossing can be 1 % or even 0.1 % (which was the case at LHC start-up in 2009). Therefore, dedicated triggers sensitive to any beam-beam interaction are needed to suppress empty bunch-crossings while selecting proton-proton collision introducing only *minimal bias*.

The work of this thesis is performed with the ATLAS experiment, one of the general purpose experiments at the LHC. This thesis describes in detail the development and deployment of such a minimum bias trigger in ATLAS based on design studies performed earlier [1]. This trigger uses a random trigger at the first trigger level and requires at the subsequent level a certain correlation of clustered hits (so called spacepoints) in the silicon sub-detectors of the Inner Detector to reject empty bunch-crossing events. In addition, it is provided with a third selection step to suppress online beam induced background events by means of rough and fast tracking which makes the deployment of the trigger more independent on varying levels of machine background.

This minimum bias trigger represents a complementary approach for selecting proton interactions to a dedicated, first level minimum bias trigger in ATLAS, the so called Minimum Bias Trigger Scintillators (MBTS). While MBTS is a system consisting of 16 plastic scintillators located on each side of the interaction point, the complementary minimum bias trigger actively selects at higher trigger levels by processing information of Inner Detector components. With both minimum bias triggers available, ATLAS was prepared for various trigger scenarios, able to efficiently select clean proton interactions not only during changing machine backgrounds but also at different luminosities which increased by four orders of magnitude during the early operation phase of the LHC.

Also, in order to quantify possible biases of the triggers from data both minimum bias triggers are necessary. This thesis presents in the first part a data driven methods to determine trigger bias, since it is a crucial ingredient to analyses of inelastic proton-proton interactions avoiding dependencies on Monte Carlos models. In the second part, this result is used for measurements of charged particle properties in different phase-space regions at $\sqrt{s} = 0.9$ and 7 TeV. This analysis is performed on an LHC-wide level, with ATLAS, CMS and ALICE agreeing on the analysis strategy and distributions. The analysis on charged particle spectra performed in this thesis, represents the ATLAS contribution for this first common LHC analysis. This agreement between the LHC experiments was made to verify measurements of experiments which surpass any previous particle physics experiment by far concerning its complexity.

The remainder of the thesis is structured as follows. Chapter 2 introduces in the first part the Standard Model, the current theoretical description of the fundamental particles and their interactions. The second part focuses on the physics of soft QCD interactions relevant for this work. Chapter 3 serves as an experimental introduction to the LHC machine and ATLAS detector while more details about the ATLAS trigger system, the software and the commissioning phase with beam is given in Chapter 4. The random based Inner Detector minimum bias trigger is outlined in Chapter 5. The subsequent Chapter 6 presents the performance of both minimum bias triggers on data taken right after the LHC start up in 2009 and over the whole low luminosity phase in 2010. The measurements of charged particle multiplicities in two specific regions of phase-space at both energies $\sqrt{s} = 0.9$ TeV and 7 TeV for the first commonly agreed LHC analysis are described in Chapter 7 with direct comparisons of measurements of ATLAS, CMS and ALICE. Finally, summary and conclusion are given in Chapter 8.

2. Physics at the LHC

This chapter gives an introduction to the physics aims at the Large Hadron Collider (LHC), outlining the general physics programme of the multi-purpose detector ATLAS in Section 2.1 for Standard Model physics and in Section 2.2 particle physics beyond the Standard Model. In Section 2.3 proton collisions are generally discussed before in Section 2.4 the physics of soft particle interaction is described in more detail that form the bulk hadronic environment at the LHC. Section 2.5 presents the most commen models to describe these soft interactions. The last two sections, Section 2.6 and 2.7, introduces the observables measured in ATLAS to characterise inelastic interactions and outlines the analysis strategy.

2.1. The Standard Model of Particle Physics

The Standard Model of Particle Physics (SM) is the theoretical framework which describes the three of the four known fundamental interactions between all known elementary particles. At the LHC, the current understanding is tested in new energy regimes accessible for the first time.

The formalism to describe the SM is called Quantum Field Theory [2]. The gauge field of the SM is composed of three symmetry groups $\mathrm{SU(3)_c} \times \mathrm{SU(2)_I} \times \mathrm{U(1)_Y}$. Each gauge field has mediators, gauge bosons characterised as particles of an integer spin to which the matter particles, fermions possessing an half-integer spin, couple. The particle content of the SM is illustrated in Fig. 2.1. The fermions are grouped in three generations. Electrons (e), muons (μ) and taus (τ) with each one having a neutrino partner (ν_e, ν_μ, ν_τ) are collectively termed leptons, while quarks appear as up and down (u,d), charm and strange (c,s) and top and bottom (t,b) quark. The electromagnetic force is mediated by massless photons (γ) and in weak interactions either a neutral (Z^0) or charged ($W^\pm$) gauge boson is exchanged.

The theory of strong interactions is Quantum Chromodynamics (QCD). Mediators of that force are called gluons which are assumed to be massless and electrically neutral, but instead carry a colour charge (colour-octet or -singlet combination of *red, green, blue* and the respective anti-colours). This enables the gluons to interact with other gluons known as self-interaction. Another property, reflected in the non-abelian type of the $\mathrm{SU(3)_c}$ group, is the confinement of the particles with colour charge, i.e. quarks and gluons are confined at long distances as only colour neutral particles (colour-singlets) are observed in nature. This is expressed in the *running coupling constant* α_s which is a function of the momentum transfer squared Q^2. The momentum transfer of the incoming particle to the outgoing particle is expressed by the Mandelstam variable

Fermion	Generation	Mass [MeV/c^2]	Charge (Q)	Colour
electron (e^-)	1	0.511	-1	
electron neutrino (ν_e)	1	$< 2 \cdot 10^{-6}$	0	
muon (μ^-)	2	106	-1	
muon neutrino (ν_μ)	2	< 0.19	0	
tau (τ^-)	3	1777	-1	
tau neutrino (ν_τ)	3	< 18.2	0	
up quark (u)	1	1.7-3.3	+2/3	rgb
down quark (d)	1	4.1-5.8	-1/3	rgb
charm quark (c)	2	$(1.27^{+0.07}_{-0.09}) \cdot 10^3$	+2	rgb
strange quark (s)	2	(101^{+29}_{-21})	-1/3	rgb
top quark (t)	3	$(172.0^{+0.9}_{-1.3}) \cdot 10^3$	+2/3	rgb
bottom quark (b)	3	$(4.19^{+0.18}_{-0.06}) \cdot 10^3$	-1	rgb
Gauge Boson	Force	Mass [MeV/c^2]	Charge (Q)	Colour
photon (γ)	electromagnetic	0	0	
$W^\pm$	weak	80,399 $\pm$ 23	$\pm$1	
Z^0	weak	91,187.6 $\pm$ 2.1	0	
gluon (g)	strong	0	0	rgb
Higgs (H^0)		?	0	

Table 2.1.: Standard Model particle content with masses from [3]. "rgb" in the last column indicate that the quarks exist in three different colour states "red", "green" and "blue".

$t = (p_{\text{in}} - p_{\text{out}})^2 = -q^2 = Q^2$. For $Q^2 \gg \Lambda_{\text{QCD}}$, where Λ_{QCD} is the scale of strong interactions, the strong coupling constant is in leading order

$$\alpha_s(Q^2) = \frac{1}{\beta_0 \ln(Q^2/\Lambda^2_{\text{QCD}})} \tag{2.1}$$

Experimentally, Λ_{QCD} is found to be of the order of 200 MeV that is the mass scale of hadronic physics as given by the pion mass or equivalently the inverse of the typical hadron size R. For non-abelian gauge bosons the coefficient β_0 in Eq. 2.1 consists of components related to the colour of the particles. Small couplings are present in bound states at short distances (*asymptotic freedom*). However, at long distances or small Q^2, the coupling becomes large which confines quarks and gluons making them uncalculable within perturbative theory.

In the parton model, quarks and gluons are commonly referred to as *partons*, while particles with two quarks are called *mesons* and a bound state of three particles are *baryons*. Examples of the mesons are neutral or charged pions $\pi^0, \pi^\pm$, the lightest of their kind with 134 MeV and 139 MeV, respectively. Baryons are for example protons, neutrons and Δ particles consisting of up and down quarks. The ensemble of quark bound states are *hadrons*, a complete particle listing can be found in [3].

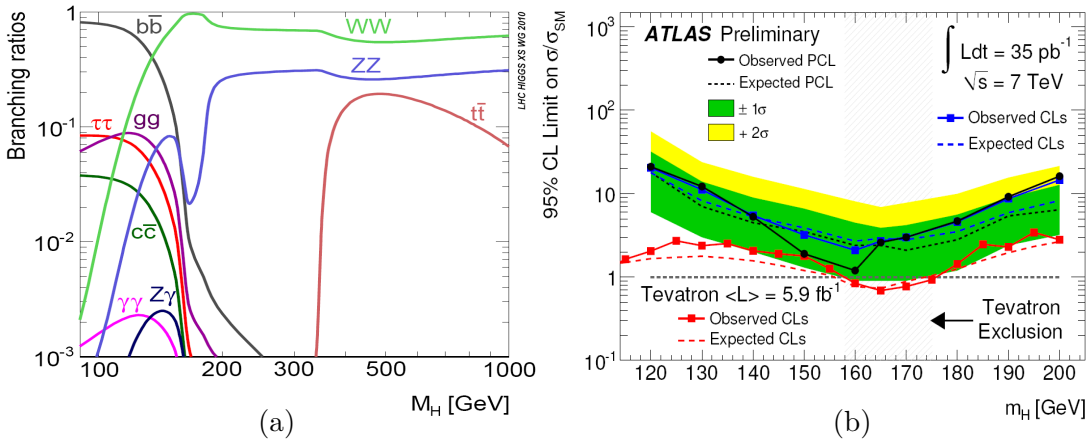

Figure 2.1.: (a) SM Higgs decay modes [4]. (b) Sensitivity analysis of ATLAS and Tevatron data with $WW^{(*)}$ decays [5].

2.1.1. The Higgs Boson

The particle that plays a key role in all electroweak interactions is the *Higgs boson* with the fundamental role to produce the masses of the electroweak gauge bosons. The SM Higgs boson emerges from spontaneous symmetry breaking in the electroweak sector (Higgs-mechanism) and produces masses for the weak gauge bosons leaving the photon massless [6]. The postulated Higgs boson itself - that is not yet discovered - would be massive, but its mass is a free parameter in the SM. However, the coupling behaviour of the SM Higgs is fully determined allowing to calculate cross-sections and decay widths as function of the Higgs mass, see Fig. 2.1. Direct constraints come from experiments and theoretical arguments. A lower limit of the Higgs mass of $m_H > 114.4$ GeV at 95% C.L. [7] was determined by direct searches at LEP, the Large Electron-Positron Collider, the predecessor of the LHC. An upper limit is set by theory allowing $m_H < 1$ TeV, otherwise unitarity is violated in vector boson scattering processes [8]. Electroweak measurements constrain the SM Higgs mass to be less than 185 GeV at 95% C.L. [9] and direct searches at the Tevatron further exclude the region between 158 and 175 GeV [10].

At the LHC, the search for the SM Higgs boson is of central concern. The main Higgs production channels at the LHC are either *direct* or *associated* production channels. Direct Higgs production would occur in gluon-gluon fusion, $gg \to H$ preferentially via a $t\bar{t}-$loop, and in vector boson fusion $qq \to qqWW \to qqH$, $qq \to qqZZ \to qqH$. An associated Higgs production would also appear in gluon-gluon fusion $gg \to t\bar{t}H$ or when quarks annihilate into a vector boson which radiates a Higgs $qq \to WH, ZH$.

The decay modes of the Higgs will exhibit distinctive event topologies. From the expected branching ratios of the Higgs boson as depicted in Fig. 2.1 (b) the search focuses on different decay modes depending on the mass range. For $m_H < 130$ GeV the dominant decay mode is the decay into two b-quarks $H \to b\bar{b}$, since the b-quark is the heaviest particle which can create an invariant mass below that limit. However, it is a purely hadronic decay and very difficult to identify from otherwise produced $b\bar{b}$ background.

The channel $H \to \gamma\gamma$ even with a much smaller cross-section is more relevant, since it would produce a small peak over the irreducible, non-resonant background. Therefore, highest performance of the electromagnetic calorimeters is essential. In mass regions up to twice the Z^0-mass and higher the most promising channel is $H \to ZZ^{(*)} \to 4l$ exhibiting a quasi background-free, very clear signature, often called the *golden channel*.

Sensitivity studies $\sqrt{s} = 7$ TeV have shown that at least 1 fb^{-1} of integrated luminosity is needed to set exclusion limits on the predicted SM cross-section [11, 12].

2.1.2. Success and Limitations

In the past, the SM has withstood all tests to describe phenomena observed at particle physics experiments. It predicted e.g. three particles, the Z^0- and $W^{\pm}$-bosons, before experimental evidence was claimed. Measurements at LEP resulted in a Z^0-mass m_{Z^0} of (91.1876 $\pm$ 0.0021) GeV [3], W-mass measurements at LEP and Tevatron yielded a W-mass of (80.403 $\pm$ 0.029) GeV [3]. Both results are in striking accordance with the SM predictions. Also, the existence of the gluon and the top quark were predicted and experimentally confirmed. Despite the series of successful predictions, the SM is believed not to represent the ultimate theory to describe nature completely. One reason is that the mass of the Higgs boson itself is not predictable in the SM despite its unique role.

With a number of free parameters, 12 for all fermion masses (including the neutrino masses), three coupling constants of the particle to the gauge field, three angles and one phase of the matrix linking mass eigenstates to electroweak eigenstates (CKM[1]-Matrix), four parameters of a similar matrix for neutrino mixing (PMNK[2]-Matrix) and the vacuum expectation value of the Higgs field, the SM lacks predictions of fundamental particle properties. They have to be extracted from experimental data instead of being derived from first principles. Another unresolved problem is that the fourth force, gravity, is not included in the theory. It is not understood why gravity compared to strength of the weak force is about 10^{-36} times smaller at low or modest energy scale.

Another insufficiency closely related to it is that the SM suffers from a problem known as the *gauge hierarchy problem*. An unnaturally precise fine-tuning covering more than 30 orders of magnitude are needed for the renormalised Higgs mass to remove corrections from higher order radiations. Many extensions to the SM or new theories have been proposed to overcome this and other problems of our current theory.

2.2. Beyond the Standard Model

One possible solution to the hierarchy problem is proposed in **Supersymmetric Theories** (SUSY) imposing a symmetry between fermions and bosons and postulating to each SM particle a supersymmetric partner particle. They have the same quantum numbers like their SM partners except for the spin which differs by 1/2. Thereby, each SM boson has a fermionic SUSY partner and each fermion has a bosonic partner *sfermion*.

[1] Cabbibo-Kobayashi-Maskawa
[2] Pontecorvo-Maki-Nagaskawa-Sakata

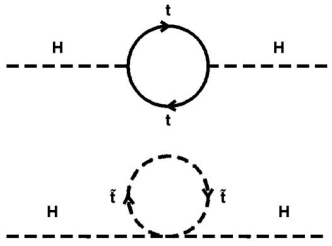

Figure 2.2.: Resolving the hierarchy problem in the SM by introducing a SUSY partner $\tilde{t}$ to the SM t. The contribution of quadratic divergencies in the Higgs production cancels out and no unnatural fine-tuning is needed in SUSY models.

If this symmetry is unbroken, evidence for the SUSY particles would have arisen from previous experiments already as their masses would be the same as their SM partners. So far, none of such SUSY particles have been observed. This requires that Supersymmetry is broken leading to masses around the TeV scale, thus much higher as for the SM masses. The benefit of introducing the concept of SUSY particles is that unnatural fine-tuning can be avoided: radiative corrections in the Higgs mass cancel out automatically (stabilisation of Higgs mass) which is illustrated in Fig. 2.2. At LHC the masses of supersymmetric partner particles should be accessible already the first two years of data-taking might bring some evidence for such particles.

Many other theories beyond the Standard Model have been formulated to include also gravity. There is Superstring Theory or just **String Theory** incorporating as an essential component Supersymmetry. String Theory claims to be able to answer to fundamental questions that are still open in the Standard Model. Moreover, it resolves conflicts of quantum mechanics and general relativity and a quantum theory of gravity emerges naturally. Experimentally this theory is expected to be probed only at very high energies, generally much higher than accessible at LHC. However, hints may be observed at the LHC, e.g. from *extra-dimensions*. Also, relevant data for String Theory are expected from LHC concerning the supersymmetric part of String Theory.

Searches for new physics signals have begun at the LHC. Several searches for the superpartners have been already made, probing various models. So far no excess with respect to the SM expectations is observed [13, 14].

2.3. Proton-Proton Collisions

The study of proton-proton collisions allows to perform the physics searches as mentioned in the previous section. Moreover, one can thereby deepen the understanding of physics processes which are still today less well understood within Standard Model QCD and need experimental data as input. This in fact is a first task to perform at the LHC, essential for understanding the hadronic environment in the experiments and one of main subjects of the present work. In the following an introduction to soft interaction

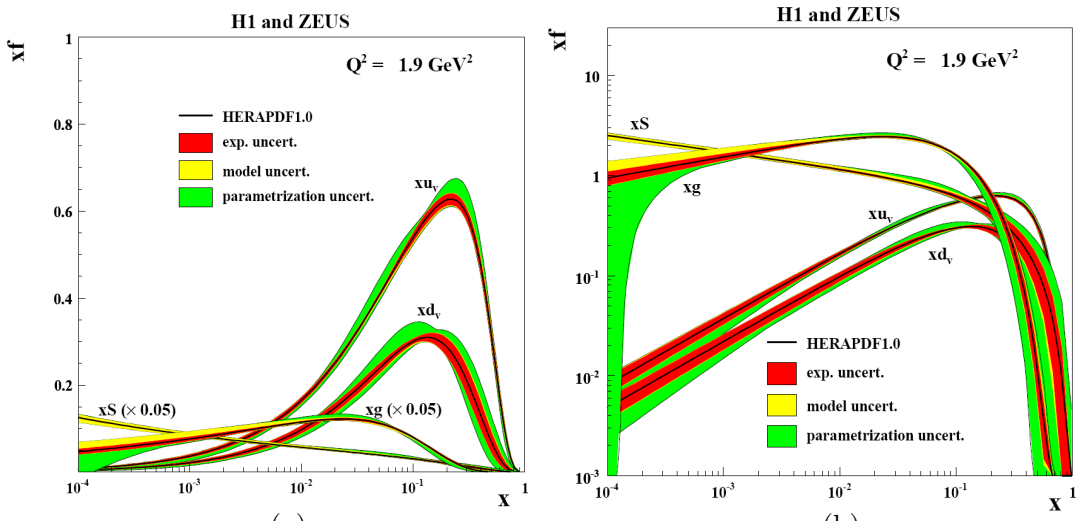

Figure 2.3.: Parton density functions for gluon (g), valence up- (u_v), valence down- (d_v) and sea-quarks (S) at $Q^2 = 1.9$ GeV^2 as a function of the momentum fraction x. In (a) the sea-quark and gluon densities are scaled down by a factor of 20. (b) highlights the same densities as in (a) on a logscale. Clearly, at x smaller than 10^{-3} the uncertainties of the gluon density increase drastically [15].

processes is given, highlighting the reactions emerging from proton-proton collisions.

Substructure of a Proton

Protons are like all hadrons composed and colour neutral objects. The substructure of a proton is rather complex and was mainly deducted in analyses of deep inelastic scattering processes, measuring parton density functions (PDFs) of a proton which indicate a certain probability of a parton to exist inside the proton. This probability depends on the energy scale at which the proton is probed and is usually denoted by the momentum transfer squared Q^2. Such a content of a proton at a fixed and relative low Q^2 of 1.9 GeV^2 is depicted in Fig. 2.3 in linear (a) and log-scale (b). This figure shows the proton contains three valence quarks, two up- and one down-quark. They make up the total electrical charge of $+1e$. The proton structure also accounts for contributions of a whole "sea" of quarks formed by a constant creation and annihilation process of quark anti-quark pairs. Finally, gluons add up to the proton structure which hold the quarks together as representatives of the strong force. Their distributions are however highly uncertain when they carry a low momentum fraction x as Fig. 2.3 (b) reveals.

When protons collide this substructure of the proton brings up a rich variety of possible reactions. They can be classified into two event classes involving *soft* and *hard* processes. Such a division of the cross-section underlines the ability to perform calculations for a given process. An overview of interaction processes is shown in Fig. 2.4, their different event topologies are discussed in more detail in the next sections.

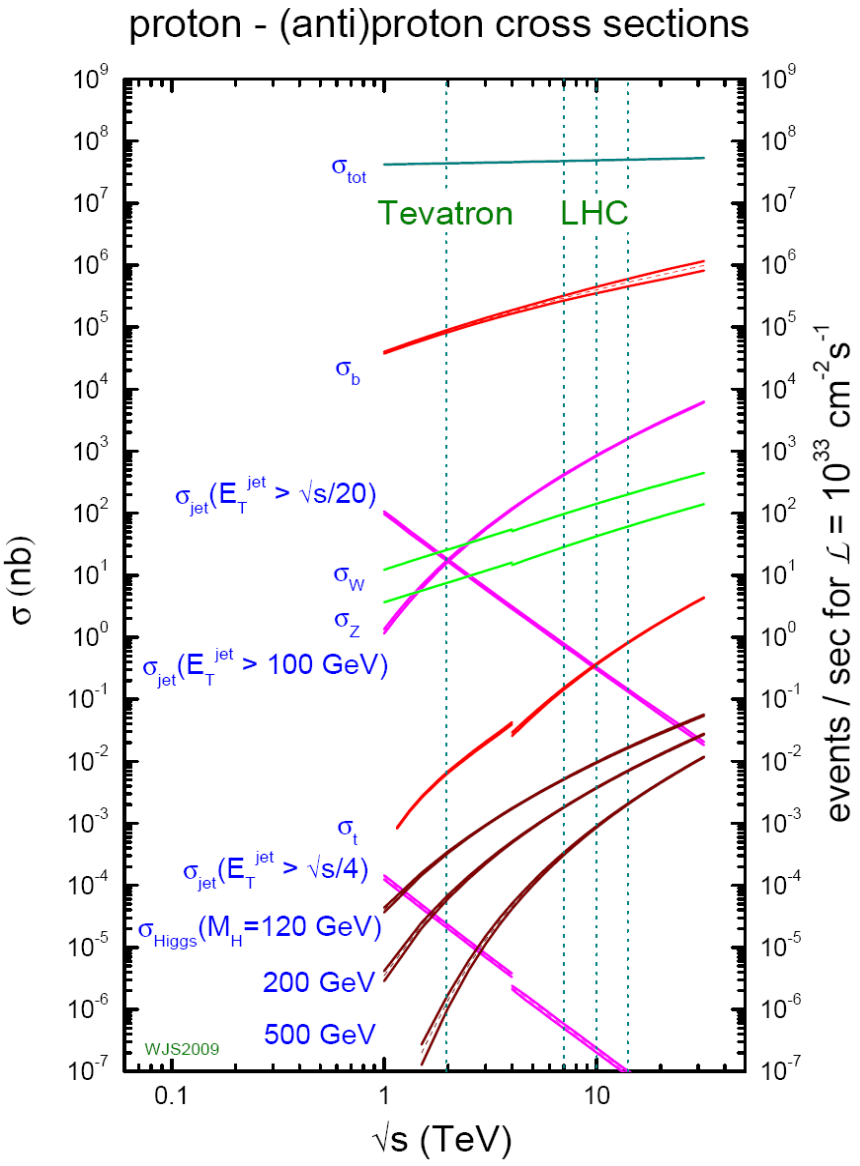

Figure 2.4.: Cross-section predictions for various processes in $p\bar{p}$ and pp collisions as function of centre-of-mass energy $\sqrt{s}$ with 4 vertical lines indicating Tevatron energy $\sqrt{s} = 1.98$ GeV and LHC energies at $\sqrt{s} = 7$, 10 and 14 TeV. At $\sqrt{s} = 7$ TeV, a heavy Higgs would be produced with $\sigma_{\text{Higgs}}(M_H = 500 \text{ GeV}) \approx 0.3$ pb. These signals must be filtered out of QCD processes that appear about 10^7 times more often. This figure is reproduced from Ref. [16].

Kinematics in Proton-Proton Collisions

Since protons have a substructure, the typical variables to describe such a collision are different from those used in collisions of elementary particles. For partonic interaction, the laboratory system of the colliding particles is in general not the same as the centre-of-mass system. Only a fraction of the centre-of-mass energy is generally used in the collision $\hat{s} \rightarrow x_1 x_2\, s$, with $\hat{s}$ the centre-of-mass energy in the parton-parton system and x_i the momentum fraction of parton from hadron i. The typical quantities for a hadronic system are **rapidity** $y \equiv \frac{1}{2} \ln \frac{E+p_z}{E-p_z}$, with E the energy of the particle and p_z the longitudinal component of the momentum in z-direction. In case the masses can be neglected, the **pseudorapidity** $\eta = -\ln \tan \frac{\theta}{2}$, with θ the polar angle, is used. Also, transverse quantities are more common like the **transverse momentum** p_{T} or **transverse energy** E_{T}, since they are conserved quantities. These are invariant under Lorentz-boosts along the z-axis and are therefore commonly used for hadron collisions.

2.3.1. Hard Scattering Processes

Hard interactions processes have a characteristic "hard" scale but expose as well a soft energy scale (see below). In hard processes, Q^2 is significantly larger than Λ_{QCD} which allows to explore QCD with the tools of perturbative calculations and partonic cross-sections can be calculated. In order to compute production cross-sections, these partonic cross-sections are convoluted with the parton densities of the constituents of the proton which incorporate the soft effects in a process. The so-called *factorisation theorem* allows that the perturbative part can be separately treated from processes of non-perturbative origin [17]. While the first part is calculable in orders of α_s, the latter is embodied in quark and gluon distributions which are extracted from measurements and possess universal validity. They can be extracted from one process and used in another. Typically, the cross-sections with a large momentum transfer are small to tiny and show a more pronounced dependencies on the centre-of-mass energy. Examples are heavy quark production, high mass lepton pairs and the anticipated Higgs as shown in Fig. 2.4. Such interaction processes will not be further investigated in this thesis, a detailed reference is e.g. [17].

2.3.2. Soft Scattering Processes

The typical energy scale of soft processes is comparable to the size[3] of the hadron $R \sim 1$ fm $= 1/200$ MeV^{-1}. The momentum transfer squared, Q^2, is usually very small in soft processes with $|t| \sim 1/R^2 \sim$ (few hundred MeV)^2. Due to the small momentum transfer perturbative calculations of QCD become unjustified in this regime and therefore phenomenological models are employed to provide qauntitative descriptions of these processes. Soft interactions have typically a large cross-section that changes only slightly (logarithmically) with the centre-of-mass energy of the collisions. These soft processes

[3] Using the *natural units* in particle physics, the speed of light c and the reduced Planck constant $\hbar = h/2\pi$ are set to 1. Thus lengths can be expressed in units of inverse energy.

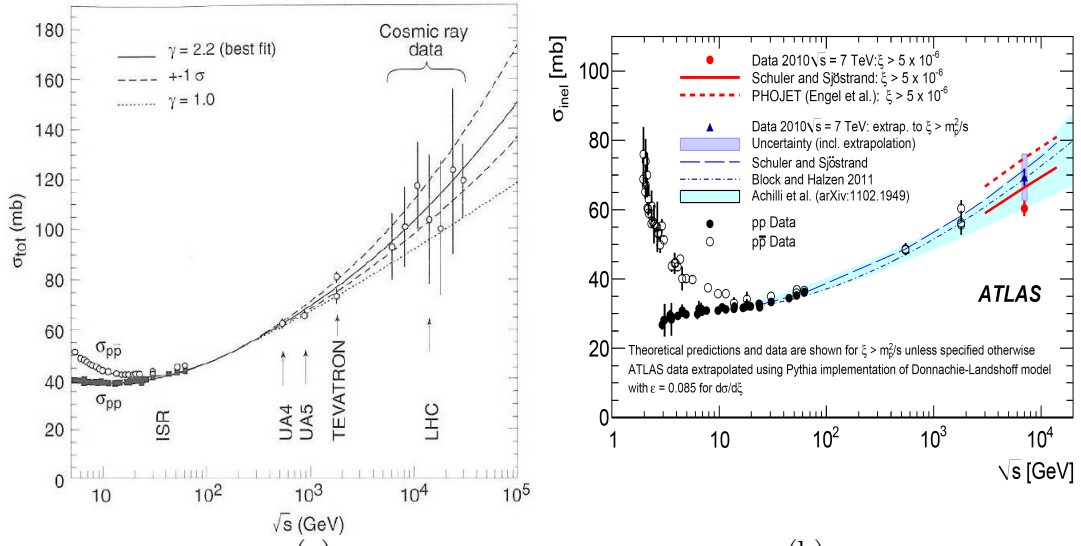

(a) (b)

Figure 2.5.: Total cross-section σ_{tot} as a function of centre-of-mass energy $\sqrt{s}$ for $p\bar{p}$ and pp collisions. (a) The data are compared to different fits of σ_{tot} to $(\ln s)^{\gamma}$ [18]. (b) σ_{inel} with comparison to ATLAS data (at $\sqrt{s} = 7$ TeV) which extrapolated to yield σ_{inel} (triangle) is comparable to previous measurements [19].

are topic of the present thesis and comprise interactions of inelastic, non-diffractive and diffractive dissociations. They are subject of the following sections.

2.3.3. Total Cross-Sections

The general behaviour of the total cross-section of proton-proton (pp) and proton-antiproton ($p\bar{p}$) reactions is depicted as a function of centre-of-mass energy $\sqrt{s}$ in Fig. 2.5 (a). Above the broad minimum at around $\sqrt{s} \sim 20$ GeV the $p\bar{p}$ and pp cross-section merge as predicted by the Pomeranchuk theorem that requires asymptotic equality of $\sigma_{\text{tot}}(p\bar{p})$ and $\sigma_{\text{tot}}(pp)$ [18]. It continues to steadily increase with the centre-of-mass energy $\sqrt{s}$. This growth is restricted by a unitarity requirement that allows σ_{tot} not to grow faster than with $\ln^2 s$ known as the Froissart-Martin bound [17]. Towards higher centre-of-mass energies measurements are highly uncertain. A first measurement in that region with LHC data is shown in Fig. 2.5 (b). A measurement of the inelastic cross-section σ_{inel} was performed in a kinematic region with $\xi > 10^{-6}$ where $\xi = M_X^2/s$ and M_X the highest invariant mass of hadrons [19]. This result has then been extrapolated using a certain model of PYTHIA (see text in figure) to compare to other measurements.

Single contributions to the total cross-section stem from elastic and inelastic interactions, both interact dominantly with small momentum transfers. The inelastic part can be further split into non-diffractive (ND) and several types of diffractive dissociations:

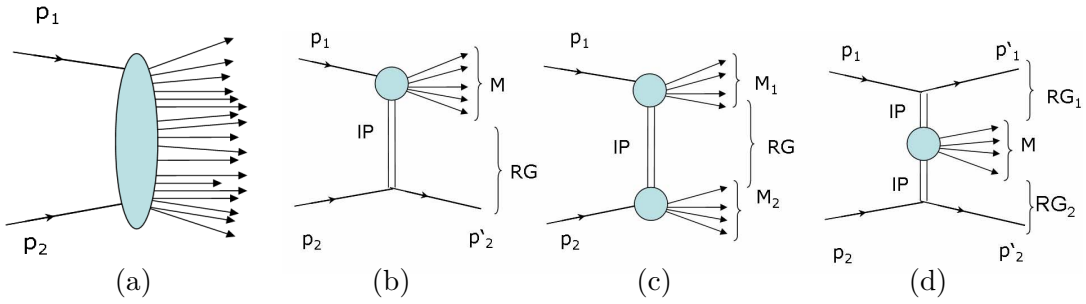

Figure 2.6.: Inelastic scattering processes of proton collisions and the topologies of final state particles. (a) ND interactions are characterised by a trail of soft particles flatly distributed in rapidity, while (b) SD, (c) DD and (d) CD dissociation are marked by rapidity gap(s) (RG) described by the exchange of a pomeron $\mathbb{P}$, a colour singlet object.

single-, double- and central-diffractive dissociations (SD, DD, CD)

$$\sigma_{tot} = \sigma_{el} + \underbrace{\sigma_{ND} + \sigma_{SD} + \sigma_{DD} + \sigma_{CD}}_{\sigma_{inel}} \tag{2.2}$$

The inelastic cross-section predictions from two different Monte Carlo generators (see also Section 2.5) are listed in Table 2.2 for $\sqrt{s} = 0.9$, 7, and 14 TeV.

Elastic Interactions

In elastic scatterings the protons remain intact and there is no excitation of any internal degree of freedom. Such processes make up a sizable fraction of the total cross-section with around $\sigma_{\mathrm{el}}(s) \approx 1/6\,\sigma_{\mathrm{tot}}(s)$ [17]. Particles that are elastically scattered peak in the very forward direction which indicates that low Q^2 processes are dominant. This is also a reason why most of the elastic scattering events disappear in the beam pipe which can only be measured with special detectors that are placed close to the beam pipe (at high rapidity values).

Diffractive Dissociation

In diffractive dissociations[4][17, 18] the scattered hadron is left in an excited state which breaks up into a low multiplicity system of hadrons for example $\mathrm{p} \to \Delta^+ \to \mathrm{n}\,\pi^+$. In case one of the scattering hadrons *dissociates* the interaction is called single-diffractive dissociation (SD), in case both protons dissociate, it is called double-diffractive dissociation (DD) [17]. The mass of the excited hadronic system M_X is typically distributed as $\mathrm{d}\sigma \sim dM_X/M_X$, while the t-dependence of the cross-section falls exponentially with a coefficient antiproportional to M_X. A characteristic signature of these events is a lack

[4]The name "diffraction" was borrowed from optics as the cross-section of these events resembled the intensity pattern of diffracted light.

Table 2.2.: Inelastic cross-section predictions indicated in mb by PYTHIA and PHOJET for three different centre-of-mass energies.

	PYTHIA 6.420			PHOJET 1.12		
$\sqrt{s}$ [TeV]	0.9	7	14	0.9	7	14
σ_{inel}	52.5	71.5	79.3	55.0	77.4	84.6
σ_{ND}	34.4	48.5	54.7	39.9	61.5	68.3
σ_{SD}	11.7	13.7	14.3	10.5	10.7	10.8
σ_{DD}	6.4	9.3	10.3	3.5	3.9	4.1
σ_{CD}	–	–	–	1.1	1.3	1.4

of particle production between the scattered and dissociated protons. Traditionally, this gap is quoted in units of rapidity. Considering for the mass system of the two dissociated protons M_1 and M_2 respectively, the rapidity gap is $\Delta y = \ln[s/(M_1 M_2)]$. Often these interactions are viewed as an exchange in the t-channel of a colour-singlet object called pomeron (see Section 2.4) as illustrated in Fig. 2.6.

A related class of events are central-diffractive dissociations (CD) which show two large rapidity gaps (more generally one speaks also of multi-gap events). They can be interpreted as the exchange of two pomerons. The emerging jet-like activity in the final states indicates the presence of a hard scale which represents the field of study of hard diffractive dissociation. With collider experiments reaching higher centre-of-mass energies, they receive more attention as diffractive models start to be explorable with means of perturbative QCD [18].

Experimentally it is found that the double-diffractive cross-section grows faster than the single-diffractive dissociation cross-section. The central-diffraction cross-section is a few per cent of the total dissociation cross-section. For these reasons only the soft diffractive processes are of interest for the present work, the central-diffractive type will not further be discussed.

Non-Diffractive Dissociation

The remainder of the events of inelastic interactions is often termed non-diffractive dissociation (ND) to which one generally associates soft inelastic collisions. This event class represents the vast majority of inelastic interactions with two fast forward traveling fragments and a trail of centrally produced soft particles [17]. These central particles have an exponentially damped p_{T} spectrum and are uniformly distributed in rapidity. Generally, the properties of such soft particles show only weak dependence on s.

Due to the soft nature of these interactions and their large production rate at the LHC it is important to quantify these properties at LHC energies. The following section therefore describes soft QCD models and different measurement strategies.

2.4. Soft QCD

The major components of the total cross-section from ND to DD and SD feature all a small momentum transfer. Perturbative QCD is not applicable to calculate cross-sections of such processes. To describe interactions in the regime of soft QCD, where $|t| \ll s$, many phenomenological models have emerged to describe processes with soft momentum transfer. Most successful models are based on Regge theory [18, 20, 21], originally formulated by T. Regge in 1957 and later extended with a series of plausible assumptions for high energy particle physics phenomena.

2.4.1. The Regge Approach

Regge theory is a mathematical formalism that describes hadronic interactions by an effective exchange of (pseudo-)particles treating the interacting extended hadrons as point-like particles. The exchanged particles are associated with singularities of scattering amplitudes expressed in partial wave expansions [20]. These expansions converge when the ansatz is used to treat the angular momentum l of the scattering amplitude as a complex variable. This was the base idea of Regge. It allowed to set up a relativistic framework in which the elements of a scattering matrix (*S-Matrix theory*) quantify the transition from an initial to final state using concepts of unitarity, analyticity and crossing[5] symmetries, e.g. a high energy s-channel can be analytically continued in the crossing t-channel [20, 22].

If a particle with spin l is exchanged, it becomes $l = \alpha_i(t)$ in"Reggeized" formulations with $\alpha(t)$ representing the singularities of the scattering amplitude $\mathcal{A}(s,t)$. These are interpreted as *Regge poles* and their amplitude can be approximated by [20]

$$\mathcal{A}(l,t) \approx \frac{G(t)}{l - \alpha(t)}.$$

with $G(t)$ a function absorbing t-dependencies in the numerator. The resulting amplitude has a Breit-Wigner form leading to the interpretation of exchanged *resonances* represented by a linear *Regge trajectory* ("reggeon" often denoted with $\mathbb{R}$). The poles are estimated neglecting higher orders by

$$\alpha_{\mathbb{R}}(t) \approx \alpha_{\mathbb{R}}(0) + \alpha'_{\mathbb{R}} \cdot t \tag{2.3}$$

with $\alpha_{\mathbb{R}}(0)$ as the intercept and $\alpha'_{\mathbb{R}}$ the slope. In so-called *Chew-Frautschi diagrams* [22] the spin $\alpha_i(t)$ is plotted against $|t| = M^2$, the mass squared of the exchanged particle. Intercept and slope are found by fitting the spins and masses of real mesons and baryons, e.g. for f_2, ρ, ω, a_2 [18].

However, to explain the rise of σ_{tot} with rising s another Regge trajectory was introduced with vacuum quantum numbers, the *pomeron* ($\mathbb{P}$) which does not correspond to a real particle. Fits to a wide range of data from $p\bar{p}$ and pp collisions at $\sqrt{s} = 5$ to

[5] Crossing refers to the three crossing channels in the Mandelstam plane.

1800 GeV [23] yielded for the pomeron

$$\alpha_{\mathbb{P}}(0) \approx 1.08 \qquad \text{and} \qquad \alpha'_{\mathbb{P}} \approx 0.25\,\text{GeV}^{-2}.$$

The intercept is slightly larger than the limit given by the Froissart-Martin bound to satisfy unitarity. Nevertheless with these starting points relative compact expressions for e.g. the total and elastic cross-sections can be derived. As example, the total cross-section [17] takes the form

$$\sigma_{\text{tot}} = \frac{1}{M_i^2}\left(\frac{s}{M_i^2}\right)^{\alpha_i(0)-1}.$$

With the pomeron ($i = \mathbb{P}$) the cross-section indeed rises slightly with s. Using the optical theorem that relates the total cross-section to the imaginary part of the scattering amplitude, one can derive formula for the cross-section of the bulk part of soft inelastic interactions. Especially diffractive scattering processes are often described using the formalism of the pomeron exchange to compute cross-sections [17, 18].

The description of the non-diffractive soft particle production is rather provided by what is known as the concept of *multiple parton interaction* which is a key ingredient to several phenomenological models employed in event generators.

Due to the success of this theoretical framework Regge's basic ideas still survived and several ansätze exist to integrate the pomeron into the language of QCD [18, 22], since it still lacks a fundamental formulation.

2.4.2. Multiple Parton Interaction

Multiple parton interaction (MPI) is a phenomenon which was introduced to describe inclusive charged particle multiplicities measured in hadron collisions. It is also an important mechanism to describe the "underlying event" activity which concerns all interactions but the hard scattering process within a proton-proton collision [24].

When Koba, Nielson and Olsen studied results on charged particle multiplicities measured at centre-of-mass energies up to $\sqrt{s} = 30$ GeV, they predicted an universal scaling law for inclusive charged particle multiplicities known as "KNO scaling" [25]. They claimed that distributions of charged particle multiplicities normalised to the mean number of charged particles are not a function of centre-of-mass energy, rather they can be rescaled for different energies. This concept was found to be in contradiction with measurements performed at higher centre-of-mass energies, when data from the Super-Proton-Antiporon collider Sp$\bar{\text{p}}$S and the Intersecting Storage Rings (ISR) at CERN became available covering energies up to $\sqrt{s} = 600$ GeV. Instead of a scaling behaviour, enhanced probabilities for high multiplicity events were observed [26, 27]. More recent are measurements by the CDF Collaboration at $\sqrt{s} = 1.8$ TeV with direct evidence of multiple parton interactions [28–30]. The concept of multiparticle production resolved the violation of the KNO-scaling making multiple scattering processes within a proton interaction responsible for the higher number of observed particles.

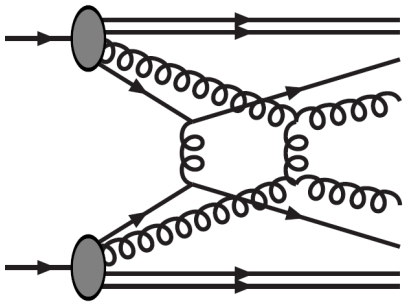

Figure 2.7.: $2 \to 2$ perturbative scattering process showing multiple parton interactions in a pp collision [31].

Modeling Multiple Parton Interactions

The basic concept for modeling MPI was initially formulated in [32] and still remains one of the few available models. The main idea to describe to some extent multiplicities of soft particle reactions is to extend perturbation theory down to relative low p_{T} values of around a few GeV remaining still above Λ_{QCD} [31]. The calculation of a partonic interaction is then described like for a hard process as illustrated in Fig. 2.7 and the cross-section keeps the form of the partonic cross-section convoluted with parton density. The **total cross-section** in perturbative QCD for the kth sub-process between parton i and j would then take the form

$$\sigma = \Sigma_{i,j,k} \int dx_1 \int dx_2 \int d\hat{t}\, \hat{\sigma}^k_{ij}(\hat{s},\hat{t},\hat{u}) \times f_i(x_1,Q^2) f_j(x_2,Q^2)$$

with x_1 and x_2 as the momentum fractions of the partons. The "hats" indicate that the quantity is related to the partonic interaction, $\hat{s}$, $\hat{t}$ and $\hat{u}$ are the Mandelstam variables satisfying $\hat{s}+\hat{t}+\hat{u} = \Sigma_i\, m_i^2$ and $\hat{s} = x_1 x_2\, s$. The structure functions $f_i(x_a, Q^2)$ give the probability of finding a parton i with a momentum fraction x_a in an incoming hadron a when probed at a scale Q^2. The **differential cross-section** tested at the scale $Q^2 = p_{\mathrm{T}}^2$ for a $2 \to 2$ perturbative parton interaction is

$$\frac{d\sigma_{\mathrm{int}}}{dp_{\mathrm{T}}^2} = \Sigma_{i,j,k,l} \int dx_1 \int dx_2 \int d\hat{t}\, \frac{d\hat{\sigma}_{ij\to kl}}{d\hat{t}} \delta\left(p_{\mathrm{T}}^2 - \frac{\hat{t}\hat{u}}{\hat{s}}\right) \times f_i(x_1,Q^2) f_j(x_2,Q^2)$$

Using perturbative QCD, one obtains for the differential cross-section a *divergent* expression proportional to $dp_{\mathrm{T}}^2/p_{\mathrm{T}}^4$ [32]. Subsequently, also the total interaction cross-section diverges for smaller p_{T} values:

$$\sigma_{\mathrm{int}}(p_{\mathrm{T}_{\mathrm{min}}}) = \int_{p_{\mathrm{T}_{\mathrm{min}}}^2}^{(\sqrt{s}/2)^2} \frac{d\sigma_{\mathrm{int}}}{dp_{\mathrm{T}}^2}\, dp_{\mathrm{T}}^2 \propto \int_{p_{\mathrm{T}_{\mathrm{min}}}^2}^{(\sqrt{s}/2)^2} \frac{dp_{\mathrm{T}}^2}{p_{\mathrm{T}}^4} \xrightarrow{p_{\mathrm{T}_{\mathrm{min}}} \to 0} \infty \tag{2.4}$$

A cut-off parameter $p_{\mathrm{T}_{\mathrm{min}}}$ is introduced which represents one of the main parameters of this model and different event generators handle this cut-off differently (see also Section 2.5.1). However, even at $p_{\mathrm{T}_{\mathrm{min}}}$ values of a few GeV, the interaction cross-section can exceed the total cross-section

$$\sigma_{\mathrm{int}}(p_{\mathrm{T}_{\mathrm{min}}}) > \sigma_{\mathrm{tot}}.$$

Two aspects play a role to explain this phenomenon [33]. Firstly, σ_{int} counts interactions, but σ_{tot} events. An event with two interactions counts twice in interaction cross-section but once in the total cross-section. Thus, the ratio of both cross-sections is a measure of the number of interactions per event which can be perfectly larger than unity

$$\frac{\sigma_{\mathrm{int}}(p_{\mathrm{T}_{\mathrm{min}}})}{\sigma_{\mathrm{tot}}} = \langle n \rangle (p_{\mathrm{T}_{\mathrm{min}}}).$$

The cut-off however is not the solution of the divergent interaction cross-section. The second aspect concerns the number of particles reduced by what is termed as *colour screening* and *colour saturation*. Both correspond to partons being unable to resolve each other as independent particles. Screening is an effect of the wave length of the exchanged parton which grows, when the wave length is made small. As consequence, the gluon can no longer resolve colour charges. This translates effectively into a decoupling of the particles with the $p_{\mathrm{T}_{\mathrm{min}}}$ as the inverse colour screening distance. Subsequently, the number of multiple interactions is reduced. This is more a heuristic description, theoretically it is not detailed understood in QCD how such a mechanism would work [33]. Saturation invokes explicit parton recombinations which reduces the growth of parton densities [34]. This reduction is rather a function of the momentum fraction x while screening effects depend on the p_{T} of the exchanged particle.

With increasing centre-of-mass energy physics at small x is probed where parton density functions rise more steeply and are less well measured. For a given $p_{\mathrm{T}_{\mathrm{min}}}$ the number of multiple interactions changes dramatically with s. At the same time, it is expected that with the increased number of partons the amount of screening grows. However, the non-trivial dependence of $p_{\mathrm{T}_{\mathrm{min}}}$ on the s is not well understood and therefore one of the important tuning parameters in Monte Carlo models to describe multiple parton interactions. Two Monte Carlo generators are therefore presented which adopt a different approach for modeling soft interactions.

2.5. Soft Interaction Models in Monte Carlo Generators

Monte Carlo event generators are computational programs calculating physics processes numerically combining perturbative and non-perturbative physics [17]. PYTHIA [33] is one of the widest used MC generators providing many free parameters to the user to adopt its model to experimental data. It is therefore outlined in more detail here. The concept of PHOJET [35] is as well described as it uses the dual parton model [36] as an alternative approach for soft particle production. In contrast to PYTHIA, PHOJET is not

anymore under active development. Both generators and various tunes (a certain set of parameters) will be confronted with measurements in Chapter 7.

2.5.1. Pythia

PYTHIA is optimised for simulations of $2 \to 1$ and $2 \to 2$ scattering processes at tree-level [31]. Most of these processes are hard interaction, but also a semi-hard and soft interaction processes use a perturbative approach as had been sketched in Section 2.4.2.

Simulation of a Hard Process with Contribution from Soft Interactions

An event with a hard interaction is simulated in different steps as depicted in Fig. 2.8. The hard process and its correlated decay products are calculated first. Therefore, the hard matrix element is computed to a particular order in perturbation theory while parton evolution is governed by DGLAP[6] equations. Initial and final state radiations are then included and multiple parton-parton interactions are added using the simulation of soft processes as described below (denoted as "Minimum Bias Collisions" in Fig. 2.8). The produced partons enter the showering sequence to which the experimentally determined PDFs are input, before in the last step all partons are hadronised, i.e. converted to colour neutral hadrons, using fragmentation models. More details of the single simulation steps can be found in [33, 34, 37].

Simulation of a Soft Process

The model of PYTHIA6 includes the simulation of non-diffractive events and the major types of diffraction (SD and DD), the latter based on Regge phenomenology. However, PYTHIA6 does not include the hard component of diffraction neither in p_{T} nor in the multiplicity distributions. This is visible in Fig. 2.9 (a,d) with the tail of the distributions consisting only of particles from ND events. The new PYTHIA version, PYTHIA8, has this component of hard diffraction incorporated [38].

For the simulation of non-diffractive events a number of options are implemented in PYTHIA. The model for MPI employed in PYTHIA ties in with the perturbative cross-section description of a $2 \to 2$ scattering.

The divergence as written in Eq. 2.4 is regulated in two steps. First, a $p_{\mathrm{T}_{\mathrm{min}}}$ cut-off is introduced which by default is not a sharp cut-off but is a sum of a fixed selected $p_{\mathrm{T}_{\mathrm{min}}}$ value and a term which is a free parameter tuned to data (in "complex" scenario).

Another parameter in PYTHIA for MPI modeling concerns the dependence of the impact parameter b in the scattering process. The largest number is expected for head-on collisions, while peripheral collisions are less probable to produce several parton-parton scatters corresponding to either a smaller or larger value of b.

To quantify the effect of overlapping protons an assumption about the time-integrated matter distributions $\rho(r)$ has to be made, chosen in PYTHIA to be a spherically symmetric double-Gaussian with individual mass densities [34]. In principle, $\rho(r)$ extends to

[6] after Dokshitzer, Gribov, Lipatov, Altarelli, Parisi

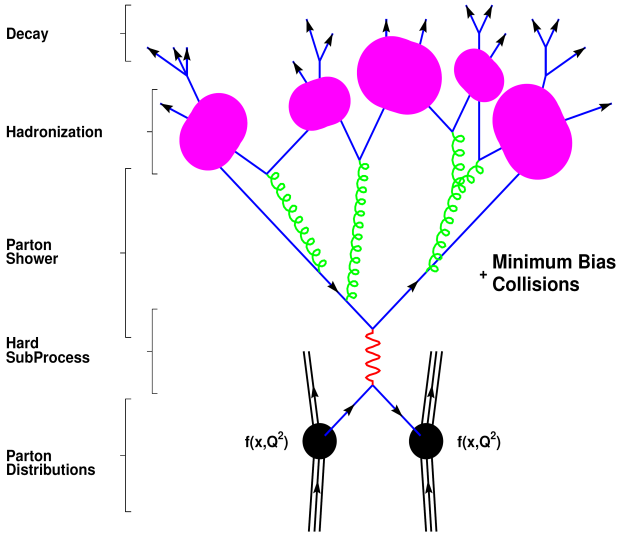

Figure 2.8.: Sub-processes of an event simulation of a hadronic interaction process [39].

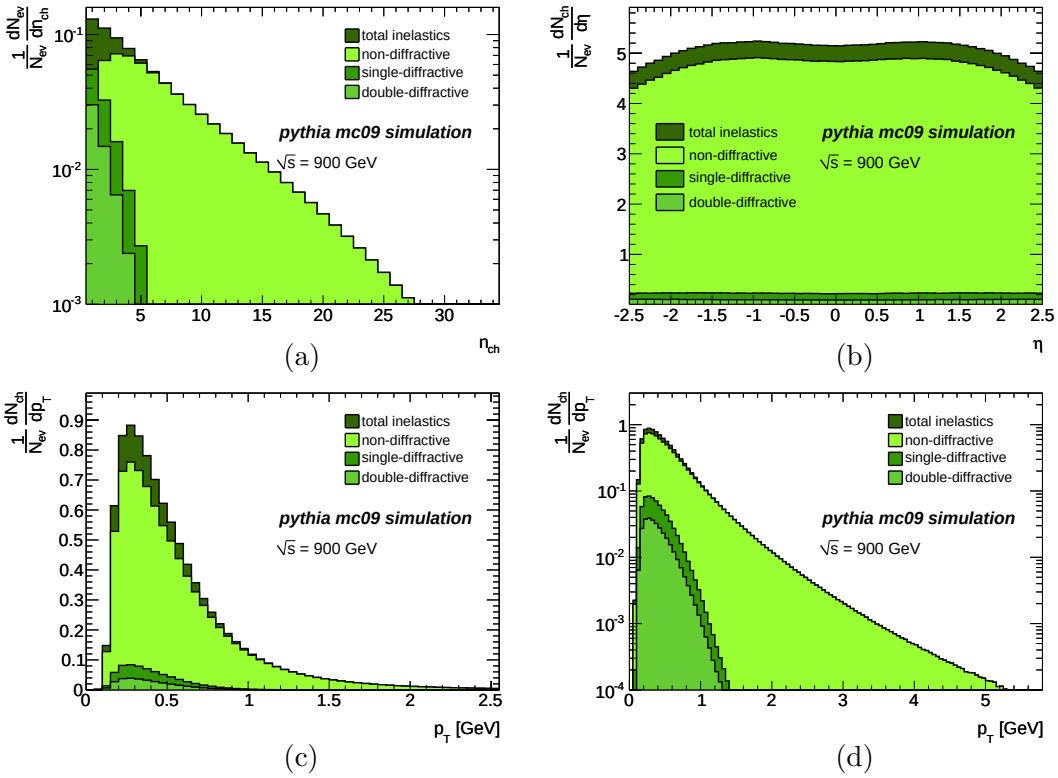

Figure 2.9.: Primary charged particle multiplicity n_{ch} (a), pseudorapidity η (b) and p_{T}-spectrum in linear (c) and log-scale (d). ND, SD and DD distributions are simulated in the ATLAS tune PYTHIA mc09 [40]. One can note the missing high multiplicity (a) and hard p_{T} (d) tail of the diffractive events.

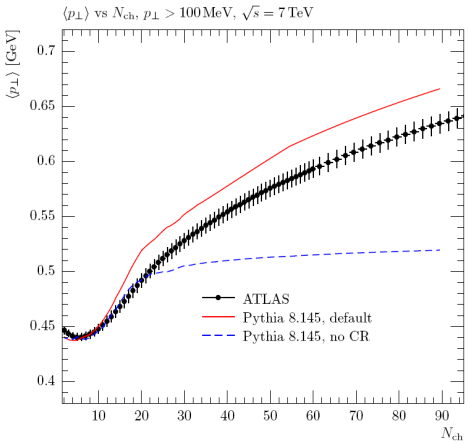

Figure 2.10.: Comparison of models in PYTHIA with and without colour reconnection (CR) compared to ATLAS data, taken from [34].

infinity generating events with very large impact parameters. To exclude these from the simulation a semi-hard interaction per event is necessary [31]. Finally, the number of interactions according to the overlap is then assumed to take place independently from each other distributed according to a Poissonian law.

One issue on how the colour charges of all parton-parton scatters are correlated remains unsolved for both versions. Certainly, there is a correlation arising from the nature of the incoming colour-singlets hadrons. The major difficulty is the modeling of multiple partonic interactions considering possible correlations between the partons of the proton. This requires multi-parton densities, i.e. joint probabilities to find n particles of flavors $\{f_i\}$ with proton momentum fractions $\{x_i\}$ when probed at interaction scales $\{Q_i^2\}$. No experimental data exists to describe multi-parton densities. PYTHIA instead *rescales* the one-parton density to model colour reconnection (CR) taking into account momentum and flavor conservation. At least from data it seems necessary that some amount of colour reconnection is needed as illustrated in Fig. 2.10 but it is equally visible that the colour flow during the hadronisation step is not fully understood. Further details can be found in [24, 31, 34].

Pythia Tunes

Several PYTHIA tunes are compared to data in Chapter 7 and are therefore briefly summarised here. Generally, ordering of objects is introduced in MC simulations. PYTHIA has several methods for ordering these objects (may they be jets or particles). More details can be found in [41, 42] and references therein.

- ATLAS MC09 [40]. This tune is PYTHIA6 based and uses the MRST LO$*$ parton density function [43] and a p_{T}-ordered showering model. It was tuned to Tevatron data from $\sqrt{s} = 630$ GeV to 1.96 TeV and was the default ATLAS choice for

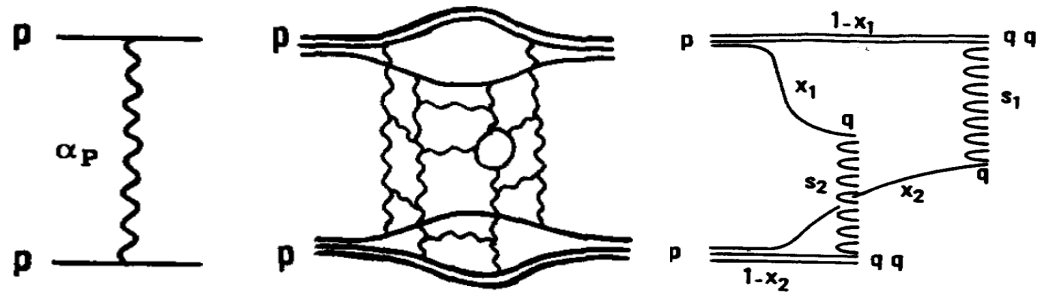

(a) (b) (c)

Figure 2.11.: $2 \rightarrow 2$ process within the Dual Parton Model [36]. (a) Single pomeron exchange in a proton-proton collision, (b) including higher order corrections from multiple pomeron exchanges. (c) The amplitude is calculated as a two chain diagram corresponding to two coloured, quark-diquark systems (only single pomeron exchange shown), obtained by applying "AGK"–cutting rules [36, 48].

event simulation before the LHC was operated with beams. The charged particle multiplicity and their kinematic spectra were shown in Fig. 2.9.

- DW [44]. PYTHIA6 based tune using Q^2-ordered showering. It was derived to describe underlying event data of CDF Run II.
- AMBT1 (ATLAS Minimum Bias Tune 1) [41, 45]. Based on PYTHIA6 and tuned to describe ATLAS data at $\sqrt{s} = 0.9$ and 7 TeV [46, 47] in a "diffraction suppressed" phase-space region ($n_{\mathrm{ch}} \geq 6$, $p_{\mathrm{T}} > 500$ MeV, $|\eta| < 2.5$).
- PYTHIA8 [38]. Default tune that contains an improved modeling of the diffractive components.

2.5.2. Phojet

PHOJET [35] deploys the *two-component Dual Parton Model* (DPM) [36] including soft and hard contribution into a single pomeron. With both these contributions it represents an attempt to give a complete picture of hadronic interactions at high energies. The DPM is a phenomenological expansion of QCD based on general properties of the scattering amplitude like duality and unitarity. These concepts were integrated into Regge theory ("Gribov's Regge Field Theory" [48]) and together with topological expansions of perturbative and non-perturbative QCD using essentially the partonic structure of the hadron a smooth transition between these regimes is obtained.

In the DPM, multiparticle production is governed by a single pomeron exchange for soft and hard processes [36]. However, to save s–channel unitarity the inclusion of multiple pomeron exchanges as higher order absorptive corrections are required as illustrated in Fig. 2.11. These have to be approximated with an appropriate description. In contrast to PYTHIA, PHOJET also describes the event class of central diffractive interactions.

2.6. Minimum Bias Observables

The usual observables for soft QCD measurements are those that characterise the basic properties of inelastic proton-proton collisions. The measurements using tracks only are reduced to measure *charged* particles, which are easily obtained by Monte Carlo generators for comparisons. The traditional multiplicity distribution of charged particles as well as their kinematic spectra generally probe the modeling of soft particle production including MPI. Another typical distribution had been shown already, the average p_{T} as function of the charged particle multiplicity which is sensitive to non-trivial changes of the colour topology in hadronic collisions. This potentially has an impact on the particle multiplicity in the final state [34]. Characteristic distributions that have been measured in the past [49–56] are

$$\frac{1}{N_{\mathrm{ev}}} \cdot \frac{\mathrm{d}N_{\mathrm{ch}}}{\mathrm{d}\eta}, \quad \frac{1}{N_{\mathrm{ev}}} \cdot \frac{\mathrm{d}N_{\mathrm{ev}}}{\mathrm{d}n_{\mathrm{ch}}}, \quad \frac{1}{N_{\mathrm{ev}}} \cdot \frac{1}{2\pi p_{\mathrm{T}}} \cdot \frac{\mathrm{d}^2 N_{\mathrm{ch}}}{\mathrm{d}\eta \mathrm{d}p_{\mathrm{T}}}, \quad \textit{and } \langle p_{\mathrm{T}} \rangle \textit{ vs. } n_{\mathrm{ch}} \tag{2.5}$$

where n_{ch} is the number of charged particles in an event, N_{ch} is the total number of charged particles in the data, N_{ev} is the number of events with a minimum number of charged particles within the selected kinematic range and $\langle p_{\mathrm{T}} \rangle$ is the average p_{T} for a given number of charged particles.

These typical distributions are measured using minimum bias data to obtain the *most inclusive results*. The first two, the **charged particle density per unit rapidity** and the **charged particle multiplicity distribution**, have often been measured in the past adding up information to improve soft QCD models. It is also standard to compare measurements of the charged particle density at $\eta = 0$. It should be noted though, that such values strongly depend on the normalisation factor N_{ev} and according to the analysis strategy, different event classes enter into that factor.

The last two distributions display in the p_{T} **spectrum** the soft character of these processes and **correlations to the charged particle multiplicity**. In Chapter 7 MB measurements have been performed in two dedicated phase-spaces following the strategy that allows direct comparisons with theoretical models.

2.7. Analysis Strategies of Minimum Bias Measurements

Several strategies under the name of minimum bias measurements exist which usually follow different intentions and are therefore not directly comparable. They can be generally classified as “NSD” and “INEL” measurements. However they have a few analysis steps in common.

INEL measurements are meant to characterise properties of *inel*astic hadron collisions in a well defined phase-space with *minimal* model dependency. The analysis essentially consists in selecting events with tracks produced from primary charged particles once reconstruction effects are mitigated. The correction of the data is done for detector effects, arising from the limited trigger acceptance, vertex and track reconstruction efficiency. The unfolding of the detector and reconstruction effects itself should as well

rely as much as possible on data, otherwise the model dependency enters indirectly into the measurements. A crucial role is taken up by the trigger used to collect the data and an independent reference trigger to quantify possible biases to the selected data. In Chapter 5 and 6, the development of such a trigger and trigger bias studies are described for exactly that purpose.

In non-single diffractive (**NSD**) measurements, one corrects as well for detector and reconstruction effects. However, the correction contains in addition a physics "correction". The approach is to measure only two event types with non- and double-diffractive interactions while one "corrects", i.e. removes contributions from single-diffractive processes. One thereby relys on the MC model to define this event class and remove the fraction that is accepted by the trigger too.

There exists also a hybrid type where one does not remove single diffractive contributions, but exptrapolates into phase-space regions which are not accessible by the detector. This as well introduces a model-dependent result.

Often, the charged particle density per unit rapidity and the multiplicity distribution have been measured following the traditional NSD strategy. The presentation of the data is then convoluted with information of Monte Carlo models. It becomes problematic, if such measurements from various experiments using different Monte Carlos models and tunes are directly compared, since the precise definition of the diffractive event types strongly model dependent.

Nevertheless, there are reasons for which the measurements of NSD distributions are thoroughly of interest. As example, for the analysis of heavy ion collisions proton-proton measurements are used as a reference to study the dynamics and models of particle production in an even more complex hadronic system. A ratio of proton-proton and nucleus-nucleus collisions can e.g. unveil properties in heavy ion collisions, that cannot arise from proton interactions [57]. Therefore, the ALICE and CMS collaborations have performed measurements following the NSD strategy [58–61]. The LHC experiments can indeed use the same Monte Carlo tune and obtain consistent results in proton-proton and lead-lead collisions.

2.7.1. The ATLAS Minimum Bias Analysis Strategy

The ATLAS Minimum Bias analyses follow the approach to measure INEL distributions presenting results with *minimal model dependency*. From such measurements it is trivial to apply model dependent cuts to compare e.g. to similar measurements in heavy ion collisions of NSD-type measurements. The emphasis for ATLAS is to produce measurements to improve Monte Carlo models in order to obtain a more precise picture of the true hadronic environment at the LHC.

The Minimum Bias analysis of this thesis in Chapter 7 was performed in the same spirit presenting measurements with minimal model dependency. With a prior agreement, ATLAS, CMS and ALICE applied the analysis method for INEL-measurements which allows for the first time a direct and consistent comparison of LHC results. Thereby, the analysis methods provide a further validation step on the roadmap to a more accurate modelling and ultimately a deeper understanding of these processes.

3. The Large Hadron Collider and the ATLAS Experiment

The LHC at CERN is a proton-proton ring accelerator with four major experiments probing the current theory of elementary particles, the Standard Model of Particle Physics, at unprecedented energies. Two general-purpose experiments, ATLAS and CMS, and two special-purpose experiments ALICE and LHCb were therefore contructed. The key operation parameters of the LHC are listed in Table 3.1 for the main phases of LHC operation. The physics programme of the two multipurpose experiments is essentially based on the highest achievable luminosity and energy, the special purpose experiments require lower luminosities. At LHCb it constantly is $\mathcal{L} = 10^{32}\,\mathrm{cm}^{-2}\,\mathrm{s}^{-1}$ over the whole operation period, while the nominal peak luminosity at ALICE is $\mathcal{L} = 10^{27}\,\mathrm{cm}^{-2}\,\mathrm{s}^{-1}$ with lead-lead collisions [62].

3.1. The LHC Complex

The design of the LHC machine [62] is driven by the physics requirements (see Chapter 2) and the available technology (and resources) that is described in the following.

3.1.1. The Accelerator Ring

The LHC complex, located at the border of France and Switzerland and around 100 m below ground level is illustrated in Fig. 3.1. It consists of a pre-acceleration part and the LHC ring itself of 26.7 km circumference. The LHC accelerator consists of eight sectors, each of them with a long straight section that is connected to curved parts (arcs), see

Table 3.1.: Machine parameters of the Large Hadron Collider. The number of colliding bunches is indicated for the high luminosity experiments ATLAS and CMS. The intensity of the proton beam is slightly higher than originally anticipated with $1.15 \cdot 10^{11}$ protons.

operation phase	start	$\sqrt{s}$ [TeV]	$\mathcal{L}$ [$\mathrm{cm}^{-2}\ \mathrm{s}^{-1}$]	# colliding bunches	intensity [protons]
commissioning	Nov. 2009	0.9	10^{27}	1	$0.9 \cdot 10^{11}$
initial physics	Mar. 2010	7	$10^{27} - 10^{32}$	1−1093	$1.2 \cdot 10^{11}$
physics	Apr. 2011	7	up to $2 \cdot 10^{33}$	1380	$1.2 \cdot 10^{11}$
nominal physics	(2014)	14	10^{34}	2808	$1.2 \cdot 10^{11}$

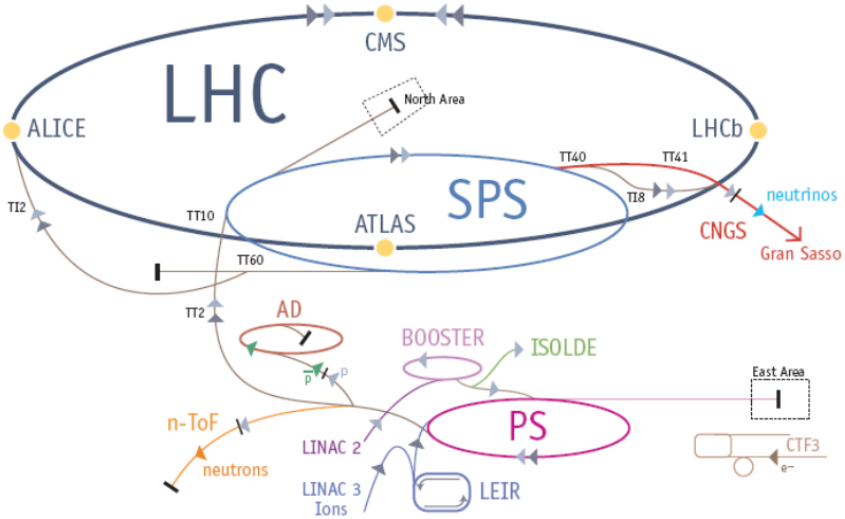

Figure 3.1.: The LHC Complex. The large experiments at CERN are constructed around beam crossing points at the LHC: ATLAS (Point 1), CMS (Point 5), ALICE (Point 2) and LHCb (Point 8).

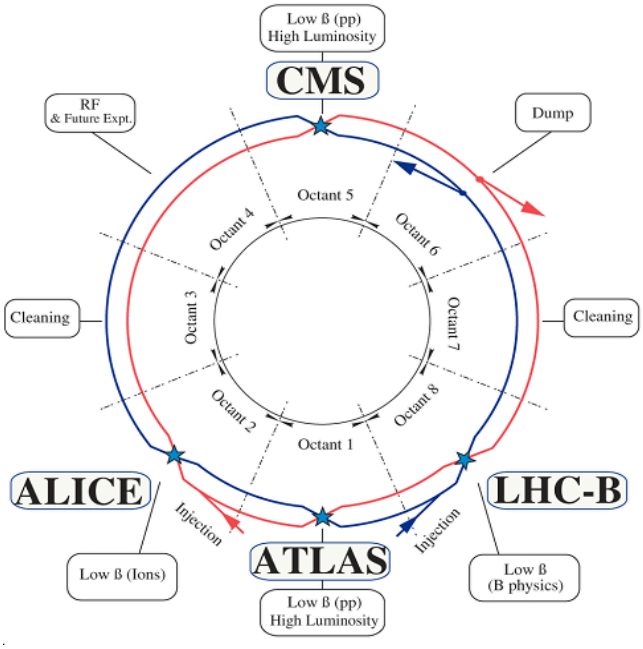

Figure 3.2.: Schema of the LHC and its 8 sections (octants). From 8 possible crossing-points four are used for experimental purposes used (stars). Other sections are used to store machine equipment for acceleration (section 4) and for momentum and betatron cleaning (section 3 and 7) [62].

Fig. 3.2. They house two independent systems for acceleration and storage of the beam particles.

The beams are injected in section 2 (beam 1, circulating clock-wise) and 8 (beam 2, rotating counter-clock-wise). Two independent super-conducting Radio-Frequency (RF) cavities are placed in section 4. In section 3 an insertion for *momentum cleaning* is installed where only particles with nominal momentum are kept for further transportation. Beam particles oscillating to far from the nominal position are intercepted by primary and secondary collimators within the *betatron cleaning* station in section 7. Two more tertiary collimators at 140 m upstream of ATLAS and CMS complete the collimation system of the LHC, essential to handle the intense beams. The task of the multi-stage collimator system is not only to prevent quenches, but also to provide passive protection of other LHC equipment and minimise halo induced background at the experiments (see also Section 3.1.4).

Pre-Acceleration of Protons Protons extracted from hydrogen atoms enter the injection chain at the linear accelerator LINAC2, see Fig. 3.1. With 50 MeV they reach the Proton Synchrotron (PS) Booster that boosts the particles to 1.4 GeV. In the PS and Super PS, the protons are accelerated to 450 GeV. They enter the LHC ring for final acceleration to nominal 7 TeV.

Acceleration of Protons Proton are injected into the LHC ring with an energy of 450 GeV which is "ramped up" in RF super-conducting cavities where they acquire the nominal energy of 7 TeV. Strong magnetic fields are needed to steer, bend and focus the protons. This is achieved using super-conducting technology. 1232 cryodipole, around 400 quadrupole and more than 4000 corrector magnets are therefore installed and immersed in a superfluid helium bath at 1.9 K. A nominal current of 12 kA generates then a magnetic field of 8.33 T. As the super-conducting magnets are sensitive to heating from the beam or other sources, they will loose super-conductivity (*quench*) if more energy than 5 mW/cm^3 is deposited by continuous heating or more on a shorter time scale [63]. Therefore, a sophisticated collimation and quench protection systems are indispensable. The LHC has experienced a failure of such a system in 2008 on September 19$^{\text{th}}$, where a small quench was undetected and led to discharge of energy into the -271° C cold helium vessel, triggering over a year of reparation work and new developments for additional safety procedures [64].

In normal conditions, the beam collides over a period of several hours for physics purposes. At the end of this period or in case of a failure detection, the beam dump (or beam abort) system in section 6 allows to extract the beam safely and dump it into a large block of concrete that is capable of absorbing fully the stored energy of the beams.

3.1.2. LHC Operation Parameter

The main characteristics of the LHC are the luminosity and the centre-of-mass energy at the crossing points. The **luminosity** can be expressed by [3]

$$\mathcal{L} = f \frac{n_1 n_2}{4\pi \, \Sigma_x \, \Sigma_y} \tag{3.1}$$

with f the revolution frequency of the particles, n_1 and n_2 the beam charge of beam 1 and beam 2 respectively and $\Sigma_x = \Sigma_y$ representing the Gaussian transverse beam profiles in the horizontal and vertical directions. The beam size can also be expressed in terms of *transverse emittance* and amplitude function β. The transverse emittance reflects the process of bunch preparation extending back to the source of hadrons. In the case of the LHC, the PS Booster, the first proton synchrotron in the injection chain, already shapes the transverse size of the bunches, while the longitudinal size is shaped only before the collision points. The amplitude function β is a quantity determined by the accelerator magnet configuration. Accelerated particles oscillate usually around their ideal path (***betatron oscillations***). The β-function describes the amplitude ("envelope") of the motions of the particles. Representing the emittance ϵ in terms of Σ and β by

$$\epsilon_i = \frac{\pi \, \Sigma_i^2}{\beta_i} \quad \text{with} \quad i = x, y \tag{3.2}$$

the luminosity formula 3.1 becomes, considering both directions x and y,

$$\mathcal{L} = f \frac{n_1 n_2}{4 \sqrt{\epsilon_x \beta_x^* \, \epsilon_y \beta_y^*}} \tag{3.3}$$

where the β^* is the beta function at the collision point. Clearly, to achieve a high luminosity one would like to make that value as small as possible, populate the bunches with a high number of protons and get the emittance as low as the accelerator hardware allows. During the acceleration process the emittance is reduced with every turn. If scaled according to the momentum, the emittance can be preserved and the luminosity $\mathcal{L}$ using the ***normalised emittance*** $\epsilon_n = \beta\gamma\epsilon$ with γ the relativistic factor, can be directly expressed as function of the machine parameters

$$\mathcal{L} = f \frac{n_1 n_2 \, \gamma}{4\pi \epsilon_n \beta^*}. \tag{3.4}$$

At the LHC when operated with nominal parameters, the bunches of particles will collide with a crossing angle, thus another factor has to be applied considering it [62]. The Rate R of a certain interaction process is given by the product of the luminosity and the cross-section of a certain process σ_{int}

$$R = \mathcal{L} \cdot \sigma_{\text{int}} \tag{3.5}$$

and the number of events with such interaction rises proportionally to the integrated luminosity $\int \mathcal{L} \, dt$. The two beams in the LHC are symmetric, i.e. it is aimed for the

same energy, shape and initial intensity. The **centre-of-mass energy** $\sqrt{s}$ is then given by the beam energy E_{beam}: $\sqrt{s} = 2E_{\text{beam}}$.

3.1.3. Filling Scheme

The filling schemes of the LHC account for the different emphasis of the high luminosity and special purpose experiments [65]. While for ATLAS and CMS the number of useful collisions is maximised, it is optimised for ALICE and LHCb. In particular, the number of collisions at ATLAS and CMS can be different by several orders of magnitudes from those in ALICE without changing optical parameters. Boundary conditions for any LHC fill is defined by the accelerator chain prior to the LHC injection which arranges the bunches in *bunch trains* for the physics runs.

The RF frequency of 400.8 MHz and the revolution frequency of the protons of 11.245 kHz define the underlying scheme for the LHC fills. In total 35640 "buckets" are available which could be filled with protons. As it is planned to operate with a bunch-crossing rate of 40 MHz, a tenth of them are potential slots to be filled. These bunches are numbered by *bunch-crossing identifiers* (BCIDs).

In order to meet the individual luminosity requirements at each interaction point in the LHC, the filling scheme follows a certain pattern. Filled bunches will collide in ATLAS and CMS, if the bunch number difference is zero and they can only collide in ALICE and LHCb, if the bunch number of both beams is shifted by a certain number, 891 or 894[1], respectively. A bunch spacing of 25 ns allows collisions in all four interaction points of the experiments. This changes for different spacings, e.g. an equidistant filling pattern of 50 ns without any shifted bunches would produce collisions at ATLAS and CMS, but none at ALICE and LHCb. Such a filling scheme but with a few shifted bunches was considered as commissioning scheme [65, 66] and was indeed used in 2011 for physics fills.

A scheme with 43 filled bunches in one beam and 43 in the counter-circulating beam ("43 × 43") was used in the initial phase of LHC running with *displaced bunches* in order to produce collisions also at LHCb [65]. Those displaced bunches can also collide in ATLAS but not at the nominal interaction point. Apart from colliding and displaced bunches, there are also *unpaired* bunches. These are single proton bunches that have an empty bunch in the corresponding bucket of the other beam such that no crossing with another filled bunch takes place at the interaction point. These bunches, in particular when they possess the same intensity and shape like the colliding bunches, are very useful to the experiments to estimate the rate of machine induced background interactions.

3.1.4. Machine Background

Machine induced background (often also just beam background) usually refers to interactions not arising from beam-beam crossings, instead the beam interacts with the machine aperture or with a residual gas molecule in the beam-pipe. In the detector they

[1] This shift accounts for the additional displacement of the interaction point 8 (LHCb) of 11.25 m.

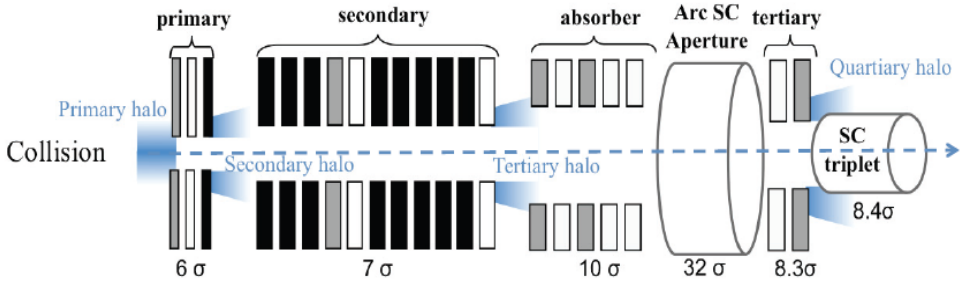

Figure 3.3.: Sketch of the multi-stage cleaning insertion of the LHC collimator system in section 7 (betatron cleaning) [67]. The positions during collision mode of the primary, secondary and tertiary collimators are indicated in units of 1 σ, a measure of the nominal beam size. Beam particles and halo particles off the beam are highlighted as spray (in blue). They can be guided until the experimental halls.

show distinct topologies which was used for in the detector commissioning phase (see Section 4.4.1).

For the experiments it is important to know at which rate such beam induced backgrounds take place for example in order to monitor the radiation dose the sub-detectors are exposed to, to study event characteristics of these events and eventually also to provide feedback to the LHC control centre which may use this to optimise e.g. settings of the collimator system.

Beam Halo

At certain places in the LHC tunnel particle losses are expected, especially at locations where the collimation systems are situated at Point 3 and 7. The beam is scraped in several stations as visualised in Fig. 3.3. Typically muons survive the last collimator station (for ATLAS and CMS these are the tertiary collimators 140 m upstram) and reach the experimental halls. The beam is accompanied by a beam halo of particles that deviate significantly from the beam orbit, but are still accelerated to the full beam energy [68]. A typical beam halo event shows parallel tracks in the detector. Their rate are expected to diminish with larger radial distance to the beam pipe.

Beam Gas

They contain interactions of the beam with a gas-molecule. Those relevant for the experiments take place at any place along the beam-axis inside the detector. Such events usually exhibit forward boosted particles and their rate strongly depends on the vacuum quality in the beampipe, the quality of the beam (ideally no losses) and the settings of the beam aperture.

3.1.5. Pile-Up

The large interaction rate at ATLAS and CMS produces multiple proton-proton collisions within one bunch-crossing, *pile-up* or more specificly *in-time* pile-up events. With a total inelastic cross-section of the order of $\sigma_{\text{inel}} \approx 100$ mb, the delivered interaction rate is 1 GHz at nominal luminosity. The foreseen bunch-crossing frequency of 40 MHz will then produce on average more than 20 proton-proton collisions per bunch-crossing and only one of them may be of interest for searches of new particles exhibiting a large momentum transfer, other events contain soft inelastic interactions (see Section 2.4).

A different type are *out-of-time* pile-up events that contain interactions from previous bunch-crossings. They have an equally strong influence on the design of the LHC detectors and physics analyses. Many sub-detectors have a response time larger than the 25 ns, thus this type of pile-up become more relevant when the bunch-spacing is reduced.

Since detector response functions are somewhat straight forward to implement into the detector simulation out-of-time pile-up can be well simulated. Condition to that is however, to know the underlying physics structure of these events which is not the case. Therefore, in-time pile-up events are more relevant for the present work being a major motivation to select and study characteristics of low p_{T} events.

3.2. The ATLAS Experiment

The ambitious physics programme of the ATLAS experiment as discussed in chapter 2 imposes stringent requirements to the design of the detector hardware, data-acquisition systems and also on the ATLAS software.

The basic layout of the ATLAS detector [69] is driven by the magnetic fields, an outer one of a field strength of up to 4 T for measuring muon momenta and an inner one of 2 T for momentum measurement of any other type of charged particle. The outer part of the detector consists of the muon system and the toroidal magnets. The inner part of the detector is composed of high precision tracking detectors immersed within the 2 T homogeneous magnetic field. In between, is the calorimetry system, an electromagnetic and hadronic calorimeter to measure the energy of particles that undergo either an electromagnetic or hadronic interaction. Most of the produced particles can be stopped in these detectors or if interacting only weakly at least unbalanced momentum of that particle can be reconstructed.

The following sections describe the hardware of the sub-detectors with emphasis on the devices used for minimum bias triggering and charged particle multiplicity analysis.

3.2.1. The Inner Detector

The Inner Detector (ID) is a multi-technology tracking system designed to provide robust pattern recognition with high p_{T}-resolution in the pseudorapidity region $|\eta| < 2.5$ for tracks with 500 MeV $\lesssim p_{\text{T}} \lesssim$ 500 GeV. A schematic view is given in Fig. 3.4 showing the

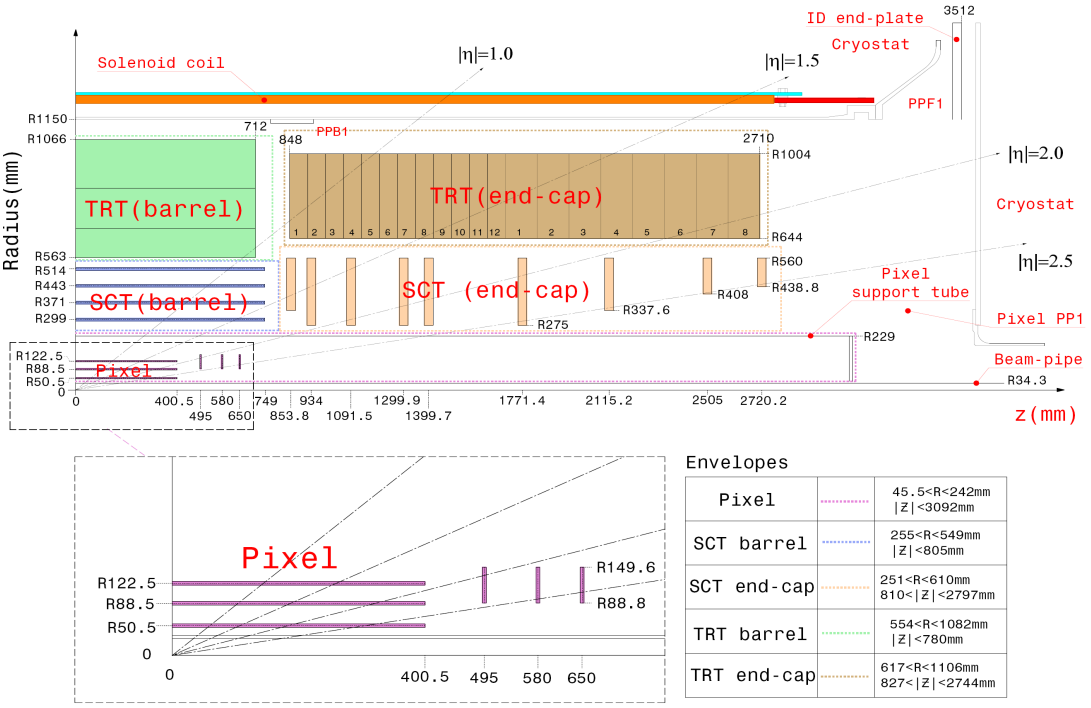

Figure 3.4.: Schematic view and detector acceptance of the Inner Detector [69].

two innermost silicon detectors Pixel and Semiconductor-Tracker (SCT) and the drift tubes based transition radiation tracker TRT.

The ID, especially the Pixel detector, is exposed to high doses of up to 160 kGy/year[2] [69]. The continuous irradiation requires not only a radiation hard sensor material but also radiation hard electronics. To minimise effects of radiation damage over the lifetime of the experiment both the Pixel and SCT detectors are operated in a cooled environment ranging from $-5°$ to $-10°$ C, enabling accurate position measurements of single particles also at high detector occupancies.

3.2.2. The Pixel Detector

The Pixel system consists of three barrel layers (with the first layer named “B-layer”, as used in Section 6.2) and two identical endcaps with each three disks. The basic unit of the Pixel detector is a unified designed module mounted on mechanical and cooling and support structure elements named staves in the barrel and sectors in the endcap. In total there are 1456 modules in the barrel region and 288 modules in the endcap regions corresponding to more than 67 and 13,2 million readout channels, respectively.

[2] A dose of 1 Gy (gray) corresponds to the absorption of 1 joule of radiation energy per kg of the absorbing material. 1 year means $8 \cdot 10^{15}$ inelastic pp collisions assuming a cross-section of 80 mb and 10^7 seconds data-taking at $\mathcal{L} = 10^{34}\,\mathrm{cm}^{-2}\,\mathrm{s}^{-1}$.

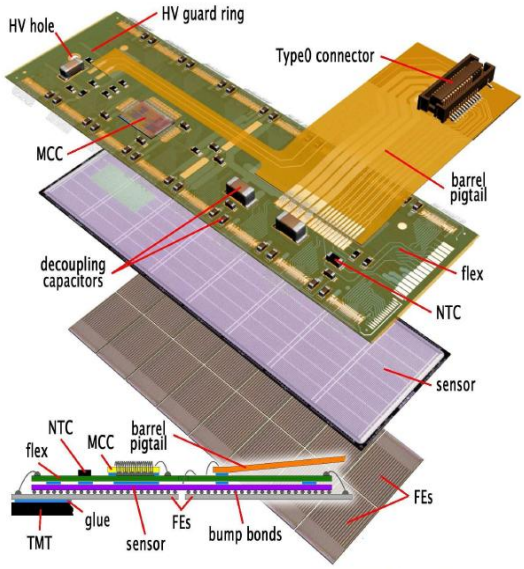

Figure 3.5.: Layout of a Pixel module showing the 16 front-end chip at the bottom, the sensor layer in the middle and the flexible printed circuit board at the top [69].

The Pixel Module

A Pixel module [70] consists of a stack of three main layers as illustrated in Fig. 3.5. The middle layer with 47,232 pixel cells is the sensitive part of the pixel detector used to detect charged particles. It consists of an array of bipolar diodes placed on an n-type bulk, the *Pixel wafer*. The sensor is made by implanting high positive (p^+) and negative (n^+) dose regions on each side of the wafer, such that a n^+–in–n junction is on the top (readout) side and a p–in–n junction on the bottom side. This novel design involving double-sided processing was chosen due to stringent specifications on radiation hardness [69].

Each pixel channel is bump-bonded to a front-end chip, 2880 per chip and 16 chips for each module. The signal of a pixel cell is read out if enough charge is released by an incident particle in order to pass a programmable threshold. The pixels are organised in column-pairs for a column-based readout architecture. This prvides a handle on such a high number of readout channels and ensures efficient data collection. Especially, empty channels are skipped in the readout (*zero-suppressed readout*).

The top layer is a flexible circuit board with the Module Control Chip (MCC). The MCC is clocked in the same frequency as the LHC clock in units of 25 ns (1 BC) and is amongst others responsible for distributing timing signals such as the clock in BCs and L1 triggers to the front-end chips. It also issues the readout of data on the front-end chip and the event building in case the data are requested as indicated by the L1 trigger signal transmitting them to the readout drivers.

The nominal size of a pixel is 50×400 μm^2, called *normal* pixels. To ensure also sensitivity at the boundaries of a module a sophisticated readout strategy is applied:

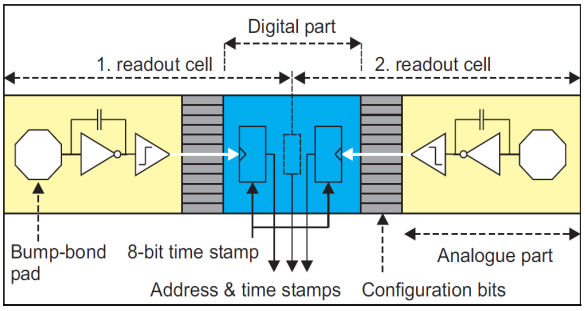

Figure 3.6.: Signal readout of a Pixel module showing the analogue and digital blocks [70].

11 % of the pixels have a size of 50 × 600 μm^2, referred to as *long* pixels, and are placed at the long sides of the frontend, covering one part of the inter-chip-region. On the short side, that region is covered with pixel pairs that are joint by a metal strip on the sensor. These are called *ganged* pixels (2%). Combination of both pixel types are possible in the corners and are called *long-ganged* pixels (2%). This reduces the total number of pixels read out to 46,080. With this interconnection stratgy a spatial resolution of 14 μm in the r$\phi-$plane and 115 μm in the z-direction is achieved.

Measuring the Time-over-Threshold The charge released by an incident charged particle is measured indirectly by the time that the signal stays above a certain threshold (time-over-threshold, ToT) measured for each pixel cell.

Each pixel cell has an analogue block and a digital block as illustrated in Fig. 3.6. In the **analogue block** the charge signal is amplified by a *charge sensitive preamplifier* and then discriminated by comparing the charge to a programmable threshold. The preamplifier has a feedback-loop that consists of a capacity with 15 ns risetime, shown in Fig. 3.6 parallel to the preamplifier, and a configurable current source that is parallel to the capacitor (not shown). That current regulates the discharge of the capacity and thereby the width of the signal. This current has also the property to produce a discriminated output charge that is almost linear response to the input charge. The width of the discriminated signal is a measure of the signal amplitude, the ToT, and is measured in units of the MCC clock cycles, i.e. in units of BCs. The tuning of the discharge current depends on the expected occupancy of the detector. Since nominal occupancy has not been attained so far, the discharge current was set to 4 nA. A charge of 20,000 e (electron charge) that is expected to be released by a minimally ionizing particle (MIP) when passing through the 250 μm thick sensor, is tuned to correspond to a ToT of 30 BCs [70]. The **digital readout block** transfers the timestamp of the leading edge and the timestamp of the trailing edge to the buffers at the chip periphery, where the ToT, the difference between these two timestamps, is calculated. An 8-bit long value is used allowing ToT values of 0 to 255 BCs. This permits each sensor to measure up to 8.5 times the charge of a MIP.

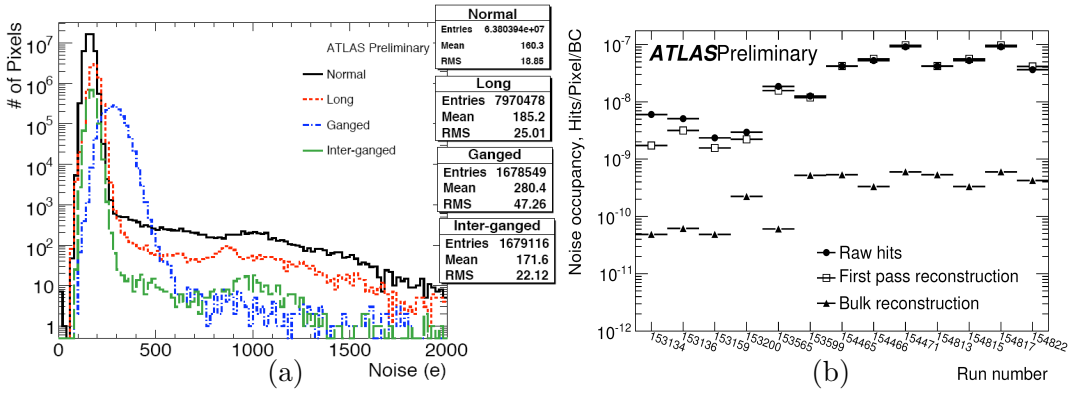

Figure 3.7.: (a) Noise of different pixels types and (b) noise occupancy per Pixel over several runs in 2010 shown for raw hits, after first pass of reconstruction without offline noise masks and after the bulk reconstruction using the offline noise masks [71].

Pixel Threshold and Noise Occupancy Before the information of a hit in the pixel sensor is transferred, it has to pass a discriminator threshold. This threshold is tuned for each Pixel such that essentially two requirements are fulfilled. Firstly, the response to a certain amount of charge should be uniform across the Pixel detector. This is achieved by setting the same preamplifier gain for all readout cells and adjusting discriminator thresholds. The second requirement for the threshold is to ensure a clear, 5σ differentiation of the signal. The noise in a normal pixel is around 160 e which can be seen in Fig. 3.7 (a), where the noise charge is shown for different Pixel types. Ganged pixels produce almost twice as much noise as a normal cell. The threshold of each Pixel was then tuned to 4000 e. Rather recent noise calibration studies motivated a threshold of 3,500 e [71].

Thus, the noise signal of each Pixel has to be significantly smaller than the threshold and most of the normal pixels meet this requirement quite well. The noise occupancy per pixel and per readout of a 25 ns window is less than 10^{-9} as one can see from Fig. 3.7 (b). It is measured by randomly reading out the Pixel detector with no observed reconstructed tracks. A noisy pixel map is generated where pixels that had an occupancy higher than 10^{-5} are masked ("noisy" channels) [72]. The reduction of noise by applying the noise mask and the stability of the noise occupancy over time confirms that most of the noise come from the same, a few hundred pixels. While an offline mask excludes single pixels from reconstruction, the online mask excludes pixels directly from the readout.

3.2.3. The Semiconductor-Tracker Detector

The Semiconductor Tracker is based on silicon strip technology and covers the complete Inner Detector acceptance. It is divided into a barrel part of four concentric cylinders at radial positions of 300 mm, 373 mm, 447 mm and 514 mm and an endcap part of nine disks on each side at z-positions ranging from $z = \pm 835\,\text{mm}$ to± 2778 mm as shown

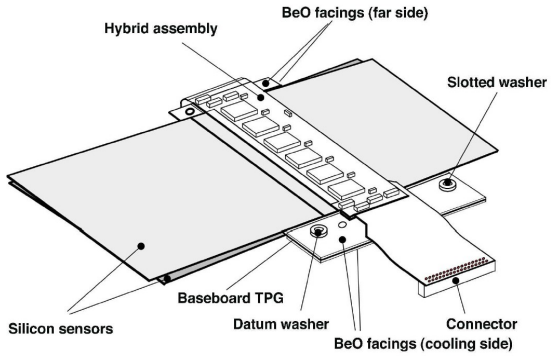

Figure 3.8.: An SCT module showing two staggered silicon sensors [69].

in Fig. 3.4. The cylindrical layers comprise in total 2112 SCT-modules while all disks count 1976 modules. The modules in the endcaps are slightly differently constructed being tapered in order to be arranged in circular sectors. On a single module four sensors are mounted, two at the front- and two at the back-side, glued back to back and shown in Fig. 3.8. Each sensor is a p-strip readout in an n-bulk silicon (p–in–n sensor). It has a size of 63.6 mm length and 64 mm width and contains 768 strips. One microstrip is 18 μm wide and 62 mm long. The strips have a constant pitch of 80 μm in the barrel and an average distance of 80 μm in the endcaps. Two of the sensors are daisy-chained forming a strip length of 12.8 cm. The back-side is staggered by a small stereo angle of 40 milliradian (2.3°) which gives a $r\phi-$resolution of about 20 μm. The introduction of a stereo angle between front- and back-sensors is primary done to be able to resolve the dimension along the z-axis, transverse coordinates given by the module position. The amount of rotation with respect to the front-side was chosen to be very small in order to reduce the crossing points of the strips. Thereby less fake spacepoints, so-called *ghosts* are formed. An advantage of the microstrip concept compared to Pixel readout is an intrinsic noise suppression due to the requirement of hit coincidence for spacepoint formation in the SCT, which is exploited for noise event rejection.

SCT Readout Per module there are six front-end chips each of them consists of control sections and 128 readout channels. The control sections are likewise clocked by the LHC frequency of 40 MHz, they receive the readout trigger signal, apply one threshold for the 128 front-end transistors and contain analogue-to-digital converters for the binary readout of the SCT. The discriminator threshold is set to 1 fC $= 10^{-15}/1.6 \cdot 10^{-19} \triangleq$ 6250 e. The target noise should not exceed 1500 e corresponding to an occupancy of $5 \cdot 10^{-4}$ [73]. The operation of the SCT detector will be at -7°C in a dry nitrogen environment to minimise radiation damage as it is foreseen to employ the SCT devices for the entire nominal LHC operation period of ten years.

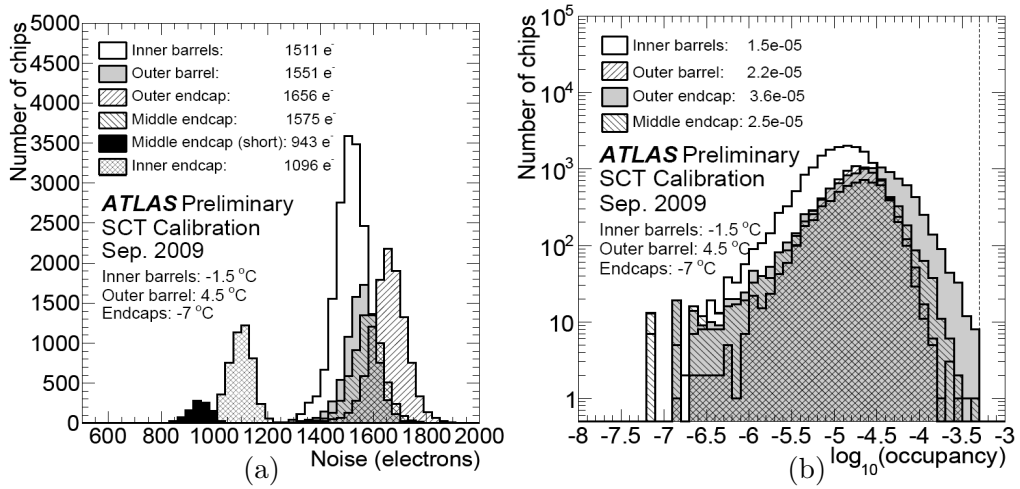

Figure 3.9.: Noise charge (a) and noise occupancy (b) in the SCT measured in the barrel and endcap modules [74].

3.2.4. The Transition Radiation Detector

The TRT is the outermost tracking system of the ID as visible in Fig. 3.4, and consists in total almost 300,000 carbon fiber drift tubes (*straws*). It is divided into a barrel region with three layers arranged around the beampipe and two identical endcaps made of eight inner and 12 outer wheels per side. Each straw, a kapton tube wound around the carbon fibre, has a diameter of 4 mm with a 31 μm thick tungsten wire and is filled with a gas-mixture of 70% Xe, 27 % CO_2 and 3 % O_2. The spatial resolution is comparatively low with 130 μm in $r - \phi$, but one track contributes on average more than 30 hits (*drift-circles*) [69]. By traversing a straw, the charged particle ionises the gas creating ions along its track. These ions will drift within a certain *drift time* specific to the gas-mixture in an high electric field to the respective electrode giving signals in the order of arrival. To produce transition radiation from electrons, radiator foils are placed in between the drift tubes. Two signal thresholds can then be passed, a lower one providing position information, and a higher one for the detection of transition radiation.

3.2.5. The Calorimeter

The calorimetric system is installed around the inner tracking system. An overview of the single components is given in Fig. 3.10. It provides high precision measurements of electrons, photons, jets and missing transverse energy. ATLAS uses the *sampling* method for electromagnetic and hadron calorimetry where active material is interleaved with passive absorber material. The operation in the environment of high multiplicity events resulted in two different techniques that are employed for the calorimeters; liquid argon (LAr) and tile technique. LAr is used for the inner parts of calorimeters, in the electromagnetic barrel and endcap region as well as in the hadronic endcaps (HEC) and forward calorimeter (FCAL). For more details on the calorimetry it is referred to [69].

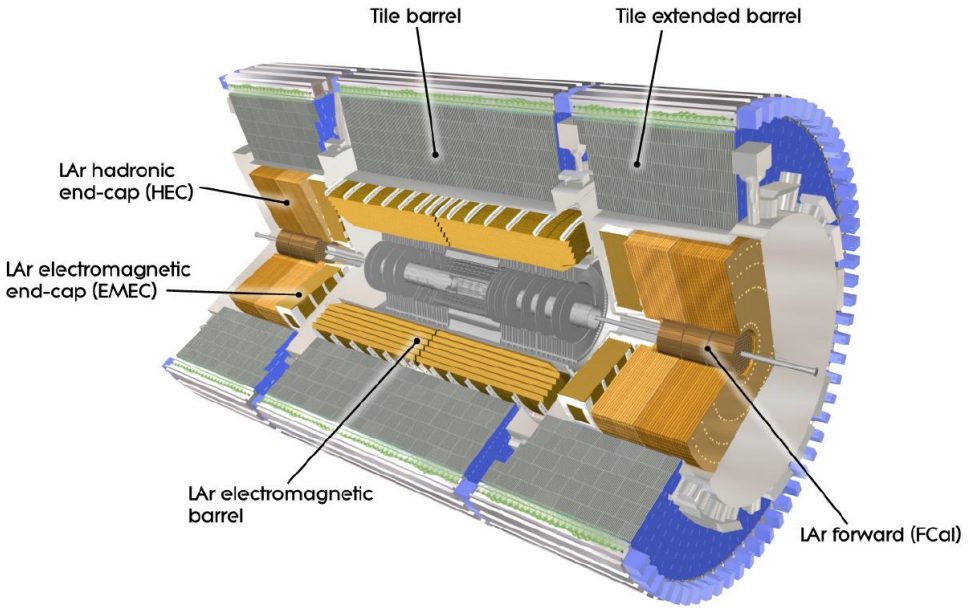

Figure 3.10.: Calorimetric system in ATLAS. The electromagnetic calorimeters are based on the LAr technique. The hadron calorimeter uses partly the LAr technique in the endcaps and iron tile scintillators at larger radii.

3.2.6. The Minimum Bias Trigger Scintillators

The minimum bias trigger scintillators (MBTS) have two purposes. Before the ATLAS detector can be operated at nominal conditions, an effective mean was needed for detector commissioning able to trigger on pp collisions and to veto beam-background events if necessary. A total of 32 scintillator counters where installed, 16 on each side of the detector mounted on the inner face of the end-cap calorimeter cryostats. The counters are segmented in two rings with each eight cells per ring covering in total a pseudorapidity range of $2.09 < |\eta| < 3.84$, see Fig. 3.11. They are about 2 cm thick and made of polystyrene ("plastic"). The light yield of this material is expected to degrade significantly after a few months of operation at higher luminosities of $\mathcal{L} = 10^{33}\,\mathrm{cm}^{-2}\,\mathrm{s}^{-1}$. These scintillator counters were doped with boron for its second purpose. Once, the scintillators loose their functionality due to irradiation, they will serve as a shield to protect the calorimeter from mostly thermal neutrons [75].

The readout of the MBTS signals is sketched in Fig. 3.12 and employs the same electronics as used for the tile-calorimeter cells. The light produced in the scintillators is collected through wavelength shifting fibers and read out by photomultipliers (PMTs) for each counter separately. The analogue signals are amplified (NIM-amplifiers) such that the noise is visible within the operating range of the leading edge discriminators in order to allow a discrimination just above the noise. The amplified signal is either

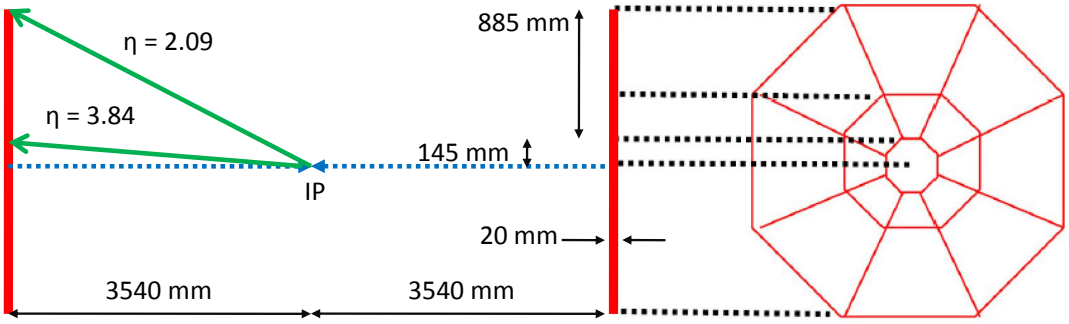

Figure 3.11.: Sketch of dimensions of the Minimum Bias Trigger Scintillators (MBTS).

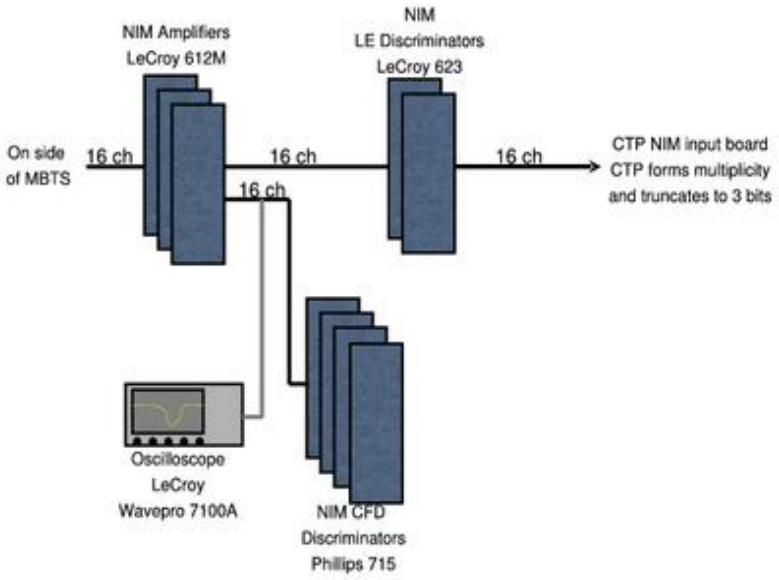

Figure 3.12.: Readout of MBTS signals for one side. The MBTS signals are amplified, discriminated and sent to the Level-1 Central Trigger Processor. For commissioning the amplified signals can be validated by an oscilloscope and discriminated by a Constant-Fraction-Discriminator (CDF) able to flag non-collision like events (not used for trigger) [76].

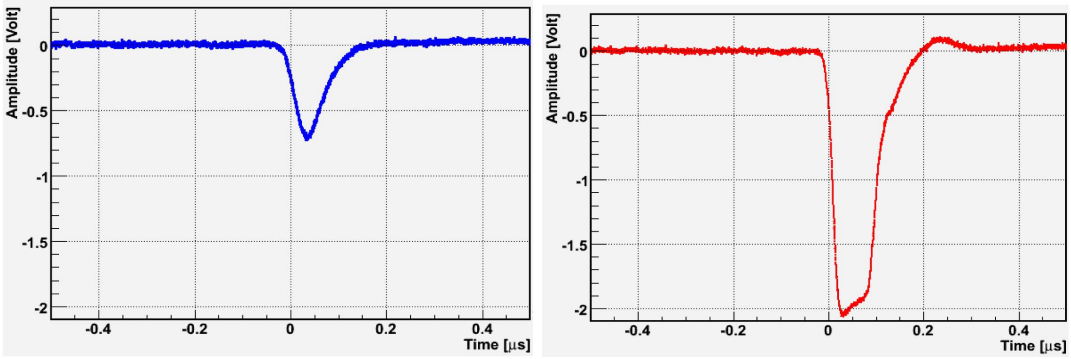

Figure 3.13.: Oscilloscope traces of MBTS signals after amplification for a cosmic ray track (a) and a beam splash event (b) [77], see also Fig. 4.8.

output of the Low-Gain (×1) or High-Gain (×64). While MBTS uses the High-Gain output, all tile-calorimeter cells use the Low-Gain output.

MBTS Signal Reconstruction

Two steps are necessary to reconstruct the signal amplitude, the phase and other quantities like the pedestal of the signal. Amplitude and phase correspond to the deposited energy and time, respectively. The pulse is first digitised with a programmable length of up to 16 samples. During the data-taking period in 2009 and 2010, seven samples were kept in case of an event accept: the first and last two provide the pedestal of the signal, the three others are used for the signal peak. Sampling is done every 25 ns, spanning a time window of 150 ns. An optimal filtering method [78] is executed on the Read-out-Drivers which are equipped with digital signal processors. These analogue-to-digital (ADC) counts are fitted and quantities like amplitude, phase, pedestral are extracted. The offline reconstruction uses the ADC counts in a more sophisticated method to extract these values [79].

Commissioning of MBTS

During the commissioning phase each counter was calibrated by charge injection and one calibration factor was obtained for all counters [80]. Initially (2009 running period), the discriminator threshold was set to 30 mV corresponding to 0.13 pC for all counters, when the PMTs were operated at 700 V. After increasing the high-voltage to the maximum of 900 V for the first pp collisions in March 2010, this threshold was raised to 50 mV (0.23 pC). In January 2010, one of the inner scintillator counters (EBC05) lost power supply and had to be turned off since. However, this was studied to have no impact on the overall sensitivity of MBTS.

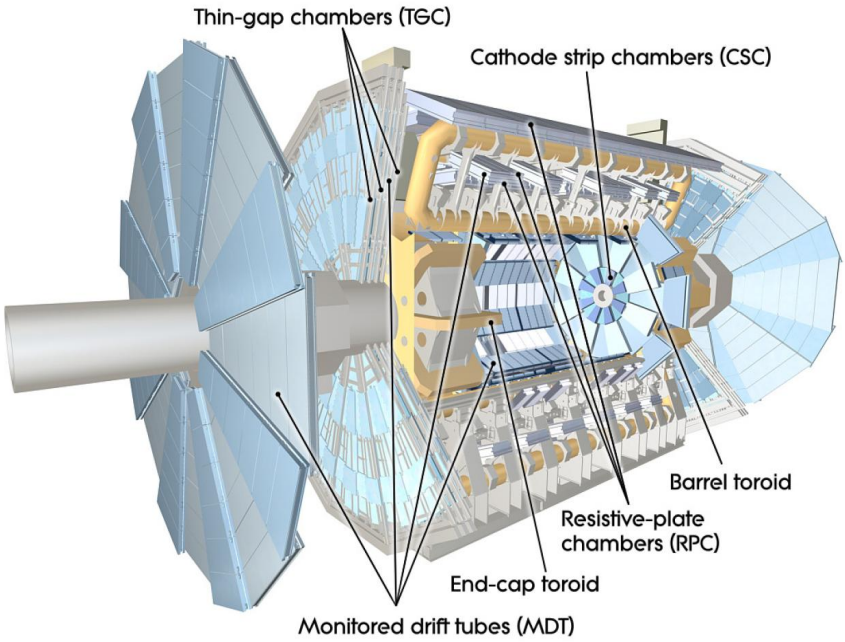

Figure 3.14.: The muon spectrometer. Thin Gap and Resistive Plate Chambers (TGCs and RPCs) provide fast trigger signals, Monitored Drift Tubes and Cathode Strip Chambers (MDTs and CSCs) provide high precision measurements. The enclosed toroidal magnet system provides strong bending power.

3.2.7. The Muon Spectrometer

A complex muon spectrometer is built instrumented with precision and trigger chambers as shown in Fig. 3.14. They operate in a toroidal magnetic field which, depending on the radius r and azimuth ϕ, varies from 0.15 T to 2.5 T, with an average value of 0.5 T, in the barrel region, and from 0.2 to 3.5 T in the endcap region. The barrel toroid covers in pseudorapidity $|\eta| < 1$ and the endcap toroids $1 < |\eta| < 2.7$. Each of the toroid parts is constructed of eight of the prominent coils located radial-symmetrically around the beam-pipe, conducting 20.5 kA of current. The trigger chambers are Resistive Plate Chambers (RPC) and Thin Gap Chambers (TGC) based on multi-wire proportional chambers. They provide trigger decisions in less than 5 ns, thus well within the LHC bunch crossing time with modest resolution of 3 to 7 mm in the RPCs and 10 mm in the TGCs. The precision chambers are Monitored Drift Tube (MTD) and Cathode Strip Chambers (CSC) building up the signal within 700 ns at most. The data are directly stored in memory buffers and only retrieved on trigger request. The CSC are multi-wire proportional chambers segmented with readout cathodes, providing a resolution of 40 μm in the radial plane. The MDT are multi-layers of drift tubes giving a spatial resolution of 35 μm along z. More details are available in [69].

3.2.8. Beam Pick-Up – BPTX

ATLAS is provided with two button pick-up detectors, BPTX [81], located 175 m upstream from the interaction point in ATLAS able to signalise beam presence. They consist of electrostatic small rings, which respond with a fast signal (100 ps) when charged particles pass through them. Being part of the LHC beam instrumentation they continuously monitor the frequency and phase of the proton bunches as well as properties of the individual bunches [82]. In ATLAS, they are used for timing purposes and as input to the trigger system. Their signals are shaped into 25 ns long pulses and then fed into the Central Trigger Processor (see Section 4.1.1) to provide filled bunch triggers for the very first pp collisions in September 2009.

3.2.9. Beam Condition Monitors – BCM

In addition, two Beam Condition Monitors (BCM) are installed to protect the detector from beam losses at the tertiary collimators which might cause damage to the detector due to an enormous instantanious rate. The BCM can act as an detector protection device which can trigger the beam abort in case of large beam losses directly upstream of the ATLAS detector. Throughout the lifetime of the experiment, the BCM can be used to distinguish potential damaging events from usual proton-proton interactions. The BCM consists of two stations each with four modules. Each module contains two radiation-hard diamond sensors located at z = $\pm$ 18.4 m, at a radius of $r = 5.5$ cm and at a pseudorapidity of $|\eta| = 4.2$. The signals have a rise time of 1 ns only which is also used for fast feedback to the LHC control centre.

3.2.10. Forward Detectors

ATLAS has three more forward detectors as highlighted in Fig. 3.15. Two of them are dedicated for luminosity measurements: the Luminosity Cherenkov Integrating Detector (LUCID) located at $\pm$ 17 m and the Absolute Luminosity for ATLAS detector (ALFA) at $\pm$ 240 m away from the interaction point. The absolute luminosity will be measured at low luminosities and with relative luminosity measurements of LUCID, the absolute luminosity measurements will be available.

In between them is the Zero-Degree-Calorimeter (ZDC), located at $\pm$ 140 m in a slot where the beampipe splits into two and where ususally the TAN (Target Absorber Neutral) is placed. The ZDC consists of two arms both comprising an electromagnetic (EM) and three hadronic modules. They are designed to detect neutrons and photons of heavy ion collisions with $|\eta| > 8.3$.

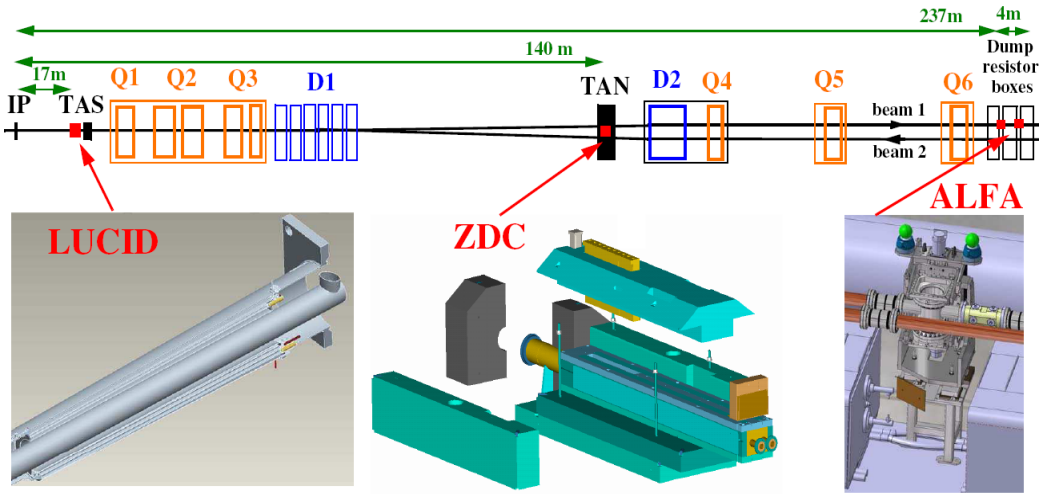

Figure 3.15.: Top view of beamline with forward detectors of ATLAS: LUCID and ALFA for luminosity measurements and the ZDC for detection of neutral particles [69].

4. The ATLAS Trigger System and Software Framework

When the LHC is operated at nominal machine parameters, ATLAS will record events every 25 ns with each event containing around 25 simultaneous proton-proton interactions. Assuming a size of an event of about 1.5 MB this translates into 1.5 PB/s data volume. It is impossible to store all the produced data and not intended from the physics point of view. A highly selective trigger is crucial for the physics programme of ATLAS. Furthermore, new concepts were developed that enable a world-wide analysis of ATLAS data. This chapter first describes the ATLAS trigger system in Section 4.1, then the computing and software framework in Sections 4.2 and 4.3 and highlights in Section 4.4 the commissioning of the detector, especially the trigger system. The end of this chapter, Section 4.5, contains an overview of data of periods in 2010 of the first year of LHC operation.

4.1. The Trigger and Data Acquisition System

The ATLAS Trigger must provide a suppression factor of more than 10^5 to achieve a recordable event rate of around 200 Hz, while keeping potentially interesting signal events with good efficiency. Two main concepts are pursued to face this task: *Step-wise* and *seeded* event selection. The first basic concept reduces the decision time by using a *step-wise* trigger system allowing an early rejection of uninteresting events. Generally, a seeded selection means that the lower trigger level provides a guided search by processing only data in so-called *region-of-interests* for deriving a trigger decision. In such a specified detector region only a small fraction of about $2-4\%$ of the whole event data are processed first. This reduces the amount of data transfer which also enables a fast trigger decision.

ATLAS realises this strategy in three trigger levels: Level-1 (L1), Level-2 (L2) and the event filter (EF) as third trigger level. Their main purpose during the selection is to ensure they make the "right" selection covering any unknown physics processes. On the one hand the trigger thresholds must be as generic as possible not to reject potentially new physic signals, on the other hand one has to identify, very fast, the content of each event. A more detailed description of the trigger system followed by an explanation of the event selection is given below.

4.1.1. The First-Level Trigger

The first level trigger (L1) is hardware based and has to reduce the event rate below 75 kHz within a fixed latency of 2.5 μs. The Level-1 trigger system can be divided

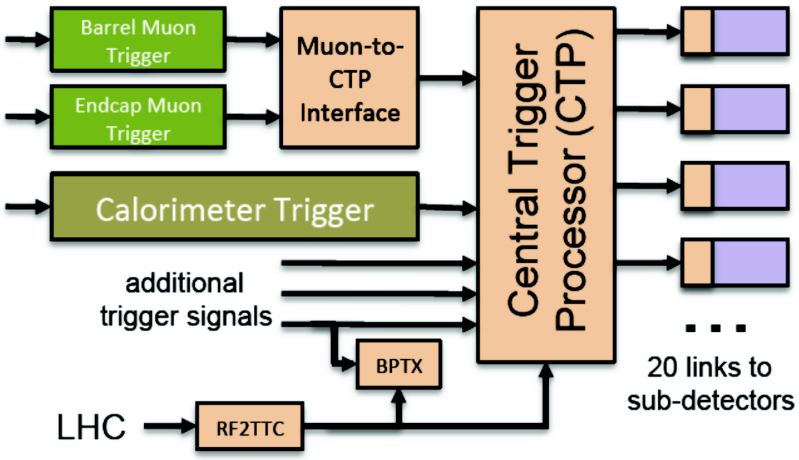

Figure 4.1.: Sketch of the Level-1: muon, calorimeter and additional trigger are input to the CTP as well as the RF clock of the LHC (RF2TTC). In case a L1 trigger fires, the CTP issues the readout of the data [83].

Table 4.1.: List of bunch-groups (BGRP). For all data collected at $\sqrt{s} = 7$ TeV physics triggers are combined with BGRP_1 at L1. For background estimation, dedicated beam-background triggers and a selection of physics triggers are duplicated to be combined unpaired bunches. The definitions of BGRPs are experiment specific and comprise essentially a list of bunch crossing identifiers (BCIDs), a number assigned to the "bucket" to the bunch.

Bunch-Group ID	name	purpose
BGRP_0	BCRVeto	all bunches except the forbidden ones from abort gap
BGRP_1	Filled	colliding BCIDs
BGRP_2	Calreq	empty bunches during long gap for calibration requests
BGRP_3	Empty	empty bunches for cosmics, random noise and pedestal triggers
BGRP_4	IsolatedUnpaired	unpaired bunches separated by at least 3 BC from any bunch in the other beam
BGRP_5	NonIsolatedUnpaired	unpaired bunches that do not fall under BGRP_4
BGRP_6	EmptyAfterPaired	empty bunches just after a filled bunch (no overlap with BGRP_3)
BGRP_7	AllUnpaired	inclusive OR of BGRP_4 and BGRP_5

into three L1 sub-systems: The calorimeter trigger L1Calo, that receives data from both calorimeters, the muon trigger L1Muon, processing information of the resistive plate chambers (muon barrel) and thin gap chambers (muon endcap), and the central trigger processor CTP, see Fig. 4.1. The L1 decision is based on multiplicities of physics objects for electron/photons, hadronic τ's/hadrons, jets and muons. It computes as well the total missing transverse energy and total transverse jet energy. These objects are selected by e/γ-, τ/h-, μ, (missing) energy- and jet-triggers respectively and taken as standard input for the CTP. Additional input is defined for minimum bias events triggered by MBTS, other forward detectors as LUCID, ZDC, BCM and BPTX and for special CTP-internal triggers. There are twelve internal triggers, two random triggers, two prescaled clocks and eight bunch-group triggers. A group can be defined, for example for filled bunches using beam pick-up monitor signals. The bunch group definitions are listed in Table 4.1. The prescaled clocks are periodic triggers taking only bunches with constant distance in between. Combinations are also possible, the limit is given by the hardware allowing up to 256 L1 items at most. The approach for triggering minimum bias events, independently from MBTS, uses one of the random triggers combined with a trigger on filled bunches. These additional triggers serve commissioning and monitoring reasons and are an important redundancy tool in order to check the systems functionality.

The CTP forms the Level-1 accept (L1A) from external and internal trigger input according to a Level-1 *trigger menu* which comprises a maximum of 256 active *trigger items* that are combinations of one or more conditions set on the trigger inputs. If e.g. MU6 symbolises a condition on a muon to possess at least a transverse momentum of 6 GeV then 1MU6 can define a L1 trigger item that *one* such a muon must be measured. Each trigger item possesses a bit mask, a prescale factor which is needed in order to suppress very high rates of some physics objects and a priority (can be set to *low* or *high*) for dead-time that will be created by the CTP. This ensures that during dead-time no new event processing is performed for that specific trigger. Within 100 ns processing time a logical OR-combination of trigger items are formed representing the L1A within the CTP.

Each event is kept in pipeline memories of the detector front-end electronics. Detector-specific readout drivers (RODs) combine the large number of readout channels into around 1600 data fragments and each fragment is sent to an individual readout buffer (ROB). Only data for events selected by L1 is transferred to these ROBs being part of a larger unit, the so-called readout systems (ROSs).

After every L1A generation, information is sent from the calorimeter and muon trigger to the Level-2 Region-of-Interest-Builder (RoIB). An RoI is a geometrical region in the detector in (η, ϕ) and additionally contains a bit pattern indicating which threshold was passed. The CTP also sends information to the read-out and data acquisition system containing data for several bunches for debugging and monitoring purposes.

4.1.2. The High-Level Trigger

The High-Level Trigger system (HLT) consists of two levels: Level-2 (L2) and Event-Filter (EF). Both are software triggers using standard PCs and are interconnected by

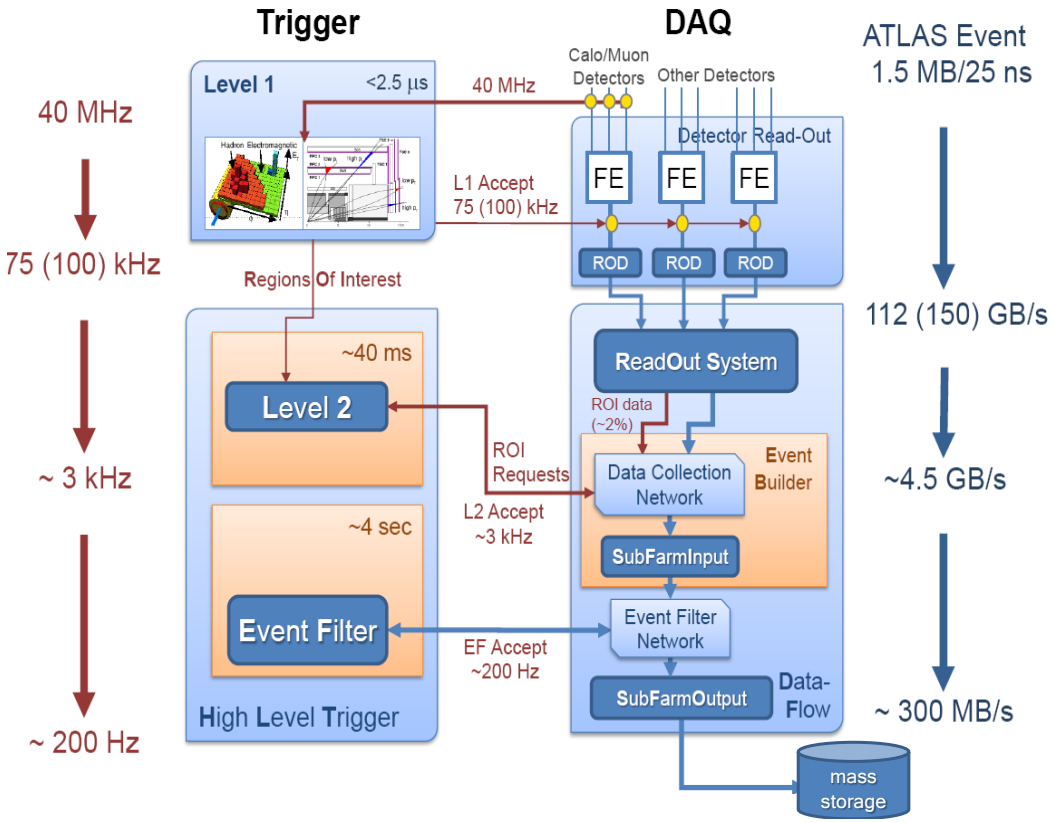

Figure 4.2.: Overview of the ATLAS Trigger and Data Acquisition System. It shows functional elements and their connections, see text for explanations. The figure was taken from [84].

ethernet network. The final HLT selection farm will consist of 17 racks with L2 and 62 racks with EF processors with each rack comprising 31 processing units. By the end of 2010 50% of the L2 and EF nodes were installed [84]. 27 of the total 79 racks can be freely configured on a "run-by-run" basis either for L2 or EF use which allows to distribute the processing power according to the needs of L2 and EF.

The basic concept at L2 is to combine high rejection power with fast and rather coarse granularity algorithms consuming modest CPU. At the EF, modest rejection power with higher precision and therefore more time consuming algorithms are employed.

Second Trigger Level - L2

The data acqusition is visualised in Fig. 4.2. Signals from L1 sub-systems are sent to RoIBs which run at the same rate as L1. The data fragments are passed to Level-2 supervisor computers (L2SV) which assign each event a Level-2 processor unit (L2PU) running on a Level-2 processor (L2P). On these processors L2 event selection algorithms are executed. Only data associated with an RoI are requested via the dedicated Level-2 network (L2N) from the ROS. For minimum bias triggers, an RoI is extended to process data of the entire silicon sub-detectors (*full scan*). After processing RoI data, the L2PU produces summary information and adds to it the L2 decision which represents the L2 result. During the processing time, more event fragments can be requested from the ROS. The L2 decision is sent back to L2SV which forwards it to the data flow manager (DFM). In case an event is rejected the DFM passes the decision to the ROS such that the event can be removed from the read-out buffers (ROB). In case of a positive decision the event building operation is initiated by the DFM. The total processing time to produce a L2 decision is limited to about 40 ms on average and the L1 rate is reduced by a factor of 25 to about 3 kHz on average.

For the event building process, a sub-farm input (SFI) is allocated for fragments of each accepted event. In the SFI the event is built in memory with a signal sent to the DFM upon completion. The event is buffered in the SFI for further processing at EF. A switching event building network (EBN) links ROS, SFI and DFM to increase efficiency as the network enables concurrent event building.

Event Filter - EF

The EF is made of several thousand farm processors (EFP) each one running an EF data flow control program (EFD) that receives a complete event "seeded" from SFI. The EFD application makes in principle the whole event available on processing tasks (PT) where EF event selection software is executed. The EF algorithms are guided by the L2 result and will only process data from an RoI but with full access to calibration and alignment constants and with a more detailed detector material description. Like at L2, minimum bias algorithms typically scan entire sub-detectors. If a PT has finished processing an event, it requests a new event from an SFI. In case the event is accepted data generated during processing on the PT are appended to the raw event which is then classified and transferred to sub-farm output buffers (SFO). Completed events are

written to the mass storage system for permanent storage. Similar to L2, an EF-network (EFN) interconnects SFI, SFO and EFP. The overall processing time on the EF is about 4 seconds on average producing an output rate of 200 Hz. Further information on the online software system can be found in [85].

4.1.3. The HLT Selection

The event selection is based on two fundamental concepts which reign the design of the HLT selection. Firstly, HLT algorithms are *seeded* by the results of the previous level in order to reduce data transfer and produce a fast decision. The seed is given in form of the already introduced region-of-interest in the detector where conditional activity has been measured. The second concept is to process the event *step-wise*. The trigger decision is initially based on coarse information but then refined at each further processing step by accessing higher granularity information from more sub-detectors. At the end of each step a new decision is made after algorithmic work is performed on the present information, allowing for the employment of algorithms with high rejection power first, and enabling early rejection of unwanted events.

The Trigger Steering [86] provides the necessary framework for such a concept in which algorithms can be plugged in, configured, controlled and monitored. The trigger algorithms communicate via restricted interfaces such as trigger elements (in which the result of the algorithms is incorporated) or error codes. Its task is e.g. to start the execution of algorithms, select and combine trigger elements (TEs) whereas the raw data processing is performed by the algorithms.

Derivation of a Trigger Decision

The trigger decision is defined in terms of *trigger chains* consisting of physics *signatures* which themselves are made of one or more logically combined trigger elements. The chains define a list of signatures or a *signature table* and are formed for each processing step. Each trigger chain provides one signature at each step. Only if at step N at least one signature is fulfilled, the event is passed to the next processing step N+1. Otherwise the event is stopped and a new event can be processed. The chains must be configured such that at N+1 each signature must correspond to exactly one signature at N. A simplified case of trigger chains and signature tables is shown in Fig. 4.3. However, signatures can also be shared by different trigger chains which will lead to split chains. Splitting is only possible at a transition to the next trigger level and in one direction only towards higher processing steps but not vice versa. The reason is that trigger efficiencies can only be determined with the help of the last signature. If chains split into higher directions, this is not given anymore an the system becomes unpredictable e.g. due to dependencies that can not be traced back.

Refinement of Trigger Elements

Another part of the configuration describes a *sequence table*, a list of algorithms necessary in order to refine event characteristics. For example, at step N there is a trigger

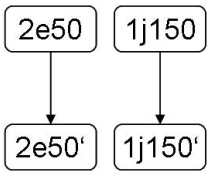

Figure 4.3.: Example for signature tables (horizontally) and two trigger chains (vertically). In case of the left trigger chain a signature consists of two equal trigger elements of an electron with at least $p_T \geq$50 GeV. The refinement is indicated by '.

element TE that is refined to TE' by a *sequence*. One sequence consists of certain refinement algorithms, usually feature extracting algorithms (FEX) extracting quantities from raw data and hypothesis algorithms (HYPO), testing if certain thresholds have been passed. In general the refinement is based on a corresponding L1 trigger item, like EM50, symbolising an electromagnetic RoI having passed the 50 GeV transverse momentum threshold. A sequence needs one trigger element as input and creates one output trigger element (or deactivates a trigger element which is dependent on the HYPO-result). According to the active trigger elements the steering decides which algorithms are run at the next step, therefore unique names of trigger elements must be ensured to identify the sequence. Also the trigger elements link a sequence table with the signature table, since sequence algorithms perform work on trigger elements and signatures are a logical combination of trigger elements. Further details like an complete configuration example can be found in [87].

For the development of a minimum bias trigger chain non-standard algorithms are needed for the full scan that they perform of the ID region. Therefore so-called unseeded algorithms are employed.

Unseeded Algorithms

This type of algorithms was originally developed for B meson decay scanning at least half of the Inner Detector region for b-tagging. Nevertheless they are also suited for minimum bias event selection. *Unseeded* means that the algorithm is started without requiring an input TE but by the mere existence of active signatures at the lower processing step as defined in the trigger chain. However, the unseeded algorithms do create an output TE which can be combined to signatures with other TEs. Minimum bias triggers use these algorithms which must not be called more than once per event.

4.1.4. Trigger Configuration System

The trigger configuration [88] that was mentioned to set up both, L1 and HLT, copes with a wide range of operational scenarios. It includes the trigger database (TriggerDB), software services to access the database and tools like the TriggerTool to view and modify the configuration data. To exploit best the current delivered luminosity, different trigger

menus are set up in which certain trigger chains are grouped. Each menu forms the frame of the configuration.

Each chain in a menu has exactly one prescale (PS) and one pass-through (PT) factor associated. In that way trigger chains can be included into the menu and activated or disabled on demand. The smallest unit when such configuration changes remain stable is per *luminosity block* (LB). To maximise the data-taking efficiency, prescales are updated towards the end of a run when the luminosity decreases and a smaller prescale factor can be applied. These updates are entered into the TriggerDB and kept for later use in analysis and trigger studies. To identify the conditions used online the trigger menu is uniquely defined by three numeric keys: the Super Master Key (SMK) containing the configuration of the trigger chains and the prescale keys for L1 and HLT. These can be generated several times per run following the luminosity of the beams.

4.1.5. Trigger Timing Performance Targets

The available time budget from data retrieval over event processing to the derivation of the trigger decision is generally about 40 ms at L2 and roughly 4 seconds at the EF. Thanks to new CPU power and the possibility to use a few racks either at L2 or EF, the latency at both levels has doubled while the throughput stayed the same compared to initial expectations [69]. However the relation between the times consumed by individual algorithms and the averaged time to produce a trigger decision is not trivial. For each step several factors have to be taken into account. It makes a difference which and how many triggers are deployed, what the rejection factor of a specific chain is (which also depends on the luminosity), the RoI multiplicity for RoI based selection, possible overheads in the steering or in the actual data retrieval. Rejection at an earlier step will lead to more time for the subsequent level, because algorithms are called less frequently. To quantify the timing consumption per trigger chain, the triggers are timed for each run, while for detailed timing information dedicated runs are necessary to measure the single contributions per sequence to the total time consumption. These time measurements were of particular interest for the ID minimum bias triggers as they execute full scan algorithms. Results of such measurements are presented in Section 5.4.

4.2. ATLAS Computing

The analysis of ATLAS data has to be organised such that the about 3000 members of the ATLAS Collaboration can perform data analysis in an efficient way. A new concept of distributed computing over the LHC computing is designed to cope with these challenges [89, 90]. The basic concept is to form *derived physics data* (DPD) specific to the need of the analysis of the end-user physicists [91].

4.2.1. Distributed Analysis Model

The events arrive from the EF farm at an averaged rate of 200 Hz, which corresponds to a data throughput of about 300 MB/s. In several layers of computing tiers, see Fig. 4.4,

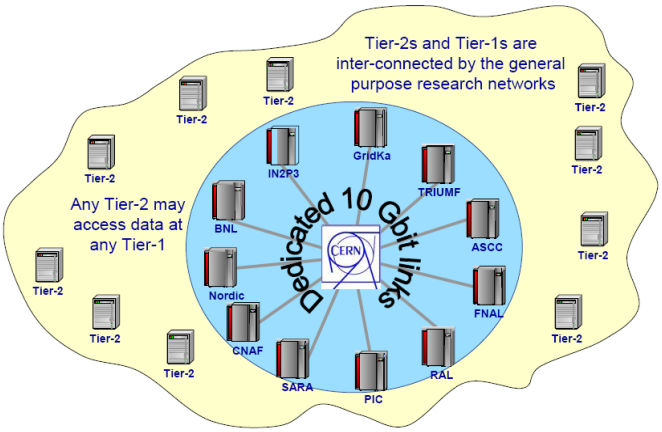

Figure 4.4.: Tier-0 (CERN), Tier-1 (blue) and Tier-2 (yellow) interconnectivity [90].

the data are reconstructed, and derived data are produced which are distributed over the grid [90]. The so-called Tier-0 is a large computer farm at CERN, performing prompt reconstruction of the data in a 36-hour calibration loop [92]. Several Tier-1 centres exist for further processing, typically one per country that is a major national computing centre. Around those many more Tier-2s are organised meant for data analysis by the end-user. During the successive data transfer from Tier-0 to the Tier-2s, the data are written out in different formats. An illustration of the data distribution is shown in Fig. 4.5.

- RAW or byte-stream (BS): this format is the output of the TDAQ system and reflects the format in which data are delivered from the detector. The event size of RAW data is therefore rather fixed and does not scale with luminosity like the subsequent formats. Raw data sum up to around 1.5 MB. One copy of RAW data files is replicated from Tier-0 to one of the Tier-1s. For trigger commissioning this format was most relevant as any modifications to the trigger were validated on raw data prior to online deployment.

- Raw Data Object (RDO): This format is not part of the data reconstruction chain, it rather replaces the RAW format for Monte Carlo datasets but provides an object-oriented format. RDO data were extensively used for trigger development and validation before real collision data existed.

- Event Summary Data (ESD): refer to the reconstruction output. They contain detector-level hit information and reconstructed quantities such as tracks or calorimeter clusters. They have an object-oriented representation and are stored in POOL ROOT files [93, 94]. A typical event size is 1.5 MB while an increased size of around 2 MB is expected with increased luminosities. Two copies of ESD are distributed to the Tier-1s. This format was used for trigger performance studies requiring detailed information from detector, trigger and reconstruction.

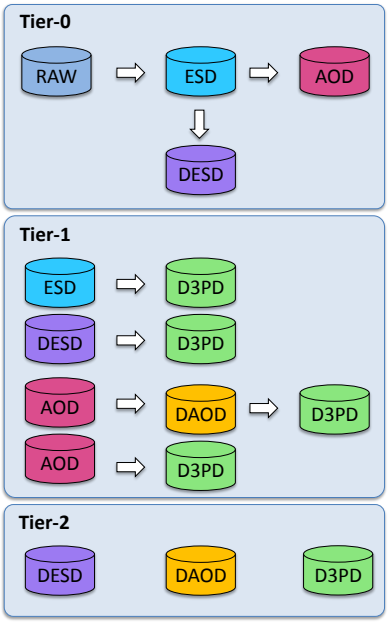

Figure 4.5.: Data distribution on the grid [95].

- Analysis Object Data (AOD): AOD, also in the POOL ROOT format, are a subset of ESD containing less detailed data. Typically, the event size in an AOD is around 150 to 200 kB and several copies are replicated to the Tier-1s. This format was less relevant for trigger development.
- Derived Physics Data (DPD): several types of derived data exist which accomplish the needs of the different physics cases. They differ in the level of details per event and the number of events, e.g. for performance studies. DESDs and DAODs are performance DPDs obtained by event selection. Primary derived data (D1PD) are derived and modified ESD/AOD which do not have a one-to-one correspondence with the events in the RAW files (in contrast to the ESD and AOD). Secondary (D2PD) and tertiary (D3PD) derived data formats exist as well. The latter are flat ntuples which are fully customised and therefore the preferred analysis format of the user. They were also extensively used in this thesis.

The data are recorded per *run* consisting of events of a time period defined by the ATLAS run control. For each run the data are written to disk grouped into different *streams*. The purpose is to reduce the number of files processing in an analysis and was therefore based on trigger chains. The streams are *inclusive* meaning the same event can appear in more than one stream. They can be categorised as "calibration" and "physics" stream. An important exception is the "express" stream which is a subset of the physics data corresponding to a recording rate of about 10 Hz and used for prompt data reconstruction [92]. The express stream is also used to obtain fast feedback for background rates and includes events selected by an ID based minimum bias background trigger,

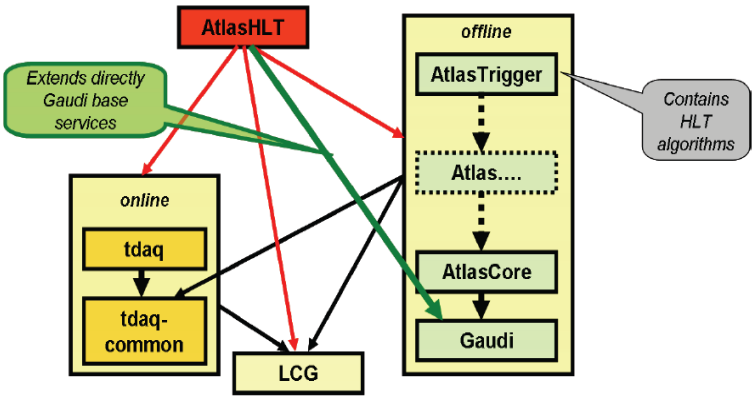

Figure 4.6.: Dependencies of the AtlasHLT project: it depends directly on data flow applications (left), LCG software (common software to all LHC experiments, middle) and the ATLAS specific offline software (right). Figure taken from [86].

mbSpBg_unpaired. This trigger was set up to select on beam-gas/halo events at low radii. These events are directly streamed into the express stream, see also Section 5.2.5.

For early 2010 data the physics streams were based on the L1 triggers: RNDM, MinBias, MuonswBeam ("muons with beam") L1Calo, L1CaloEM, CosmicCalo, CosmicCaloEM. With increased luminosity ATLAS moved to the final streaming model for 2010: ZeroBias, MinBias, EGamma, Muons, JetTauEtMiss, CosmicCalo merging the RNDM seeded events into the MinBias stream.

4.3. The ATLAS Software

Data reconstruction takes place in a common software framework, the *Athena* framework [89], using common tools across ATLAS. Since software development was an important part of the thesis, the ATLAS software infrastructure is briefly described. Emphasis was put on the validation steps from development to online deployment of a trigger. More general information of the ATLAS software is given in [89] and a recent review of the online software can be found in [86].

4.3.1. Structure of the ATLAS Software

The ATLAS software framework Athena comprises the software for event simulation, the trigger, event reconstruction and high level analysis tools. It is based on the GAUDI framework [96] realising a component-based architecture that accomplishes the requirements for data processing and physics applications. The ATLAS software is organised in *packages* which contain C++ and Python classes. One such package contains rather simple functionalities and therefore represents the smallest development unit. With dependencies against other packages, more complex functionalities are created. Each package is maintained in a single *project* and packages with similar dependencies and

scope go into one project which can be built together. There are ten projects which use the offline environment like `AtlasCore`, `AtlasReconstruction` or `AtlasTrigger`. In addition, there is the `AtlasHLT` project which directly depends on data flow applications as well as all the other offline software projects. As Fig. 4.6 depicts, the trigger code is included in the `AtlasTrigger` project on which `AtlasHLT` depends on. These were the offline and online developing environments of the ID based Minimum Bias trigger.

Developing ATLAS Trigger Software

The software is built on several platforms using a set of different compilers in order to guarantee the robustness and proper validation of the produced code [97]. Important tools have been developed and put in place to ensure robust code base maintenance, correct and rapid bug fixing, software change submission, compilation and validation on a large number of build machines, testing and finally reporting the results to the developers.

Even though there are online and offline environments, it was essential that the code used for triggering can be executed offline as well. This allowed offline studies of the trigger performance but also the re-use of the offline reconstruction software for online deployment.

For this work, online trigger software was developed, tested, validated and optimised using both, the online and offline validation framework. Specific tests for each minimum bias trigger configuration has been setup. Furthermore, they were deployed in **technical runs** where simulated data are preloaded to the read-out buffers and triggering is simulated with all the available HLT computers and sub-detectors integrated into the TDAQ system at that time. A major step in the validation of the trigger was achieved when the trigger was used for cosmic ray data-taking. Since minimum bias triggers are highly sensitive to inelastic proton-proton interactions, they played an important role in the commissioning of the detector with beam.

4.4. Commissioning of the ATLAS Detector

The commissioning of the ATLAS detector with cosmic-ray data was useful for the overall commissioning activity, especially when the data was taken with the full detector installed (in "global cosmic-ray runs") in 2008 and 2009 which allowed to extensively exercise operation, data-taking and distributed data analysis. The analysis of several hundred millions recorded events allowed to produce first calibration and alignment constants and to study the combined-tracking performance of algorithms combining both, tracks in the the ID and in the muon spectrometer [99]. In addition, algorithms for lepton identification, jet and missing transverse energy reconstruction could be commissioned with cosmic-ray data [100]. An example of such an event with a track passing very close to the nominal interaction point and featuring hits in all sub-detectors is shown in Fig. 4.7.

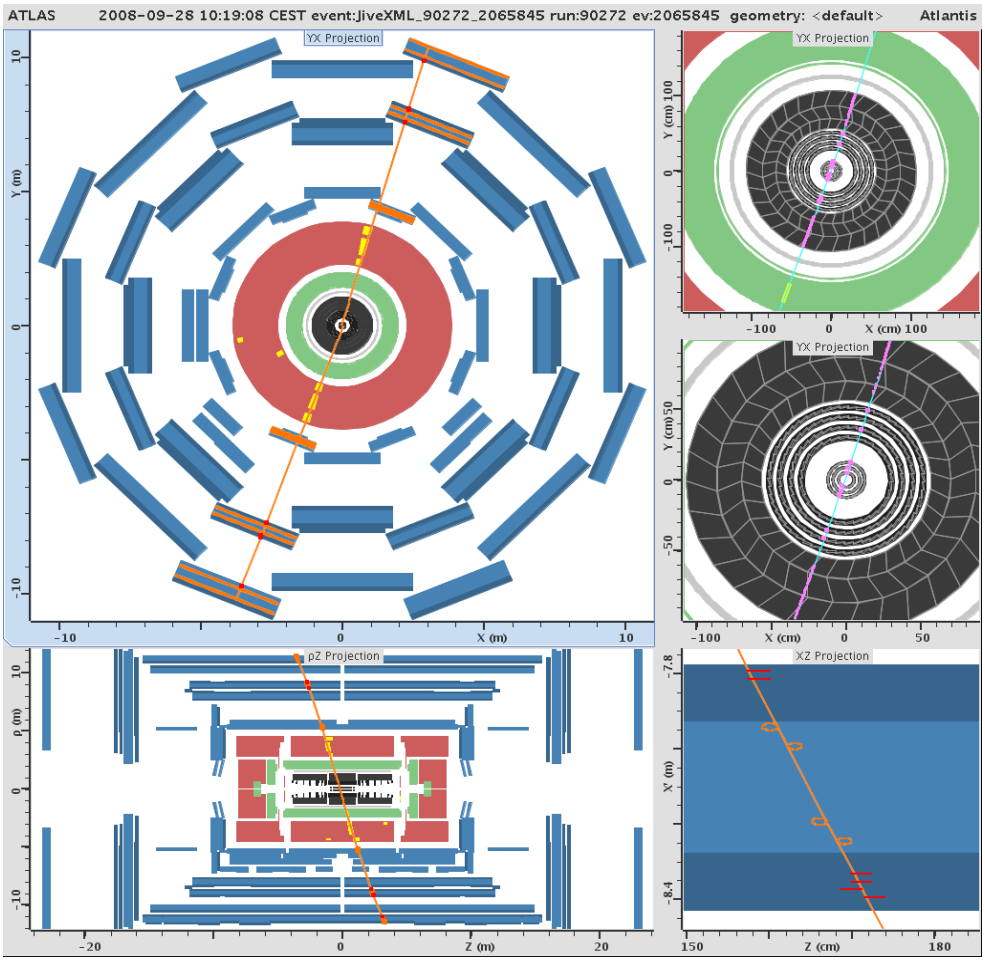

Figure 4.7.: Cosmic ray track passing through the middle of the detector [98].

First Beam Event (beam splash), 10:19:10 CEST, 10.September 2008

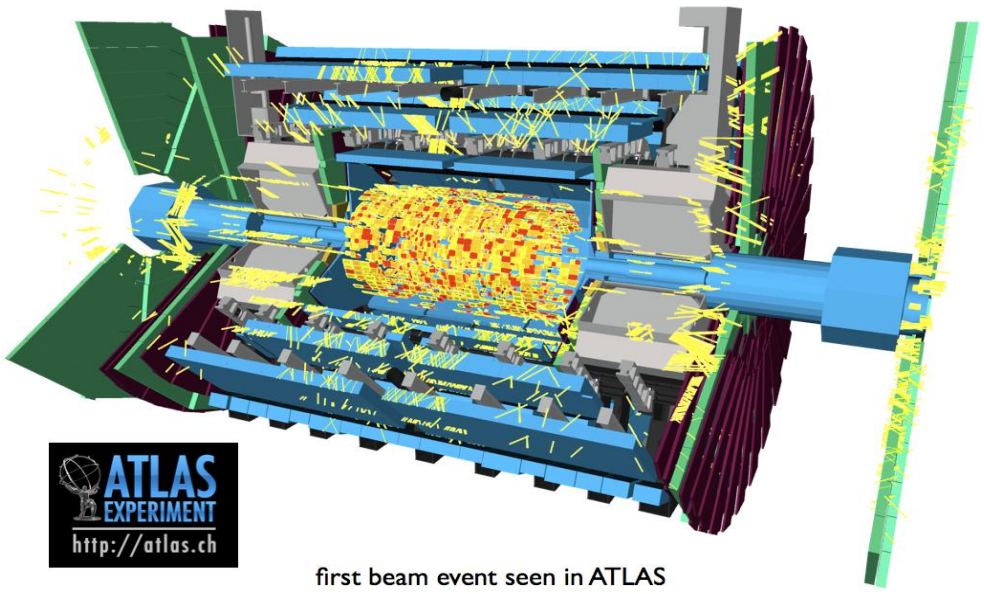

Beam Halo Event, run 87863 event 1450, September 2008

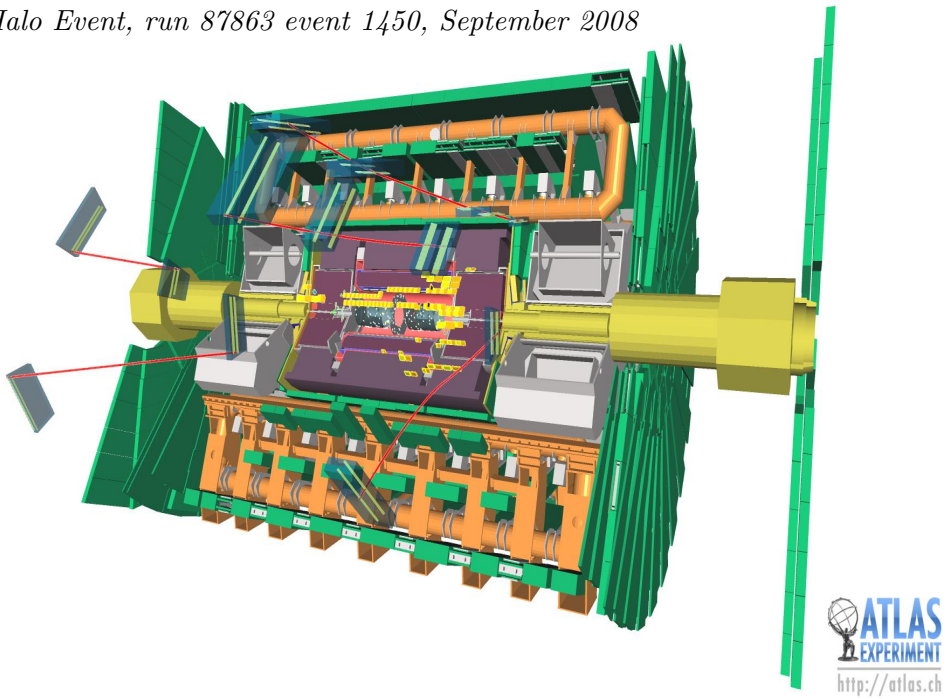

Figure 4.8.: First beam events in 2008, beam splash event (top) and a beam halo event (bottom), both taken from [101].

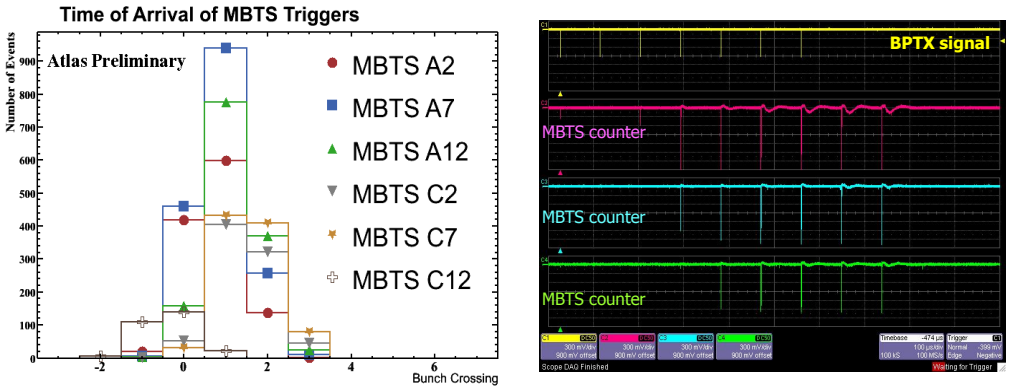

(a) (b)

Figure 4.9.: (a) Relative timing signals of single MBTS counters to the nominal bunch-crossing at zero. (b) Oscilloscope traces of discriminated BPTX and MBTS signals during an injection of 1 bunch of beam 2 without RF capture (the beam turns only a few times) [77].

4.4.1. Commissioning of the Trigger System

While present documentation [102, 103] outline the trigger performance of L1 and HLT during the initial phase, a particular part during that phase concerning the *timing-in* of the sub-detectors, has been less verbosely documented. Since the L1 MBTS trigger played a central role during that time this procedure is described here in more detail.

The commissioning of the trigger using the online system started 2008 in technical runs where simulated collisions were selected by a trigger menu and processed by the HLT. This provided first experiences running a large parallel system. As mentioned above, reconstruction algorithms were exercised on cosmic-ray data, even though with slightly different parameters accounting for the different incident angles and timing structure of cosmic-ray tracks.

When the LHC machine delivered proton bunches to ATLAS on September 10^{th} in 2008 two more kinds of events were recorded as visualised in Fig. 4.8. First so-called *splash* events were produced. They are produced by completely closing the tertiary collimators 140 m upstream which served as a target for the single proton bunches. The collisions created an avalanche of particles which "illuminate" the ATLAS detector. In addition, beam-gas and beam halo events (Section 3.1.4) were created. Clear halo tracks are visible in the event display of Fig. 4.8.

Timing-in the Trigger System

Both kind of events were very useful to extract important information for the detector and trigger commissioning. The primary task was to set up the timing of the signals, such that data produced in the sub-detectors can be correctly identified and selected for read-out. Therefore, basically three timing tasks were necessary. Task 1 comprised the

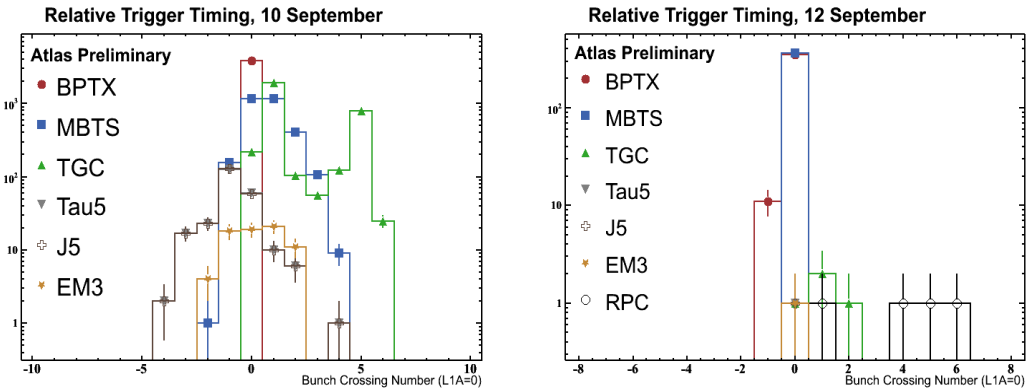

(a) (b)

Figure 4.10.: (a) Timing distribution of L1 triggers on the first day of single beam data on 10. September 2008, triggered by BPTX. (b) On the 3rd day of single beam data, 12.September 2008, events were triggered by MBTS which was then in excellent overlap with the BPTX [77].

alignment of all trigger input signals at the CTP in steps of 25 ns. In task 2, the readout of the subdetectors were adjusted to the right bunch-crossing. The last task consisted of fine-tuning the clock phase to the detector signals which is a sub-detector specific task and usually done last. Task 2 needs the first task to be completed but could already be achieved to a large extend with cosmic ray data with tracks passing through the barrel parts of the sub-detectors.

For task 1, various trigger signals including those of sub-detector parts positioned in the endcap regions could be aligned with respect to BPTX signals when proton collisions took place. The procedure in 2008 was to measure the phase differences of a device that "sees" the beam, BPTX, and other L1 trigger signals. The MBTS were also used to not only confirm the beam presence registered by the BPTX, but also to signalise collision event. This is depicted in Fig. 4.9, (a) shows the distribution of the relative timing signals from a few MBTS counters, (b) is a different view using oscilloscope traces of BPTX and MBTS signals at the same run which gives an independent confirmation of beam presence in ATLAS. This figure visualises how the bunch manages to circulate a few times. While the BPTX indicate beam presence in the first few turns, they give only a small activity in the MBTS. After three to four turns however, MBTS counters show saturated signals for the next five, six turns. The last turns are no longer detected by the BPTX as the intensity falls below the BPTX discrimator threshold.

With only a small amount of single beam data each scintillator was synchronised with the BPTX. After two days many L1 triggers using various sub-detectors could be synchronised as shown in Fig. 4.10. Especially the TGC (endcap triggers of the muon system) were expected to not match the signals of other triggers using barrel regions. However with a reference given by the BPTX one could adjust the signals to require a coincidence with them.

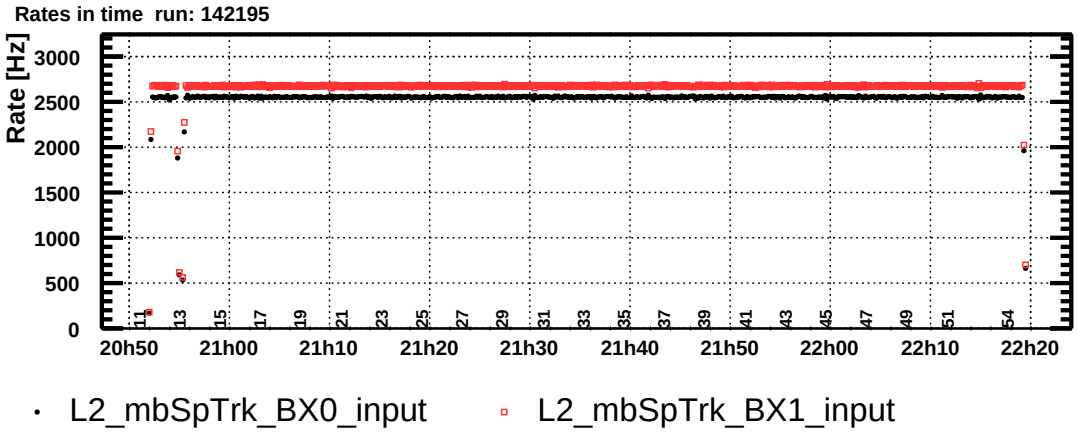

Figure 4.11.: Input rate of the first HLT trigger (mbSpTrk) running in active selection mode on $\sqrt{s} = 0.9$ TeV collisions for run 142195 on Sat, 12th December 2009. The L1 input were BPTX trigger for both beams, each one seeding the same L2 and EF algorithms. The recording rate was around 1 Hz.

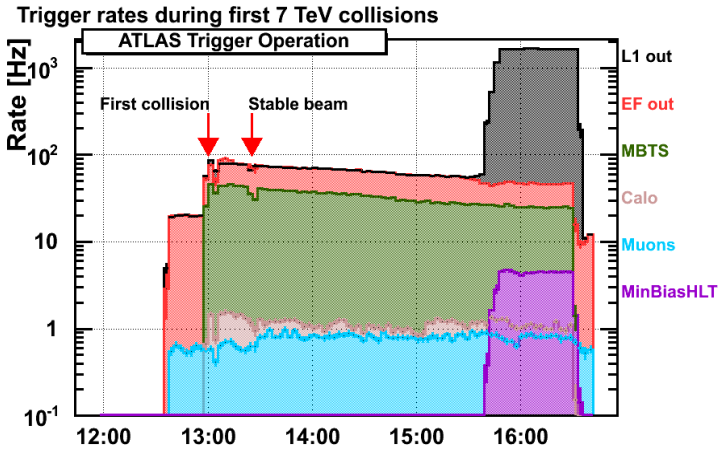

Figure 4.12.: Recording rates during the first pp collisions at $\sqrt{s} = 7$ TeV. At around 15:40 local time the rate increased when the HLT selecting ID minimum bias trigger (mbSpTrk) was enabled [103].

For final timing-in, the LHC and the ATLAS reference clock were synchronised. This happened after collision data were taken in November/December 2009 which allowed the commissioning of the bunch-groups (see Chapter 5.1).

Commissioning of the HLT System

The trigger commissioning was completed with beam data from 2009 when also the HLT was turned on for selection [103]. In the beginning, only L1 trigger selected the pp collisions and no HLT was running online since the luminosity was very low with a rate of only a few Hz of bunch-crossings. Instead, the HLT triggers were exercised offline on the collision events within hours after recording. After less than two weeks of running HLT algorithms offline and having verified they behave as expected, algorithms have been enabled online in *transparent* or *flagging-only* mode, i.e. without active rejection and but flagging whether the HLT trigger would have passed the event or not. The flagging-only mode can be set for each chain individually. One chain was quickly moved to make an active HLT selection, namely the Inner Detector Minimum Bias trigger which was run at high input rates as shown in Fig. 4.11 to enhance the statistics of pp collisions during the initial low luminosity of $\mathcal{L} = 10^{27}\,\mathrm{cm}^{-2}\,\mathrm{s}^{-1}$. Also, this enabled ATLAS to measure the trigger efficiency of the L1 MBTS trigger from data which was a critical ingredient for the first ATLAS publication [46].

For the first collisions at $\sqrt{s} = 7$ TeV in March 2010, the HLT was initially disabled but within two hours of data-taking and offline reprocessing, the HLT was enabled in flagging mode as shown in Fig. 4.12 while once more the Inner Detector Minimum Bias trigger was turned on early for selection.

4.4.2. From Commissioning to Physics Triggers

During the first half year of data-taking the luminosity was ramping up from $\mathcal{L} = 7 \cdot 10^{28}$ to 10^{29} $\mathrm{cm}^{-2}\mathrm{s}^{-1}$. During this period the L1 output rate was controlled by prescaling the L1 MBTS rates while other low-threshold L1 items selected unprescaled. However, the trigger menu evolved several times starting off with around 170 chains in 2009 increasing to 220 chains during $\sqrt{s} = 7$ TeV runs and almost doubled until middle of 2010 when the luminosity reached $\mathcal{L} = 10^{29}\,\mathrm{cm}^{-2}\,\mathrm{s}^{-1}$. This ensured that many of the chains were exercised even at very low luminosity. At a luminosity of $\mathcal{L} = 5 \cdot 10^{28}\,\mathrm{cm}^{-2}\,\mathrm{s}^{-1}$ more HLT chains in addition to the HLT minimum bias chains were progressively turned on and with a luminosity of $\mathcal{L} = 2 \cdot 10^{30}\,\mathrm{cm}^{-2}\,\mathrm{s}^{-1}$, the commissioning phase was superseded by the physics menu which contained around 300 chains that were fully deployed [102]. Minimum Bias trigger continued to be used for data selection, but generally at a much lower rate. For special soft QCD analysis however, a high multiplicity trigger was derived from the ID minimum bias trigger which is still in use.

For the trigger commissioning it was a valuable feature of the trigger configuration, that chains could be enabled, prescaled or fully disabled essentially seamlessly while taking data. This provided the ability to quickly remove faulty chains or enable new chains for testing without any impact on the data-taking efficiency. The successful

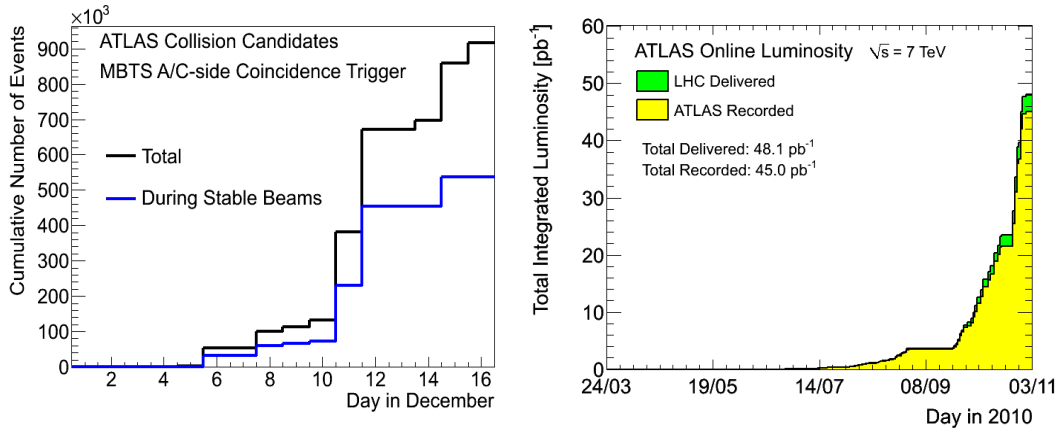

(a) (b)

Figure 4.13.: Integrated luminosity at $\sqrt{s} = 0.9$ TeV in 2009 (a) and at $\sqrt{s} = 7$ TeV in 2010 (b). Figures are replicated from [105, 106].

operation of the LHC machine, the ATLAS detector and trigger systems allowed to move quickly from a commissioning to a physics programme exceeding a luminosity of $\mathcal{L} = 10^{32}\,\mathrm{cm}^{-2}\,\mathrm{s}^{-1}$ and collecting in total an integrated luminosity of 12 nb^{-1} at $\sqrt{s} = 0.9$ TeV in 2009 and 45 pb^{-1} at $\sqrt{s} = 7$ TeV in 2010 as shown in Fig. 4.13.

A similar set of chains as used for the first pp collisions at $\sqrt{s} = 0.9$ TeV as the luminosity were deployed for the heavy ion runs of Pb-Pb collisions end of 2010. Starting with one bunch and a luminosity of $\mathcal{L} = 5 \cdot 10^{23}\,\mathrm{cm}^{-2}\,\mathrm{s}^{-1}$ a luminosity of $\mathcal{L} = 5 \cdot 10^{28}\,\mathrm{cm}^{-2}\,\mathrm{s}^{-1}$ was reached [104]. Minimum bias triggers and other triggers without track reconstruction were therefore used to collect approximately 9.2 $\mu\mathrm{b}^{-1}$ of Pb-Pb collisions.

4.5. ATLAS Data Periods

The data taken with ATLAS are categorised in *data periods* denoting a coherent configuration of the detector and trigger menu. Any significant changes to the trigger, detector configuration or calibration usually result in a new definition of a period. This kind of data categorisation has been introduced with data-taking at $\sqrt{s} = 7$ TeV. Since the low luminosity phase is of interest for the present work only the periods for proton-proton collisions of 2010 are listed in Table 4.2.

Throughout this thesis, it is often referred to the *initial phase of data-taking*. If not specified differently, this period comprises runs until the "InitialBeams" menu is replaced by an initial physics menu, i.e. up to period D.

Table 4.2.: ATLAS data periods of proton-proton collisions in 2010 (all at $\sqrt{s} = 7$ TeV). More information can be found in [107]. The comments only relate to minimum bias triggers.

Period	Run Range	Luminosity (nb^{-1})	Comments
A	152166 – 153200	0.4	Starts with single bunch in the machine. InitialBeams trigger menu runs with all MB triggers unprescaled.
B	153565 – 155160	9	MB triggers run prescaled. Machine improvements: typical beam spot width in x and y reduced from 50 – 60 microns to 30 – 40 microns.
C	155228 – 156682	9.5	No significant change to previous period concerning minimum bias trigger.
D	158045 – 159224	320	Towards end of this period, MB trigger are essentially prescaled out.
E	160387 – 161948	1,118	Supersede the InitialBeams menu with Physics menu. Introduce new data streams (merging of MBTS and mbSpTrk data.
F	162347 – 162882	1,980	runs for high-luminosity physics
G	165591 – 166383	9,070	
H	166466 – 166964	9,300	
I	167575 – 167844	23,000	

5. The Inner Detector Minimum Bias Trigger

The Inner Detector Minimum Bias Trigger represents a complementary approach to the first level minimum bias trigger MBTS. The initial phase of LHC operation started with low luminosities of 10^{27} $cm^{-2}s^{-1}$ by only a few proton bunches producing an interaction rate of 0.1 % per bunch-crossing. This leaves 99.9 % of the bunch-crossings empty that had to be filtered out by minimum bias triggers.

The basic design of the Inner Detector Minimum Bias Trigger (mbSpTrk) builds on earlier work [1] and uses a random trigger at Level-1 with further event selection at the high-level trigger (HLT) based on clustered hits in the silicon tracking detectors.

Two main criteria were decisive in the development of a minimum bias trigger and a compromise between minimising bias and operation stability had to be found. "Minimum bias" implies to apply the lowest possible selection thresholds in the trigger and the least requirements to the event. The ideal working point for mbSpTrk is to operate just above the noise levels of the Pixel and SCT systems. This enables an efficient suppression of noise events while bias in the proton-proton selection is reduced close to a minimum. At the same time, trigger robustness must be ensured against sudden detector problems, which could occur during data-taking at any time. An internal protection of the mbSpTrk was developed backing up the reliability of the trigger.

Another feature of mbSpTrk is the ability to suppress machine induced background, beam gas and halo events. Especially in the beginning of the LHC operation, when primary minimum bias triggers provide the data samples, it can not be assumed that the runs are constantly performed with nominal vacuum parameters. Therefore, the mbSpTrk trigger was prepared to suppress online beam background events.

The levels of mbSpTrk are illustrated in Fig. 5.1 and described in the following sections in detail, Section 5.1, 5.2 and 5.3 for L1, L2 and EF respectively.

5.1. Level-1 of the ID Minimum Bias Trigger

The Inner Detector Minimum Bias trigger performs the event selection essentially at higher trigger levels. In order to obtain a first reduction of the rate that the Level-2 (L2) readout can handle a random event selection is deployed at Level-1 (L1) which introduces no bias.

For the data taken in 2009, a preliminary setup was used based on BPTX signals since the bunch-group mechanism (see Section 4.1.1) was not introduced at that time. Thus, BPTX signals seeded mbSpTrk resulting in two chains (mbSpTrk_BX0 and mbSpTrk_BX1). The difference to the nominal setup is that no random selection is applied

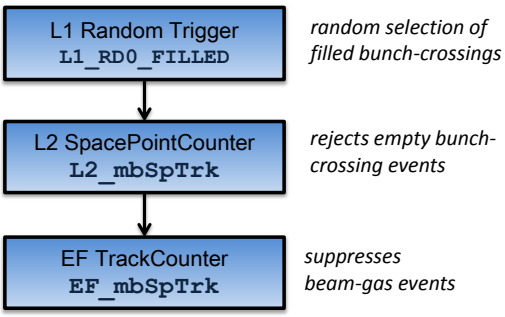

Figure 5.1.: Trigger levels of the ID minimum bias trigger mbSpTrk. Hit-clustering (SpacePointCounter) and tracking (TrackCounter) based algorithms perform the event selection at L2 and EF, respectively.

but every potential proton bunch-crossing is checked for beam activity. This was a rather welcome solution due to the low initial luminosity of $\mathcal{L} = 10^{27}\,\mathrm{cm}^{-2}\,\mathrm{s}^{-1}$.

Once the bunch-group mechanism was fully commissioned in 2010, certain bunch-groups (for definitions see Table 4.1) were used to select on paired (also called colliding or filled), unpaired or empty bunches. They were combined with a random trigger to select either at a high or low rate (RD0, RD1). Usually, RD0 was run at rates of the order of around 10 kHz and the rate of RD1 ranged from Hz to kHz. However, for the actual input to L2 possible prescales have to be considered as well which were adjusted to the luminosity of the run.

Multiple items were relevant for mbSpTrk depending on the purpose of the trigger. They use both bunch-groups and random triggers:

- L1_RD0_FILLED: the high-rate random trigger combined with filled bunches for proton-proton selection.
- L1_RD1_FILLED: the low-rate random trigger combined with filled bunches for efficiency measurements (accepting all events and forming trigger quantities of mbSpTrk). They needed to be permanently saved ("persistified") in order to reproduce offline trigger quantities.
- L1_RD0_UNPAIRED(_ISO[1]): the high-rate random trigger combined with unpaired bunches for estimation of background.
- L1_RD0_EMPTY: random trigger combined with empty bunches for threshold tuning (accepting all events and forming trigger quantities of mbSpTrk)

[1]Newer name since period E.

5.2. Level-2 of the ID Minimum Bias Trigger

At the second trigger level (L2) empty bunch-crossings have to be efficiently suppressed while ideally all of the proton-proton collisions are retained. The criterion at this level is to differentiate between events with and without beam interaction. The most critical functionality is to handle the electronic noise in empty bunch-crossings. mbSpTrk uses initial steps of pattern recognition algorithms forming hit clusters. Since no track finding algorithm is involved at this stage, the trigger gains on robustness against detector misalignment as a precise position of the hit clusters is not important, but only the number of formed hits matters.

5.2.1. Online Reconstruction Algorithms for Spacepoint Formation

Hit-clustering algorithms, in particular spacepoint formation, represent the initial steps of track reconstruction algorithms. Spacepoints are formed in essentially three steps and are very similar at L2 and EF.

To reconstruct **pixel spacepoints** raw data from the readout buffers are first unpacked (known as *Bytestream Decoding* or *Bytestream Unpacking*). The second step is the *clustering* of neighbouring Pixel cell information. These hit clusters can be in the third step directly transformed into Pixel *spacepoints* by a "local-to-global" transformation. For a hit-based selection the transformation of clusters to spacepoints is merely a technical step and therefore treated indifferently, i.e. pixel clusters are physically the same as pixel spacepoints.

The **SCT spacepoint** formation follows in principle the same formation steps as the Pixel measurements, however the last step is different. The "local-to-global" transformation cannot be performed. Instead, the spacepoints are formed out of cluster pairs of opposite sides of one module. Thereby, SCT spacepoints feature an intrinsic noise suppression during this step of spacepoint formation.

5.2.2. Selection Variables

The working point just above the level of electronic noise makes the trigger rather sensitive to changes of noise level. Handling noise hits at this early stage while maintaining trigger robustness was therefore carefully investigated. As already mentioned, the SCT spacepoint formation provides an intrinsic suppression of noise hits. The Pixel spacepoint formation needed an extra handling of noise. Several quantities were exploited to optimise the functionality of noise suppression and to provide sufficient fall-back solutions:

- Total pixel cluster time-over-threshold.

  One option is to make use of the amount of charge that is released by an incident particle as illustrated in Fig. 5.2. The readout of the Pixel detector (see also Section 3.2.2) is by design based on the time-over-threshold (ToT), producing a signal that is nearly proportional to the collected charge. Since the measurement of

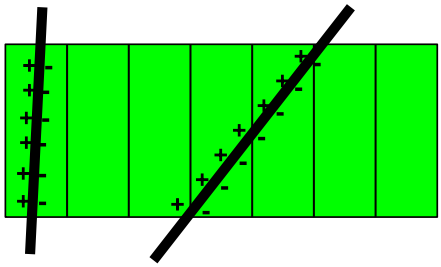

Figure 5.2.: Schematic view of pixel sensors (green boxes) and two incident particles [108]. Without a magnetic field the particle hits the sensor in most of the cases perpendicular. In some cases the angle of incidence is smaller than 90° leading to more sensors being hit and a larger amount of released charge created corresponding to a signal with higher ToT values.

the charge requires a calibration curve, it was more advantageous for the robustness of the trigger to directly use the total ToT of a pixel cluster.

- Pixel cluster size.

  The pixel cluster size is the number of pixels contributing to the pixel cluster and is determined by the positions where charge is released and by the charge mobility in the silicon. The illustration in Fig. 5.2 shows that depending on the incident angle of the particle one or several Pixel sensors are hit and can contribute to the cluster. If the particle hits the sensor perpendicular and no magnetic field is present, the most probably cluster size is one. However additional effects mitigate the perpendicular inclination of the particle and cluster sizes greater than one are created. Charge diffusion, δ-electrons or edge effects can then cause the adjacent sensor to produce a signal as well. Thereby and with increasing incidence angles, clusters with a larger number of pixels are formed.

  Since charged particles move within an electromagnetic field, there is a systematic shift of the incidence angles, influencing thus the pixel cluster sizes. Other effects have an impact on the size as well. Charge release fluctuations can cause the charge in one of the edge pixels to become too small to pass the discrimination threshold. Similarly, if the charge of a particle with a large incidence angle is spread over many pixels, clusters get split in case the charge is not sufficiently large to pass the threshold.

- Barrel/Endcap separation.

  Separation according to the detector position allows to exploit topological properties of event types. Beam-gas interactions are expected to produce more activity in the forward direction. A functionality was added to the trigger to select on multiplicities according to the module position. For the selection of pp events such a separation is not desirable and thus not used. Nevertheless, for monitoring and debugging purposes the positions according to barrel/endcap were very informative for monitoring the functionality of the trigger.

- Total number of pixel clusters.

  This global event feature exploits no specific detector region, giving the least possible bias on the event topology.

- Total number of SCT spacepoints.

  The same reason as above applies for SCT spacepoints as well.

5.2.3. Distribution of Selection Variables

In the following, signal and background distributions of the selection variables are compared in a data driven manner without prior selection cuts applied, if not indicated differently, using essentially randomly selected events.

One early run in 2010 was chosen as a representative run for the first period of data-taking at $\sqrt{s} = 7$ TeV when the LHC fill contained only one colliding bunch. In Fig. 5.3 one can see that the conditions were stable within 20−30 % for mbSpTrk over several weeks. At the end of run 152345 a large spike is visible. This happens when the Pixel and SCT detectors go into stand-by mode[2] but their readout has not been switched off nor has the trigger stopped (or switched to a different menu). In the two lower plots of Fig. 5.3 a few dips are visible. These are a general feature of the instantaneous luminosity of that run and other triggers like L1_MBTS_1 follow the same trend. However, the statistics of run 152409 were sufficient (more run characteristics are listed in Table 5.1) to extract *benchmark datasets* for signal and background:

- Signal: events with proton-proton interactions obtained by a random trigger selecting on filled, colliding bunches (in the following labeled as filled bunches) which forms mbSpTrk quantities. The L1 seed was L1_RD1_FILLED running unprescaled, but the output of L2 was prescled and 9,115 events were eventually recorded by that random trigger. These events contain also a small fraction of beam induced background and noise events.

- Background: empty bunch-crossing events recorded by L1_RD0_EMPTY seeding a dedicated trigger that forms as well mbSpTrk trigger quantities without rejecting at HLT. The rate is controlled by the L1 prescale and resulted in a recording rate of around 1 Hz providing 68,243 events in total.

Total Pixel Cluster Time-over-Threshold Distributions

The total time-over-threshold (ToT) of a pixel cluster is collected over several units of time, defined by the LHC clock cycle of 25 ns bunch-crossings (BC). The maximal time over which the charge release is integrated is smaller than the L2 latency. ToT distributions for signal and noise are shown in Fig. 5.4 for different detector regions with a clear contribution of a MIP signal visible around 30 BC in Fig. 5.4 (b). This figure

[2]The voltage changes from -20 to 50 V which releases electric charge in the silicon detectors.

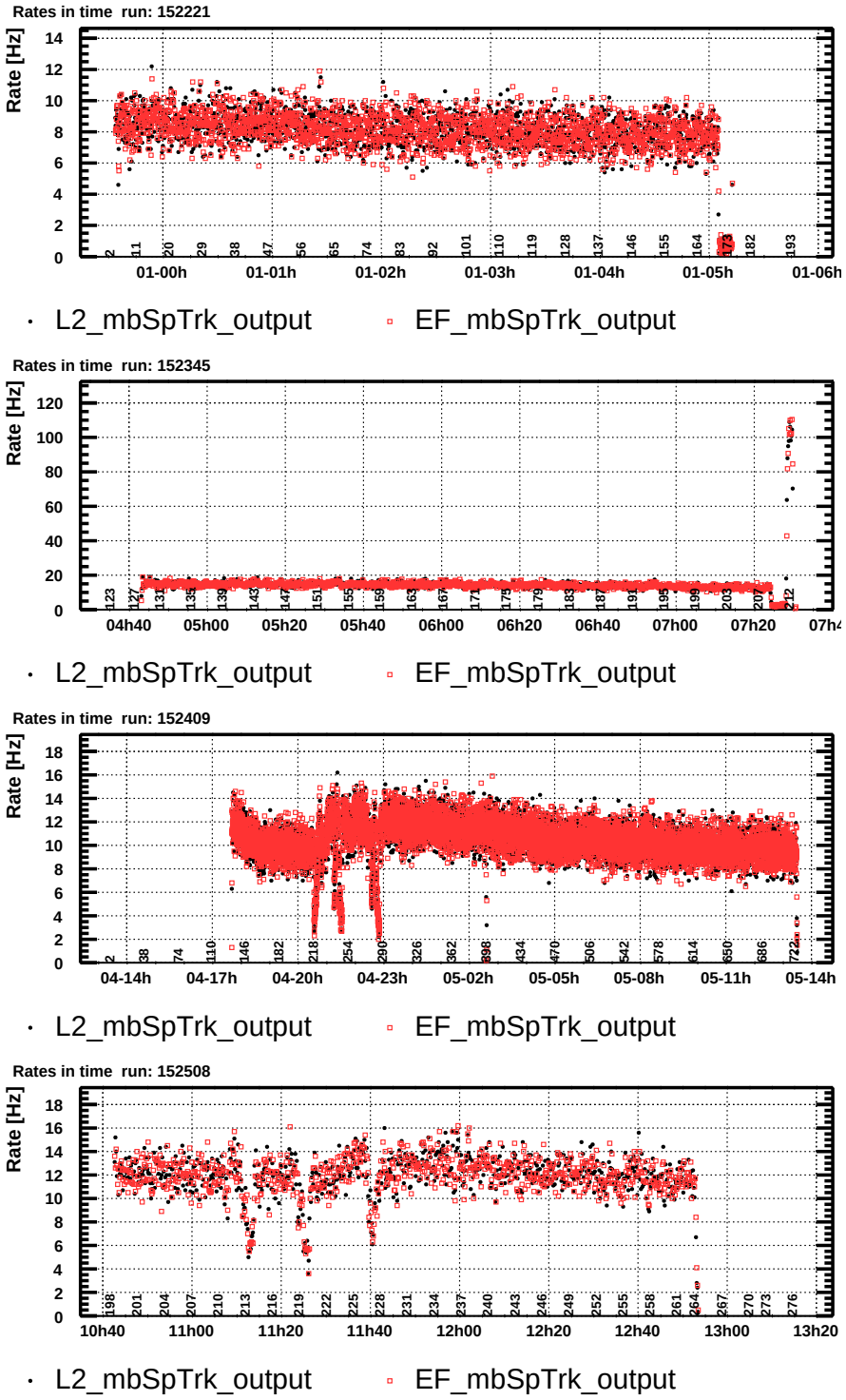

Figure 5.3.: Trigger rates during the initial phase. The rate of the ID minimum bias trigger mbSpTrk was constant within roughly 20 to 30 %, i.e. no large spikes are observed during data-taking.

Table 5.1.: Characteristics of run 152429 with around 20 hours of stable beam and the ID fully functional. Source [109].

number of colliding bunches	1
number of unpaired bunches	2
beam intensity [protons]	$1.2 \cdot 10^{10}$
peak luminosity	$1.6 \times 10^{27}\,\mathrm{cm}^{-2}\,\mathrm{s}^{-1}$
start date (local time)	Sun, 4^{th} April 2010, 13:33 h
end date (local time)	Mon, 5^{th} April 2010, 13:37 h
number of total recorded events	$6.7 \cdot 10^6$ ($85\ \mu\mathrm{b}^{-1}$)
number events in RNDM stream	$1.4 \cdot 10^6$
number events in MinBias stream	$5.6 \cdot 10^6$
average number of interactions per bunch-crossing	0.01
Lumiblocks with stable beam flag OFF	$1 - 119$
Lumiblocks with stable beam flag ON	$120 - 723$

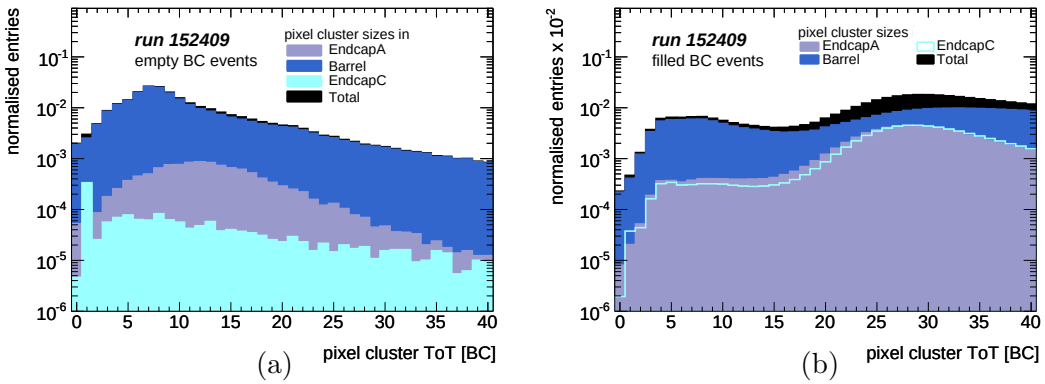

Figure 5.4.: Pixel cluster time-over-threshold in empty (a) and filled (b) bunch-crossings for three detector regions. (b) shows a clear contribution of a MIP around 30 BC.

also points out that a cut at 20 BC on the ToT is able to remove the bulk part of the noise. With a cut at 20 BC on the total pixel cluster ToT, less pixel clusters are formed as shown in Fig. 5.5. A projection of these distributions is shown in Fig. 5.6 to compare filled and empty BC events.

Thus, a cut on the ToT seems to provide a powerful mean to differentiate between noise hits and those generated by particles.

Pixel Cluster Size Distributions

Pixel cluster sizes are shown, separated according to their detector position in barrel or endcap, in Fig. 5.7 for noise (a) and proton (b) collisions. Noise is expected to form mostly only clusters of size one while particles can more often create larger cluster sizes. Possible contributions from cosmic-ray tracks in empty events can be estimated. Assuming a rate of the order of 1 Hz for cosmic-ray tracks hitting the ID [100] and considering the wider readout window of the Pixel detector at that time (5 BC corresponding to 5 $\times$ 25 ns, see also Section 5.2.6), the fraction of cosmic-ray events in the 68,243 recorded empty events is with 0.01 cosmic events fully negligible. It is thus assumed that the empty bunch-crossing events contain only noise from the electronics.

As Fig. 5.7 demonstrates, empty events possess much fewer pixel clusters of sizes greater than one compared to events with beam activity. However in both cases a large fraction of pixel clusters with one Pixel only are formed. Therefore, two ratios of the number of clusters with different sizes were investigated in more detail. The first ratio, labeled as ratio A, is formed by dividing the number of clusters with size different to one by the total number of pixel clusters:

$$\text{ratio A} = \frac{\#\text{ clusters of size} \neq 1}{\#\text{all clusters}}$$

Another ratio, called ratio B, directly compares the two most common pixel clusters:

$$\text{ratio B} = \frac{\#\text{ clusters of size 2}}{\#\text{ clusters of size 1}}$$

These ratios are shown in Fig. 5.8 for empty events (shaded area) and proton collisions (points). Both ratios indicate that many events are in the zero-bin, essentially for empty events which are also present in the paired bunch-crossing events. Therefore, a cut at e.g. very low ratio values is an option of mbSpTrk for both ratios which contributes to the flexibility of the trigger in rejecting noise events.

Total Pixel Cluster and Spacepoint Multiplicity

A relative simple mode was initially investigated in [1] selecting on the total number of formed Pixel and/or SCT spacepoints as depicted in Fig. 5.9. This proved to be powerful enough for mbSpTrk, however in a slightly modified way. Prior to a hit multiplicity requirement a ToT cut on the total ToT of a pixel cluster is applied which removes many

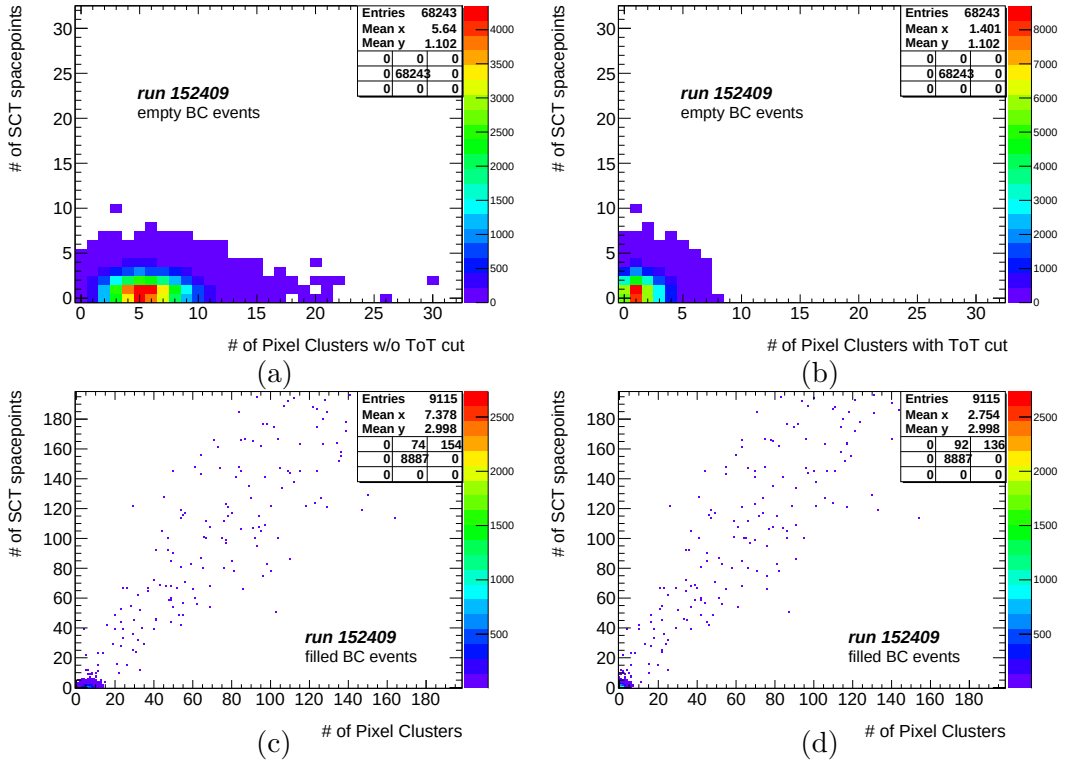

Figure 5.5.: Pixel and SCT spacepoint scattering in empty (a,b) and filled (c,d) bunch-crossings without ToT cut (a,c) and with ToT cut at 20 BC (b,d). In noise events Pixel and SCT hits are uncorrelated while they are for pp collisions. Note, the different scale of (a,b) and (c,d). The pad on the top left indicates how many entries are visible (central field) and how many are present in under- and overflow bins (other fields).

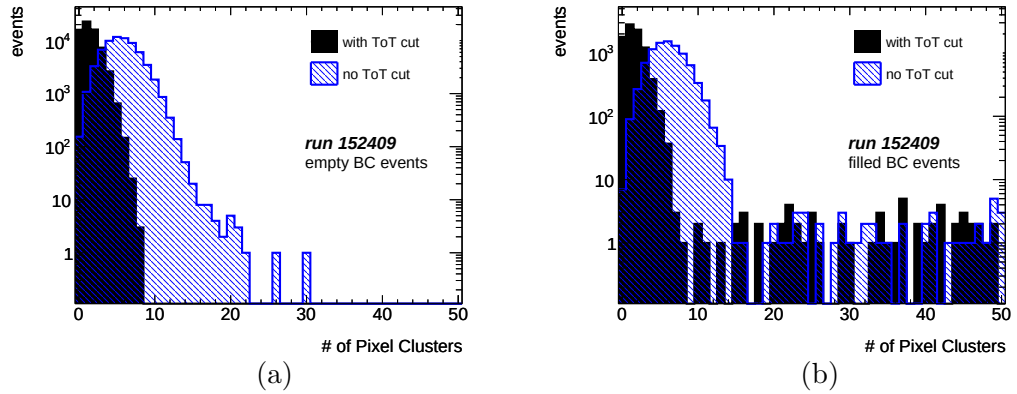

Figure 5.6.: Projection of Fig. 5.5 to the number pixel clusters for empty (a) and filled (b) bunch-crossings. The ToT cut shifts the distributions towards smaller number of pixel clusters.

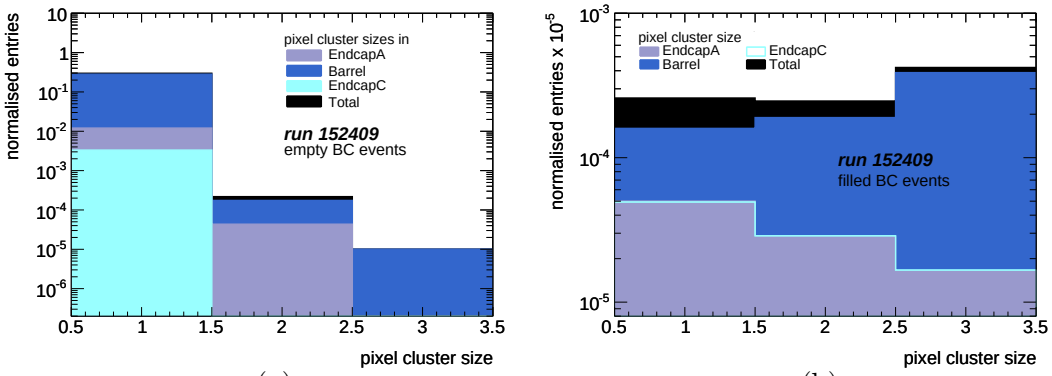

(a) (b)

Figure 5.7.: Pixel cluster sizes in events with empty (a) and filled bunches (b). The third bin contains entries from sizes of three or more.

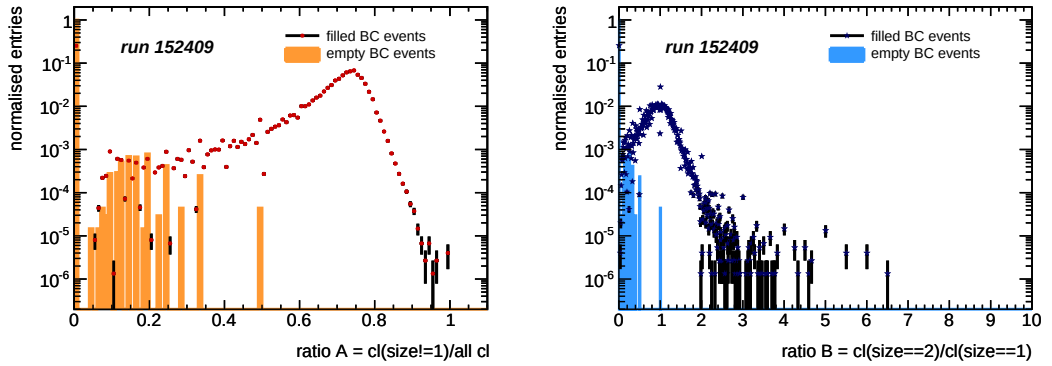

(a) (b)

Figure 5.8.: Ratio A (a) and ratio B (b) of pixel cluster sizes in events with empty (shaded area) and filled bunches.

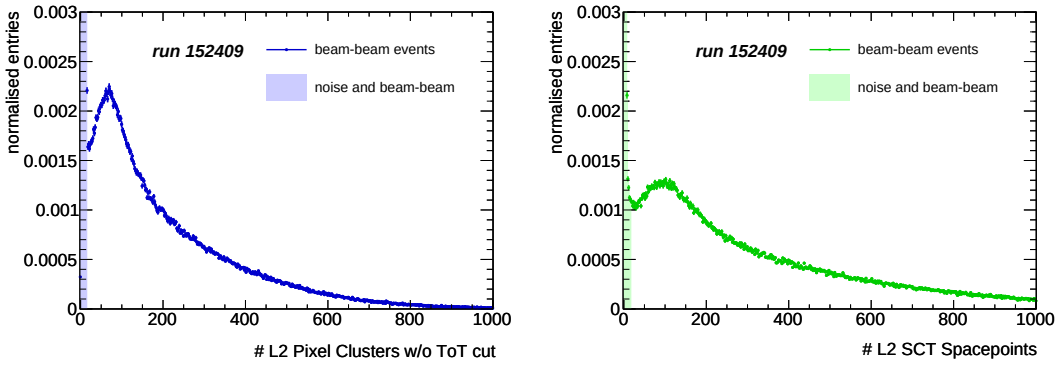

(a) (b)

Figure 5.9.: Pixel cluster (a) and SCT spacepoint (b) distributions at $\sqrt{s} = 7$ TeV normalised to the total number of events. The left shaded areas of both plots indicates the contribution from noise events.

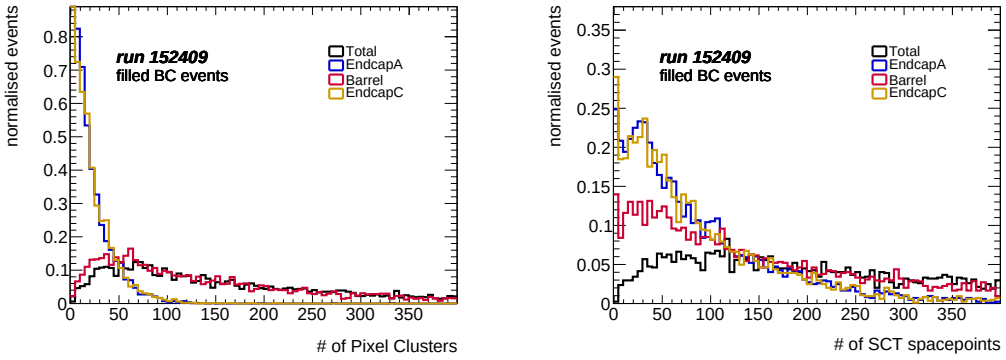

(a) (b)

Figure 5.10.: Spacepoint distribution separated according to barrel and endcap region of Pixel (a) and SCT (b) normalised by the total number of events.

of the noise hits. For the selection of proton-proton collisions it was obvious to exploit the correlation of Pixel and SCT spacepoints that was already visible in Fig. 5.5 (c,d).

Barrel/Endcap Separation

In Fig. 5.10, the number of formed pixel clusters (a) and SCT spacepoints (b) are shown for proton-proton events with contain at least one reconstructed silicon track (selected by mbSpTrk initially). One can observe that the spacepoint production is significantly higher for the barrel part than for the endcaps, which is expected simply by the larger number of modules in the barrel. The total number of spacepoints formed per barrel/endcap thus served as a simple check for monitoring online the data quality of mbSpTrk.

5.2.4. L2 Trigger Modes for Proton-Proton Selection

Several trigger modes were developed which select on the variables mentioned above to efficiently suppress noise events. These trigger modes are all based on Pixel and SCT information. A few trigger modes were chosen to benchmark the selection efficiency:

1. A minimum requirement of *pixel clusters* `AND`-combined with a minimum requirement of SCT spacepoints in the total detector.

2. A minimum requirement of *pixel clusters with enough ToT* `AND`-combined with a minimum requirement of SCT spacepoints in the total detector.

3. A minimum requirement of the pixel cluster *ratio A* `AND`-combined with a minimum requirement of SCT spacepoints in the total detector.

4. A minimum requirement of the pixel cluster *ratio B* `AND`-combined with a minimum requirement of SCT spacepoints in the total detector.

Table 5.2.: Benchmark trigger modes for proton-proton selection. These results are indicative only and should be constantly re-evaluated when the noise level in the detectors changes. For the pp selection efficiencies a lower limit at 68.3 % C.L. is given.

trigger mode	Pixel requirement	threshold	SCT cut	empty events suppression [%]	pp–selection [%]
1	pixel cl w/o ToT cut	≥ 4	≥ 4 Sp	97.70 ± 0.06	≥ 99.7
2	pixel cl w/ ToT cut at 20 BC	≥ 4	≥ 4 Sp	99.87 ± 0.01	≥ 99.7
3	cluster size ratio A	≥ 0.01	≥ 4 Sp	97.25 ± 0.06	≥ 99.7
4	cluster size ratio B	≥ 0.01	≥ 4 Sp	99.99 ± 0.01	≥ 99.7

These trigger modes were tested on the benchmark datasets. The "signal-sample" was further refined such that the acceptance of mbSpTrk can be tested on actual proton-proton interactions. The additional requirement which was imposed was that at least one (online reconstructed) track with $p_{\mathrm{T}} > 200$ MeV in the silicon detectors had to be present[3]. The results for various modes are listed in Table 5.2. Overall, the suppression efficiencies of empty events are very high while the selection efficiencies for proton interactions are all at least 99.7 % at 68 % C.L. indicating that the entire signal sample was triggered by mbSpTrk.

Conclusion

A trigger cut based on pixel cluster sizes has the potential of removing a significant part of empty bunch-crossing events. Using either ratio A or B yield both good suppression. Ratio B seems more efficient than ratio A, leaving a smaller fraction of empty events.

Compared to the simple trigger modes requiring a total number of pixel clusters and SCT spacepoints, these modes yield similar results. The final choice of the selection mode of mbSpTrk was thus mode 2, suppressing (99.87 ± 0.01) % of empty bunch-crossings.

Other combinations are as well available, e.g. the `AND`−combination can be configured to be an `OR`−combination. This mode however favors the selection of noise or beam induced background as one can see from Fig. 5.11. The events close to either of the axes contain mostly hits in one of the detector. More background is visible in Fig. 5.11 (b) with many events containing a high number of spacepoints in the SCT but not in the Pixel. One example of such an event is shown in Fig. 5.12 in an event display.

[3]This selection corresponds to the EF selection of mbSpTrk outlined in Section 5.3

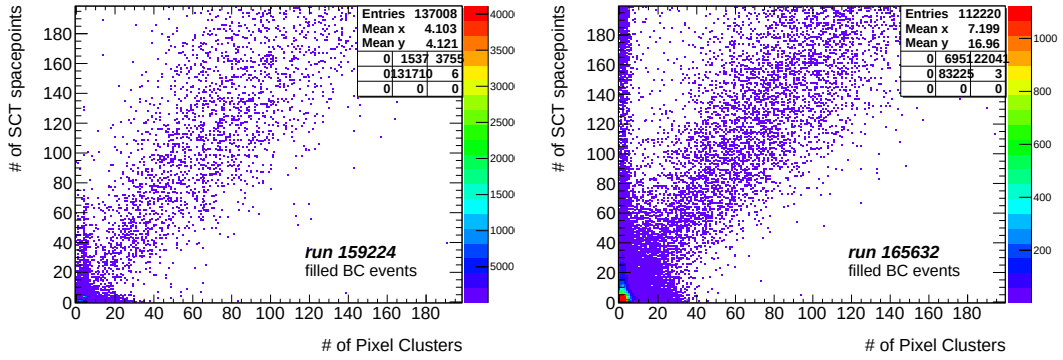

(a) (b)

Figure 5.11.: Pixel cluster and SCT Spacepoint scatter plot for two runs, (a) with modest beam background (b) with significant more background leaving uncorrelated hits in the SCT. Events were selected by a random trigger on filled bunches.

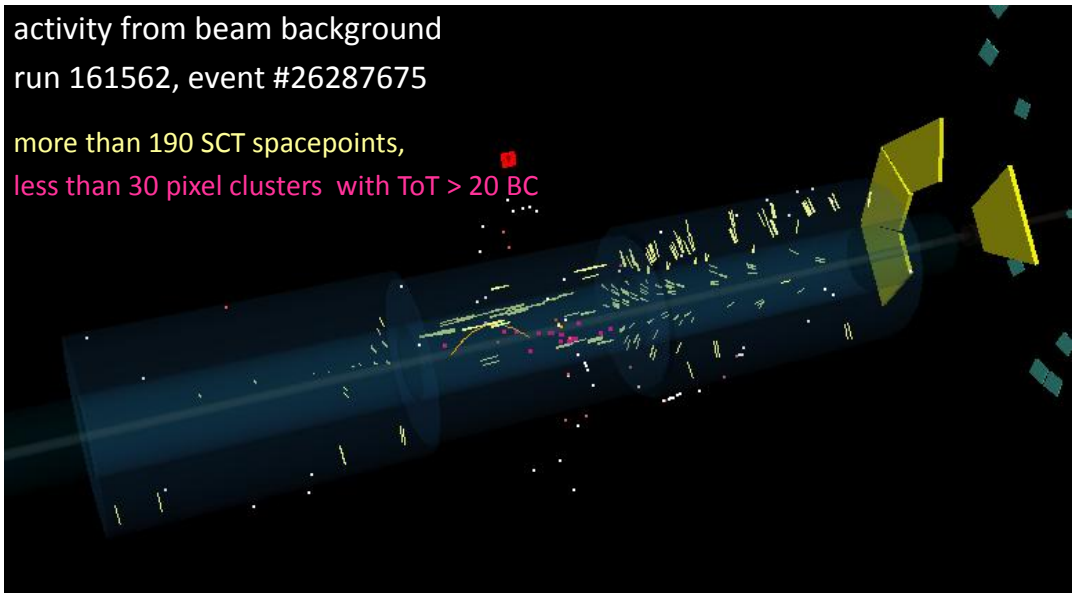

Figure 5.12.: Example of an background like event which hit mostly only one of the silicon detectors, in this case the SCT. Also MBTS is hit on one side only.

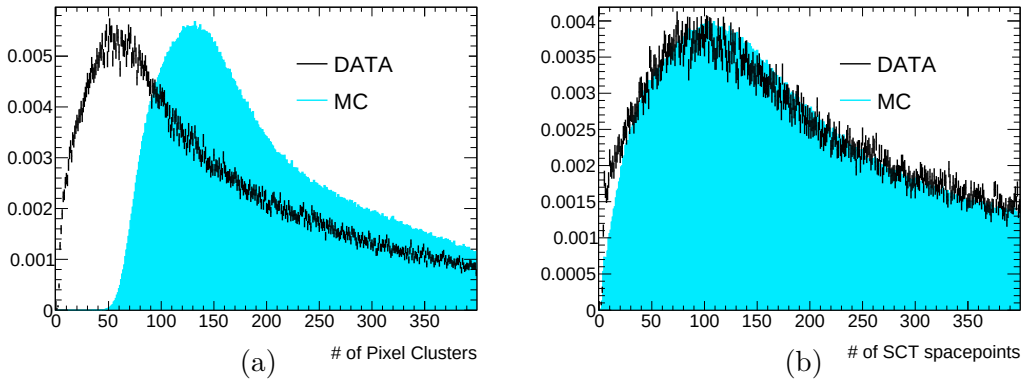

Figure 5.13.: Comparison of real data and simulation of inelastic proton-proton collisions at $\sqrt{s} = 7$ TeV. (a) pixel cluster and (b) SCT spacepoint distributions, both after a low p_{T} track requirement and L2 noise removal cuts. Similar discrepancies were present in the corresponding MC sample at $\sqrt{s} = 0.9$ TeV.

5.2.5. L2 Trigger Modes for Beam-Gas Selection

Possibilities were investigated to select on activity in unpaired bunch-crossings when beam-gas/halo reactions take place in the fiducial volume of the ID.

The topology of halo events suggest to use only one of the silicon sub-detectors for selection of such events. A trigger was set up, named mbSpBg_unpaired, and configured to require only a minimum activity in the Pixel detector sensitive down to small radii to which other detectors like the MBTS cannot reach.

A trigger for events with activity in the forward regions of the ID could also be considered. It would impose a maximum of activity in the barrel parts, while the endcaps must contain a minimal number of hits. These options were not deployed, but can be used for further studies on beam induced background. The possible modes are:

1. A minimum number of pixel clusters with enough ToT.

2. A minimum requirement in one of Pixel endcaps `AND`-combined with a minimum requirement of SCT spacepoints in one of the SCT endcaps.

3. Same like 2., but additionally a maximum number of pixel clusters and SCT spacepoints is allowed in the barrel.

5.2.6. L2 Threshold Tuning with Data

Tuning the trigger thresholds was performed with one of the first data runs containing proton collisions. Initial thresholds were extracted from empty events selected during cosmic ray data-taking. Unfortunately Monte Carlo datasets were less reliable for threshold validation. Variables which would require a good description of the noise level in the region where possible trigger cuts would be applied, show only poor agreement with

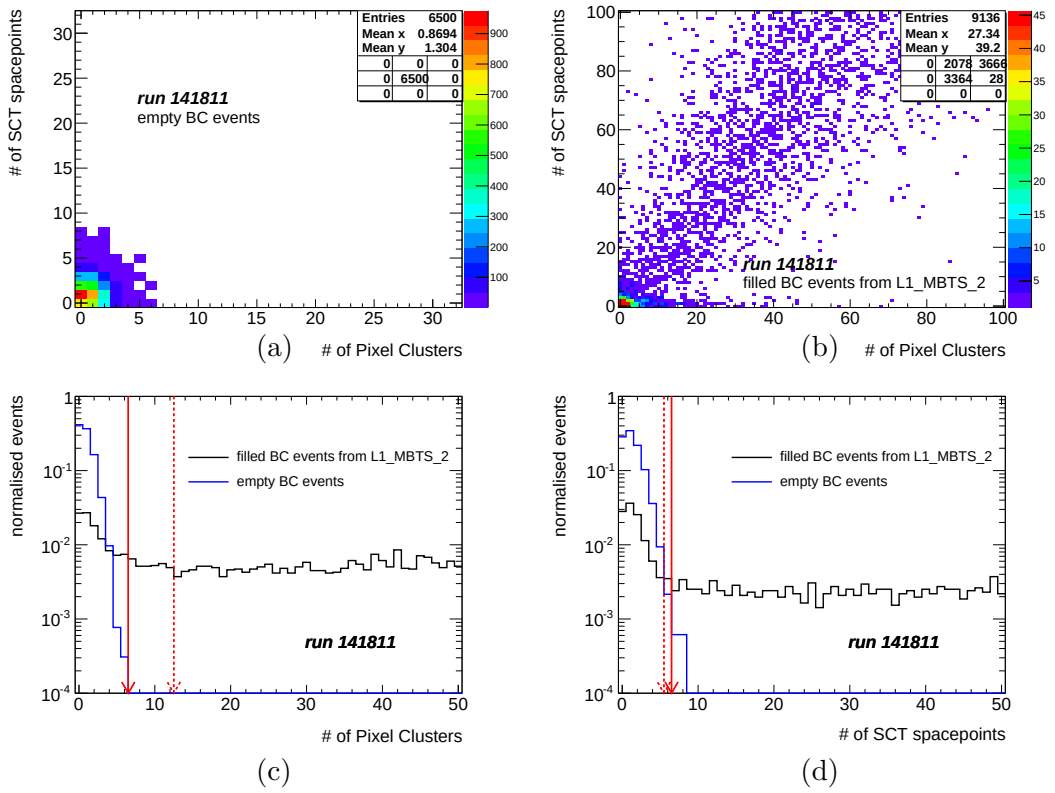

Figure 5.14.: Spacepoint scatter plot of (a) empty events and (b) beam interactions selected by L1_MBTS_2 in an early run of 2009. The bottom plots show the (c) pixel cluster and (d) SCT spacepoint distributions. The dashed arrow indicates the old cut of mbSpTrk at L2 (Pixel at 12 and SCT at 5) while the continuous line indicates the new thresholds of 6 and 6 respectively.

data. This is clear from Fig. 5.13 (a). A relative good agreement was visible in other variables as depicted in Fig. 5.13 (b).

The detector noise in Monte Carlo samples were tuned with relative long delay times in the early phases. Track reconstruction algorithms are rather robust against these noise levels even when the difference is as large as 100 pixel clusters. For these reasons it was more reliable to use data for threshold tuning.

The L2 trigger thresholds evolved since the trigger was deployed for proton-proton selection. The initial configuration of mbSpTrk at L2 were set to require more pixel clusters than SCT spacepoints, see Table 5.3, defining the minimum activity from proton-proton collisions, if more than 12 Pixel and 5 SCT spacepoints are formed. When the silicon detectors were operated at nominal conditions and a stable beam situation was present in Nov. 2009, the thresholds were tuned to yield close to 100% suppression of noise events affecting only little the proton-proton selection. The pixel cluster requirement could safely be reduced from 12 to 6 whereas the SCT cut was slightly tightened from 5 to 6 spacepoints. These new thresholds were deduced from run 141811 as shown Fig. 5.14.

Table 5.3.: Trigger thresholds (mode 2) evolution since beam operation. The thresholds were successively tuned from MC, cosmics and proton-proton beams and were optimized to yield more than 99 % suppression of noise events.

run	date	# pixel clusters	# SCT spacepoints
before 142149	before Nov. 2009	12	5
since 142149	Nov. 2009	6	6
since 152166	Mar. 2010	3	3
since 177531	Mar. 2011	2	3

Table 5.4.: Read-out/trigger modes for the Pixel and SCT. The configurations were the same for the phase when mainly minimum bias triggers provided beam data (from end of 2009 to spring 2010).

run number (recording date)	Pixel read-out mode	SCT trigger mode
before 155112	5 BCs	XXX (any-hit)
since 155112 (15. May 2010)	4 BCs	XXX
since 158632 (05. Jul. 2010)	3 BCs	XXX
since 165732 (25. Sep. 2010)	1 BCs	XXX

These threshold settings had a direct impact on the analysis outlined in Section 6.7.1.

Constant monitoring of noise level seen by mbSpTrk lead to a further relaxation of the L2 thresholds. They were derived in a very similar manner as before. Runs taken shortly after run 141811 (e.g. run 142149, 142154, 142166, 142191) indicated that lower requirements yield a similar good suppression. With a threshold of three pixel clusters that have a ToT of at least 20 BC and three SCT spacepoints the remaining fraction of empty events is less than 0.07 %.

A specific detector setting was relevant for trigger threshold tuning. During the initial data-taking phase (until May 2010), the readout of the Pixel detector comprised five times the nominal time window, 125 ns. As consequence, each event contained five times as many noise hits. The larger readout window of the Pixel detector and other sub-detectors of ATLAS allowed for example to synchronise their timing signals such that event fragments can be associated to the right bunch-crossing. With increasing luminosities, i.e. higher occupancy from proton-proton collisions, the readout window was further reduced as listed in Table 5.4.

The situation is slightly different for the SCT detector. The SCT always reads out three time bits, i.e. a time window of three bunch-crossings, but the data compression reduces the number of hits according to a selected hit pattern. There are four options available for possible hit patterns [73]. For 2010 data-taking only the test mode (also called *any-hit mode*) was activated corresponding to the pattern XXX which stands for the three time bins of 25 ns each which are read out together. Effectively, this means

that triple noise is read out per event. In contrast, the so-called *level-sensing pattern* with X1X requires a signal over threshold in the triggered (middle) time bin in order to be read out. This mode is employed at higher luminosities [73].

Even if the readout window had changed, the overall noise level in the respective sub-detector can have changed too such that both effects have an effectively negligible impact on the trigger threshold settings. After the initial phase of LHC operation was superseded by the physics programme, minimum bias triggers were only selecting at small rates, so the bulk part of minimum bias data profited from constant readout settings of the Pixel and SCT detectors.

5.2.7. Trigger Robustness

Since the L2 selection is sensitive to the noise levels in the Pixel and SCT detector, the trigger has to be robust against noise variations. Detector changes as mentioned above are considered as long-term changes. They usually do not cause problems during data-taking if one adapts the trigger thresholds to the new situations. In other cases, when there are less predictable issues appearing during the data-taking, it has to be assured that the trigger is not prone to these problems.

Most of the detector problems can be handled either manually by the shifter or automatically for cases which would affect the data-taking efficiency and a fast reaction is required, as example when the synchronisation of the data fails and corrupted data are generated. However, for the rare case that single pixels become intermittently noisy but do not cause problems in the DAQ (and therefore no automatic procedure steps in to mask it), mbSpTrk may accept events which consist actually only of noise.

To avoid situations in which the L2 filtering is basically disabled as a noisy module fakes beam activity, an internal protection for such rare cases was developed.

Dynamic Masking of Noisy Modules

The internal protection mechanism of the mbSpTrk trigger consists of identifying a noisy module and excluding it in the feature extraction process (see Section 4.1.3). This dynamic, event-by-event masking of noisy modules identifies a noisy module by the number of formed pixel clusters and SCT spacepoints per module, respectively. If this value is higher than the respective threshold that module is not further considered.

The Pixel occupancy in the nominal operation scenario is for the innermost layer is around 1.5 hits/module/BC [70]. The SCT occupancy per channel is expected to be smaller, since it is further away from the interaction point.

To determine a threshold from which on a module is identified as noisy, two types of high-occupancy events were studied: simulated $t\bar{t}$ and heavy ion events. These gave an indication of how many times a module would be mis-identified leading eventually to an event reject. As a result none of the tested events would have been rejected due to limiting the maximal allowed number of clusters and spacepoints for a Pixel and SCT module. Rather conservative thresholds per module were chosen for the initial phase which were 100 for Pixel and 50 for SCT.

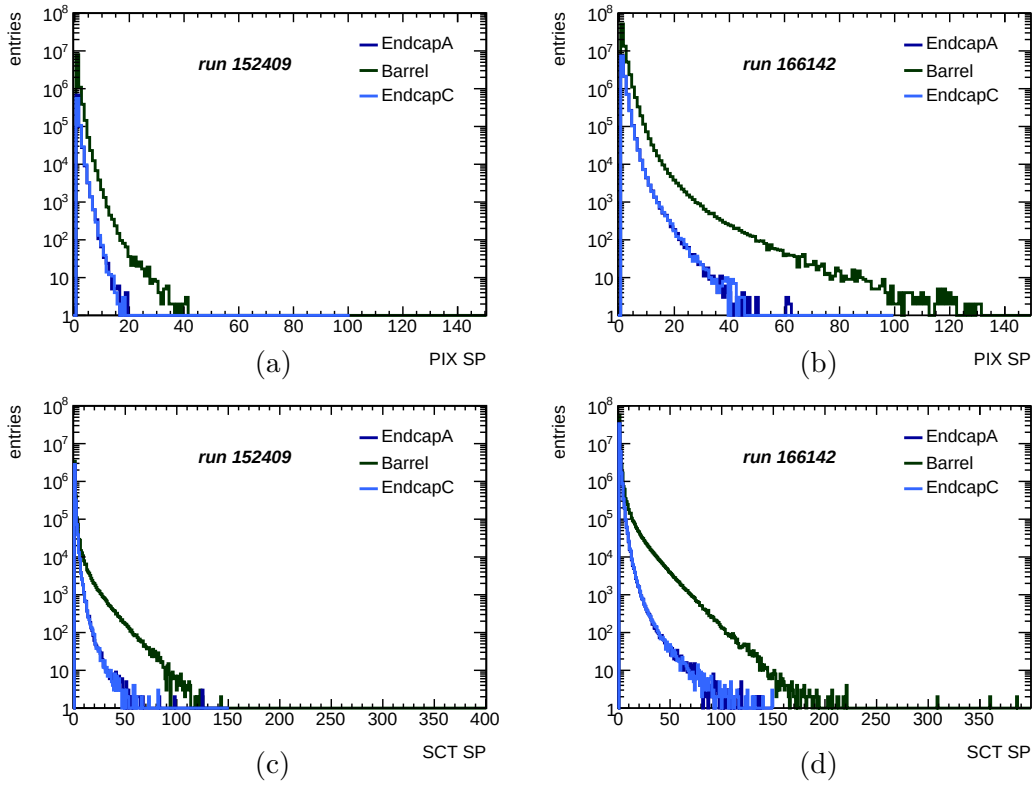

Figure 5.15.: Distributions of number of Pixel (a,b) and SCT (c,d) spacepoints per module for an early proton-proton run with an beam intensity of $1.2 \cdot 10^{10}$ protons (a,c) and a later run with 140 colliding bunches and beam intensities of $1.6 \cdot 10^{13}$ protons (b,d). A threshold defining a noisy module has to be significantly higher than the occupancy from pp collisions.

The number of clusters and spacepoints formed per module was also studied for two different occupancies in data runs which had different beam intensities. The two beams in an early run, run 152409, had an intensity of 1.2 10^{10} protons, while a run recorded later that year, run 166142, had beams with intensities of 1.6 $\cdot 10^{13}$ protons [109]. The distributions per module, separated by the detector position, are shown in Fig. 5.15. These figures suggest to use different thresholds for a barrel and endcap model to identify noisy modules for both, Pixel and SCT. Currently, only an option to set the total threshold is implemented. Both thresholds that identify a noisy Pixel or SCT module need to be re-evaluated with new data once this internal protection is deployed. As for the entire 2010 data this option was in place but not used.

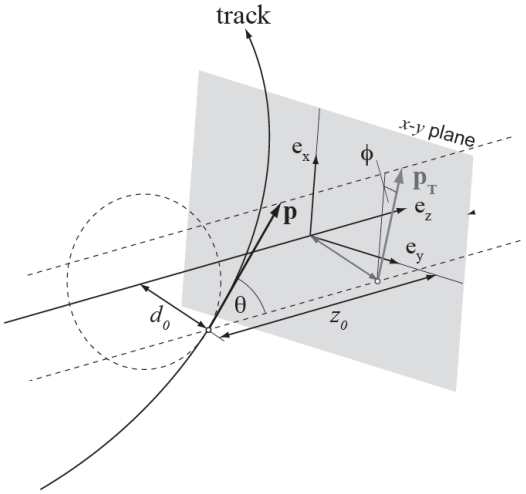

Figure 5.16.: Visualisation of track parameter definitions in ATLAS [111]. The transverse track parameter d_0 is the shortest distance of the track to the IP, z_0 is the corresponding parameter along the z-axis.

5.3. Event Filter Selection of the ID Minimum Bias Trigger

The purpose of an additional selection step at the Event Filter is to suppress, if necessary, beam induced background events online while low-p_{T} tracks shall be best possibly retained. In [1] it was found that the standard track reconstruction [110] needs modifications for trigger deployment in order to obtain a higher efficiency for low p_{T} tracks. Optimal performance of the standard tracking algorithms is achieved when the charged particle passes through all three sub-detectors. This requires the particle to posses at least a p_{T} of around 500 MeV in order to extrapolate the track from the silicon detectors out to the TRT (*inside-out* sequence). Results of optimisation studies of online track reconstruction for low p_{T} tracks are discussed in the following.

5.3.1. Track Reconstruction at Event Filter for Minimum Bias Events

The available processing time at the Event Filter (EF) is more relaxed compared to L2 which allows the use of offline tools for repeatedly performed tasks. Nevertheless minimum bias algorithms may be time critical as minimum bias triggers process the full event data of the silicon sub-systems performing a *full scan* of these detectors.

The algorithms for reconstructing tracks in minimum bias events are reduced to the initial parts of the inside-out sequence [110] using essentially the steps before the track extension to the TRT. The reconstruction steps used with the modified parameters are outlined here in more detail. The track parameters as used in the ATLAS tracking are illustrated in Fig. 5.16. The reconstruction steps for $\mathrm{EF}_{\mathsf{mbSpTrk}}$ are:

1. `PixelClustering` and `SCTClustering`: Pixel and SCT clusters are formed in a similar way at L2.

2. The `SiTrigSpacePointFinder` takes the clusters and provides *seeds* for the next algorithm. The seeds are identified with a vertex constraint and formed from two pixel clusters to build the longitudinal track parameter (z_0) of the track. Only if the seed is compatible with a configurable minimum p_{T} and d_0, and comprises at least three clusters, it is further considered.

3. The `SiTrigTrackFinder` uses the seeds to mark the direction in which a *road* of detector elements is built-in order to search for more associated hits to one track candidate. The combination of hits yielding the lowest residuals (squared distance of measurement and track extrapolation) are taken to build the road. At this level a spacepoint object is still dissolved in clusters, of which it originally consists. Only cluster collections that are located on the road are further processed by the so-called Kalman-Fitter-Smoother to form track candidates. It follows the track trajectory and adds hits successively. At each step the track information is progressively updated by performing a fit. Thus, on the next measurement surface the track representation is more precisely predicted.

4. `TrigAmbiguitySolver` resolves which track candidates are kept for further processing as the output of the Kalman-Fitter-Smoother contains in general more than one candidates for one true track. This number can be very high depending which kind of event is processed. Track candidates can have shared hits or can be incomplete. They can also describe fake tracks for which the majority of the hits do not originate from a single particle. With detailed material description a global fit is performed. In a second step the tracks are evaluated using a scoring strategy allowing to take into account the morphological character of a track. If it falls beyond a certain quality cut it is not further considered, otherwise the resulting track is kept for the next step.

   While the standard tracking foresees as next step the extension to the TRT and a final fit to extract the track parameters, the sequence developed for minimum bias selection works as follows.

5. `TrigTrackCounter` is a new class and used to process the previously formed track candidates. An instance of that class for mbSpTrk is `EFMbTrkFex`. It forms the event features of total track multiplicity within configurable parameters and counts the number of tracks inside a certain region along the beam-axis. This information is passed to the hypothesis algorithm.

6. The algorithm of class `TrigTrackCounterHypo` decides based on the features from the fex-algorithm[4] about the event accept or reject (in mbSpTrk the algorithm is called `EFMbTrkHypo`).

Before the instance of `TrigTrackCounter` is executed, three more algorithms are run to store permanently (*persistify*) detailed track information in case of an event accept:

[4] fex means *feature extraction*, see Section 4.1.3.

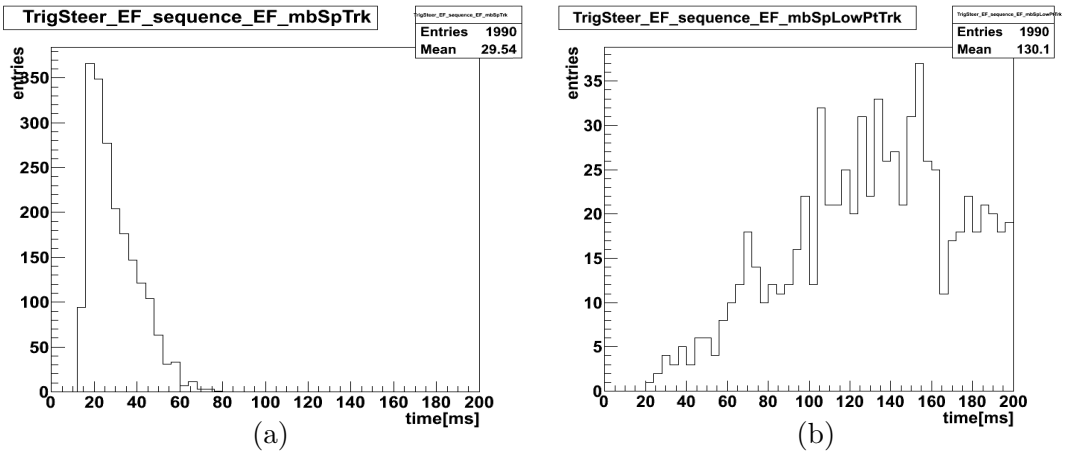

Figure 5.17.: Time consumption of (a) the modified standard tracking sequence and (b) the two-pass low-p_{T} sequence on simulated PYTHIA non-diffractive events. The dedicated low-p_{T} tracking shows significantly worse timing performance but would still stay within the time budget of the EF.

`InDetTrigTrackSlimmer`, `TrigVxPrimary` and `InDetTrigParticleCreation`. They all together are known as the Minimum Bias TrigEFIDSequence, see also Fig. 5.20.

The modifications made to the reconstruction sequence (step 1−4) were extending the event processing to a full scan and a lower minimum reconstruction p_{T} to 150 MeV (default is at 500 MeV). An alternative to that modified standard sequence was to adopt the offline low p_{T} reconstruction at trigger level as well. It consists of the inside-out tracking with standard reconstruction parameters and a subsequent sequence which repeats the track inside-out sequence with the remaining hits and softer reconstruction parameters (*two-pass reconstruction*). In benchmark tests the performance of both sequences was tested and it turned out that lowering the p_{T} cut to 200 MeV of the standard tracking yield good results (see Section 5.3). The timing performance of the modified standard tracking was well within the time constraints at the EF while it was significantly worse, more than four times slower[5], for the two-pass reconstruction sequence, see Fig. 5.17. In principle one could expect twice the time consumption for the two reconstruction sequences, if the number of hits to form the initial seeds is about the same for the two sequences. This seems not to be the case and the initial seed finding is slowed down due to a high number of possible combinations of hit clusters. A more detailed tuning of reconstruction parameters was not performed, instead the sequence deployed in the trigger is the modified standard tracking sequence.

5.3.2. Selection Variable and Distributions

The EF observable for the mbSpTrk trigger is the track multiplicity within a certain z_0-region. These quantities, the p_{T}- and η-spectra are shown in Fig. 5.18. Two reconstructed

[5]This was measured on a local machine pcatr66 with no interference from other algorithms executed.

Table 5.5.: Cut flow for threshold studies the EF level of mbSpTrk with data at $\sqrt{s} = 0.9$ TeV (run 141811). A pre-selection by L1_MBTS_2 provided sufficient statistics.

# events	filled bunch-crossings	unpaired bunch-crossings
L1_MBTS_2 selection	9136	59
after L2 requirements (3,3)	8044	42
after EF requirement of 1 track	7737	5
after EF requirement of 2 tracks	7429	2
ratio 1-track/L2 requirement	0.9618	0.1190
ratio 2-track/L2 requirement	0.9235	0.0476

distributions are compared. Once, the simulation of non-diffractive PYTHIA events are shown reconstructed with the trigger code using the standard tracking optimised for minimum bias. In addition, the same quantities are shown using this time the offline two-pass reconstruction sequence.

5.3.3. Threshold Tuning and Beam-Gas Suppression Efficiency

From initial MC studies in [1] further beam-gas suppression was anticipated by tightening the internal reconstruction cut of $|z_0| < 250$ to 200 mm and requiring within that region at least two tracks. Both requirements could be immediately relaxed as the analysis of run 141811 shows. The EF track multiplicity of paired and unpaired bunch-crossing events selected by L1_MBTS_2 is depicted in Fig. 5.19 for L2 and additional EF requirement of mbSpTrk. While initially many empty events are selected, their fraction diminish after the L2 spacepoint requirements (trigger mode 2). The same is true for unpaired bunches, which underline that noise events (significantly present in unpaired bunches) are highly suppressed. Only a few events are left which are assumed to arise from beam-gas interactions.

In the initial phase the beam position was not optimised and tracks could be reconstructed at rather high z_0 values. Therefore, the requirement on z_0 was loosened to maximal value of 250 mm. Furthermore, both figures in Fig. 5.19 and the cut flow in Table 5.5 for the same run show that the track requirement could be lowered. Apart from the L2 trigger requirement (trigger mode 2 and denoted as (3,3)), two options for an EF selection are indicated, either requiring one track or two. With these numbers one can estimate the contribution of beam background in beam-beam events.

Contribution of Beam-Gas in Paired Bunch-Crossing Events The L1_MBTS_2 trigger on paired bunches selected 9,136 events of which around 12 % is assumed to be noise (considering the L2 noise removal cuts of mbSpTrk), leaving 8,044 events. After the application of the same noise removal cuts on unpaired bunch-crossing events, 42 events are left which are supposed to be due to beam gas interactions, i.e. around 0.5 % in paired bunches interactions stem from beam gas collisions. It will drastically be reduced, if

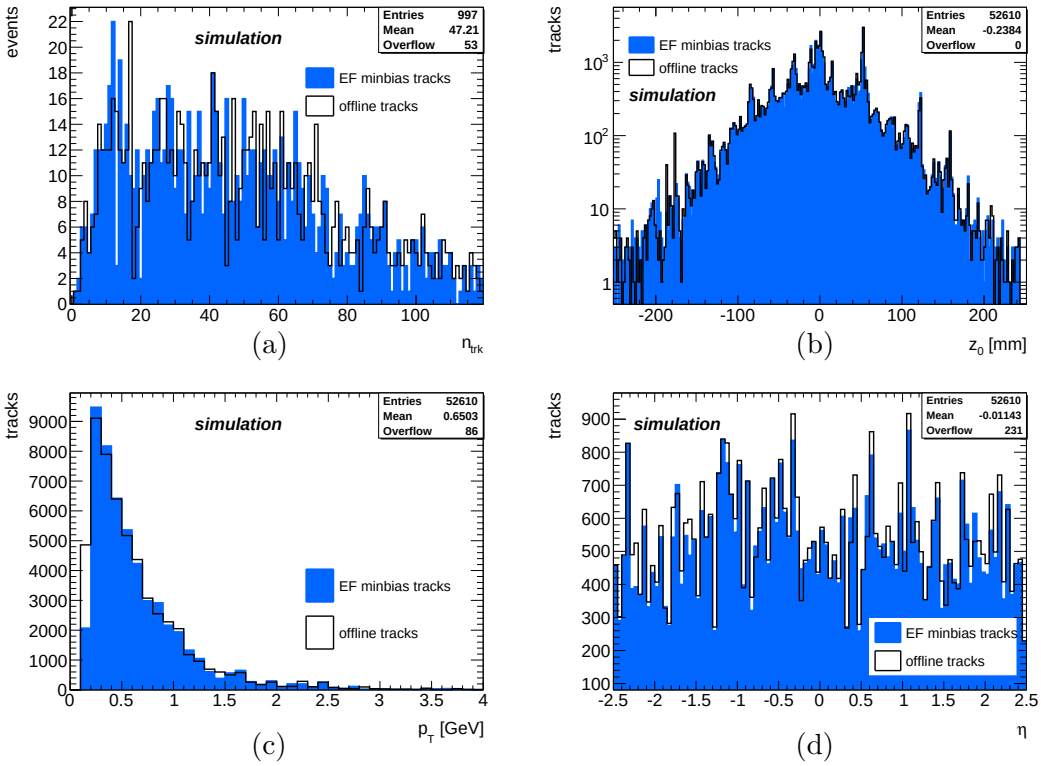

Figure 5.18.: Distributions of simulated non-diffractive events for tracks reconstructed at the EF with the special minimum bias setup (blue, shaded) and offline (black line). Crucial quantities to derive the trigger decision are the track multiplicity (a) and the longitudinal impact parameter z_0 (b) reconstructed w.r.t. the nominal beam spot (0,0,0). p_{T} (c) and η (d) are also shown.

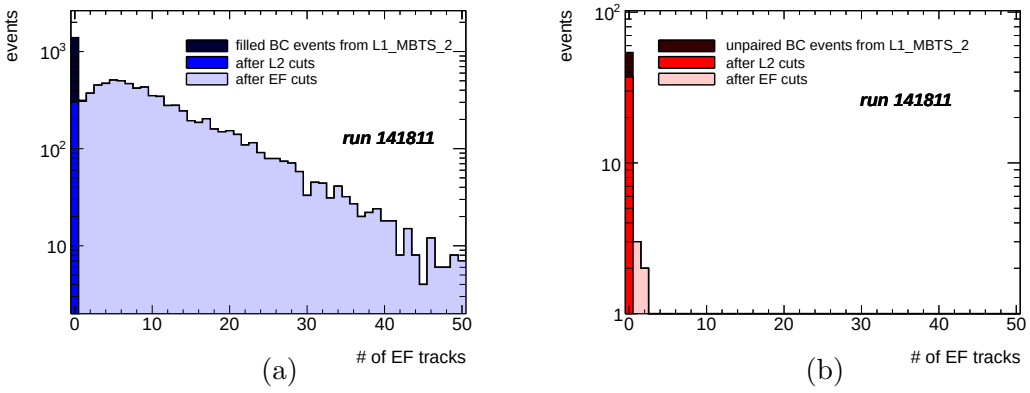

Figure 5.19.: EF track multiplicity in paired (a) and unpaired (b) BC events selected by L1_MBTS_2 for no selection, L2 and EF cuts (the distributions are plotted in the order as the legend indicates).

Table 5.6.: Trigger thresholds evolution since beam operation. The initial thresholds turned out to be too pessimistic and were lowered in the runs in 2009, and disabled since 2010.

run	date	$\|z_0\|$ requirement	# of required tracks
before 141811	before Nov. 2009	200 mm	2
since 142149	Nov. 2009	400 mm	1
since 152166	Mar. 2010	OFF	OFF

already one EF track is required, then 2 out of 7427 remain, i.e. the contamination is down to about 0.02 %.

EF Threshold Evolution of mbSpTrk The threshold evolution of the EF part of mbSpTrk is listed in Table 5.6. Also this trigger level profited from stable thresholds over the entire data-taking period in 2010. With rising luminosity a new trigger was derived from `EF_mbSpTrk` used to collect high track multiplicity events.

5.4. Timing Performance

The requirement to introduce only minimal bias in the event selection translates into processing silicon hits in the full ID coverage. Such algorithms are well possible if the required bandwidth stays well within the capacities and no problems in the data acquisition are caused. Since the Pixel detector is read out in a zero-suppressed mode and also the SCT is equipped with data compression functionalities, the actual bottleneck is, if data of these detectors are queried at a high rate. It was measured, if the nominal target time budget of 40 ms and 4 s on average as mentioned in Section 4.1.3 are met for the chains at L2 and EF, respectively. The specific algorithm sequence of mbSpTrk are illustrated in Fig. 5.20.

The L2 chain `L2_mbSpTrk` consists of two sequences. First, an initiator sequence was introduced `L2_mbDummyRoI` for performance reasons. The steering can thereby recognise a common root of several minimum bias chains using similar sequences which allows to enable *algorithms caching* in case the same event is processed from several minimum bias chains. It is followed by the sequence consisting of the feature extraction algorithm `L2MbSpFex` that performs hit-clustering in the entire Pixel and SCT and `L2MbSpHypo`, the hypothesis algorithm that derives a decision about the event.

The EF chain `EF_mbSpTrk` is seeded by `L2_mbSpTrk` and runs as first part of the sequence the inside-out tracking with parameters specific for minimum bias track reconstruction. The second part of the sequence executes `EFMbTrkFex` and `EFMbTrkHypo`.

The time consumption for both sequences are shown in Fig. 5.21. One can see that at both levels, L2 and EF, the average time is well below the average target time. With around 200 ms on average, the EF algorithms even stayed significantly below the available time budget of around 4 seconds. However a few outliers with easily ten times

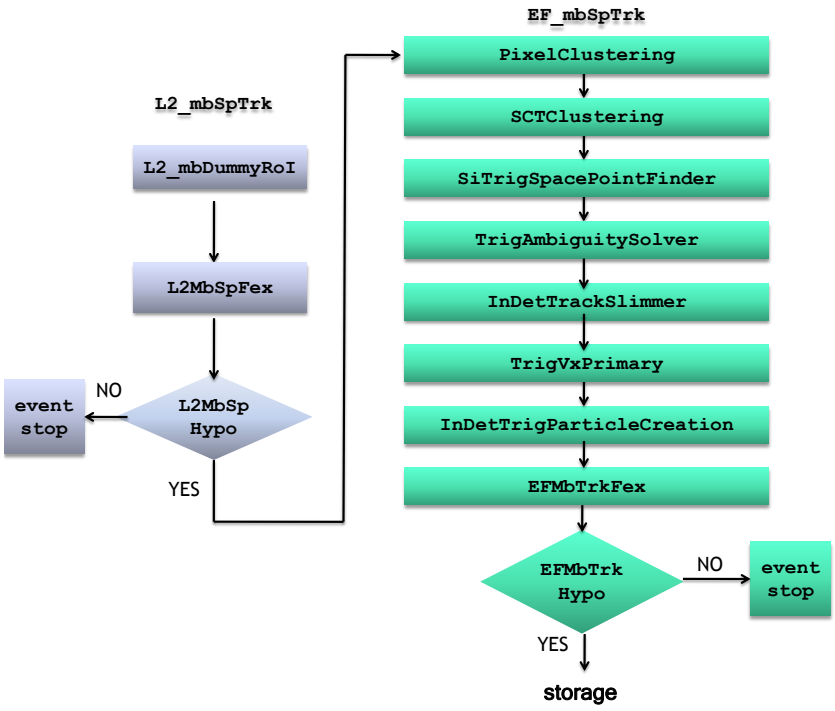

Figure 5.20.: Full HLT sequence of mbSpTrk. Common tracking algorithms usually have specific names for the trigger in which they are employed (minBias_EFID in case of mbSpTrk, not shown).

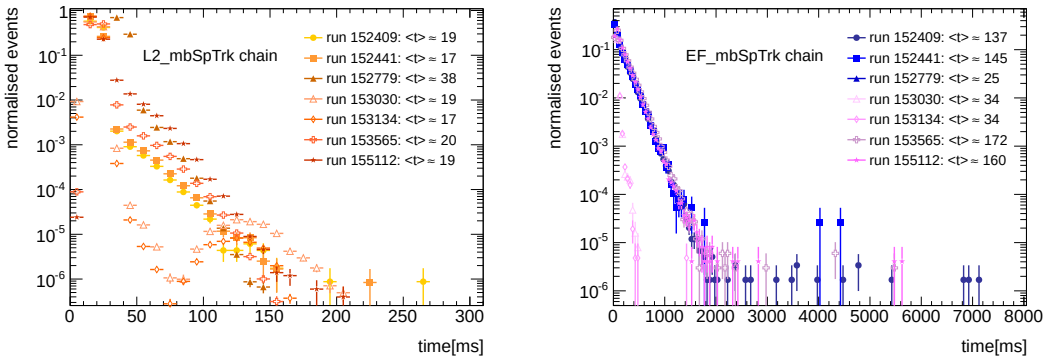

Figure 5.21.: Timing performance of L2 and EF minimum bias chains for several (example) runs. The mean time consumption per event is also indicated in ms. The tail is due to events with higher occupancies.

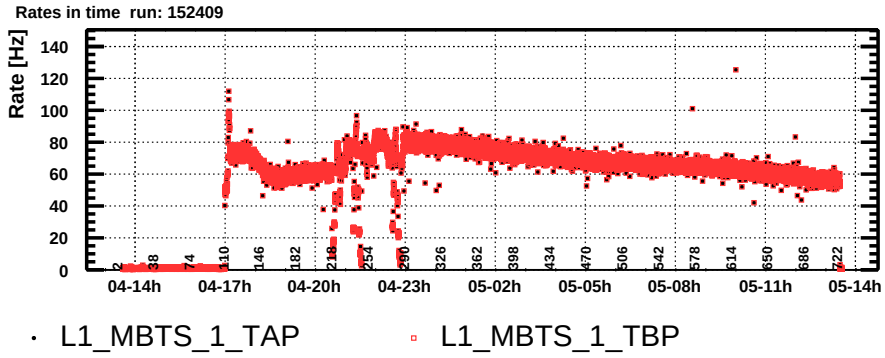

Figure 5.22.: Recording rate of L1_MBTS_1, the main minimum bias trigger during the initial phase, here shown before and after prescale (TBP, TAP).

as much time consumption are also visible (at L2). In one case so far, a time-out during an event processing was observed. Such events end up in the *debug* stream for analysing the issue offline. Also, with increasing luminosity the mean processing time shifts to longer processing times.

5.5. Minimum Bias Trigger Chains

Several chains were setup for different purposes and can be categorised accordingly:

- Primary physics triggers: L1_MBTS_1 and mbSpTrk both were assigned around 4 Hz of recording rate at $\mathcal{L} = 10^{31}\,\mathrm{cm}^{-2}\,\mathrm{s}^{-1}$. Before this luminosity was reached, both triggers, especially L1_MBTS_1 were assigned a much higher recording rates, see for example Fig. 5.22. For normal operation the rates were adjusted such that L1_MBTS_1 was primarily selecting and mbSpTrk is used for efficiency measurements of MBTS triggers. In case of issues with one of the used detector systems, the other trigger would serve also as back-up.

- Supporting triggers: For threshold calibration and trigger efficiency measurements so-called "calib" (later "eff") chains were set up which form the trigger quantities of mbSpTrk and MBTS at L2. Various versions of the calib/eff chains were active, all differing only by the L1 seed but executing in pass-through the HLT minimum bias algorithms. Examples of these chains are mb_RM_calib, seeded by L1_RD0_FILLED, mb_MS_calib, seeded by L1_MBTS_2, mb_M1_calib, seeded by L1_MBTS_1, mb_M2_calib, seeded by L1_MBTS_2.

- Trigger for threshold tuning. The most useful chain was the random trigger on empty bunch-crossings, mb_RM_calib_cosmic.

- Trigger for beam background selection. These were (amongst others) set up as a copy of the primary triggers but seeded by unpaired bunch triggers: mbSpTrk_unpaired and L1_MBTS_1_UNPAIRED. In addition, a trigger was put in place

that is sensitive to beam-gas interactions at small radii, mbSpBg_unpaired, seeded by L1_RD0_UNPAIRED and requiring at L2 at least 10 pixel clusters with a ToT $\geq$ 20 BC. Rates of this trigger are shown in Fig. 5.23.

Several more purposes as luminosity measurements [112] and various dedicated soft QCD analyses [113] have kept minimum bias triggers in the trigger menu even when the luminosity was increased such that the probability of an interaction per bunch-crossing was significantly higher than 50 %.

5.6. Conclusions

The ID Minimum Bias mbSpTrk was successfully set up and operated during the entire period of LHC operation in 2009 and 2010. The stable and robust performance is a result of an extensive use of the offline and online validation frameworks in which most of the functionalities were developed, refined and validated.

The trigger is equipped with several possible configurations to suppress empty bunch-crossing events. The default configuration bases the trigger decision on a total number of pixel and SCT spacepoints with a refinement on the pixel requirement to require at ToT of at least 20 BC. It can also be changed to use the pixel cluster size in different ways but preference was given to simple trigger conditions.

For future deployment, a few details have to be verified in order to use the same configuration as in 2010. The readout window for the pixel is already down to 1 BC. However, this together with the feedback current used to define the signal width in the pixel cell, would have impact on the trigger threshold for any pixel requirement. Similar, the data compression mode of the SCT should be verified and the threshold should be re-evaluated.

Furthermore, flexibility to changing background conditions was achieved by deriving a new configuration for online low-p_{T} track reconstruction at EF for this trigger. Tracks with a minimum of $p_{\mathrm{T}} = 200$ MeV can be reconstructed in a *full-scan* processing data of the entire Pixel and SCT systems. These represent relative high costs in terms of CPU, but the relative low occupancies present during low luminosity phases as in 2009/2010 kept the processing time well below the targeted average of 4 seconds. This can change for higher occupancies which are currently present at ATLAS. The two-pass track reconstruction could be optimised for online deployment. The potential advantage is that after the first reconstruction step, the used hits will no longer be considered in the second step. Any combinatorial effects could thereby be avoided that are the most time consuming parts. First attempts were made to use the two-pass reconstruction online as discussed, but were rejected due to the worse timing performance obtained when using the standard parameters for the offline two-pass reconstruction.

During the entire data-taking of mbSpTrk in 2010, this trigger profited from stable trigger thresholds. In particular, the EF selection was not actively deployed. This results in a dataset with least possible bias which can be used for various purposes. In the next chapter, the most relevant use cases are described. Especially, the use as control trigger to understand the performance of the MBTS is outlined in detail.

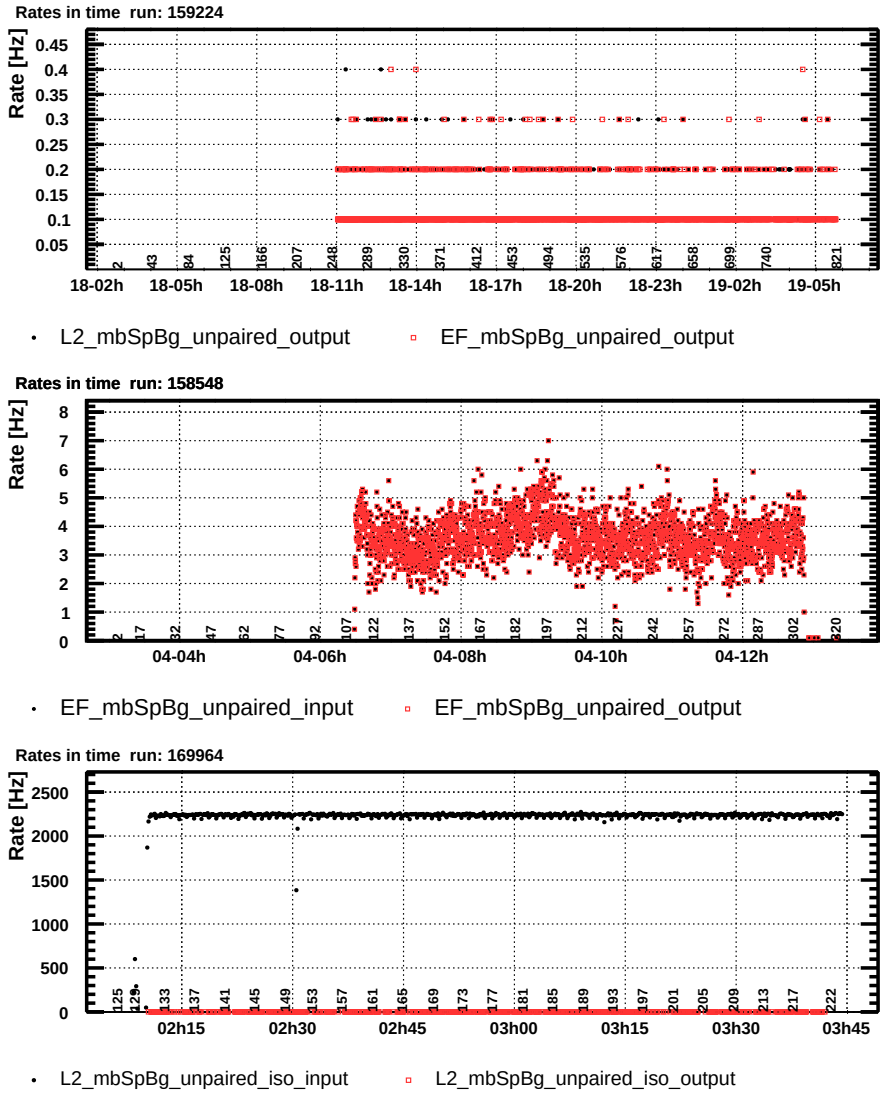

Figure 5.23.: Rates of mbSpBg_unpaired, a dedicated beam gas trigger. In run 159224 the input rate to L2 was about 100 Hz at $\mathcal{L} \approx 10^{27}\,\mathrm{cm}^{-2}\,\mathrm{s}^{-1}$. The output was reduced to around 0.1 Hz (see top plot), meaning the suppression of mbSpBg_unpaired was a factor 10^3. The middle plot shows a significant higher recording rate, also the luminosity was increased to around $\mathcal{L} = 6 \cdot 10^{29}\,\mathrm{cm}^{-2}\,\mathrm{s}^{-1}$. The bottom plot visualises the high input rate in a later run, 169964, where Pb collided at a luminosity of around $\mathcal{L} \approx 10^{24}\,\mathrm{cm}^{-2}\,\mathrm{s}^{-1}$. The resulting rate was similar as in run 159224 fluctuating between 0 and 0.5 Hz, thus a suppression factor was of the order 10^5.

6. Performance and Use of Minimum Bias Triggers at $\sqrt{s} = 0.9$ and 7 TeV

The general purpose of a minimum bias trigger is to inclusively select proton-proton interactions for measurements of charged particle spectra like those outlined in Chapter 7 and in [41, 46, 114]. In the early phase of data-taking in 2009 and 2010, only 0.1 % of bunch-crossings contained a proton-proton interaction. The main trigger to select proton-proton interactions in that phase were using the Minimum Bias Trigger Scintillators, MBTS, as they provided already at the first trigger level a reduction of empty events. As the MBTS cover a different pseudorapidity acceptance than the tracks of charged particles used in several analyses [41, 46, 115, 116], it is important to quantify the bias of the MBTS. Therefore, the ID based Minimum Bias Trigger, mbSpTrk, was used which is in several aspects complementary to the Level-1 (L1) MBTS. Not only higher trigger levels are used in mbSpTrk, it directly bases the trigger decision on signals of the ID as was outlined in Chapter 5.

This chapter describes in detail the performance of L1 MBTS at $\sqrt{s} = 0.9$ and 7 TeV using data as reference collected by the High-Level-Trigger mbSpTrk. Furthermore, the performance of mbSpTrk using MBTS as a reference has been investigated. Trigger efficiency and bias studies of both triggers are discussed in this chapter. First, MBTS signals in data and Monte Carlo are studied in Section 6.1. Offline selection criteria used for data performance studies of both minimum bias triggers are introduced in Section 6.2, followed by the definition of trigger efficiency and bias in Section 6.3. Both triggers are tested against each other on a quantitative and visual level in Section 6.4 and 6.5 respectively, before efficiencies and biases of mbSpTrk in Section 6.6 and MBTS in Section 6.7 are discussed in more detail. Another relevant quantity is the operational stability of the triggers which is outlined in Section 6.8. Finally, concluding remarks are given at the end of the chapter in Section 6.9.

6.1. Data versus Monte Carlo Comparison of MBTS Signals

The MBTS simulation is compared to data in order to validate its description in Monte Carlo (MC) and possibly extract properties of MBTS triggers from MC. The lowest level at which the MBTS trigger is studied is the signal of each counter. At a next level the trigger quantity is compared which is the L1 hit multiplicity of the scintillator counters. For this study a special trigger commissioning setup was used which recorded the trigger decision per counter in each event.

The following naming convention for L1 MBTS triggers is applied in ATLAS: the total multiplicity of counters in which enough charge is released to pass the discrimination

threshold is expressed by L1_MBTS_X with X the total number of counters required to fire. Another trigger condition requires a coincidence of MBTS cells firing, denoted by L1_MBTS_X_Y, where X counters are required to fire on one and Y on the other side.

The analysed data were selected by L1_MBTS_1 during period A (see Table 4.2), while the simulated events are a mixture of soft inelastic MC09 events at $\sqrt{s} = 7$ TeV.

6.1.1. Analysis Method

A set of requirements were chosen to obtain data samples with different degrees of purity, i.e. contributions of noise and beam background. The selection criteria were: the L1_MBTS_1 trigger, the mbSpTrk trigger, an offline selected track (denoted as $n_{\text{sel}}^{\text{BS}} \geq 1$, described in detail in Section 6.2) and a reconstructed vertex. These criteria were applied separately to the events (and not subsequently) in order to view the impact of the single requirements.

The single counter signals are depicted in Fig. 6.1 (a,b) for the tightest selection criterium, i.e. after a vertex requirement. Values below the discrimination threshold are visible, since the event was selected if *any* of the MBTS counters fired. One can thereby compare the signal of the two particular counters in data and MC. Large differences to the noise description in MC are apparent. Furthermore, only the simulation shows the contribution of a MIP peak at around 0.6 pC and 0.5 pC for the inner and outer counters, respectively. It is basically invisible in the data even though each scintillator is operated already at the highest possible voltage; the MBTS counter thresholds were tuned by increasing the discrimination threshold of each counter from 30 mV to 50 mV corresponding to 0.16 pC and 0.23 pC respectively, aiming at an improvement of the signal-to-noise ratio [80].

The ratio of data and MC signals are shown for all counters in Fig. 6.1 (c,d). Also here, large differences are observed especially in the threshold region at 0.23 pC. This makes a reliable estimate of the trigger acceptance for different event types rather impractical.

For the next comparison level, the L1 multiplicities of the counters that fired are considered. They are compared in Fig. 6.2 (a,b) for the different selection criteria. Ratios of hit multiplicities formed in data and MC are shown below in Fig. 6.2 (c,d). One can nicely observe that the selection criteria influence only the low multiplicity bins showing a spread in the ratio values. The criteria have essentially no effect from four hits onwards for both, the inner or outer ring. However, in no bin MC matches the data.

6.1.2. Conclusion

The differences observed in data and Monte Carlo comparison of MBTS signals and their multiplicities can have two reasons. While the discrepancy of a single counter signal is rather due to a poor simulation of the scintillator response, the differences in the multiplicities can in addition stem from differently modeled physics in the Monte Carlo simulation.

Due to the discrepancies of the noise calibration for MBTS signals, which are even larger for mbSpTrk as shown in Fig. 5.13, only data (unless it is indicated differently) is

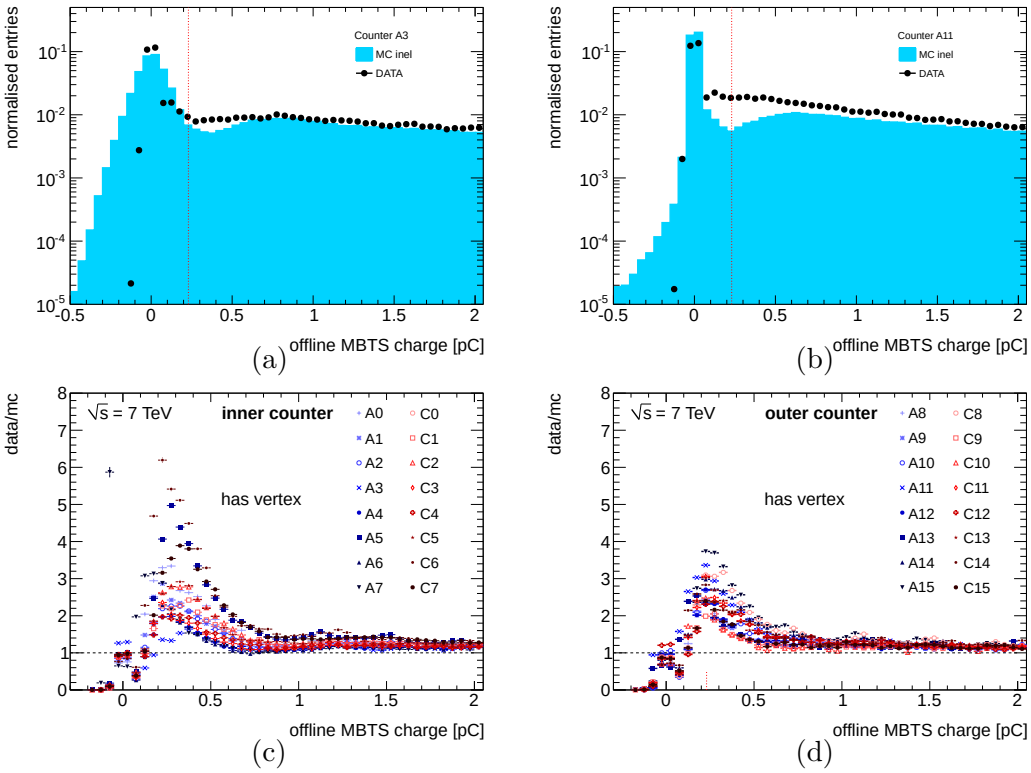

Figure 6.1.: Comparison of inner (a,c) and outer (b,d) counter signals and data/MC ratios (c,d). Vertical lines in (a,b) indicate discrimination thresholds at 0.23 pC.

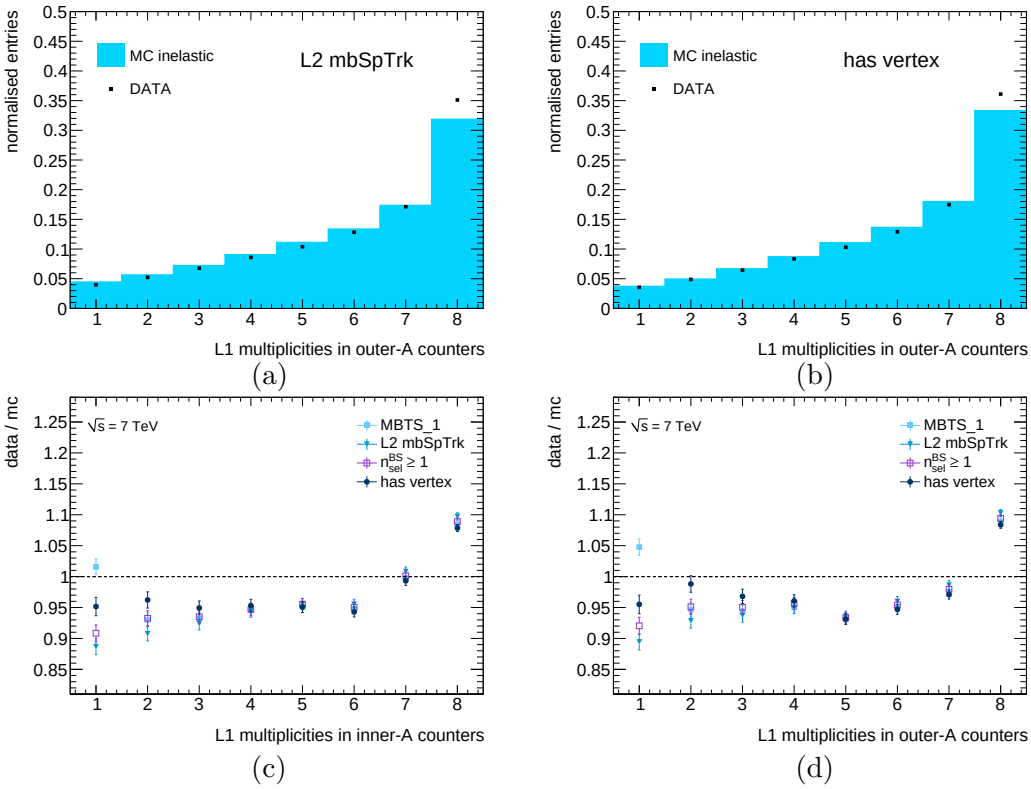

Figure 6.2.: Comparison of L1 MBTS multiplicities in data and MC for indicated selection criteria.

analysed in more detail in the next sections. Hence, possible trigger correlations or trigger acceptances for the different event types cannot be fully trusted when obtained from MC, unless a better simulation of the detector response and more realistic description of noise levels are available. No significant disadvantage for performance studies arises by not using MC. Precise predictions of acceptances of different event types cannot be made, but this would in any case not be possible as the modeling of soft processes itself is highly uncertain.

6.2. Offline Selection for Trigger Studies

For the data analysis, offline selection criteria are introduced that define the analysed phase-space regions. It is assumed that machine background events, i.e. interactions of the beam with residual gas molecules, are removed to a large extent.

For the presented trigger studies, the applied offline selections result in a variable which quantifies the selected track multiplicity, $n_{\mathrm{sel}}^{\mathrm{BS}}$. It uses track parameters relative to beam-spot (BS) instead of a reconstructed primary vertex.

In the trigger analysis, a phase-space region is slightly differently defined than for the analysis of charged particle multiplicities outlined in Section 7.1.2. The difference concerns events in which no vertex is reconstructed. Such events are considered for the trigger analysis while they would not be for the charged particle multiplicity analysis. As consequence, requirements on track parameters with respect to a reconstructed primary vertex are not used, instead those relative to the beam-spot.

6.2.1. Kinematical Phase-Space Cuts

Two trigger phase-space regions were studied as listed in Table 6.1, in the following referred to as "MB1" and "MB2". MB1 focuses on regions in which the track reconstruction performance is well understood [46, 117] and therefore requires the presence of at least one reconstructed track with $p_{\mathrm{T}} > 500$ MeV. MB2 is more inclusively considering tracks down to 100 MeV of which at least two are required. This requirement was imposed due to a vertex requirement in the charged particle multiplicity analyses [41]: vertexing algorithms use at least two tracks as input along with track parameter information with respect to the beam-spot [118]. With such a requirement, the vertex reconstruction efficiency becomes high in the phase-space regions considered for charged particle multiplicity analyses.

6.2.2. Datasets

The analysed data at $\sqrt{s} = 0.9$ TeV were taken in December 2009 streamed into two datasets, the MinBias stream which contains data collected by MBTS triggers, and the BPTX stream, with of events selected by the ID Minimum Bias trigger. The analysed data taken $\sqrt{s} = 7$ TeV fall into period A, split as well into MinBias and RNDM stream.

Table 6.1.: Selection criteria defining two phase-space regions MB1 and MB2. The nominal track parameter cut for the trigger is on d_0^{BS}. For systematic uncertainty studies, parameters were used defined w.r.t to a primary vertex (PV).

	MB1	MB2
	phase-space cuts	
$n_{\mathrm{sel}}^{\mathrm{BS}}$	≥ 1	≥ 2
p_{T}	> 500 MeV	> 100 MeV
$\lvert\eta\rvert$	< 2.5	< 2.5
	track quality requirements	
# pixel hits on track	≥ 1	1 in B-layer if expected
# sct hits on track	≥ 6	2 if 100 MeV $< p_{\mathrm{T}} \leq 200$ MeV
		3 if 200 MeV $< p_{\mathrm{T}} \leq 300$ MeV
		if $p_{\mathrm{T}} \geq 300$ MeV
$\lvert d_0^{\mathrm{BS}}\rvert$	< 4.0 mm	< 1.8 mm
$\lvert d_0^{\mathrm{PV}}\rvert$	< 1.5 mm	same as MB1
$\lvert z_0^{\mathrm{PV}} \cdot \sin\theta^{\mathrm{PV}}\rvert$	< 1.5 mm	same as MB1
pile-up veto	# tracks of 2nd reconstructed vertex ≥ 4	

6.3. Definition of Trigger Efficiency and Trigger Bias

The trigger efficiency is measured from data in the phase-space regions mentioned in Table 6.1. The fact that it can be measured in data makes use of the independent trigger systems of mbSpTrk and MBTS. Generally, the trigger efficiency is expressed by formula 6.1 with ϵ_{T1} the trigger efficiency of a trigger T1 measured with respect to an orthogonal trigger T2 providing the control sample in the phase-space region defined by offline selection criteria e.g. MB1 or MB2:

$$\epsilon_{\mathrm{T1}} = \frac{\mathrm{T1\ \&\ T2\ \&\ offline}}{\mathrm{T2\ \&\ offline}} \tag{6.1}$$

Bias in the event selection is caused by inefficiencies of the trigger due to a dependency on an event variable. Such a dependency on an event property is called *trigger efficiency*. The term *trigger bias* is used to express the selection towards certain event types. In the following it is understood as the *difference* to the distribution for which no trigger requirement is imposed and is used for quantities that appear *several* times per event for example tracks. The determination of trigger bias follows directly from formula 6.1. The indicated conditions define two samples, which differ only in the T1 trigger condition. Trigger bias can also be defined for a track-wise quantity like p_{T} or η, by forming the ratio of the track-wise distribution obtained from Eq. 6.1. Deviations from the denominator distribution can then be interpreted as trigger bias.

For illustration of the terminology, distributions of the most common event- and track-wise quantities are shown in Fig. 6.3, the track multiplicity $n_{\mathrm{sel}}^{\mathrm{BS}}$ at $\sqrt{s} = 0.9$ TeV and

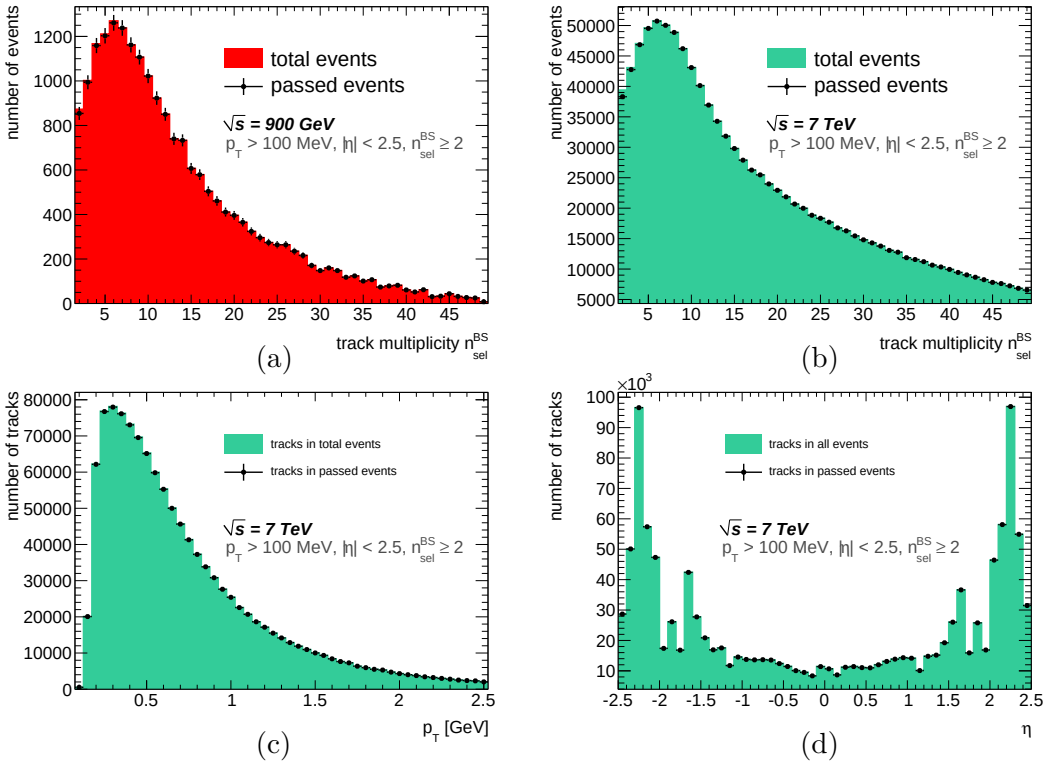

Figure 6.3.: Track multiplicities and track properties of events accepted by the control trigger mbSpTrk (shaded) and events passing also the probe trigger L1_MBTS_1 (points) in MB2.

7 TeV in (a,b) and p_{T} and η of the tracks in 7 TeV data in (c,d). The control trigger T2 is mbSpTrk, the probe trigger T1 is L1_MBTS_1 while the offline selection criteria are given by MB2. The more similar the distributions, the less inefficient is the probed trigger (a,b) and the less bias is introduced towards events with certain tracks (c,d).

The treatment of statistical uncertainties for trigger efficiencies, especially when they are close to 1 or 0, is detailed in the appendix A.

6.4. Trigger Overlap of mbSpTrk and MBTS

Trigger bias in the event selection was first investigated by determining event "overlap" and "uniqueness" of minimum bias triggers. While overlap counts events that both triggers would select in common, the uniqueness is defined here as the number of events selected by one trigger only. For example if one trigger has a large uniqueness rate, the other trigger would introduce bias. This study is performed using the well-defined phase-space regions mentioned in Table 6.1.

To investigate how inclusive the complementary minimum bias triggers are, a set of

Table 6.2.: Overlap and uniqueness of mbSpTrk and L1_MBTS_1, L1_MBTS_2. Reference events were randomly selected proton-proton collisions at $\sqrt{s} = 7$ TeV passing the MB2 offline selection yielding 631 events. Exceptions are cases where an MBTS trigger is required, then higher statistics are available.

trigger condition	number of events	%
mbSpTrk and L1_MBTS_1	630 out of 631	$99.8 \pm^{0.1}_{0.4}$
mbSpTrk and not L1_MBTS_1	1 out of 631	$0.2 \pm^{0.4}_{0.1}$
not mbSpTrk but L1_MBTS_1	0 out of 159,312	$\leq$ 0.0012
not mbSpTrk and not L1_MBTS_1	0 out of 631	$0.0 \pm^{0.3}_{0.0}$
mbSpTrk and L1_MBTS_2	627 out of 631	$99.4 \pm^{0.3}_{0.5}$
mbSpTrk and not L1_MBTS_2	4 out of 631	$0.6 \pm^{0.5}_{0.3}$
not mbSpTrk but L1_MBTS_2	0 out of 158,989	$\leq$ 0.0012
not mbSpTrk and not L1_MBTS_2	0 out of 631	$0.0 \pm^{0.3}_{0.0}$

benchmark configurations was chosen and overlap and uniqueness were studied using the loosest configurations.

For mbSpTrk, the configuration which was nominally deployed in 2010 for most of the data taken at $\sqrt{s} = 7$ TeV is considered (trigger mode 2 in Table 5.2).Regarding MBTS, two benchmark configurations of MBTS were chosen: L1_MBTS_1 and L1_MBTS_2. While the requirement of L1_MBTS_1 is clearly the loosest configuration, it is also most prone to noise variations in the electronics. Therefore, L1_MBTS_2 was considered to be the main trigger mode of MBTS for proton-proton selection in case noise becomes an issue. Since both MBTS configurations still represent generally very low requirements for an event selection, both are considered in the following.

The analysis of trigger overlap and uniqueness requires a reference trigger. The only trigger with even looser requirements than minimum bias triggers is a zero-bias trigger that selects purely randomly events. The yield of period A are 94,261 randomly selected events. After the MB2 offline selection criteria are applied, only 631 events are left. The results of the overlap and uniqueness counts of mbSpTrk and the two loosest MBTS trigger configurations are shown in Table 6.2.

Due to the low statistics of randomly selected events in MB2 one can merely conclude that both, mbSpTrk and L1_MBTS_1 select all types of proton interactions equally well. Also, a lower limit of the selection efficiency of mbSpTrk with respect to L1_MBTS_1 is found to be compatible with 100 % at 68.3 % C.L.. A tendency is nevertheless visible that mbSpTrk seems to select with a higher efficiency than L1_MBTS_2.

6.5. Visual Analysis of Minimum Bias Event Topologies

For further characterisation of the performance of L1_MBTS_1 it was investigated if event classes exist which are accepted by mbSpTrk but not by MBTS. Given the analysed

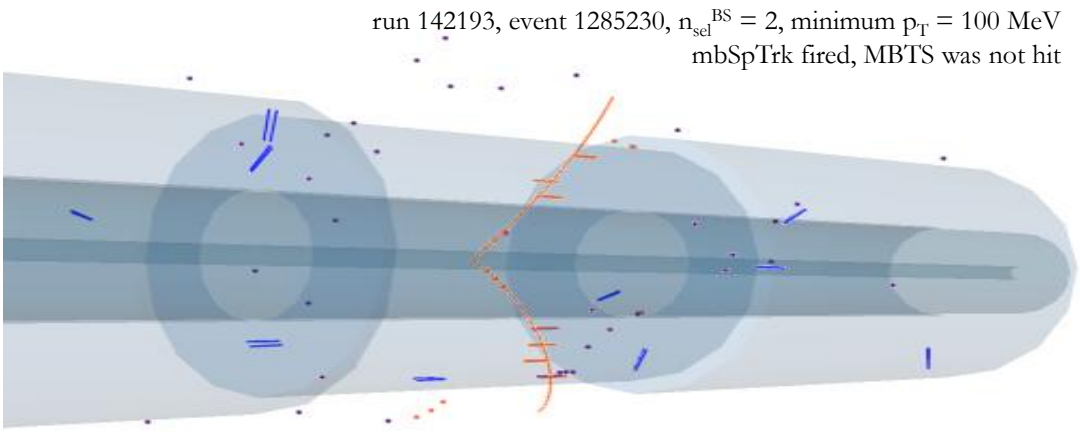

Figure 6.4.: Event (run 142193, event 1615837) with no hits above the MBTS trigger threshold but with two reconstructed and selected tracks of a minimum p_T of 100 MeV.

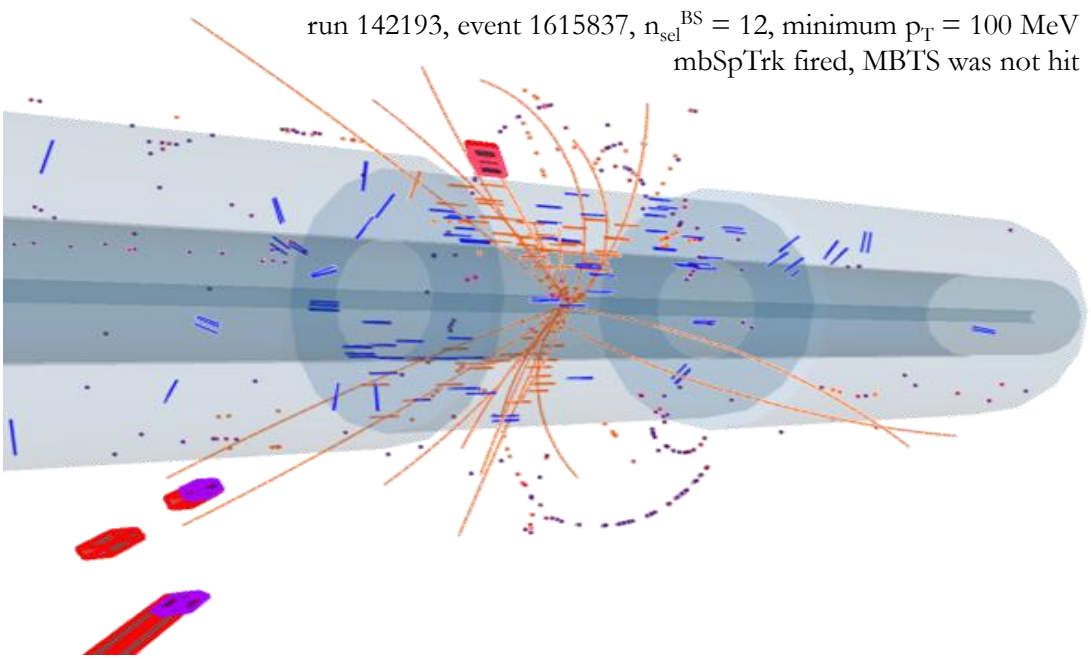

Figure 6.5.: Run 142193, event 1615837 does not contain any hits in the MBTS but 12 selected tracks with a minimum p_T of 100 MeV. Such event types occur less frequent than low-multiplicity events failing MBTS.

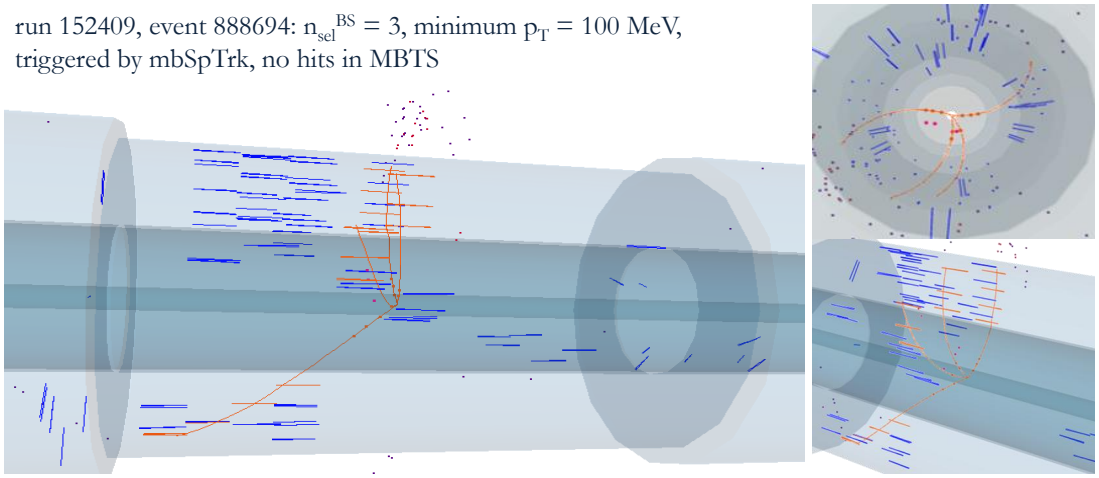

Figure 6.6.: Event in which L1_MBTS_1 did not fire although it contains four reconstructed and three selected tracks with a minimum p_T of 100 MeV.

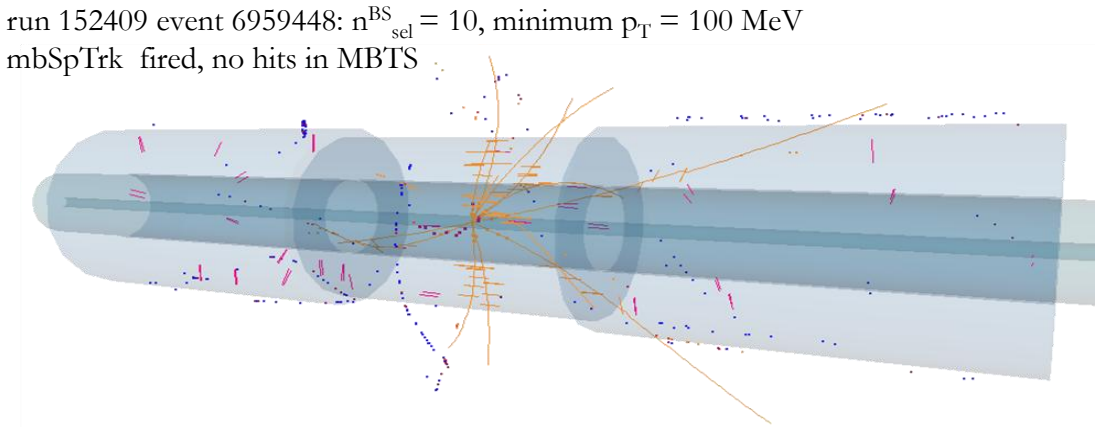

Figure 6.7.: Event without hits in the MBTS passing the discrimination threshold, but 10 selected tracks.

phase-space region defined by MB2, the other case did not appear in the analysed data where mbSpTrk fails to select an event but L1_MBTS_1 or L1_MBTS_2 do not. Thus, only events that do not pass L1_MBTS_1 but are accepted by mbSpTrk were investigated visually and are shown in Fig. 6.4 and 6.5 for collisions at $\sqrt{s} = 0.9$ TeV and in Fig. 6.6 and 6.7 at $\sqrt{s} = 7$ TeV.

The figures indicate that at both centre-of-mass energies two events types exist on which MBTS fails. One of them are low-multiplicity events with centrally produced tracks, see Fig. 6.4 and Fig. 6.6. The other type of events exhibit a rather high track multiplicity but with comparatively low-p_{T} tracks that do not reach out to the MBTS counters, see Fig. 6.5 and Fig. 6.7.

6.5.1. Conclusion

These figures illustrate that only events with tracks above a certain p_{T} are able to trigger an MBTS counter. This implicit p_{T}-threshold causes a bias towards events containing particles above a certain p_{T}. Also, events in which particles are produced in the central region only can miss the MBTS acceptance. The combination of low-p_{T}, central tracks in low-multiplicity events are the least favorable event class for MBTS causing inefficiencies due to its geometrical acceptance.

This is a clear disadvantage of MBTS compared to mbSpTrk that uses directly the reconstructed hits in the silicon tracking volume. Nevertheless, the impact of this effect is small as will be shown in the next sections.

6.6. Trigger Efficiency and Bias of mbSpTrk

Measurements of trigger efficiencies and biases were performed with different reference triggers providing the control sample used for the denominator distribution of Eq. 6.1. Three reference triggers were used, a random trigger, L1_MBTS_1 and L1_MBTS_2. For all these cases the measurements were made against a reference defined by the MB2 offline selection criteria.

As the available statistics from the random trigger as mentioned in Table 6.4 is rather limited, measurements w.r.t. to a random trigger in phase-space MB2 possess relative large statistical uncertainties. The efficiency of mbSpTrk w.r.t. a random trigger is shown in Fig. 6.8 (a).

Higher statistical precision is obtained when using MBTS as reference trigger. The trigger efficiency of mbSpTrk is measured against L1_MBTS_1 and shown in Fig. 6.8 (b) and against L1_MBTS_2 depicted in Fig. 6.8 (c) which provides the most precise efficiency of mbSpTrk.

In all three cases the mbSpTrk trigger efficiency is compatible with 100 %.

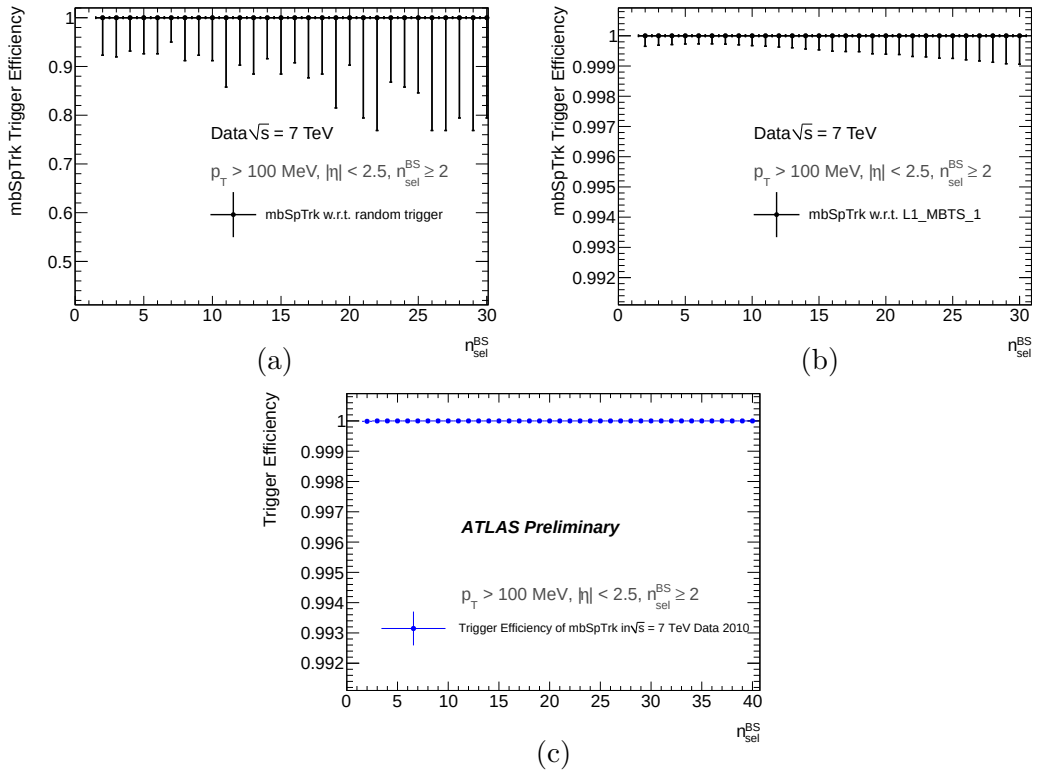

Figure 6.8.: Trigger efficiency of mbSpTrk for MB2 selected events. The reference trigger in (a) is a pure random trigger, in (b) L1_MBTS_1 and in (c) L1_MBTS_2. For (c) see also [119].

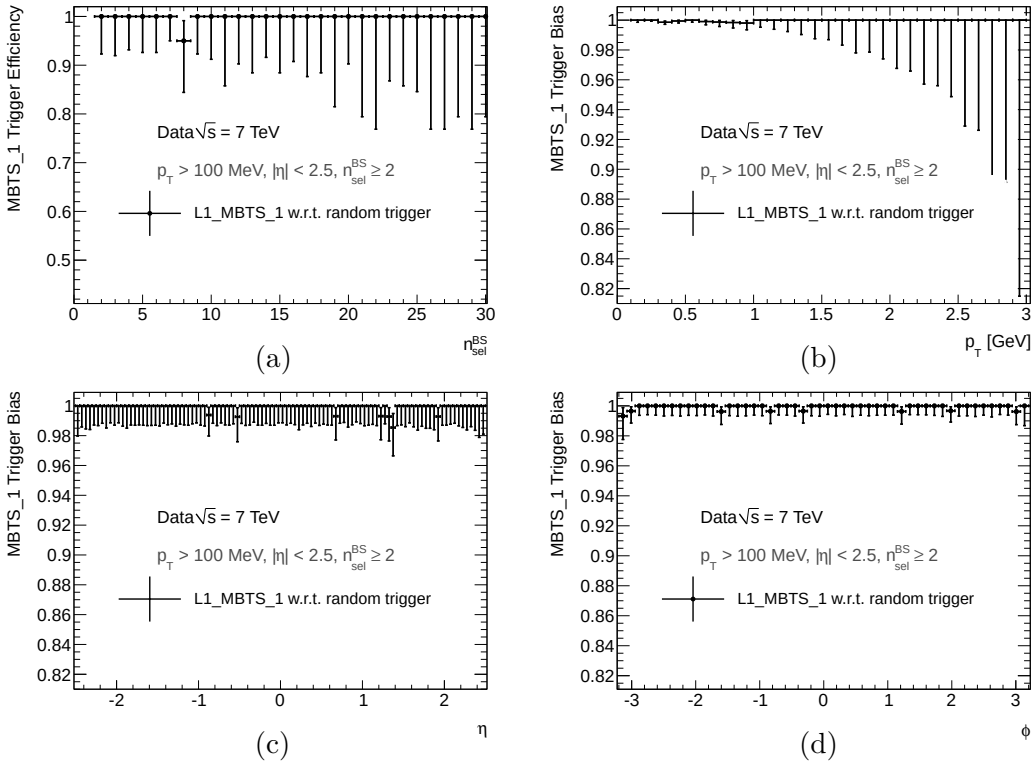

Figure 6.9.: Trigger efficiency and biases of L1_MBTS_1 w.r.t. a random trigger in MB2.

6.7. Trigger Efficiency and Bias of MBTS

The trigger efficiency and biases of L1_MBTS_1 are also measured relative to the random trigger and shown in Fig. 6.9. The limited statistics available from the zero-bias trigger led to the choice of using mbSpTrk as a control trigger. The measurement of the L1_MBTS_1 trigger efficiency from data is a relevant contribution to the first ATLAS publication [46] and several succeeding analyses. These analyses emphasize as mentioned earlier on minimal model dependency in their measurements. In the next sections, the determination of the MBTS performance is measured relative to the mbSpTrk trigger applying the offline criteria in Table 6.1. Different MBTS trigger configurations were as well investigated: L1_MBTS_1, L1_MBTS_2, L1_MBTS_1_1 and L1_MBTS_4_4. Bias and efficiency of the loosest trigger condition, L1_MBTS_1, were studied in more detail and are described in the following.

6.7.1. Evaluation of Systematic Uncertainties

Two sources of systematic uncertainties for the determination of a selection efficiency and biases of L1_MBTS_1 bias were investigated. They consider uncertainties from the choice of a reference trigger that itself can be correlated to the probed trigger. In addition, there is an uncertainty on the considered event samples. Amongst the

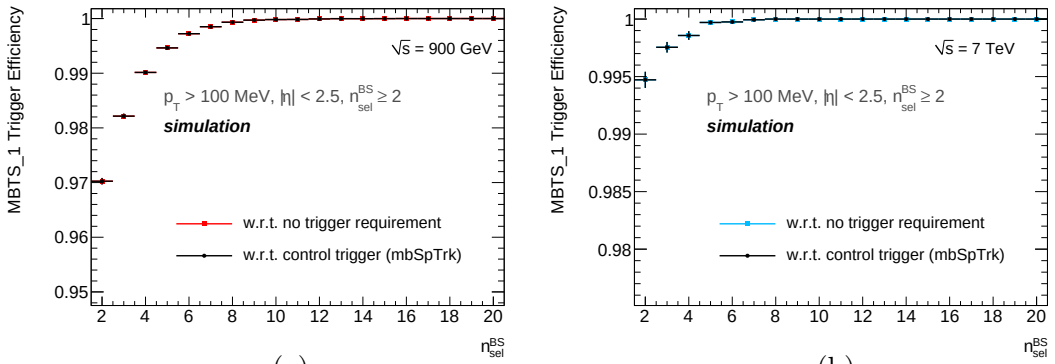

Figure 6.10.: Possible correlations investigated in MC at (a) $\sqrt{s} = 0.9$ TeV and (b) at $\sqrt{s} = 7$ TeV in MB2. No influence of the control trigger mbSpTrk onto the L1_MBTS_1 trigger efficiency is visible.

target events of proton-proton collisions, events containing beam-gas interactions can contribute to the analysed dataset.

Trigger Correlation

A possible source of systematic uncertainty can arise from the control trigger, if its selection imposes conditions and introduces thereby itself a certain amount of bias in the event selection, as mbSpTrk in case of the trigger efficiency measurement of L1_MBTS_1. In MB1, it was estimated that $\epsilon_{\text{L1\_MBTS\_1}}$ changes by 0.2 % in the first track bin, $n_{\text{sel}}^{\text{BS}} = 1$, in case the control sample consists of all offline selected events. This originates from the tighter trigger configuration of mbSpTrk in 2009 and was determined in MC after scaling the MBTS signal to match the data signal [120].

With the looser trigger settings of mbSpTrk in 2010 the amount of trigger correlation is expected to decrease and has therefore been neglected in MB2 analyses. Nevertheless, a test with MC events and MBTS signals has been made. In Fig. 6.10, the trigger efficiency of L1_MBTS_1 is shown with and without mbSpTrk as reference trigger in MB2. No significant correlation effect was found that would be visible, if the reference trigger had an influence of the L1_MBTS_1 trigger efficiency. Thus no contribution from that source was therefore considered in the final result. Unfortunately, the quantities to mimic the trigger decision offline are only poorly comparable to the data. This effect, if investigated with sufficient statistics recorded by a zero-bias trigger, would be certainly more reliable.

Track Parameter Variation

A further source concerns the offline selection criteria. The efficiency and biases of a trigger depend strongly on these offline criteria. Vertex related requirements are supposed to remove background events such as beam-gas interactions faking a proton-proton inter-

action at any positions along z. Since no vertex related cuts were applied in the trigger studies, contribution from beam background events should be expected. A variation of track parameters was thus chosen to estimate this contribution used for the systematic uncertainty. Three cases were distinguished:

- Case 1: events with a reconstructed vertex and tracks fulfilling certain quality criteria relative to the primary vertex (PV) as in Table 6.1 are considered.
- Case 2: if no vertex is reconstructed, a slightly looser requirement on d_0^{BS} is used, see also Table 6.1.
- Case 3: no requirements on track parameters are made for the track selection.

These cases were used to determine the systematic uncertainties of the L1_MBTS_1 trigger efficiency at $\sqrt{s} = 0.9$ and 7 TeV in MB1 and MB2. The effect of the variations are shown in Fig. 6.12 for the MB2 phase-space. However, for the MB2 phase-space a special method had to be applied to the data at $\sqrt{s} = 0.9$ TeV before due to the tighter trigger configuration of mbSpTrk at $\sqrt{s} = 0.9$ TeV compared to the one at $\sqrt{s} = 7$ TeV.

Method for data at $\sqrt{s} = 0.9$ TeV The reference trigger mbSpTrk was differently configured in 2009 and 2010 as mentioned in Table 5.3 and 5.6 concerning both levels, L2 and EF. The selection cuts in 2009 were much stricter compared to the offline selected events in MB2. The efficiency of L1_MBTS_1, $\epsilon_{\mathsf{L1\_MBTS\_1}}$, would appear to be higher than it would be the case if the control sample was chosen with looser requirements as have been used in 2010. The procedure to determine the systematic uncertainties in MB2 at $\sqrt{s} = 0.9$ TeV is the following.

The underlying assumption is that the ratio of the trigger efficiency of L1_MBTS_1 with respect to mbSpTrk in the "loose" (configuration enabled in 2009) and "tight" (configuration enabled in 2010) is the same for the two centre-of-mass energies:

$$\frac{\mathsf{L1\_MBTS\_1}\,|\mathsf{mbSpTrk}_{\mathrm{loose}}}{\mathsf{L1\_MBTS\_1}|\mathsf{mbSpTrk}_{\mathrm{tight}}}@900\mathrm{GeV} = \frac{\mathsf{L1\_MBTS\_1}\,|\mathsf{mbSpTrk}_{\mathrm{loose}}}{\mathsf{L1\_MBTS\_1}|\mathsf{mbSpTrk}_{\mathrm{tight}}}@7\mathrm{TeV} \qquad (6.2)$$

which is used to apply a correction to the efficiency of L1_MBTS_1 w.r.t. $\mathsf{mbSpTrk}_{\mathrm{tight}}$ taken at $\sqrt{s} = 0.9$ TeV to obtain the trigger efficiency of L1_MBTS_1 w.r.t. $\mathsf{mbSpTrk}_{\mathrm{loose}}$ also at the same centre-of-mass energy.

This procedure is visualised in Fig. 6.11. The right term of Eq. 6.2 is the correction factor (open circles in Fig. 6.11) that is applied to the trigger efficiency of L1_MBTS_1 w.r.t. $\mathsf{mbSpTrk}_{\mathrm{tight}}$ at $\sqrt{s} = 0.9$ TeV (open squares). This results in the corrected trigger efficiency $\epsilon_{\mathsf{L1\_MBTS\_1}}$ (filled dots). One can see that the only correction to be applied concerns the $n_{\mathrm{sel}}^{\mathrm{BS}} = 2$ bin, where the efficiency is corrected downwards by 0.3 %. This effect is negligible in the p_{T}, η and ϕ distributions of the tracks.

With this procedure applied to the $\sqrt{s} = 0.9$ TeV data beforehand, the systematics for the trigger efficiency at $\sqrt{s} = 0.9$ TeV in the MB2 phase-space were determined. The results of the track parameter variations are shown in Fig. 6.12 (a–d).

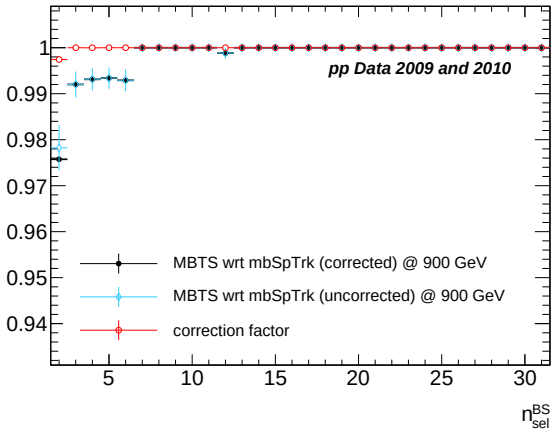

Figure 6.11.: Correction of $\epsilon_{\text{L1\_MBTS\_1}}$ at $\sqrt{s} = 0.9$ TeV as a function of $n_{\text{sel}}^{\text{BS}}$. The right term of formula 6.2 is the correction factor applied to the $\epsilon_{\text{L1\_MBTS\_1}}$ at $\sqrt{s} = 900$ GeV.

Bias in p_{T} A certain aspect was more closely investigated. A slight bias is visible in Fig. 6.12 (b,f) in the lower p_{T}-bins which does not only decrease with smaller p_{T} but exhibits a minor but visible rise towards the lowest p_{T}-bins. The correlation between the transverse momentum and pseudorapidity of the selected tracks, shown in Fig. 6.13, make clear that central, low-p_{T} are missed by MBTS. This inefficiency of MBTS is due to the acceptance, being less able to detect central particles. The shape of this bias visible in Fig. 6.12 (b,f) can be explained as the superposition of two reconstruction efficiencies. Considering for example the data taken at $\sqrt{s} = 7$ TeV, the pseudorapidity distributions of two p_{T}-bins confirm that the few very low-p_{T} tracks are more often reconstructed in the endcaps, while tracks of a higher p_{T} for example from around 175 MeV onwards are more homogeneously spread in η, illustrated in Fig. 6.14 (a). Related tracking studies, showing for low-p_{T} tracks a higher reconstruction efficiency if they are in the endcaps as centrally produced, support this observation [121]. This effect is reversed when the particles possess a higher p_{T}, see Fig. 6.14 (b). The overall bias in p_{T} is however below 0.5 % in Fig. 6.12 (b) and with 0.05 % in (f) even smaller and not further considered.

The bias in p_{T} was also investigated for tighter configurations of MBTS where it is increasingly visible as shown in Fig. 6.15.

Bias in η The shape of the ratio as shown in Fig. 6.12 (c,g) indicates as well a bias of MBTS towards events with tracks produced in the forward directions. Nevertheless, this effect is smaller than 0.3 % and 0.05% for (c) and (g) respectively and herewith negligible.

Conclusion

The results shown in Fig. 6.12 give reason to believe that the variations of the track parameter requirements are only non-negligible as function of the event variable $n_{\text{sel}}^{\text{BS}}$

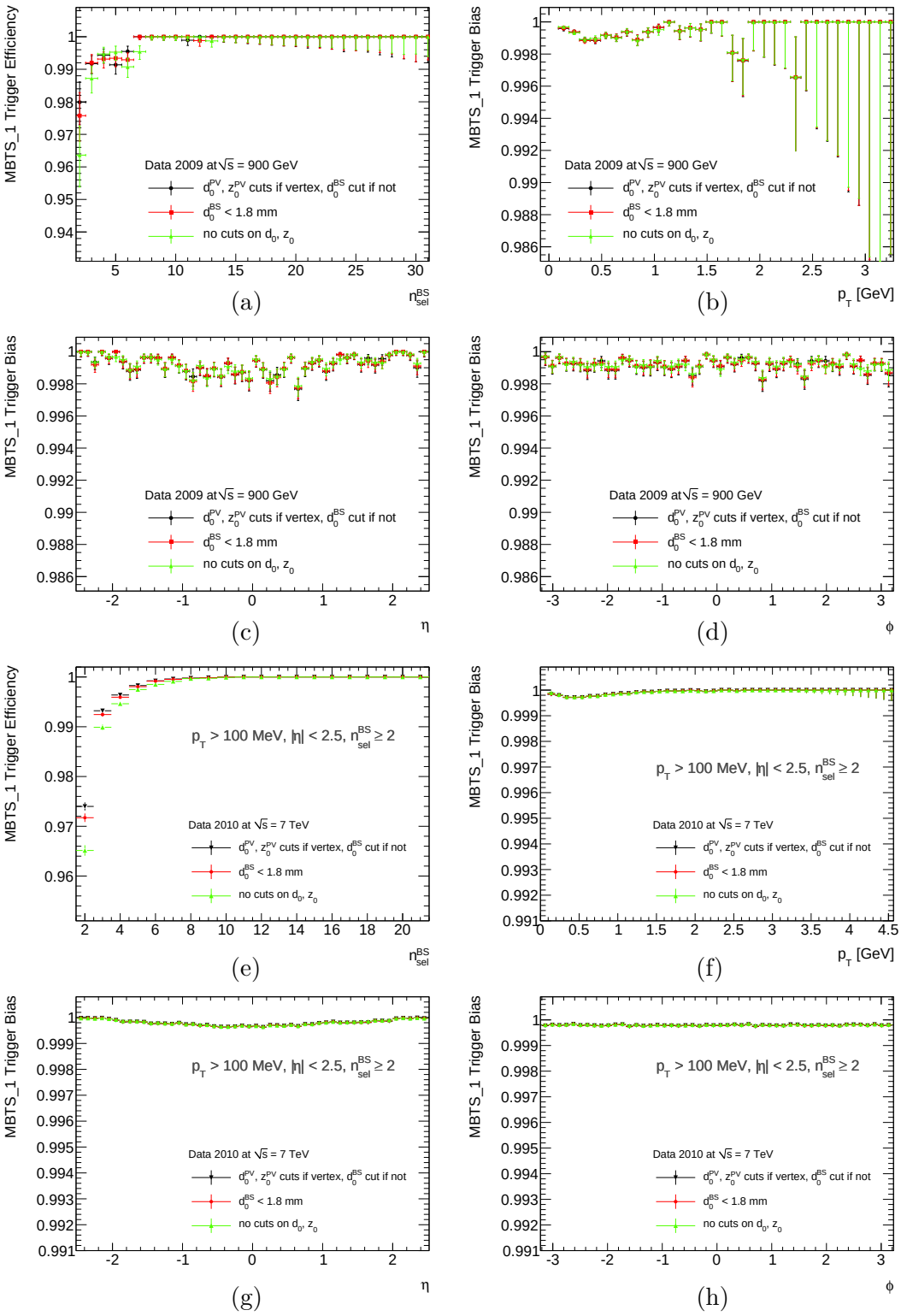

Figure 6.12.: Evaluation of systematic uncertainties of data at $\sqrt{s} = 0.9$ TeV (a-d) and at $\sqrt{s} = 7$ TeV (e-h) distinguishing three different cases to select a "good" track.

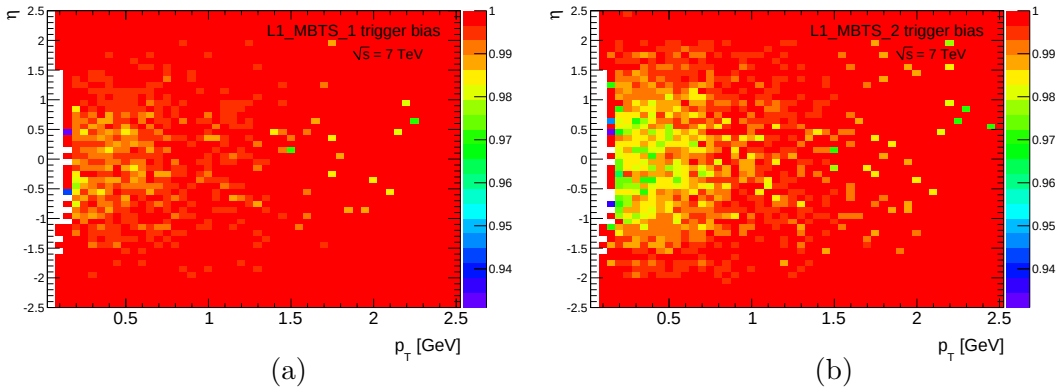

(a) (b)

Figure 6.13.: Bias of (a) L1_MBTS_1 and (b) L1_MBTS_2 in η and p_{T} measured w.r.t. mbSpTrk at $\sqrt{s} = 7$ TeV in the MB2 phase-space. The white areas are due to binning effects at the phase-space border of 100 MeV.

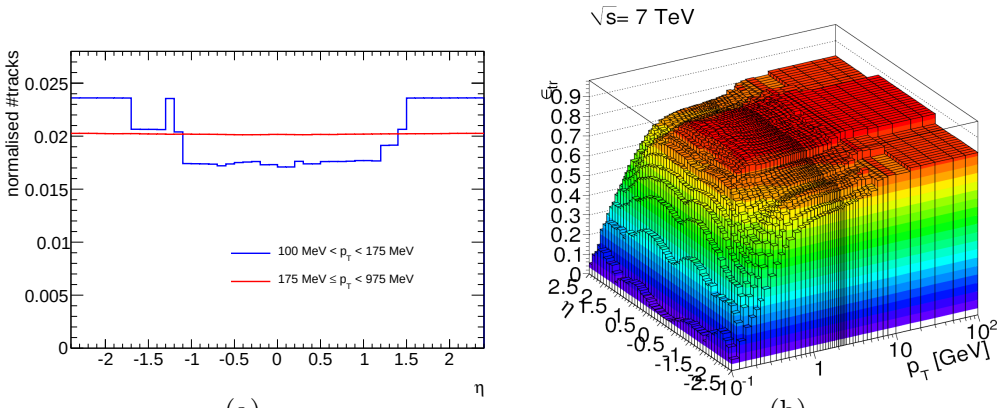

(a) (b)

Figure 6.14.: (a) η projection of low-p_{T} bins of Fig. 6.13 (a). (b) Tracking efficiency in p_{T} and η, taken from [121].

and not as function of p_{T}, η or ϕ. The trigger efficiency of L1_MBTS_1 changes by 1 % in the bin $n_{\mathrm{sel}}^{\mathrm{BS}} = 2$ as can be seen in Fig. 6.12 (a) and by 0.7 % different at $\sqrt{s} = 7$ TeV in the same $n_{\mathrm{sel}}^{\mathrm{BS}} = 2$ track bin, see Fig. 6.12 (e). These variations are distributed over the p_{T} and η bins and show only a negligible influence.

6.7.2. Results

The efficiencies and biases for various other MBTS trigger configurations are shown in Fig. 6.15 for the more inclusive MB2 criteria. Low-multiplicity events are less efficiently triggered by MBTS trigger the more counters are required to fire. Especially, the bias towards higher p_{T} particles increases for the hit-coincidence requirements.

The inefficiency and biases of the loosest trigger condition, L1_MBTS_1, are shown for MB1 in Fig. 6.16 and MB2 in Fig. 6.17. Other biases in the track p_{T} and η spectra

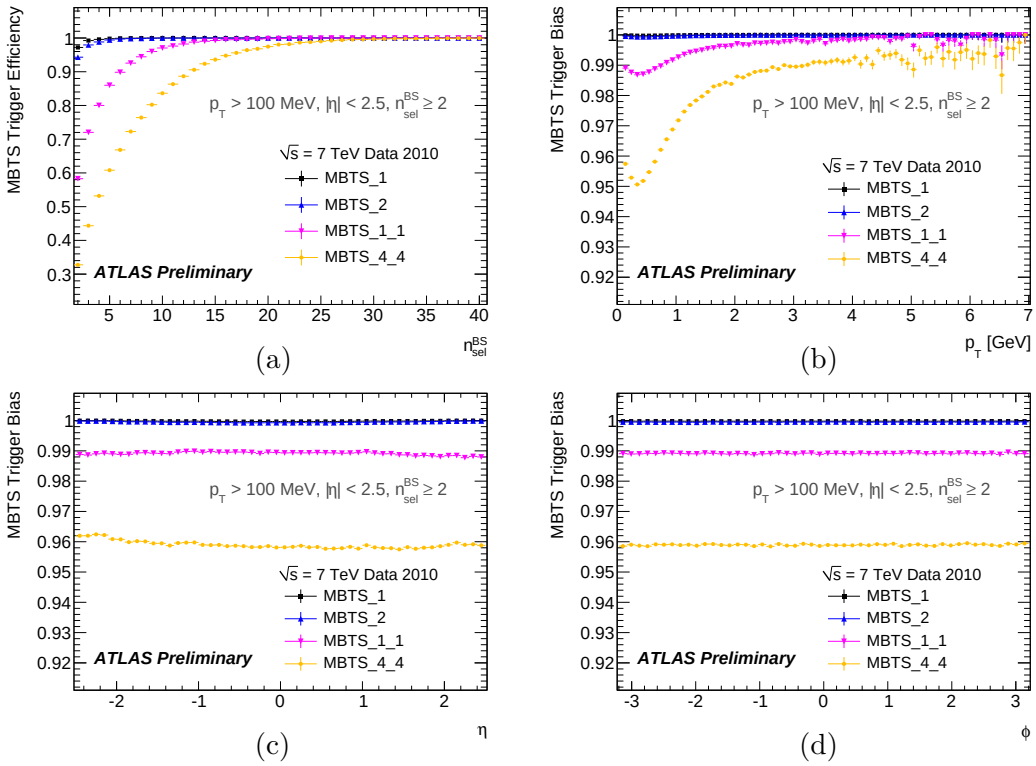

Figure 6.15.: Trigger efficiency and bias for different MBTS configurations evaluated relative to mbSpTrk at $\sqrt{s} = 7$ TeV. Only statistical uncertainties are shown.

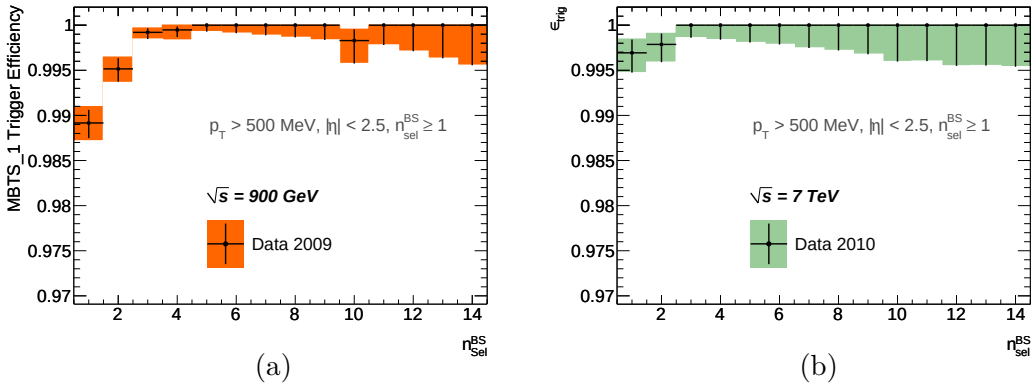

Figure 6.16.: Trigger efficiency of L1_MBTS_1 measured w.r.t. mbSpTrk in MB1 as used in Chapter 7 and [41, 46, 114]. For (b) only one run 152166 was used.

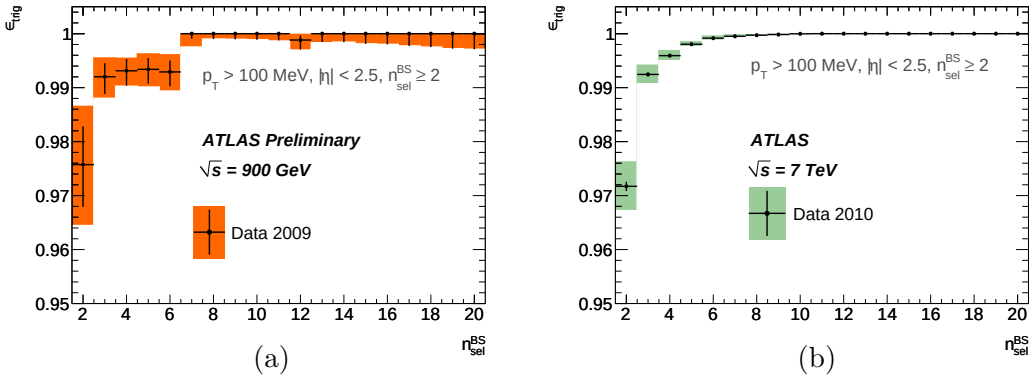

Figure 6.17.: Trigger efficiency of L1_MBTS_1 w.r.t. mbSpTrk in MB2 as used in [41].

were less than 0.2 % and less than 0.05 % for $\sqrt{s} = 0.9$ and 7 TeV respectively and were thus neglected for further consideration in charged particle multiplicity analyses.

6.8. Operational Trigger Stability

The measured trigger efficiency of L1_MBTS_1 is also studied as function of time to determine the stability of this trigger. Therefore the behaviour of the spacepoint counting algorithms was investigated as function of time. Once the control trigger can assumed to be sufficiently stable, i.e. spikes and large deviations of spacepoint formation can be excluded in the analysis, one can examine the stability behaviour of MBTS.

The rate of the control trigger is found to vary not more than 30 % as was shown in Fig. 5.3. The stability of L1_MBTS_1 was thus tested by evaluating the trigger efficiency per run integrating over the total number of track multiplicities, i.e. according to Eq. 6.1 with N the number of events:

$$\epsilon_{\text{L1\_MBTS\_1}} = \frac{N_{\text{pass}}}{N_{\text{total}}} \tag{6.3}$$

The results are shown in Fig. 6.18 for MB1 at $\sqrt{s} = 0.9$ TeV and for MB2 at $\sqrt{s} = 7$ TeV. The large uncertainties in Fig. 6.18 (a) are due to statistical limitations. Within uncertainties one can conclude that the MBTS trigger was operating stable in early 2010.

6.9. Conclusion

6.9.1. Performance of mbSpTrk

The mbSpTrk trigger has shown excellent performance and reached for all three reference triggers an efficiency compatible with 100 % (Fig. 6.8). No sizable bias is introduced by mbSpTrk with respect to the most inclusive analysed phase-space region MB2. The result using the random trigger as reference can be refined with higher statistics than recorded in period A.

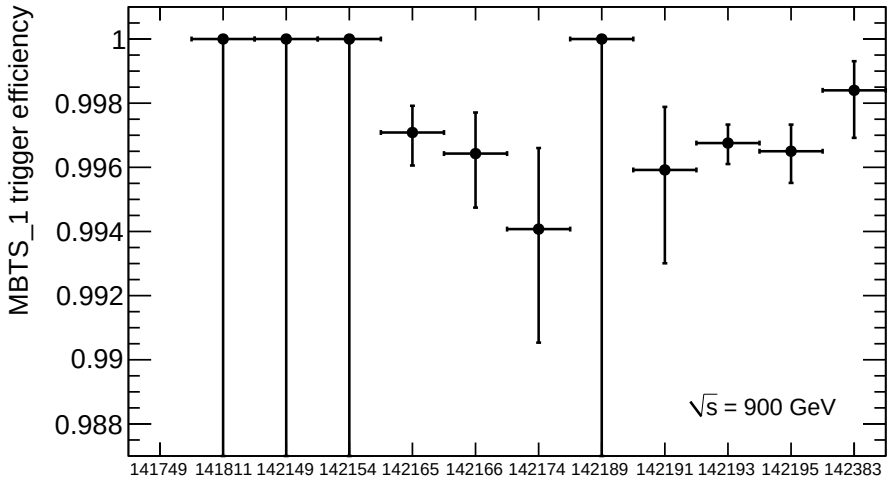

(a)

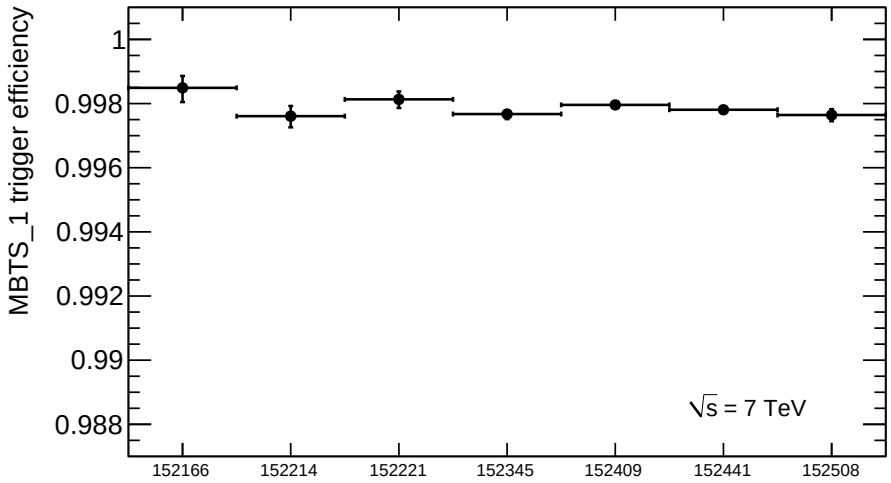

(b)

Figure 6.18.: Trigger efficiency (see Eq. 6.3) as a function of run number at (a) $\sqrt{s} = 0.9$ TeV and (b) $\sqrt{s} = 7$ TeV. The available statistics at $\sqrt{s} = 7$ TeV has much improved. One observes an overall stable trigger efficiency over time.

Beyond the use of the ID based Minimum Bias Trigger for proton-proton selection, mbSpBg_unpaired was derived to investigate beam background rates as has been presented in Section 5.2.5. The analysis of its events in correlation with other measurements from different detector signals are discussed in [122] and machine related phenomena like *debunched bunches*, i.e. proton bunches with bad bunch structure where protons are contained in buckets not meant to be filled, were observed.

Concerning trigger operation it has as well proven to be running stable, see Fig. 5.3, with input rates of around 100 Hz. The system load needed to derive a trigger decision is nevertheless higher than for MBTS. The complementary role of mbSpTrk to MBTS allows the MBTS trigger efficiency to be measured from data. Once, MBTS will no longer be available as trigger due to irradiation damage of the scintillators, ATLAS is still provided with the ID Minimum Bias Trigger. When the LHC reaches the design centre-of-mass energy, properties of charged particles will be studied and this trigger will be available for selecting efficiently and in an unbiased way proton-proton interactions.

6.9.2. Performance of MBTS

The Minimum Bias Trigger Scintillators have proven to be very efficient in selecting inelastic proton-proton interactions. Due to this sensitivity they played an essential role in the initial and successful commissioning period of ATLAS.

For measurements of charged particle multiplicities this L1 Minimum Bias trigger collected the data with high efficiency. The latter was measured in two phase-space regions (MB1 and MB2) and at both centre-of-mass energies of $\sqrt{s} = 0.9$ and 7 TeV as shown in Fig. 6.16 and Fig. 6.17, respectively.

In MB1, the trigger efficiency $\epsilon_{\text{L1\_MBTS\_1}}(n_{\text{sel}}^{\text{BS}} = 1)$ is 98.92 $\pm^{0.15}_{0.12}$ (stat) $\pm$0.11 (syst) % at $\sqrt{s} = 0.9$ TeV and 99.69 $\pm^{0.15}_{0.22}$ (stat) $\pm$ 0.03 (syst) % at at $\sqrt{s} = 7$ TeV. In MB2, the efficiency $\epsilon_{\text{L1\_MBTS\_1}}(n_{\text{sel}}^{\text{BS}} = 2)$ is 97.6 $\pm$ 1.1 (syst) $\pm$ 0.7 (stat) % at $\sqrt{s} = 0.9$ TeV and 97.2 $\pm$ 0.5 (syst) $\pm$ 0.1 (stat) % at $\sqrt{s} = 7$ TeV. The leading source at $\sqrt{s} = 0.9$ TeV which became the sole source at $\sqrt{s} = 7$ TeV of systematic uncertainty considers possible contributions from beam-background contamination in the trigger efficiency measurement estimated by variation of track paramters.

Bias of L1_MBTS_1 in p_{T} and η is found to be negligible within the investigated phase-space regions. If however trigger configurations are used where more counters are required to fire, in particular if required in coincidence, Fig. 6.15 (b) clearly points out the bias of such configurations. The inefficiency of L1_MBTS_1, L1_MBTS_2, L1_MBTS_1_1 and L1_MBTS_4_4 becomes larger and events containing low-p_{T} particles are lost.

One other issue concerns the hardware of the MBTS. In none of the scintillator counters a MIP peak was clearly visible, even though the maximal bias voltage was already used which was due to the poor light yield efficiency of the fibres [80].

Nevertheless, the MBTS were useful right from the beginning of data-taking, selecting highly efficient proton intactions over the entire low luminosity phase. Many analyses were possible allowing to study the hadronic environement at the LHC [19, 41, 46, 114–116, 123, 124], one of them is outlined in the next chapter.

7. Measurement of Charged Particle Multiplicities

At LHC luminosities multiple proton-proton interactions pile up within a single bunch-crossing and make searches for new rare physics signals extremely challenging. An important step towards understanding the hadronic environment at the LHC with highest precision is the measurement of charged particle multiplicities, their dependency on pseudorapidity and transverse momentum and correlations between the average p_{T} and the number of charged particles. Such measurements are needed as input to improve phenomenological models in order to obtain more precise Monte Carlo predictions. Also an accurate description of hard interactions is concerned as such a process is always accompanied by soft processes. The early phase of data-taking in 2010, without significant contribution of pile-up events at low luminosities of $\mathcal{L} = 10^{27}\,\mathrm{cm}^{-2}\,\mathrm{s}^{-1}$, permits a clean selection of single proton-proton interactions and a study of their general properties is presented in this chapter.

In Section 7.1 the analysis of charged particle multiplicities representing the contribution from the ATLAS Collaboration is presented and compared to Monte Carlo predictions from theoretical models. A direct comparison of the results is made to available measurements by the CMS and ALICE Collaborations in Section 7.2.

7.1. Central Charged Particle Multiplicities in ATLAS

LHC measurements of charged particle multiplicities were performed [41, 46, 58–61] that are not directly comparable due to different analysis strategies that were described in Section 2.7. A first LHC combined analysis was agreed on to verify, if three of the major LHC collaborations, ATLAS, CMS and ALICE, agree on measurements of general properties of soft inelastic proton-proton interactions. The three collaborations agreed to measure charged particle multiplicities and the underlying event in two dedicated phases-space regions at both energies, $\sqrt{s} = 0.9$ TeV and 7 TeV introducing only minimal model dependencies. The present work covers the measurements of charged particle multiplicities, more specifically the four distributions outlined in Section 2.6 in the two commonly agreed phase-space regions at both energies. The contribution of the ATLAS Experiment, this analysis, is described here in detail.

The section starts with a description of data quality in 7.1.1, while phase-space regions and event selection are explained in 7.1.2. The selection efficiency in Section 7.1.3 contains already discussions about systematic uncertainties. In Section 7.1.4, the correction procedure is introduced before it is applied to each distribution, Section 7.1.5 to 7.1.8. The correction procedures are probed in so-called closure tests in Section 7.1.9 and

Table 7.1.: Phase-space regions for the first common LHC analysis with n_{ch} the number of charged particles, in the following referred to as PS1 and PS2. In addition, comparisons are made to regions covering the full η-range of the ID.

PS1	$n_{\mathrm{ch}} \geq 1$, $p_{\mathrm{T}} > 500$ MeV, $\lvert\eta\rvert < 0.8$
PS2	$n_{\mathrm{ch}} \geq 1$, $p_{\mathrm{T}} > 1$ GeV, $\lvert\eta\rvert < 0.8$
full–η PS	like is PS1 but with $\lvert\eta\rvert < 2.5$
inclusive PS	$n_{\mathrm{ch}} \geq 2$, $p_{\mathrm{T}} > 100$ MeV, $\lvert\eta\rvert < 2.5$

partly by comparisons in Section 7.1.10. Finally, the results are presented and discussed in Section 7.1.11 before the conclusion is outlined in Section 7.1.12.

7.1.1. Data Quality

The analysed data was taken in December 2009 and in March to April 2010 selected by L1_MBTS_1. The 2009 data were recorded at $\sqrt{s} = 0.9$ TeV, while the data taken in 2010 were produced at $\sqrt{s} = 7$ TeV. As track reconstruction is essential for the analysis, the tracking detectors, especially the Pixel and SCT trackers had to perform at nominal conditions and without problems. The data quality flags were required to be ready for analysis for these systems. A short period of time was also excluded (run 152441, luminosity blocks 406−410, $\sim$ 70k events) which showed a wider beam size than in the other blocks [125]. This imposes a problem for the parametrisation of the trigger and vertex reconstruction efficiency, where a beamspot constraint is used, that - in the case of the wider beam - had no effect. The total considered data correspond to an integrated luminosity of around 7 $\mu\mathrm{b}^{-1}$ at $\sqrt{s} = 0.9$ TeV and around 190 $\mu\mathrm{b}^{-1}$ at $\sqrt{s} = 7$ TeV.

7.1.2. Phase-Space Regions and Event Selection

The considered phases-spaces are defined by kinematic cuts as listed in Table 7.1. The pseudorapidity coverage is motivated by the ALICE tracking detector acceptance, while the p_{T} cuts were chosen in order to operate in a region in which track reconstruction is known with the highest precision. Two phase-space regions were adopted to conclude on possible trends in the measurements. The analysis was carried out in the same spirit as in [41] using the same track quality criteria. Thus, the event selection of this analysis required that

- L1_MBTS_1 trigger fired,
- at least 1 vertex was reconstructed,
- no second pp-collision (pile-up) was present, i.e. any other reconstructed vertex must have fewer than 4 associated tracks,
- at least one good track with $p_{\mathrm{T}} > 500$ MeV, 1 GeV and $\lvert\eta\rvert < 0.8$ was reconstructed, where “good” means that the track has

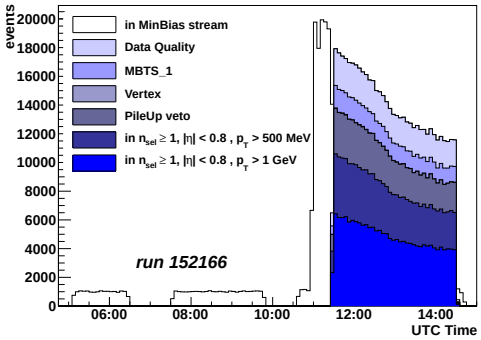

Figure 7.1.: Cutflow for 7 TeV data (one example run shown).

Table 7.2.: Selected number of events N_{ev} and selected number of tracks n_{sel} for the considered phase-space regions and energies.

	$\sqrt{s} = 0.9$ TeV		$\sqrt{s} = 7$ TeV	
	N_{ev}	n_{sel}	N_{ev}	n_{sel}
PS1	246,930	660,973	7,781,332	34,066,553
PS2	108,475	173,861	4,640,752	11,515,746

- at least one hit in one Pixel layer,
- if expected, the Pixel hit must be in the B-Layer,
- at least 6 hits in the SCT detector,
- $|d_0^{\mathrm{PV}}|$ (transverse impact parameter w.r.t. the primary vertex) smaller than 1.5 mm,
- $|z_0^{\mathrm{PV}} \sin\theta|$ (longitudinal impact parameter direction w.r.t. the primary vertex) smaller than 1.5 mm,
- a track-fit probability $\mathrm{P}(\chi^2)$ of at least 0.01 for tracks with $p_{\mathrm{T}} > 10$ GeV to remove mis-measured tracks.

An event fulfilling these requirements is characterised by the number of selected track, n_{sel}. An example run visualising data quality and the number of events after various stages of the selection process is shown in Fig. 7.1 and Table 7.2 lists the number of events and selected tracks for the different phase-space regions and energies.

7.1.3. Selection Efficiency

The data distributions obtained after applying the selection criteria are corrected back to hadron-level by accounting for inefficiencies of the trigger and reconstruction. Associated systematic uncertainties are evaluated considering the same sources of systematic uncertainties as in [41], adapted to PS1 and PS2 as discussed in the following.

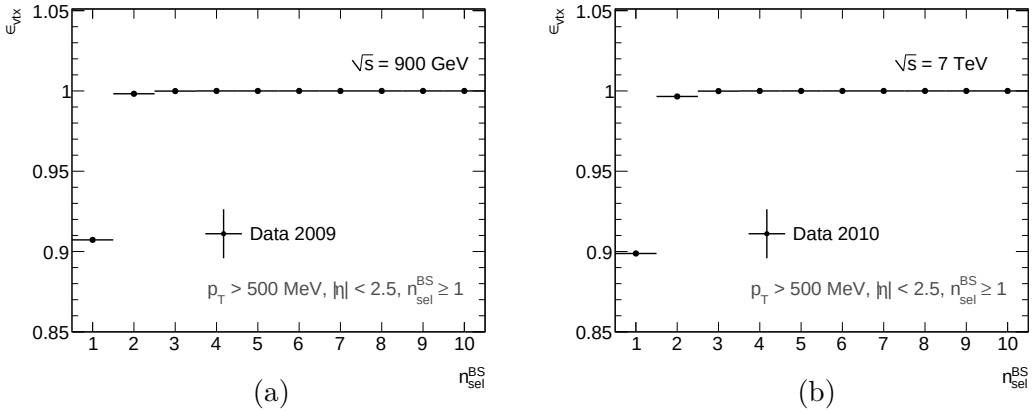

Figure 7.2.: Vertex reconstruction efficiency ϵ_{vtx} at (a) $\sqrt{s} = 900$ GeV and (b) 7 TeV as used in the analysis (only statistical uncertainties shown here) [126].

Trigger Efficiency ϵ_{trig} The trigger that collected the dataset was L1_MBTS_1. Its trigger efficiency, see Fig. 6.16, was measured in data and the method was presented in detail in Section 6.7. With an efficiency in the $n_{\text{sel}}^{\text{BS}} = 1$ track bin of 98.92 $\pm^{0.15}_{0.12}$ (stat) $\pm$ 0.11 (syst) % at $\sqrt{s} = 0.9$ TeV and 99.69 $\pm^{0.15}_{0.22}$ (stat) $\pm$ 0.03 (syst) % at $\sqrt{s} = 7$ TeV a highly efficient trigger was used. Since no significant dependency of the L1_MBTS_1 trigger efficiency on η and p_{T} was found, the same trigger efficiency was used in PS1 and PS2.

Vertex Reconstruction Efficiency ϵ_{vtx} This efficiency was taken from [41] and was determined in a data-driven method for the full-η PS. They are shown in Fig. 7.2 for $\sqrt{s} = 0.9$ and 7 TeV. A dependency of ϵ_{vtx} on η of the tracks formed by the vertex algorithms in events with $n_{\text{sel}}^{\text{BS}} = 1$ and has been considered in the analysis.

The reconstruction efficiency ϵ_{vtx} was derived using events selected by L1_MBTS_1 to which the same track quality cuts are applied as for the trigger efficiency and likewise parametrised by $n_{\text{sel}}^{\text{BS}}$. Furthermore, machine background events are estimated using the trigger L1_MBTS_1_UNPAIRED which imposes the L1_MBTS_1 requirement on unpaired bunch-crossings. These events are after offline selection substracted from the data sample that was obtained by L1_MBTS_1. The resulting events form the control sample. The numerator is obtained by requiring a reconstructed vertex and the ratio of numerator and control sample yields the vertex reconstruction efficiency as function of $n_{\text{sel}}^{\text{BS}}$. The systematic uncertainties were estimated by taking the difference to the ratio without prior removal of the estimated beam background events.

Track Reconstruction Efficiency Detailed studies were performed [121] that are used here in this analysis. Inefficiencies of the track reconstruction algorithms are outlined in more detail below as they produce the largest source of systematic uncertainties.

The tracking efficiency, ϵ_{trk}, was obtained using MC09 events and is parametrised as function of p_{T} and η, see Fig. 6.14 (b) and Fig. 7.3. It is defined as

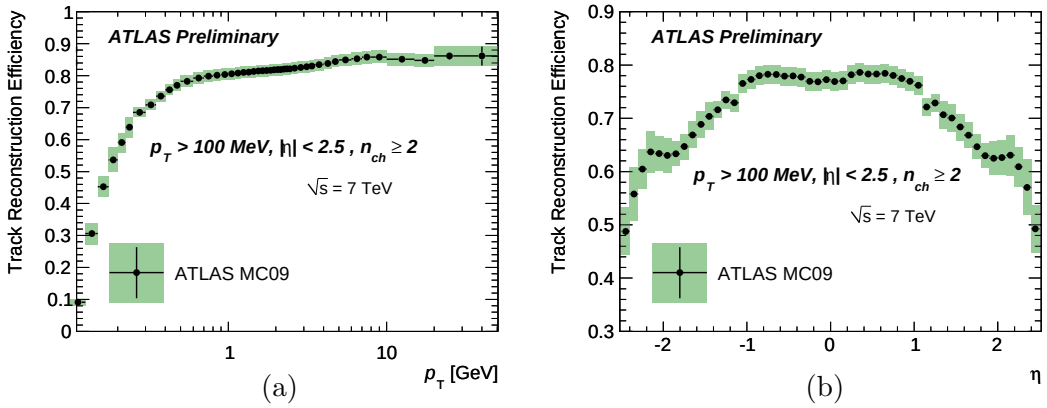

Figure 7.3.: Track reconstruction efficiency ϵ_{trk} projected to p_{T} (a) and η (b) [121].

$$\epsilon_{\mathrm{trk}}(p_{\mathrm{T}}, \eta) \;=\; \frac{N_{\mathrm{rec}}^{\mathrm{matched}}(p_{\mathrm{T}}, \eta)}{N_{\mathrm{gen}}(p_{\mathrm{T}}, \eta)} \tag{7.1}$$

where $N_{\mathrm{rec}}^{\mathrm{matched}}(p_{\mathrm{T}}, \eta)$ is the number of reconstructed tracks matched to a generated charged particle and $N_{\mathrm{gen}}(p_{\mathrm{T}}, \eta)$ is the number of generated charged particles in that bin. The track matching uses a cone-algorithm in the η-ϕ plane which associates the particle to the track with the smallest $\Delta R = \sqrt{(\phi_{\mathrm{particle}} - \phi_{\mathrm{track}})^2 + (\eta_{\mathrm{particle}} - \eta_{\mathrm{track}})^2}$ within a cone radius of R = 0.15.

The systematic uncertainties were obtained by considering sources due to material description in MC, alignment, high p_{T} mis-measured tracks (χ^2-cut) and other effects on high p_{T} track reconstruction [121].

Pile-Up Removal Cut In the analysis pile-up is removed by requiring that the track multiplicity of a second reconstructed primary vertex should not be higher than 4. In the inclusive PS (see Table 7.1), it was found that less than 1 % of non-pile-up events were as well rejected from the dataset at $\sqrt{s} = 7$ TeV [47]. This represents an upper limit in PS1 and PS2 due to the higher transverse momenta of the tracks. Data at $\sqrt{s} = 0.9$ TeV are not affected by this cut, since the luminosity was too low. More details are available in the appendix of [47].

Beam Background Cuts The amount of background in the selected sample was estimated with two methods [46, 127] analysing data selected by MBTS on unpaired bunches using the trigger L1_MBTS_1_UNPAIRED. Both, the MBTS time difference and the number of hits in the Pixel detector that are not associated to any reconstructed track are sensitive to beam induced background. The vertex requirement suppresses almost all but a negligible fraction of such events. In [41] the remaining fraction of events after full event selection for the inclusive PS was estimated to be around 0.1 % and had

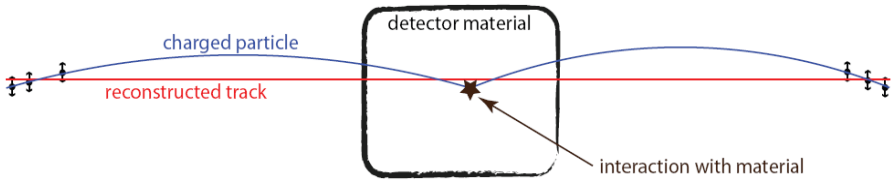

Figure 7.4.: Illustration of reconstructing low p_{T} particle (curved, blue) as a high momentum track (straight, red) in the (r, ϕ)-plane. Due to material interaction the track of the low p_{T} particle can not be resolved. The hits in the silicon detectors are represented by the black dots [121].

been thus neglected. In the present analysis, the phase-space cuts impose even stricter requirements. It is expected that the fraction of remaining background is comparable or lower and therefore negligible.

Track Quality Cut The tracks are required to pass certain quality requirements in order to be counted as well-reconstructed, primary particles. Extensive studies have been performed to optimise selection criteria and to quantify their uncertainties which were used also for this analysis [121]. The following problem was encountered. When reconstructing low p_{T} tracks down to $p_{\mathrm{T}} = 100$ MeV the reconstruction algorithm may not be able to distinguish two low p_{T} tracks, one originally from a primary particle, the other from a secondary particle created in a hadronic interaction with detector material flying into the same direction as the primary particle. The reconstruction software may then mis-reconstruct the low p_{T} particle with a high p_{T}. This is illustrated in Fig. 7.4. Two quality requirements were imposed to get a handle of such mis-measured tracks, one concerning the *track length*, the other the *track-fit probability.*

Track length cuts. As the hit efficiency in the silicon tracking devices was close to 100 %, the particle p_{T} is a good measure of how many detector layers are expected to be hit. Therefore, a minimum hit requirement of at least 6 hits of the track in the SCT has been applied for tracks used in this analysis. The systematic uncertainties due to this requirement were studied by investigating possible discontinuities in the p_{T}-spectrum [121]. As data and MC comparisons of possible discontinuities showed good agreement within the statistical uncertainties, no uncertainty was taken into account for the implicit SCT track length cut.

Another cut is applied to suppress the remaining mis-measured, high p_{T} tracks, concerning only tracks with a $p_{\mathrm{T}} > 10$ GeV. These mis-measured tracks predominantly have high η-values due to larger distances in the forward regions between the outer Pixel layer and the closest SCT layer which can reach up to 1 m. Even though this analysis considers centrally produced particles, the fraction of such mis-measured tracks in data was estimated also for this analysis.

The distribution of the **track-fit probability $\mathbf{P}(\chi^2)$** of high p_{T} tracks turned out to provide a good handle on such tracks. This is visualised in Fig. 7.5 (a) showing $\mathrm{P}(\chi^2)$ of generated particle p_{T} against the reconstructed p_{T}. The $\mathrm{P}(\chi^2)$-distribution of the mis-measured high p_{T} tracks is shown in Fig. 7.5 (b), defining tracks as mis-measured

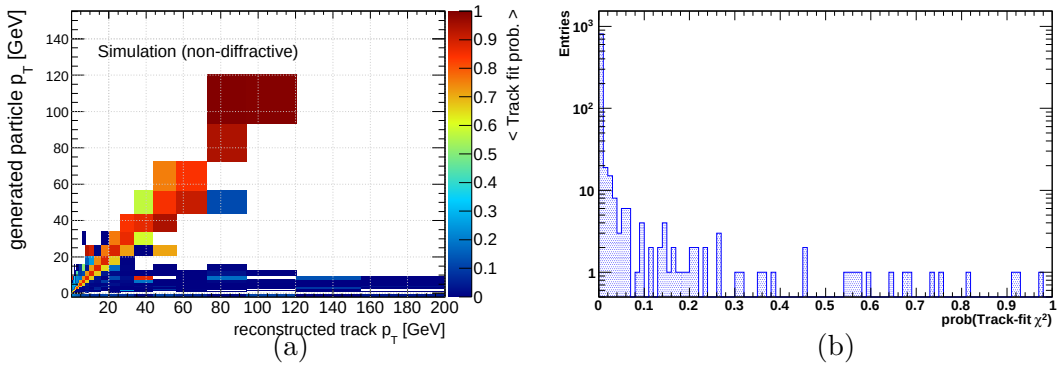

(a) (b)

Figure 7.5.: (a) Track-fit probability distribution for generated and reconstructed track p_{T}. (b) The same probability $\mathrm{P}(\chi^2)$ for mis-measured tracks only [121].

when the generated and reconstructed p_{T} differ by more than 50 %. It was thus required that tracks with a high p_{T} should have a $\mathrm{P}(\chi^2) > 0.01$. The uncertainty associated with this cut was taken as the difference of the $\mathrm{P}(\chi^2)-$distributions for reconstructed tracks above 10 GeV between data and MC. It was estimated to be 10 %.

Furthermore, other track requirements provided a powerful **discrimination of primary and secondary** particles. In particular the impact parameters, d_0 in the transverse plane and $z_0 \cdot \sin\theta$ in the longitudinal direction were required to be close to the primary vertex. Secondary tracks are mainly produced from hadronic interactions, decays from long lived particles and photon conversions. Such secondary tracks populate the tails of the d_0 distributions, their contribution is estimated using MC predictions of the d_0-shape [41, 128]. The contribution of secondaries in the full-η PS is estimated to be 1.6 % [41] and is used in this analysis as an upper limit.

7.1.4. Overview of the Correction Procedures

The correction for trigger and reconstruction inefficiencies is performed using different correction procedures for each distribution. Each of them follows the same approach as developed for [41]. Two types of corrections are applied, an event level one and a track-by-track one.

The distribution of events lost due to inefficiencies of trigger and vertex reconstruction is recovered by assigning an event weight w_{ev} to each event:

$$w_{\mathrm{ev}}(n_{\mathrm{sel}}^{\mathrm{BS}}) = \frac{1}{\epsilon_{\mathrm{trig}}(n_{\mathrm{sel}}^{\mathrm{BS}})} \cdot \frac{1}{\epsilon_{\mathrm{vtx}}(n_{\mathrm{sel}}^{\mathrm{BS}}, \eta)} \tag{7.2}$$

The dependency of ϵ_{vtx} on η of the tracks used by the vertexing algorithms was recognised for $n_{\mathrm{sel}}^{\mathrm{BS}} = 1$ events. The p_{T} and η distributions of selected tracks are corrected with a track-by-track weight w_{trk}:

$$w_{\mathrm{trk}}(p_{\mathrm{T}}, \eta) = \frac{1}{\epsilon_{\mathrm{trk}}(p_{\mathrm{T}}, \eta)} \cdot (1 - f_{\mathrm{sec}}(p_{\mathrm{T}})) \cdot (1 - f_{\mathrm{okr}}(p_{\mathrm{T}}, \eta)) \tag{7.3}$$

where f_{sec} is the fraction of secondary tracks and f_{okr} is the fraction of particles lost as they were reconstructed as tracks outside the kinematical range, but belong to the considered phase-space region. Other migration effects are discussed per distribution. As tracks are reconstructed with a certain resolution in p_{T} and η, the data spectra of p_{T} and η are smeared. This produces boundary effects which need to be corrected. While smearing in η is negligible [121], the effect of the p_{T}-smearing needs to be considered (see Section 7.1.7).

Each correction procedure applied to the data is probed in **closure tests** by applying the corrections to simulated data. The resulting differences of reconstructed simulated data corrected back to hadron-level and the generated distribution is the amount of *non-closure* of the tests. They are accounted as systematic uncertainties and are discussed after the description of the correction procedures.

7.1.5. Corrections to $\mathbf{d}N_{\mathrm{ev}}/\mathbf{d}n_{\mathrm{ch}}$

The charged particle multiplicity distribution is obtained after essentially three correction steps. First, an event weight is applied to the n_{sel} distributions according to Eq. 7.2. In the second step, the event level corrected n_{sel} distribution is unfolded in an iterative method based on a Bayesian approach [129] in order to account for track reconstruction inefficiencies. It uses a 2-dimensional matrix $M_{\mathrm{ch,sel}}$ constructed with MC09 events which expresses the probability that an event with n_{sel} selected tracks originate from n_{ch} primary charged particles.

The resulting n_{ch} distribution is in a final step corrected for one remaining effect. In the third step events are recovered which were lost due to track reconstruction inefficiencies and thereby migrate out of the kinematical phase-space. This is considered by applying a factor f which is a function of n_{ch}:

$$f(n_{\mathrm{ch}}) = 1/[1 - (1 - \langle\epsilon_{\mathrm{trk}}\rangle)^{\mathrm{n_{ch}}}]$$

with $\langle\epsilon_{\mathrm{trk}}\rangle$ the *effective* tracking efficiency and determined by tuning $\langle\epsilon_{\mathrm{trk}}\rangle$ to obtain closure. Even though $\langle\epsilon_{\mathrm{trk}}\rangle$ depends on n_{ch}, a variation with n_{ch} was found to be small and only the value for $n_{\mathrm{ch}} = 1$ was used for all n_{ch} values.

Systematic Uncertainties

The nominal "input" distribution is corrected as described above yielding a nominal "output" distribution. To estimate the effect of systematic uncertainties, a new input distribution for each considered source of systematic uncertainty is produced, unfolded and the difference of the output of modified n_{ch}-distribution to the nominal n_{ch}-distribution quantifies the systematic uncertainty. The matrix is left unchanged.

Two sources of systematic uncertainties contribute most to the total uncertainty. The dominant source is due to the track reconstruction efficiency uncertainty, the other source accounts for the correlation between p_{T} and n_{ch} when constructing the unfolding matrix.

The effect of the inefficiency of track reconstruction was estimated by removing data tracks from the n_{sel}-distribution randomly and according to the uncertainty of ϵ_{trk}: for

each track a random number is generated and compared to the track reconstruction efficiency. All those tracks are removed if the random number is below the efficiency decreased by the downward uncertainty. The difference to the nominal n_{ch}-distribution produces a downwards fluctuation and the same amount is taken for an up-variation. The other source, the dependency on the MC p_{T}-spectrum denoted as "p_{T}-spectrum", was estimated in a similar way by changing the nominal ϵ_{trk} by the difference between two average tracking efficiencies, calculated by:

$$\begin{aligned} \langle \epsilon_{\mathrm{trk}} \rangle &= \frac{\mathrm{N}_{\mathrm{reco}}}{\mathrm{N}_{\mathrm{gen}}} \\ &= \frac{\int \rho_{\mathrm{reco}}(p_{\mathrm{T}})\mathrm{d}p_{\mathrm{T}}}{\int \rho_{\mathrm{gen}}(p_{\mathrm{T}})\mathrm{d}p_{\mathrm{T}}} = \frac{\int \rho_{\mathrm{reco}}(p_{\mathrm{T}})\mathrm{d}p_{\mathrm{T}}}{\int \frac{\rho_{\mathrm{reco}}(p_{\mathrm{T}})}{\epsilon_{\mathrm{trk}}(p_{\mathrm{T}})}\mathrm{d}p_{\mathrm{T}}} \end{aligned}$$

where ρ_{reco} and ρ_{gen} are the number of reconstructed and generated tracks per p_{T}-bin, respectively. Taking the reconstructed tracks to calculate $\rho(p_{\mathrm{T}})$which is the number of tracks in a unit p_{T} once from data and once from MC yield two different average tracking efficiencies and their difference produces a modified n_{sel}-distribution.

The individual systematic uncertainties which contribute most are visualised in Fig. 7.6. The dominant uncertainty is caused by the material desciption in MC for both phase-space regions. In PS1, the second largest systematic uncertainty is due to the p_{T}-spectrum, but the uncertainty arising from the estimate of secondary particles is comparable. In PS2, the secondaries are much less significant.

7.1.6. Correction to the Charged Particle η-Spectra

The charged particle η-spectra of for both phase-space regions and centre-of-mass energies are corrected with event-level and track-level weights using Eq. 7.2 and Eq.7.3, respectively.

The systematic uncertainty is determined by adding single contributions in quadrature and then accounting for (anti-)-correlation of tracks. The leading contribution is due to the uncertainty of track reconstruction due to the material description. The second largest uncertainty comes from the estimate of the fraction of secondary charged particles.

7.1.7. Corrections to the Charged Particle p_{T}-Spectra

The correction of the measured p_{T}-spectrum consists of applying the event weight, the track weight and the correction for the contamination of secondary tracks according to Eq. 7.3. After these correction steps, the distribution is unfolded using a Bayesian unfolding method similar to the n_{ch}-unfolding. The binning of the matrix is chosen such that more bins are used than in the final distributions. This ensures that small fluctuations in MC do not get amplified with each iteration of the unfolding process.

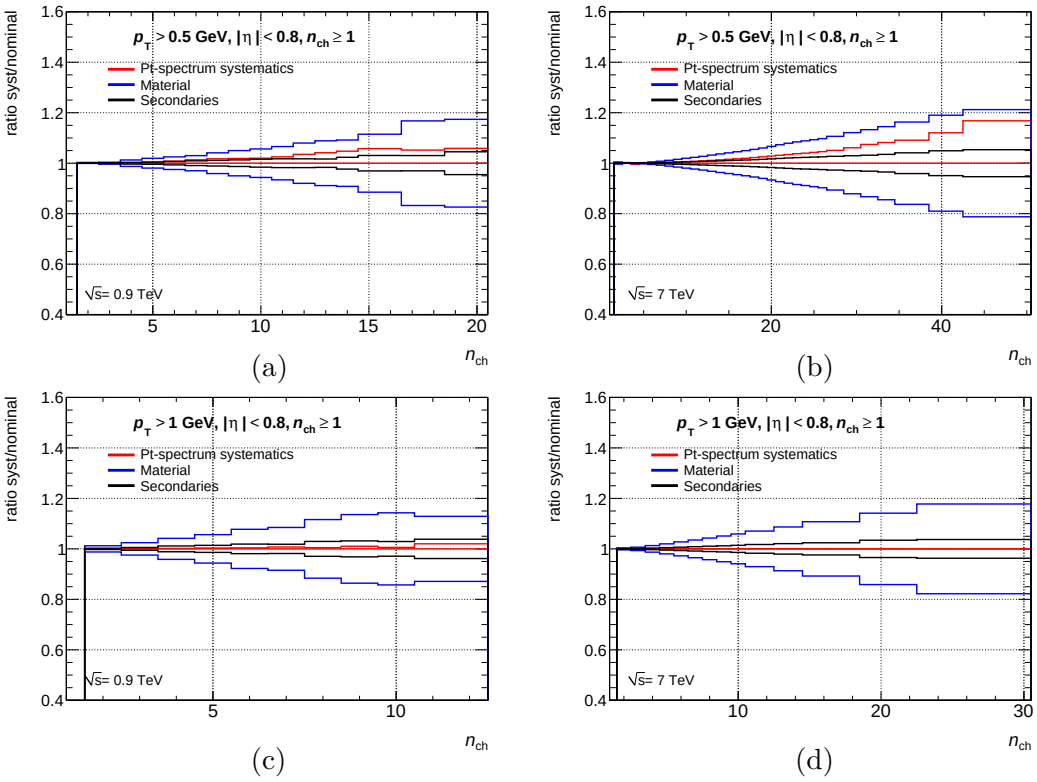

Figure 7.6.: Ratios of the modified distribution affected by a systematic uncertainty over the nominal values of $1/N_{\mathrm{ev}}\mathrm{d}N_{\mathrm{ev}}/n_{\mathrm{ch}}$ in PS1 (a,b) and PS2 (c,d) at $\sqrt{s} = 0.9$ TeV (a,c) and $\sqrt{s} = 7$ TeV (b,d). Overall, the uncertainty caused by detector material contributes most. The second largest source is due to the MC p_{T}-spectrum in PS1. The uncertainty from estimating secondary charged particles is comparable. The latter becomes negligible in PS2.

Table 7.3.: Comparison of one component of the systematic uncertainties due to the estimate of high p_{T} tracks in phase-space regions up to $|\eta| < 0.8$, and $|\eta| < 2.5$ and at both energies. The percentage refers to the nominal bin content. The negative signs indicate that the uncertainties are considered as downwards fluctuations only, since mis-reconstructed tracks would only add up to the high-p_{T} tracks.

	$\lvert\eta\rvert < 0.8$		$\lvert\eta\rvert < 2.5$	
p_{T} [GeV]	$\sqrt{s} = 0.9$ TeV	$\sqrt{s} = 7$ TeV	$\sqrt{s} = 0.9$ TeV	$\sqrt{s} = 7$ TeV
10 - 20	-8 %	-6 %	-20 %	-10 %
20 - 30	n/a	-6 %	n/a	-20 %

Systematic Uncertainties

The method to determine the uncertainties is similar to the procedure for the uncertainties of n_{ch} as described in Section 7.1.5, the input distribution is varied according to each considered source of systematic uncertainties separately. Each modified input distribution is put through the p_{T}-unfolding matrix and the resulting difference compared to the nominal output is taken into account. For high p_{T} tracks, the evaluation of systematic uncertainties is done in two parts.

The first source accounts for mis-alignment which becomes significant for the tail of the p_{T}-spectrum. Due to resolution effects tracks migrate into neighboring bins. However, when the spectrum is steeply falling like in the tail of the p_{T}-distribution, more tracks migrate to higher p_{T}-bins than to lower ones. The difference of the unfolded p_{T}-distribution whose resolution for tracks with $p_{\mathrm{T}} > 10$ GeV was smeared by 10 % and the nominal distribution without high p_{T} smearing were considered as systematic uncertainty. The effect is estimated to be less than 7 % [41].

The second source of systematic uncertainty concerns mis-reconstructed, high p_{T} tracks, also for $p_{\mathrm{T}} > 10$ GeV. The fraction of such tracks was determined from MC, defining a mis-measured track as one for which the true and reconstructed p_{T} differ more than 50 %. To estimate the fraction in data several methods were studied [121]. They yield scaling factors for different detector regions with which one can estimate the residual fraction of these mis-reconstructed tracks in data. The systematic uncertainties of these high p_{T} tracks are listed in Table 7.3 compared to the analysis performed with the full-η PS [41, 130]. As a result of considering only tracks from the central barrel region, smaller systematic uncertainties are obtained in this analysis in the higher p_{T}-bins due to fewer poorly measured tracks and the fact that the alignment is better known in the central detector.

7.1.8. Corrections to $\langle p_{\mathrm{T}} \rangle$ versus n_{ch}

A method was employed for correcting the correlation distribution of $\langle p_{\mathrm{T}} \rangle$ and n_{ch} that differs from earlier measurements of this distribution [46, 118]. The correction consists in dividing two corrected distributions. The numerator is the corrected $\langle p_{\mathrm{T}} \rangle$-distribution

as a function of n_{ch}, the denominator is the corrected distribution of the sum over each charged particle in each event that is also a function of n_{ch}. One can write for the uncorrected numerator N and denominator D, both for a given n_{sel}:

$$\begin{aligned} N(n_{\mathrm{sel}}) &= N_{\mathrm{ev}} \int P(n_{\mathrm{sel}}) \cdot \rho(p_{\mathrm{T}}|n_{\mathrm{sel}}) \cdot p_{\mathrm{T}}\ dp_{\mathrm{T}} \\ D(n_{\mathrm{sel}}) &= N_{\mathrm{ev}} \int P(n_{\mathrm{sel}}) \cdot \rho(p_{\mathrm{T}}|n_{\mathrm{sel}})\, dp_{\mathrm{T}} \end{aligned}$$

where $P(n_{\mathrm{sel}})$ denotes the probability of having an event with n_{sel} tracks and $\rho(p_{\mathrm{T}}|n_{\mathrm{sel}})$ is the probability to observe a certain p_{T} given the event has n_{sel} tracks.

The first correction aims at replacing the dependency on n_{sel} by one on n_{ch}. It consists of applying the track weight w_{trk} to each p_{T} per n_{sel}-bin. With these two assumptions

1. the number of charged particles stay in the same n_{sel} bin
2. the track weight w_{trk} is independent of n_{sel}.

an intermediate result is obtained for which event and track weights are assumed to restore the number of charged particles per unit p_{T} for each n_{sel}-bin:

$$\rho_{\mathrm{ch}}(p_{\mathrm{T}}|n_{\mathrm{sel}}) = \rho(p_{\mathrm{T}}|n_{\mathrm{sel}}) \cdot w_{\mathrm{ev}}(n_{\mathrm{sel}}^{\mathrm{BS}}) \cdot w_{\mathrm{trk}}(p_{\mathrm{T}}, \eta).$$

In the second correction step, the n_{sel}-distribution is unfolded using the same n_{ch}-unfolding matrix from Section 7.1.5 to obtain charged particles. Mathematically, this translates into the sum over all n_{sel}-bins:

$$\begin{aligned} \mathrm{N}(n_{\mathrm{ch}}) &= N_{\mathrm{ev}} \int \sum_{n_{\mathrm{sel}}} P(n_{\mathrm{ch}}|n_{\mathrm{sel}}) \cdot P(n_{\mathrm{sel}}) \cdot \rho_{\mathrm{ch}}(p_{\mathrm{T}}|n_{\mathrm{sel}}) \cdot p_{\mathrm{T}}\ dp_{\mathrm{T}} \\ \mathrm{D}(n_{\mathrm{ch}}) &= N_{\mathrm{ev}} \int \sum_{n_{\mathrm{sel}}} P(n_{\mathrm{ch}}|n_{\mathrm{sel}}) \cdot P(n_{\mathrm{sel}}) \cdot \rho_{\mathrm{ch}}(p_{\mathrm{T}}|n_{\mathrm{sel}})\, dp_{\mathrm{T}} \end{aligned}$$

where $P(n_{\mathrm{ch}}|n_{\mathrm{sel}})$ represents the migration probability of an event having n_{sel} tracks originating from an event with n_{ch} particles. After summation over n_{sel} one obtains the probability that a certain p_{T} is observed in events with n_{ch} charged particles denoted as $\rho_{\mathrm{ch}}(p_{\mathrm{T}}|n_{\mathrm{ch}})$. Taking the ratio of numerator and denominator one obtains the variable of interest, $\langle p_{\mathrm{T}} \rangle$ as a function of n_{ch}:

$$\langle p_{\mathrm{T}} \rangle\ (n_{\mathrm{ch}}) = \frac{\int \rho_{\mathrm{ch}}(p_{\mathrm{T}}|n_{\mathrm{ch}}) \cdot p_{\mathrm{T}}\, dp_{\mathrm{T}}}{\int \rho_{\mathrm{ch}}(p_{\mathrm{T}}|n_{\mathrm{ch}})\, dp_{\mathrm{T}}}.$$

Systematic and Statistical Uncertainties

The systematic uncertainties arise either from the correction procedure itself by making the assumptions mentioned above or they are due to the uncertainties of quantities obtained from MC used during the correction procedure. In particular, this concerns uncertainties from the track reconstruction efficiency and the unfolding matrix. The

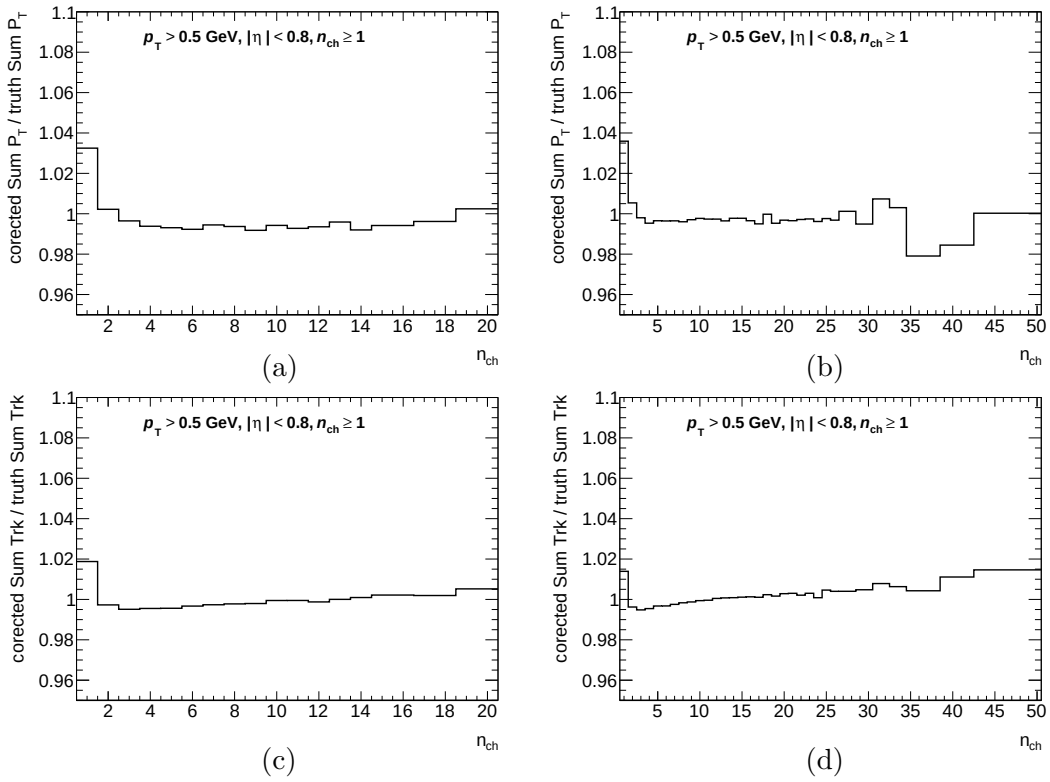

Figure 7.7.: Numerator (a,b) and denominator (c,d) for $\sqrt{s} = 0.9$ TeV (a,c) and $\sqrt{s} = 7$ TeV (b,d) in PS1. Non-closure is mostly visible in the first bin for all cases. This can arise from the dependency of the tracking efficiency ϵ_{trk} on n_{ch} being slightly different for low n_{ch} events. The dips in (b) between $n_{\mathrm{ch}} = 35$ and 45 are due to the 2 small spikes in the truth MC.

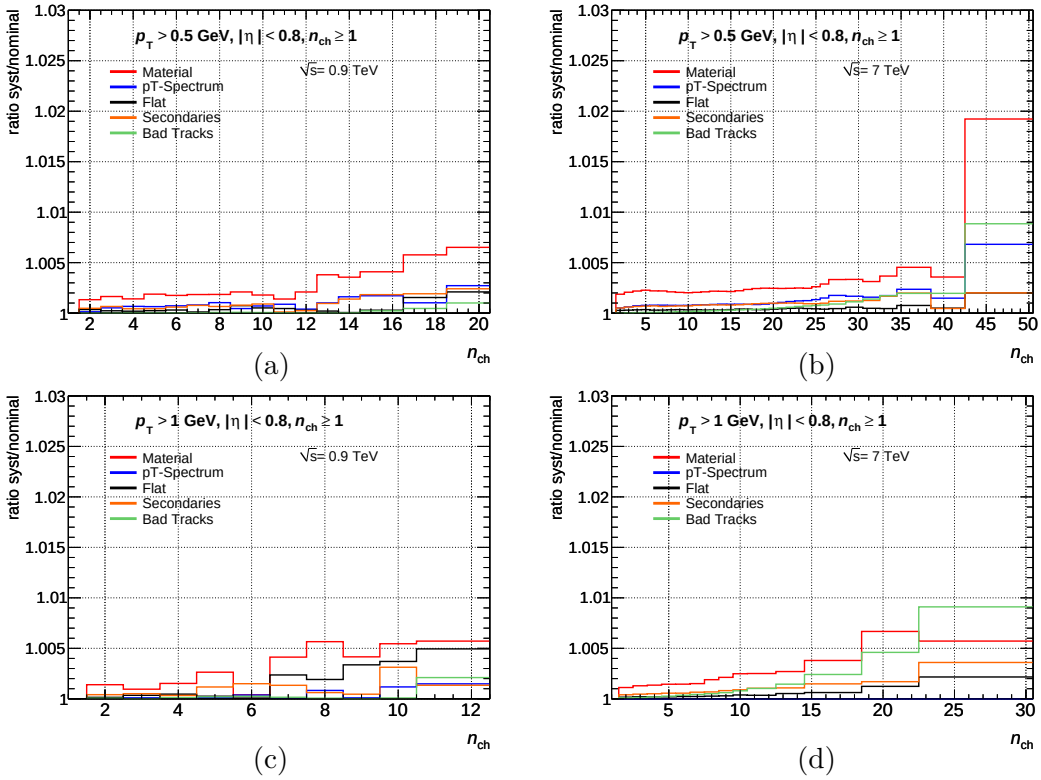

Figure 7.8.: Ratios of the modified distribution affected by a systematic uncertainty over the nominal values of $\langle p_{\mathrm{T}} \rangle$ vs. n_{ch} in PS1 (a,b) and PS2 (c,d) at $\sqrt{s} = 0.9$ TeV (a,c) and $\sqrt{s} = 7$ TeV (b,d). Overall, the uncertainty caused by detector material contributes most except for the last bin in (d) in which the systematic due to estimation of mis-measured tracks is slightly larger.

first source of uncertainty leads to non-closure. The closure tests are shown in PS1 for numerator and denominator in Fig. 7.7 at both energies. When divided by each other, the final closure test on $\langle p_{\mathrm{T}} \rangle$ is obtained where a few of the systematic uncertainties cancel. They are discussed in Section 7.1.9. The single contributions to the systematic uncertainty are shown for PS1 and PS2 and both energies in Fig. 7.8. The effect of material description in the detector simulation is the dominant source of uncertainty in all cases.

The statistical uncertainties for numerator and denominator were separately computed and added in quadrature as it was done in [41]. This was found to be a conservative choice, however a future study might perform a better treatment of statistical uncertainties and consider particle correlations within an event.

7.1.9. Discussion of Closure Tests

The closure tests as mentioned earlier probe the individual correction procedures that aim at restoring the distribution on hadron level (however they give no indication about uncertainties). Closure is obtained, if the generated MC distribution is reproduced by the reconstructed and corrected distribution of the generated events.

For the charged particle multiplicity distributions the effective tracking efficiency $\langle \epsilon_{\mathrm{trk}} \rangle$ was tuned to achieve very good closure, see Fig. 7.9, which results in less than 0.3 % non-closure at most. The closure tests for the η-distributions in Fig. 7.10 also reproduce the MC distribution on a similar level with 0.5 % non-closure at most. The correction procedure applied to the p_{T}-distributions works up to a 0.5 % level of non-closure. Only in the last p_{T}-bins the tests exhibit a non-closure of less than 1 %, see Fig. 7.11. The closure behavior of $\langle p_{\mathrm{T}} \rangle$ vs. n_{ch} is very similar for all four distributions shown in Fig. 7.12 agreeing up to a 2 %-level non-closure. This non-closure can be explained by the limits of the assumptions made in the correction of $\langle p_{\mathrm{T}} \rangle$ versus n_{ch} and has been considered in the systematic uncertainties with 2 % for each n_{ch}-bin.

7.1.10. Comparison with Measurements extending to $|\eta| < 2.5$

For a consistency check, the charged particle multiplicity distribution as function of η are compared to the results in the full-η phase-space that were presented in [41]. The ratio should and is found to yield a constant value corresponding to the ratio of the normalisation factors $1/N_{\mathrm{ev}}$ of the respective distribution. This is shown in Fig. 7.13. The measurement at $\sqrt{s} = 0.9$ TeV in Fig. 7.13 (a) shows an almost perfect constant value. Minor fluctuations are visible in the measurement at $\sqrt{s} = 7$ TeV in Fig. 7.13 (b) but were not significant enough for further consideration.

7.1.11. Results and Discussion

The distributions of charged particle multiplicities after the full correction procedure for the two analysed phase-space regions and energies are shown in Fig. 7.14 - 7.20. The precision of these measurements allows to highlight clear differences between the Monte Carlo tunes and that were explained before (see Section 2.5).

Charged Particle Multiplicity Spectra $\frac{1}{N_{\mathrm{ev}}} \cdot \frac{\mathrm{d}N_{\mathrm{ev}}}{\mathrm{d}n_{\mathrm{ch}}}$ These distributions are shown emphasizing the low n_{ch} region in Fig. 7.14 and the high n_{ch} tail in Fig. 7.15. Generally, more particles are produced in the lower multiplicity region in data than predicted by the MC models which leads to an under-prediction of particles in the n_{ch} tail due to the normalisation of $1/N_{\mathrm{ev}}$. This seems to be a general feature of the particles as the same effect has been observed for the full-η PS [41]. Predictions of AMBT1 get closest to the data, however the agreement is better in the low than in the high n_{ch} region. PHOJET is more successful in modeling PS1 data at $\sqrt{s} = 0.9$ TeV than in PS2 where discrepancies reach 50 % and even increase when compared to data at $\sqrt{s} = 7$ TeV.

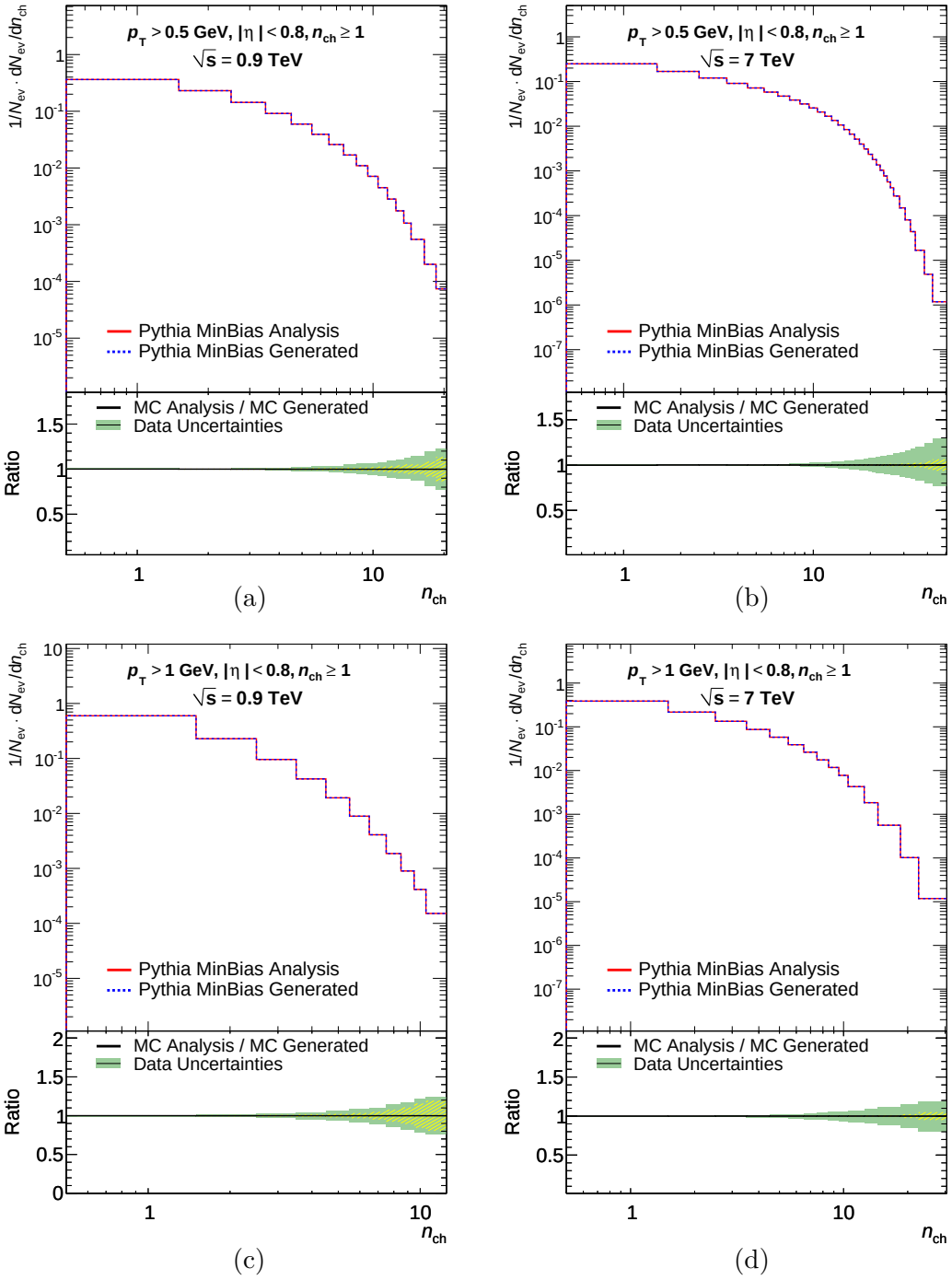

Figure 7.9.: Closure tests of $1/N_{\mathrm{ev}} \mathrm{d}N_{\mathrm{ev}}/n_{\mathrm{ch}}$ at $\sqrt{s} = 0.9$ TeV (a,c) and $\sqrt{s} = 7$ TeV (b,d). The effective tracking efficiency was tuned to obtain perfect closure such that the two compared distributions overlap precisely. The light shaded area indicate the statistical uncertainties, green bands show the total uncertainties.

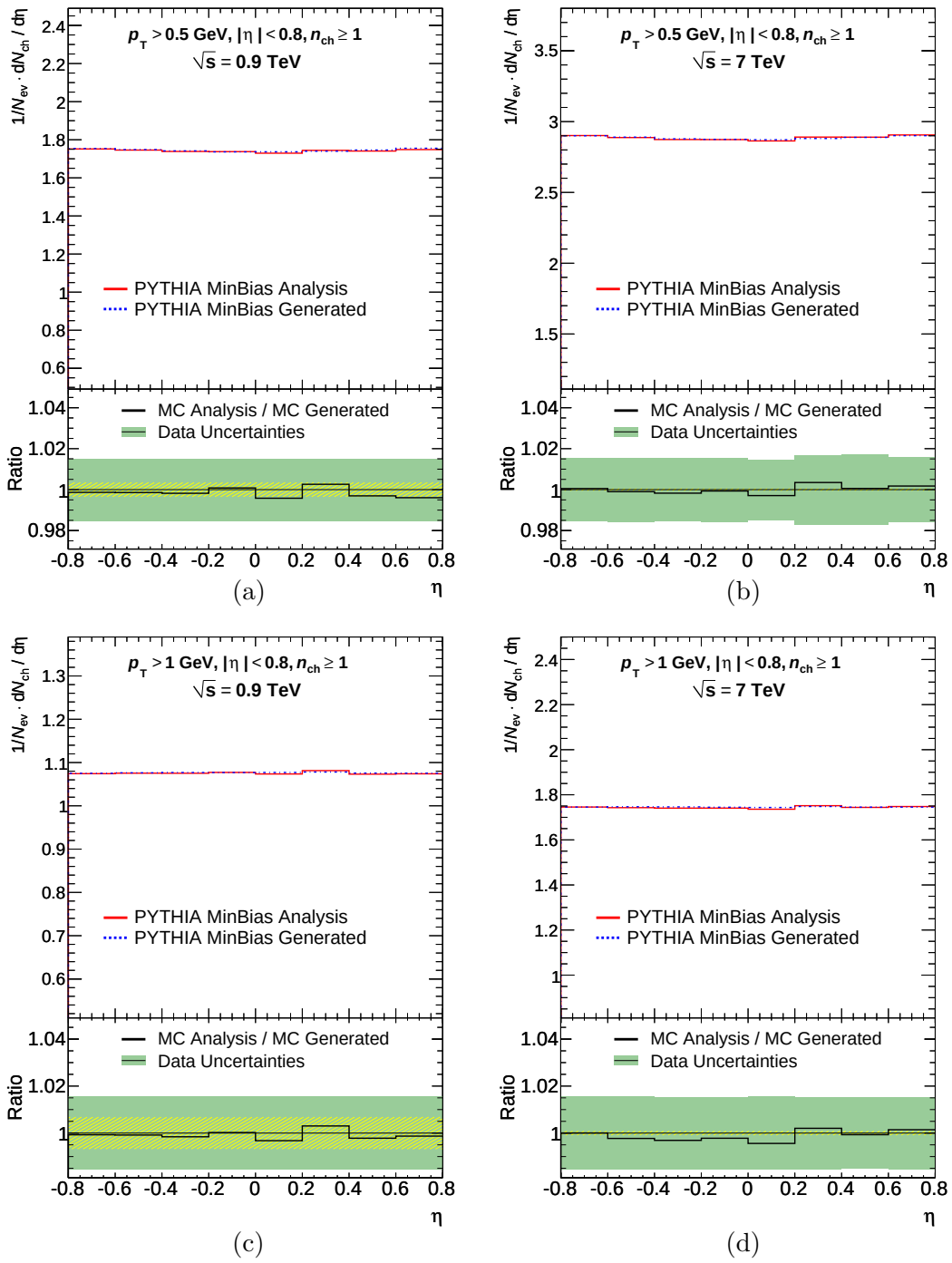

Figure 7.10.: Closure tests for $1/N_{\mathrm{ev}}\mathrm{d}N_{\mathrm{ch}}/\eta$ for $\sqrt{s} = 0.9$ TeV (a,c) and $\sqrt{s} = 7$ TeV (b,d). The light shaded area indicates the statistical error while the green band shows the total uncertainties.

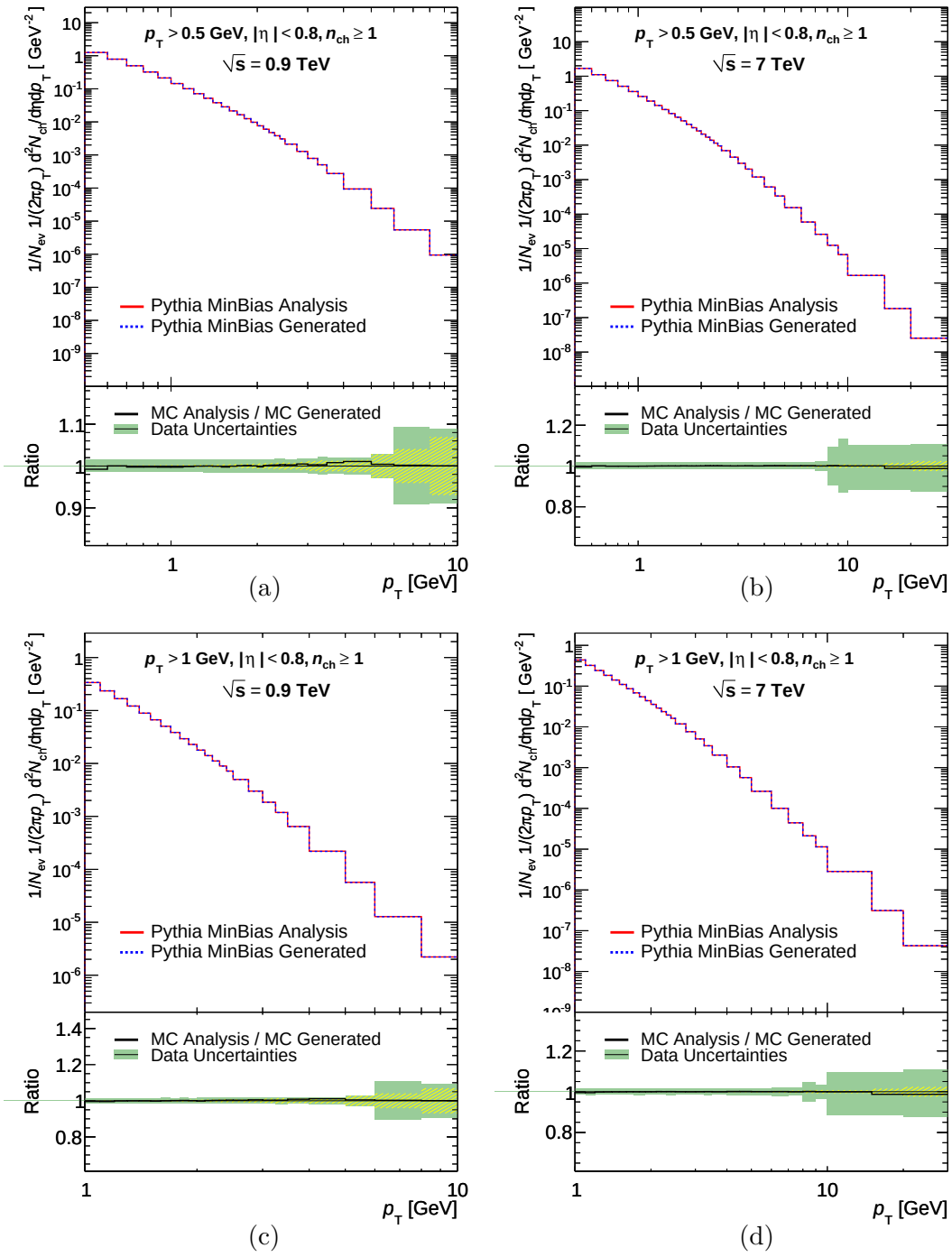

Figure 7.11.: Closure tests for $1/N_{\mathrm{ev}}\, 1/(2\pi p_{\mathrm{T}})\, \mathrm{d}^2N_{\mathrm{ch}}/\mathrm{d}\eta\mathrm{d}p_{\mathrm{T}}$ for $\sqrt{s} = 0.9$ TeV (a,c) and $\sqrt{s} = 7$ TeV (b,d). Uncertainties around 10 GeV in (b) are due to transition regions of the unfolding matrix when a flat distribution was used as input to probe the stability of the result. Light shaded areas indicate the statistical and green bands the total uncertainties.

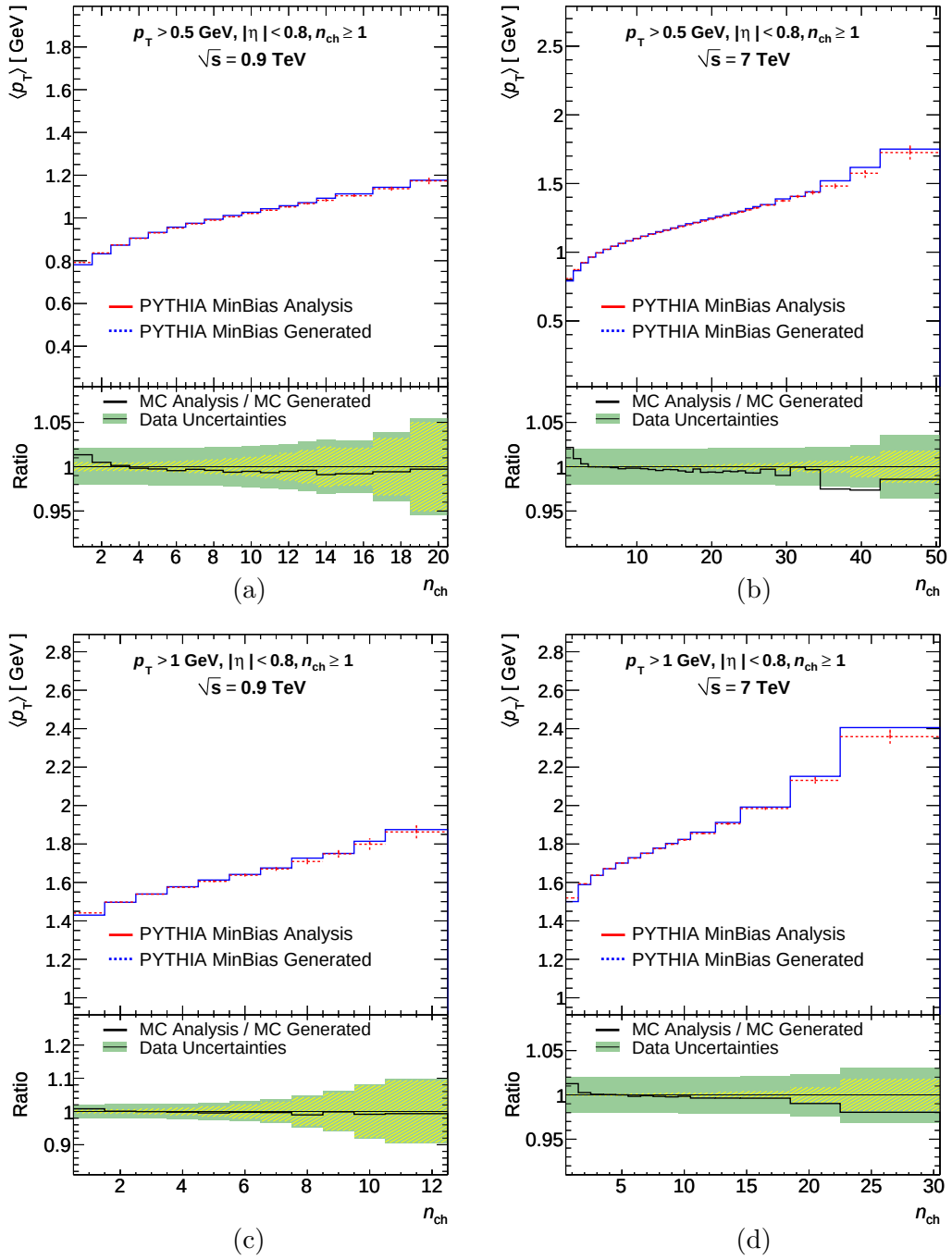

Figure 7.12.: Closure tests on $\langle p_{\mathrm{T}} \rangle$ vs. n_{ch} for $\sqrt{s} = 0.9$ TeV (a,c) and $\sqrt{s} = 7$ TeV (b,d). Non-closure behaviour is similar for all cases (a–d) and is assumed to be due to the assumptions made during the correction. Slightly better closure is obtained at $\sqrt{s} = 0.9$ TeV. The light shaded area indicates the statistical error while the green band shows the total uncertainties.

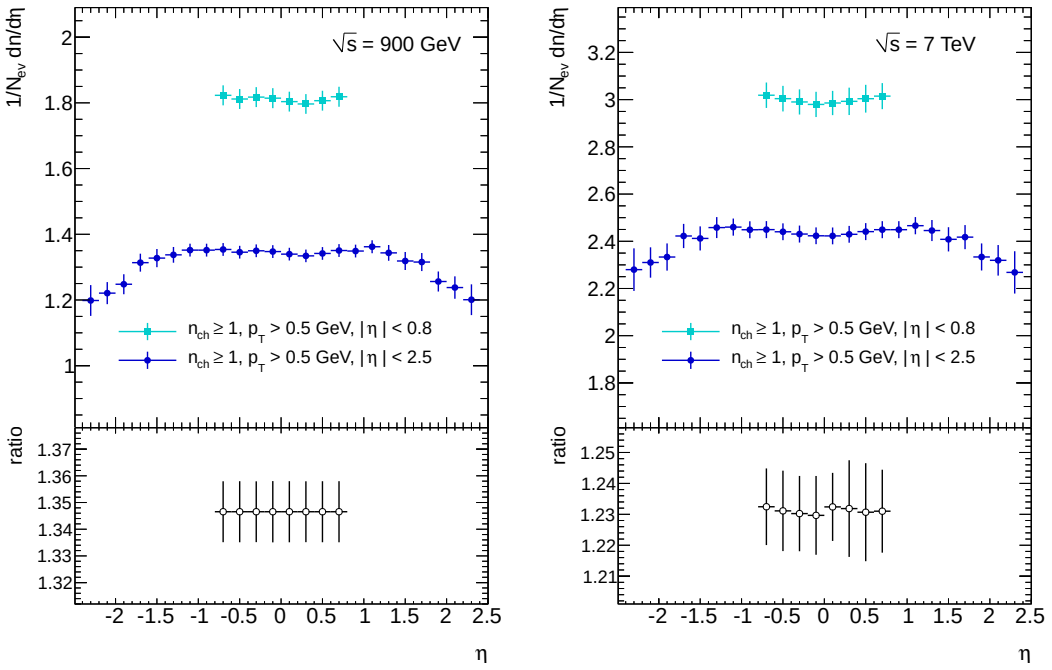

(a) (b)

Figure 7.13.: Comparison of $1/N_{\mathrm{ev}} dN_{\mathrm{ch}}/d\eta$ measurements in PS1 and the full-η PS at $\sqrt{s} = 0.9$ TeV (a) and 7 TeV (b). The bottom insert shows the ratio which indicates a constant value due to the different normalisation. The ratio uncertainty account for 100 % correlation of the uncertainties of the respective measurements. One can see, both measurements are fully compatible.

Table 7.4.: Charged particle multiplicity densities at $\eta = 0$.

phase-space region	$\sqrt{s}$ [TeV]	$1/N_{\text{ev}} \cdot \mathrm{d}N_{\text{ch}}/\mathrm{d}\eta\,|_{\eta=0}$
$n_{\text{ch}} \geq 1$, $\lvert\eta\rvert < 0.8$,$p_{\text{T}} > 500$ MeV	0.9	1.809 ± 0.006 (stat) ± 0.030 (syst)
	7	2.983 ± 0.001 (stat) ± 0.054 (syst)
$n_{\text{ch}} \geq 1$, $\lvert\eta\rvert < 0.8$,$p_{\text{T}} > 1$ GeV	0.9	1.056 ± 0.006 (stat) ± 0.011 (syst)
	7	1.661 ± 0.001 (stat) ± 0.024 (syst)

Pseudorapidity Spectra of Charged Particles $\frac{1}{N_{\text{ev}}} \cdot \frac{\mathrm{d}N_{\text{ch}}}{\mathrm{d}\eta}$ An almost flat distribution for central charged particles is measured in both phase-space regions and at both energies as Fig. 7.16 shows. The best agreement is obtained with AMBT1 for all distributions. In fact, AMBT1 reproduces the data in PS2 for both energies. In PS1 generally more particles are observed than predicted which changes in PS2 for most of the tunes at $\sqrt{s} = 7$ TeV. The PHOJET normalisation is off by 20 % at $\sqrt{s} = 7$ TeV but matches the shape of the data.

Charged Particle Multiplicity at $\eta = 0$ For purposes of comparisons with measurements of other experiments, a mean charged particle density at $\eta = 0$ is shown in Table 7.4. They were obtained by averaging bins with $|\eta| < 0.2$.

Transverse Momenta of Charged Particles $\frac{1}{N_{\text{ev}}} \cdot \frac{1}{2\pi p_{\text{T}}} \cdot \frac{\mathrm{d}^2 N_{\text{ch}}}{\mathrm{d}\eta \mathrm{d}p_{\text{T}}}$ The double-differential distribution was measured as a single-differential distribution in p_{T}, normalised as indicated but averaged over the η-range of twice 0.8. These spectra of the transverse momentum are shown in Fig. 7.17 and Fig. 7.18 which zoom into the lower p_{T} region and the full-p_{T} range in Fig. 7.19. Again, AMBT1 reproduces the data best in the lower p_{T} region. PYTHIA8 is in fair agreement with the data, in particular for the tighter phase-space region PS2 as one can observe in Fig. 7.17 (d). Comparing the p_{T} tails of data and Monte Carlo at $\sqrt{s} = 7$ TeV, PYTHIA8 still performs reasonably well, while discrepancies with AMBT1 reach up to 50 %. PHOJET is fairly good in describing the p_{T} tail of the data at $\sqrt{s} = 7$ TeV. A similar behaviour is observed for PYTHIA8 which is close to the data, however at $\sqrt{s} = 7$ TeV only. The observation that there is no model which can describe the whole range of the data [41] is also true for this analysis.

Correlation of Average Transverse Momentum and Charged Particle Multiplicity $\langle p_{\text{T}} \rangle$ vs. n_{ch} The measurements of the average transverse momentum as function of the charged particle multiplicity are shown in Fig. 7.20. The measurements show an interesting shape, that is more pronounced in the data at $\sqrt{s} = 7$ TeV. At low n_{ch} a slight slope is visible which changes over into an apparent saturation curve rather quickly for $n_{\text{ch}} \approx 5$ latest. However, other effects must contribute in addition to a saturation effect showing a steadily increasing curve. While most of the models are able to describe the data at $\sqrt{s} = 0.9$ TeV with AMBT1 reproducing best the absolute values, all of the models fail to describe the data at $\sqrt{s} = 7$ TeV, generally with deviations around 20

to 30 % in PS1 and 10 to 20 % in PS2. Clearly visible is the feature that all models overestimate the correlation between $\langle p_{\mathrm{T}} \rangle$ and n_{ch}.

7.1.12. Conclusions

Charged particle multiplicities have been measured in the central region for $|\eta| < 0.8$ and two different p_{T} requirements of $p_{\mathrm{T}} > 0.5$ and > 1 GeV at both centre-of-mass energies $\sqrt{s} = 0.9$ and 7 TeV. The concentration on a more central η-range yields smaller systematic uncertainties compared to previous ATLAS measurements [41, 46]. It was anticipated that the analysis of centrally produced charged particles in PS1 may lead to conclusive differences when comparing to the full-η PS analysis. The latter is more sensitive to physics processes with higher activity in the forward regions.

From the comparisons of the measurements to Monte Carlo, one can conclude that also for centrally produced charged particles no Monte Carlo model or tune is clearly favorable. For example, different parts within the charge particle multiplicity distributions (Fig. 7.14 and 7.15) favor different models. Some models agree with the data at a 5 %-level or better in certain distributions. The PYTHIA6 tune AMBT1 which was already tuned using LHC data and PYTHIA8 were most often successful (Fig. 7.15(a,b), Fig.7.16). An exception for AMBT1 is the description of the p_{T} tails of the central particles. They differ up to 50 % in some bins independent of phase-space and centre-of-mass energy. The energy dependency seems to be generally a problematic parameter in the models. The average p_{T} as function of the charged particle multiplcity at $\sqrt{s} = 0.9$ TeV can be fairly well modeled, but this turns out to no longer hold for data at $\sqrt{s} = 7$ TeV (Fig. 7.20).

These measurements represent another view on general properties of charged particle production analysing new phase-space regions with ATLAS. They can, like previous analyses [41, 46], be used to produce new tunes of Monte Carlo generators and improve their models of soft inelastic scattering processes. Obviously, the best tune is obtained the more measurement points are used, the more precise the measurements are and the wider the range is of available distributions. Once, the new LHC data can be consistently described with previous measurements and also be accurately reproduced in simulations, such measurements may eventually lead to a more fundamental approach of the description of soft particle production.

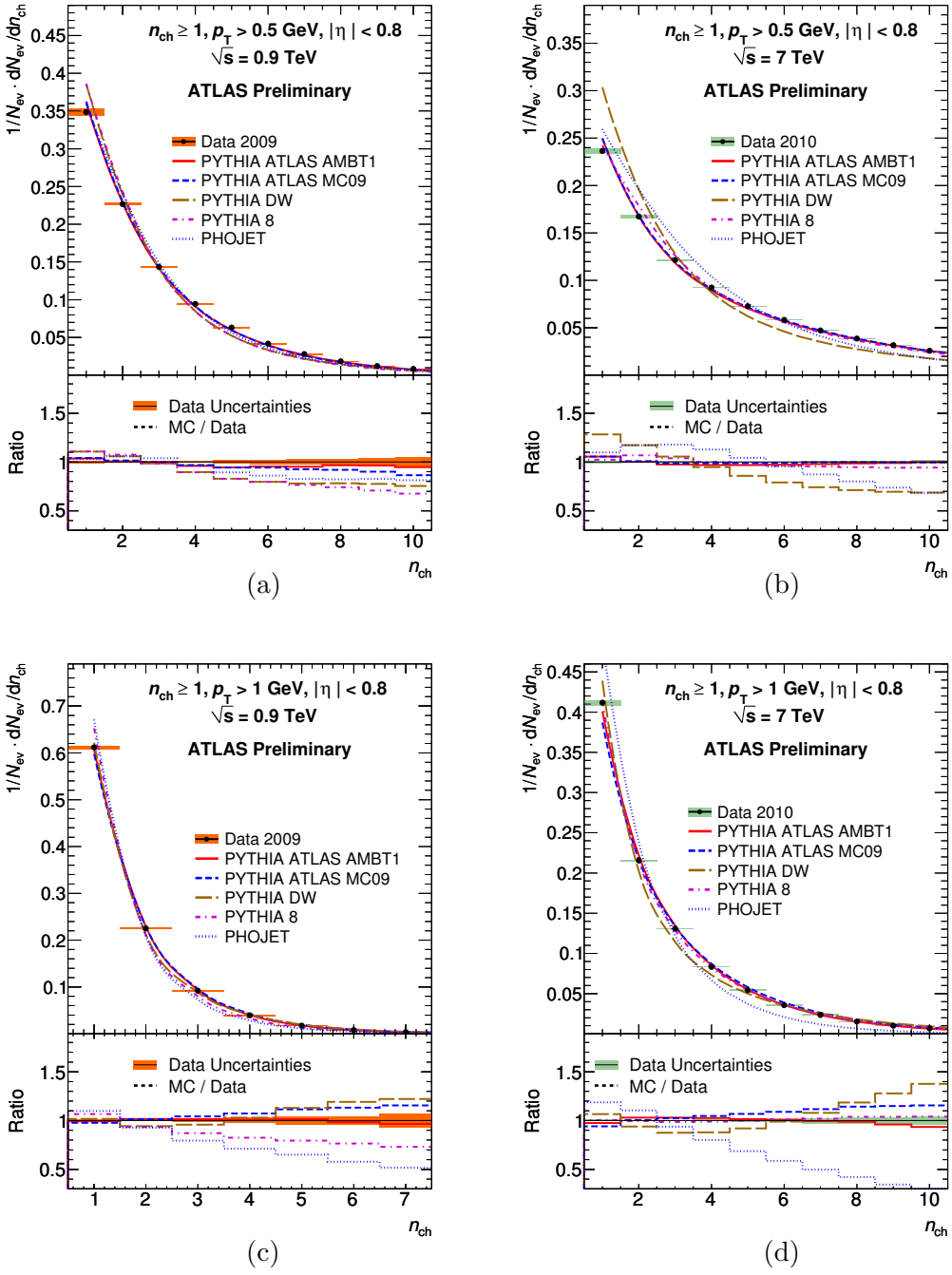

Figure 7.14.: Primary charged particle multiplicity distributions zoomed to low n_{ch} values in PS1 (a,b) and PS2 (c,d) at $\sqrt{s} = 0.9$ TeV (a,c) and $\sqrt{s} = 7$ TeV (b,d). The shaded areas represent the total uncertainties, the vertical bars the statistical uncertainties only. The bottom inserts show the ratio of a particular MC over the data (the line in the bottom legend is representative). The values of the ratio histograms refer to the bin centroids.

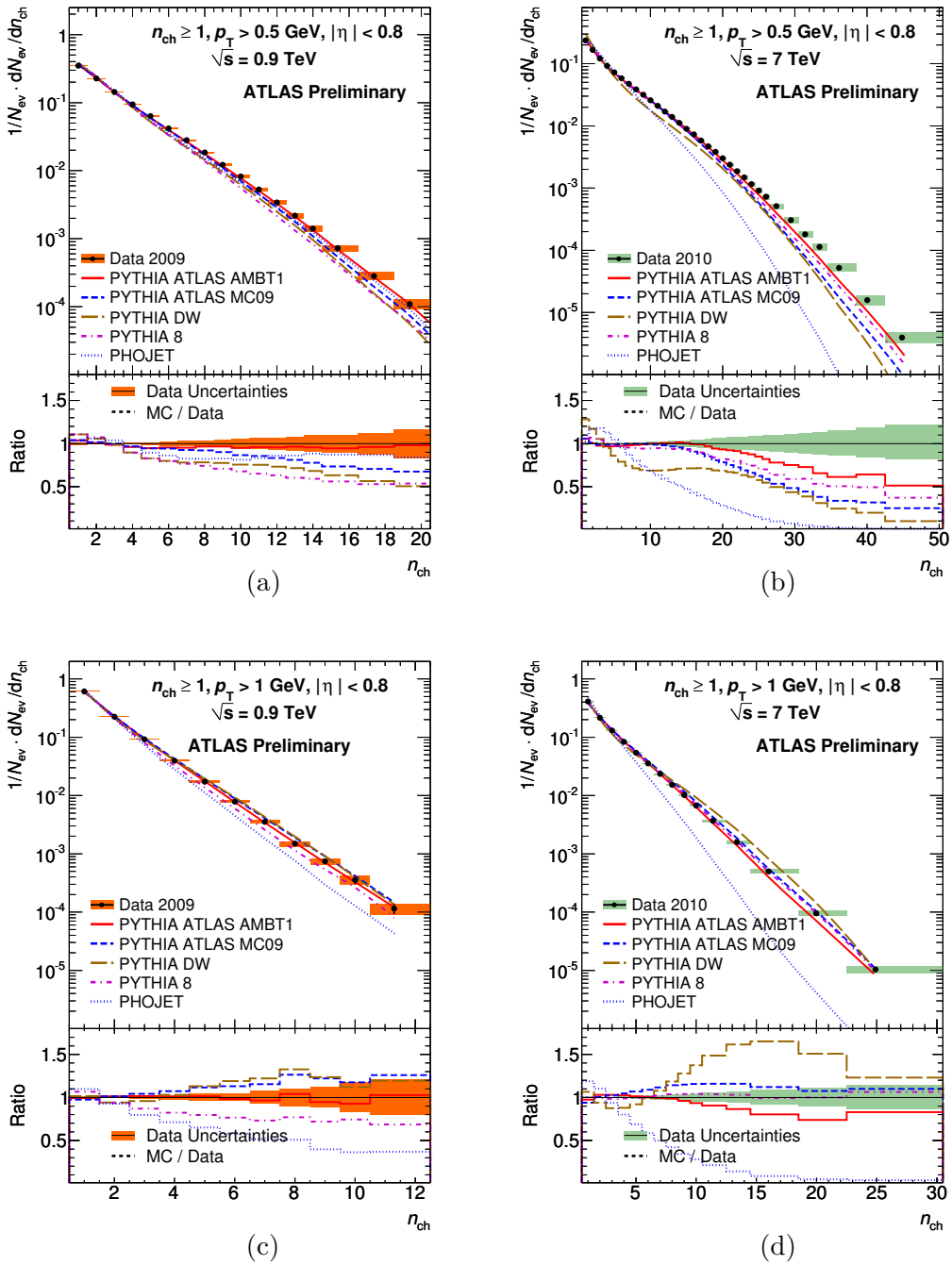

Figure 7.15.: As Fig. 7.14 but showing the full n_{ch}-range.

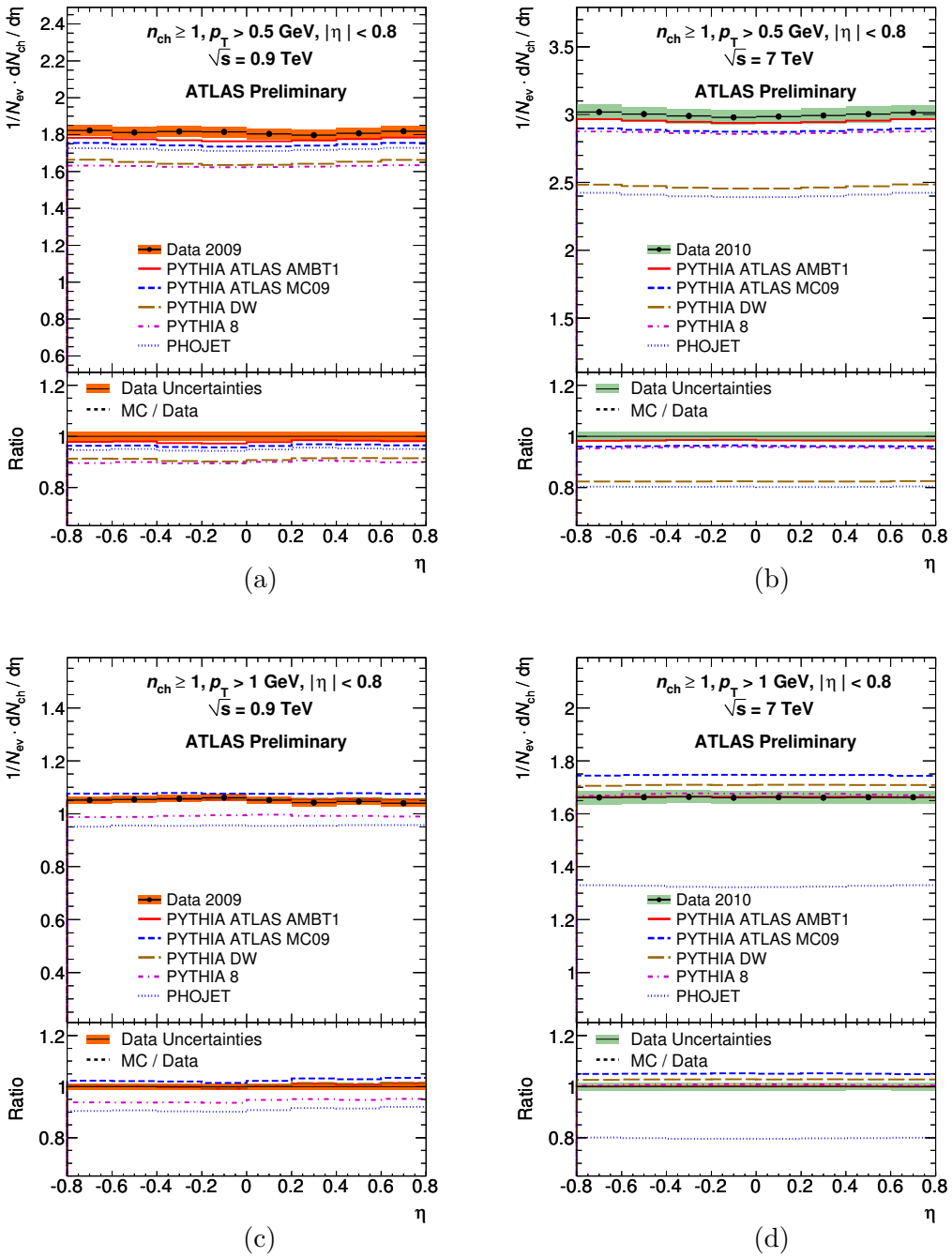

Figure 7.16.: Pseudorapdity density of charged particles in PS1 (a,b) and PS2 (c,d) at $\sqrt{s} = 0.9$ TeV (a,c) and $\sqrt{s} = 7$ TeV (b,d) with uncertainties indicated as in Fig. 7.14.

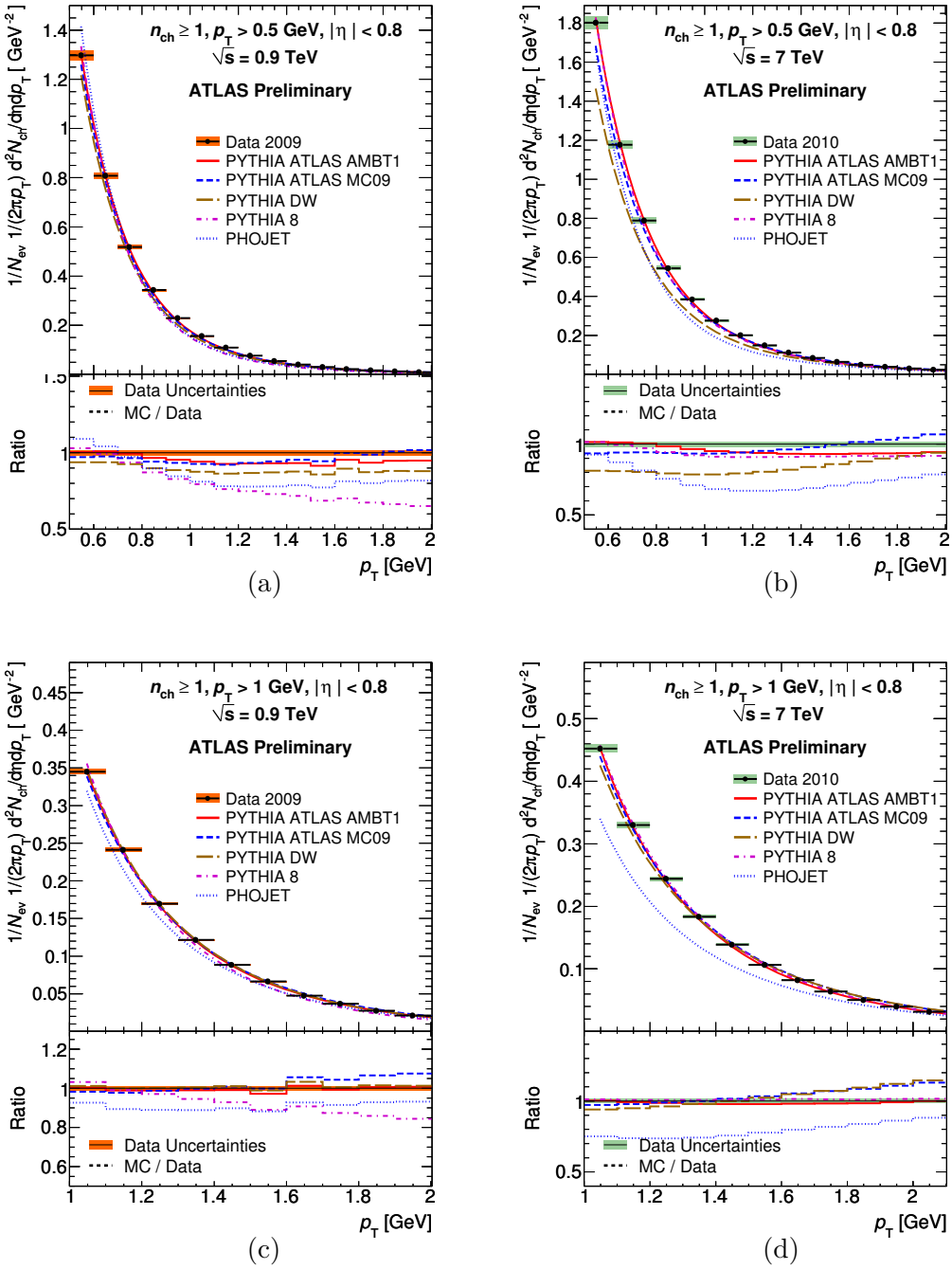

Figure 7.17.: p_{T}-spectrum of primary charged particles in PS1 (a,b) and PS2 (c,d) at $\sqrt{s} = 0.9$ TeV (a,c) and $\sqrt{s} = 7$ TeV (b,d) in a linear scale and zoomed into the low-p_{T} region. Uncertainties are indicated as in Fig. 7.14.

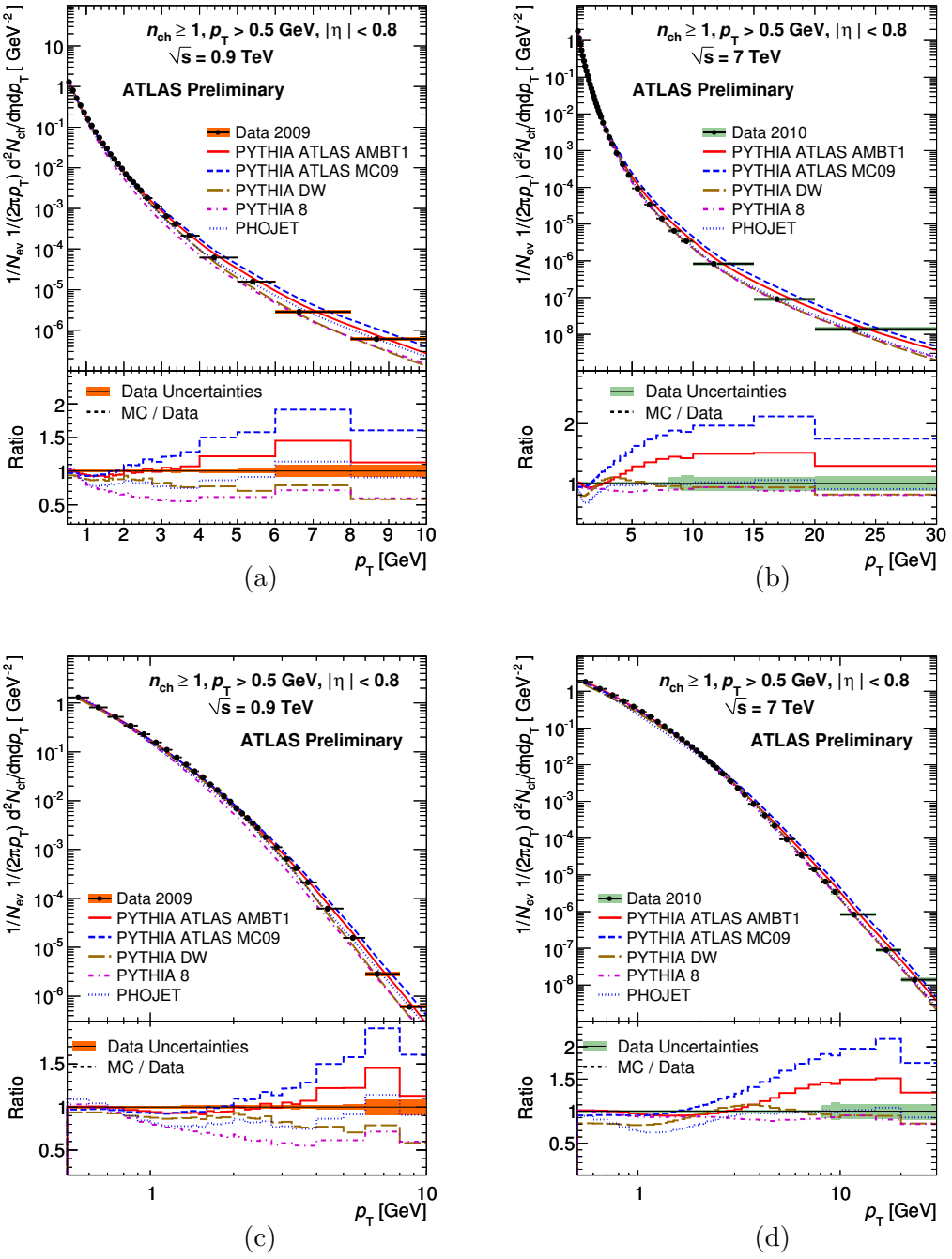

Figure 7.18.: Full p_{T}-spectrum of primary charged particles in PS1 (c,d) at $\sqrt{s} = 0.9$ TeV (a,c) and $\sqrt{s} = 7$ TeV (b,d) in a linear- (a,b) and log-scale (c,d). Uncertainties are indicated as in Fig. 7.14.

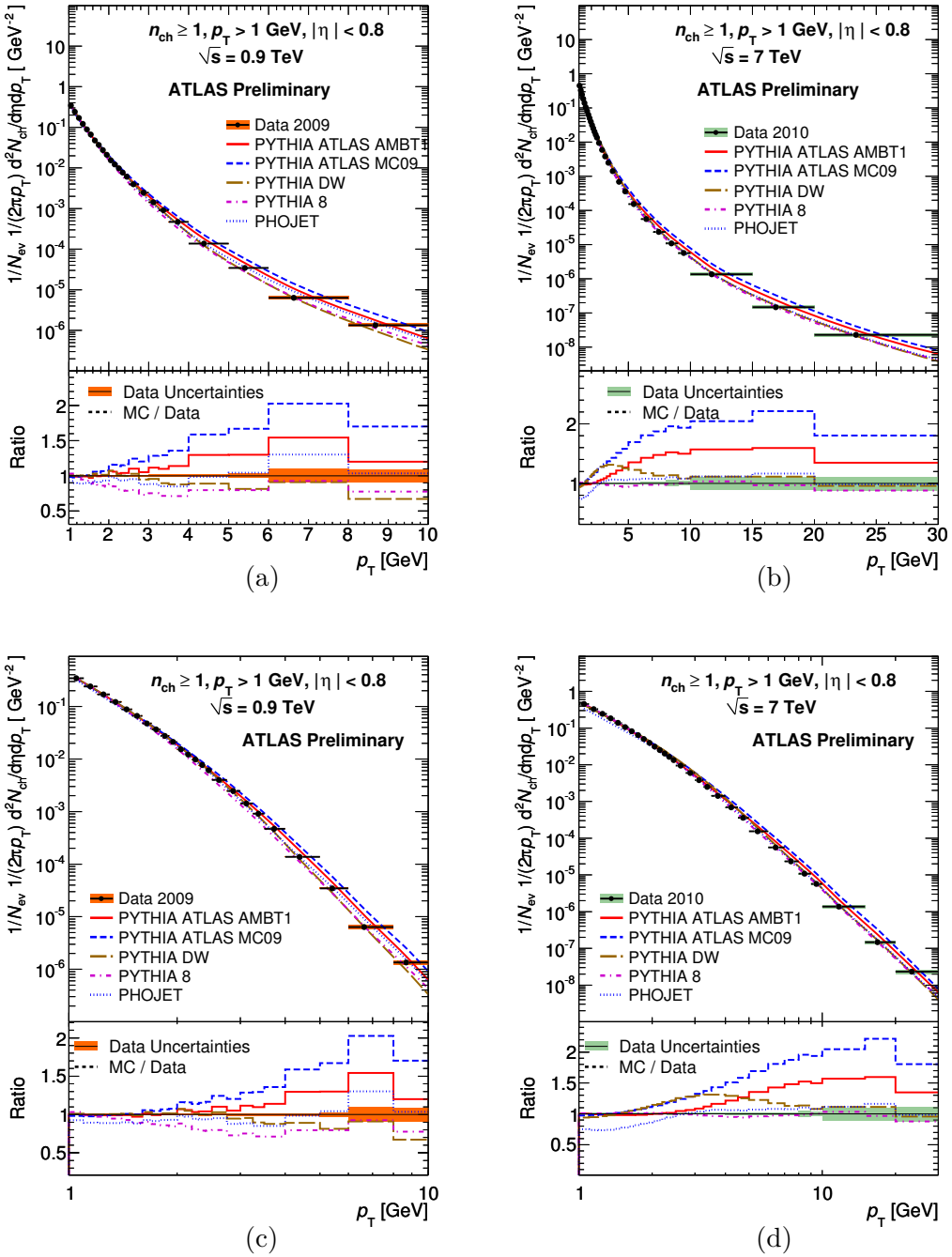

Figure 7.19.: As Fig. 7.18 but for PS2.

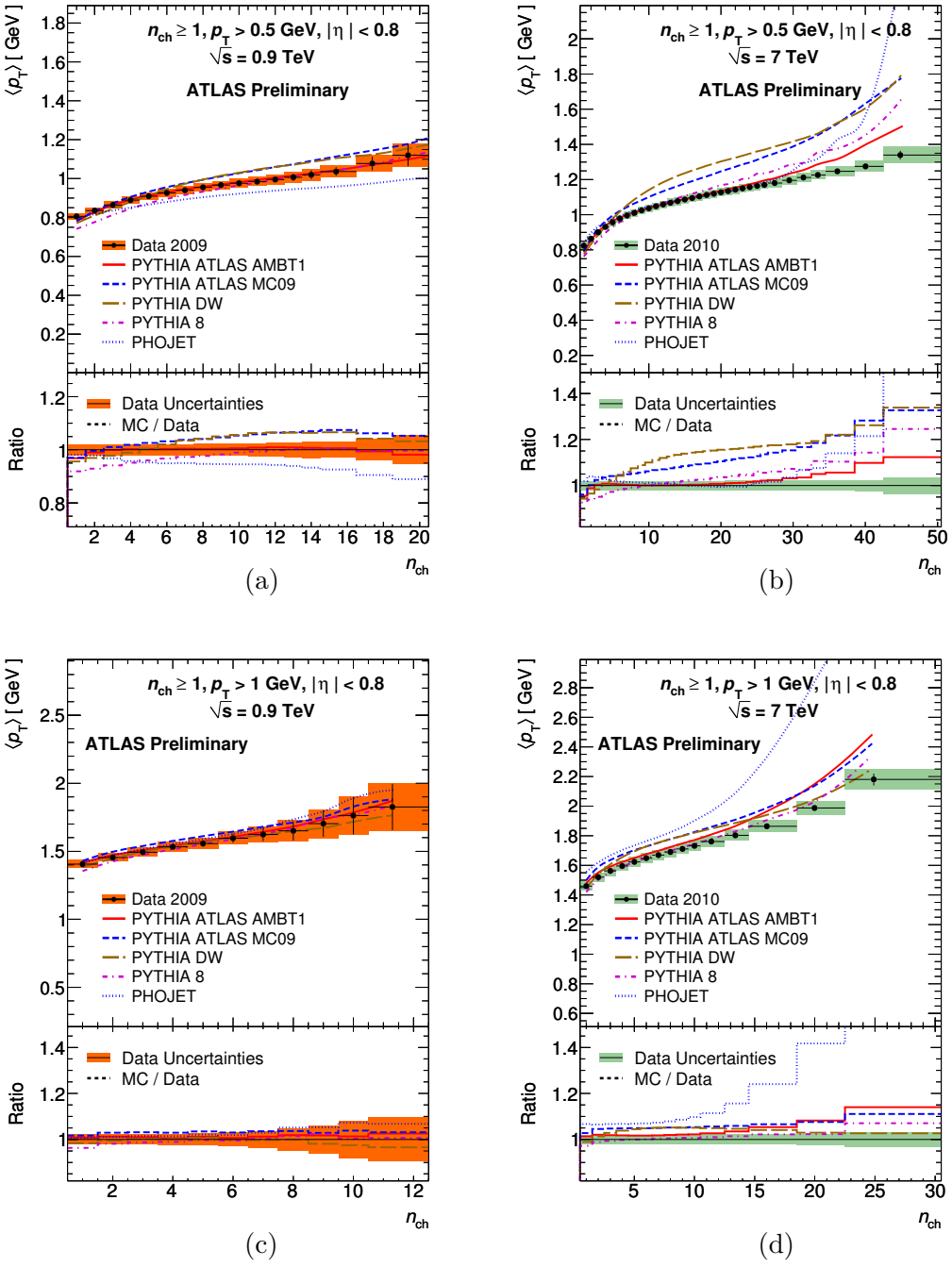

Figure 7.20.: Average p_{T} distributions of charged particles as a function of n_{ch} in PS1 (a,b) and PS2 (c,d). Uncertainties are indicated as in Fig. 7.14.

7.2. Comparison of Minimum Bias Measurements by the ATLAS, ALICE and CMS Experiment

The commonly defined phase-space regions PS1 and PS2 (see Table 7.1) and a common analysis strategy allow the important step to compare independent measurements with different systematic uncertainties between the different LHC experiments ATLAS, CMS and ALICE. This represents the first combined LHC analysis for which the results obtained in the previous section are used as the ATLAS contribution. Further agreements were made on observables on the underlying event which is still progress. Partial results are already available [131].

7.2.1. Results and Discussion

At the time of writing[1] measurements of pseudorapidity distributions of charged particles exist from all three experiments at both centre-of-mass energies [114, 132, 133]. These are shown in Fig. 7.21 but for a better visibility of the single data points additional plots can be found in Appendix B.2. Ratios of the measurements have been added with the error bars indicating the combined uncertainty of the two compared experiments.

One can see that the measurements of the three experiments agree well within uncertainties. Minimal differences of less than 1.2 standard deviations are visible in Fig. 7.21 (a) where the ALICE points in PS1 at $\sqrt{s} = 900$ GeV lie systematically below ATLAS and CMS measurement points. An opposite trend can be noted at $\sqrt{s} = 7$ TeV in PS2, where ALICE points lie systematically above ATLAS and CMS points, however this deviation is smaller than half a standard deviation as can be seen in Fig. 7.21 (d). No further systematic differences are observed between the measurements of the three experiments.

For a more detailed view on the measurements, the total uncertainties are split into systematic and statistical contributions and are listed in the Appendix B.3 in Table B.2, B.3 and B.4. As one can see, the total uncertainty is clearly dominated by systematic effects in all cases[2].

The combined uncertainties of the ratio values of the measurement points cover comfortably any variations of the ratios. This could be an indication that the total (or essentially the systematic) uncertainties of the ratios are a conservative estimate. It is likely that correlations between the bins exist which systematically shift the values. The tracking efficiency being almost the same for all bins in the considered η-region for ATLAS is for example one candidate source. Such a source of uncertainty is also present in the two other experiments which is why a combination of them results in a conservative, overestimated systematic uncertainty.

The most statistics is obtained for the PS1 at $\sqrt{s} = 7$ TeV. For these measurements, all three experiments show an excellent agreement even on the absolute value which can be seen in Fig. 7.21 (b). Comparing the measurements with the least statistics, in PS2

[1] 09.09.2011

[2] Note, that only absolute uncertainties are indicated.

at $\sqrt{s} = 0.9$ TeV shown in Fig. 7.21 (c), the measurement points exhibit a larger spread of the absolute values, however this is still comprised in the total uncertainties.

The remarkable good agreement of the measurements is also visible in the comparison the charged particle density at $\eta = 0$ as function of $\sqrt{s}$, shown in Fig. 7.22. While ATLAS and CMS determine these values by averaging over two bins around $\eta = 0$, ALICE performed a fit to the measurements extracting the value at $\eta = 0$. The measurements do not only agree with each other, they also confirm the predictions of the MC tune AMBT1.

In addition to these comparisons, ATLAS and CMS have performed the same measurement in the full available η-range [41, 133] with twice as many measurement points compared to the commonly defined distributions. The comparison is shown in Fig. 7.23. Due to the slightly differently defined phase-space region given by the different pseudorapidity coverages (ATLAS covers $|\eta| < 2.5$ and CMS $|\eta| < 2.4$), CMS could in principle miss one type of events in which only one or more charge particles with $p_{\mathrm{T}} > 0.5$ GeV are produced exactly between $|\eta| = 2.4$ and $|\eta| = 2.5$. Such events would be missing in the normalisation factor, but the comparisons show that this is not noticable effect at all. Both experiments match the shape and the normalisation with striking accordance.

7.2.2. Conclusion

The presented results by ATLAS, CMS and ALICE agree strikingly well, confirming independently the measurements of each other. These results show that measurements of charged particle properties at the LHC are performed with a good understanding of the rather complex tracking devices. Despite the different uncertainties which each of the experiment possesses, all three of them provided measurement points with a precision of around 2 to 3 %. The total uncertainties at both centre-of-mass energies are clearly dominated by systematic effects. The largely overlapping error bars of the ratios indicate the presence of a correlated source of systematic uncertainty.

It will be exciting to compare the remaining distributions, since more complex unfolding methods are involved in the other distributions. Their direct comparison should be performed in the largest possible range. It was therefore suggested to use a binning that is compatible with the one chosen in this work. Details are outlined in the Appendix B.1.

The goal of comparing measurements of charged particles by three of the major LHC experiments could be achieved with very positive results for the pseudorapidity density at $\sqrt{s} = 0.9$ TeV and $\sqrt{s} = 7$ TeV in two different phase-space regions. This puts substantial weight on these measurements to be used for improving models to describe and possibly explain soft interaction processes.

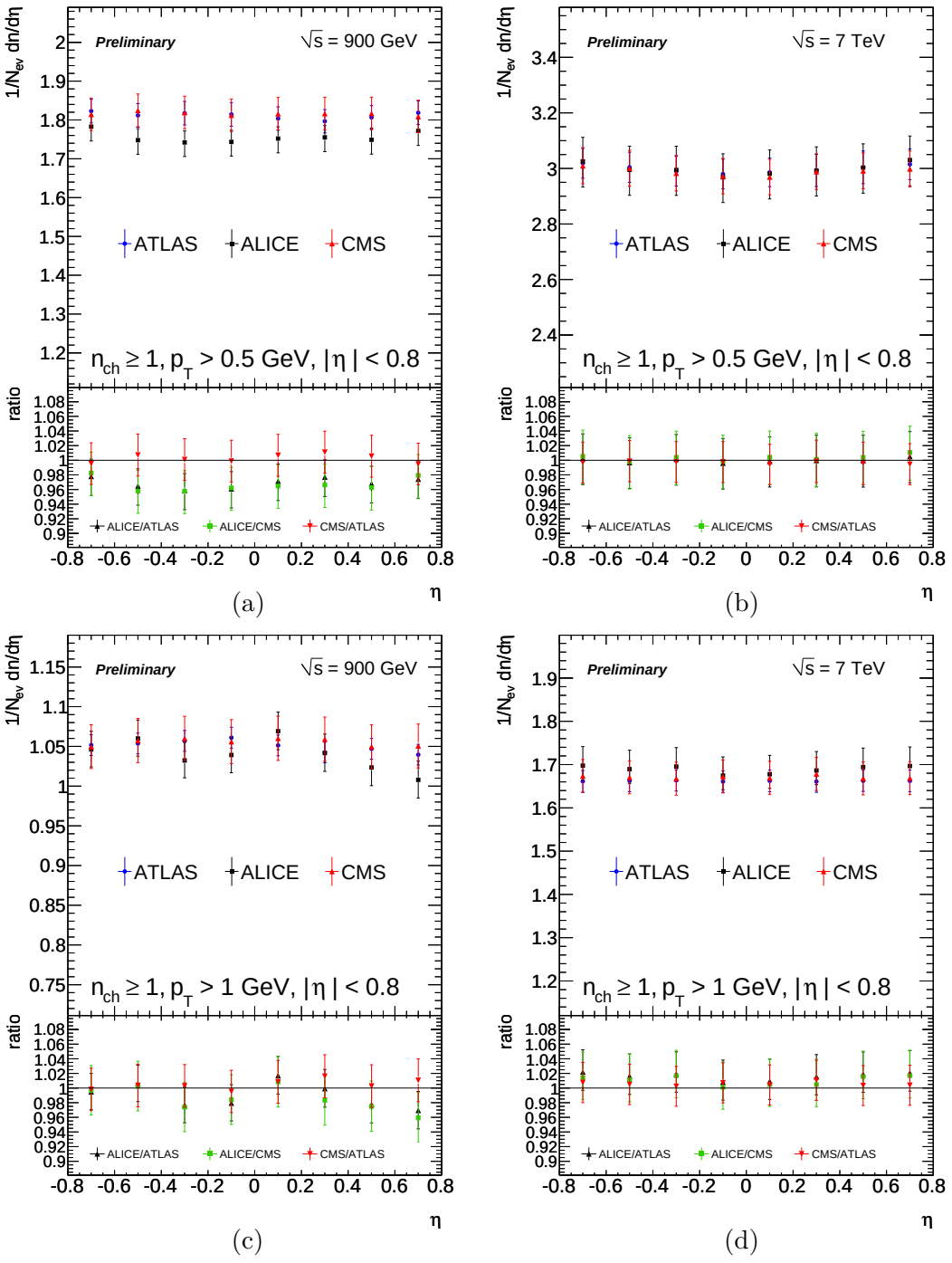

Figure 7.21.: Comparisons of $1/N_{\mathrm{ev}} dN_{\mathrm{ch}}/d\eta$ measurements with ALICE, CMS and ATLAS at $\sqrt{s} = 0.9$ TeV (a,c) and 7 TeV (b,d) in the indicated phase-space regions. The error bars in the top pads show the total uncertainty. The bottom shows ratios with the respective uncertainties of two experiments added in quadrature.

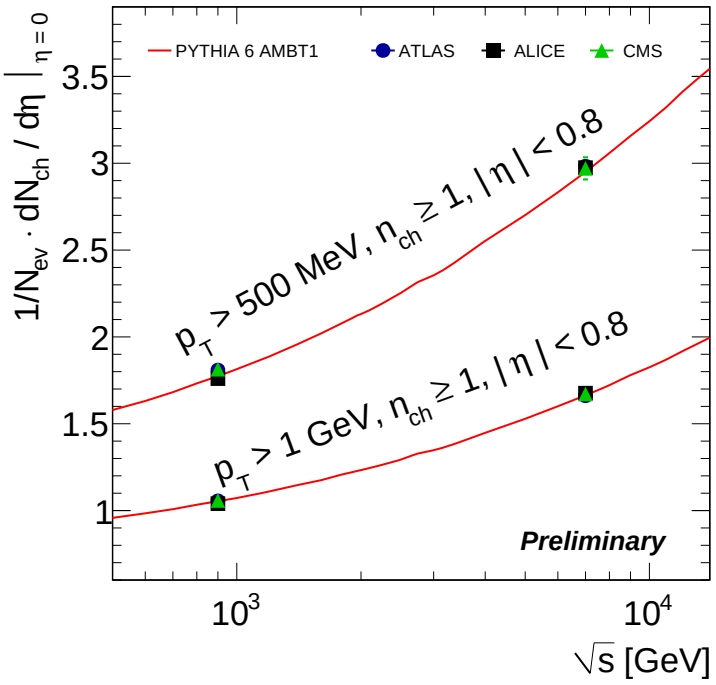

Figure 7.22.: Comparisons of $1/N_{\mathrm{ev}} dN_{\mathrm{ch}}/d\eta$ measurements at $\eta = 0$ by ALICE, CMS and ATLAS at $\sqrt{s} = 0.9$ TeV and 7 TeV for CMS and ATLAS only. Also, predictions by the ATLAS tune AMBT1 are shown as (red) lines.

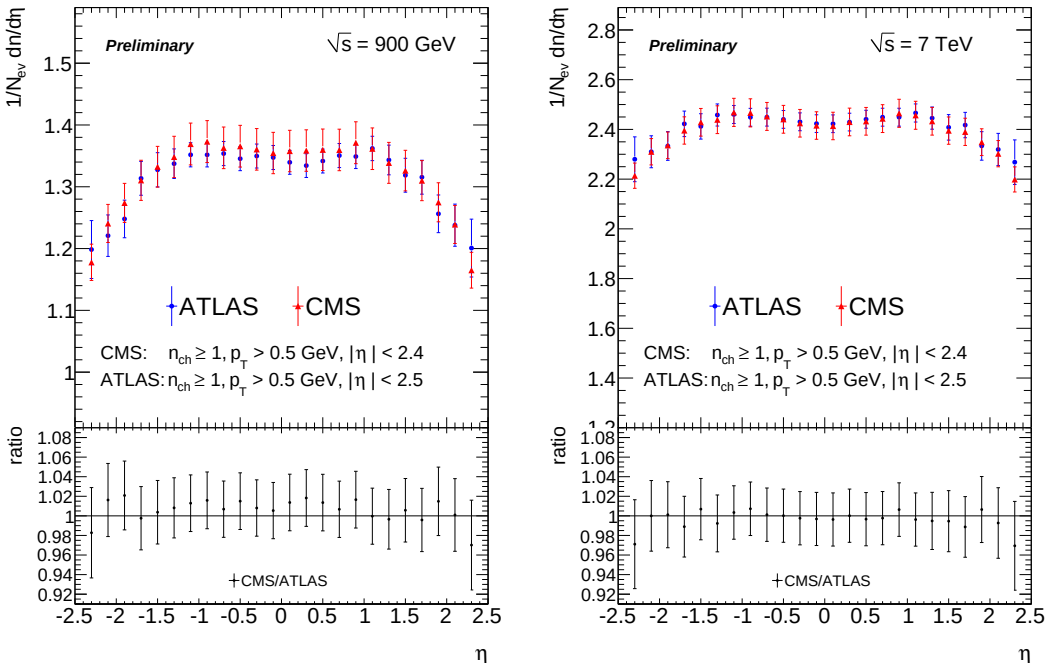

(a) (b)

Figure 7.23.: Comparisons of $1/N_{\mathrm{ev}} dN_{\mathrm{ch}}/d\eta$ measurements by CMS and ATLAS at $\sqrt{s} = 0.9$ TeV (a) and 7 TeV (b). The analysed phase-space regions are not exactly the same, differing in the the η-coverage of $2.4 < |\eta| < 2.5$. In contrast to the common plots, these measurements extend to the full η range of the experiments.

8. Summary and Conclusions

In low luminosity phases of LHC operation when the luminosity ranges from $\mathcal{L} = 10^{27}$ to 10^{31} cm^{-2}s^{-1}, minimum bias triggers are crucial for the selection of beam collision events. ATLAS has two minimum bias trigger systems available. In this thesis, one of them has been developed, used for data-taking over the entire low luminosity phase in 2009 and 2010 and data of both minimum bias triggers have been analysed.

The Inner Detector Minimum Bias Trigger (mbSpTrk), based on design studies described in Ref. [1], was successfully set up for triggering proton-proton interactions with the ATLAS detector right from the machine start-up. It uses at Level-1 a random trigger and identifies beam activity in the Inner Detector by hit-counting algorithms at Level-2. In order to remain flexible during periods of varying machine background, another selection step was added at the Event Filter. If necessary, one can suppress beam-gas events at that level. Therefore, a dedicated minimum bias trigger configuration for tracking was derived with which tracks down to $p_{\mathrm{T}} = 200$ MeV are reconstructed. This ensured that signal events, bunch-crossings with any type of proton-proton interactions, can be identified and selected with a high efficiency. The good vacuum conditions over the full period during which the trigger was actively used, permitted to disable this functionality for the entire 2010 data-taking.

Redundancy of the trigger functionality to reject empty bunch-crossing events was stressed during the development. Several possibilities were studied which can potentially give a handle on electronic noise. Quantities are exploited specific to the used sub-detectors like time-over-threshold of a pixel cluster or the coincidence of silicon strips to suppress the formation of noise hits. This leads to several options in the trigger to efficiently suppress empty bunch-crossing events. Different benchmark trigger modes were investigated with data taken in 2009 and 2010 and results were summarised in Table 5.2. A relative simple mode turned out to be also one of the most efficient ones. By requiring that more than three pixel clusters with a time-over-threshold longer than 20 BC (1 BC, bunch-crossing, is a time window of 25 ns) and more than three SCT spacepoints, the trigger rejects (99.87 $\pm$ 0.01) % of empty events. This trigger mode had been used for the entire time the trigger actively selects. However, to further reduce possible bias its trigger thresholds were adapted to the effective noise level at Level-2. Nevertheless, this was done on a time scale which provided stable trigger configuration over several months.

A further emphasis for the trigger was *robustness*. When modules in the silicon detectors fail by becoming noisy, the trigger may record events of bad quality. Usually, this is avoided by so-called noise-masks which exist for the Pixel and SCT detectors. These are part of the system configuration in which the noisy channels, modules and front-end chips are blocked from the readout. Only for the case when a new module becomes noisy

during triggering an internal protection can be useful and was therefore implemented. The problematic module is dynamically identified through a unreasonable high number of produced hits and is excluded in the trigger decision. However, such cases never occurred and were also meant to be highly unlikely [134]. Thus, mbSpTrk was deployed for online recording and could be run stable without operational problems. This is as well a result of thorough validation before LHC operation with beam has started.

The complementary nature of the high-level minimum bias trigger mbSpTrk and the Level-1 Minimum Bias Trigger Scintillators, MBTS, made it possible to measure their trigger performance from data. In particular, the selection efficiency and bias of both triggers were studied. The results are specific to the phase-space region and were driven by the analysis of general properties of charged particle multiplicities [41, 46]. The most inclusive studied phase-space region includes tracks with a p_{T} down to $p_{\mathrm{T}} = 100$ MeV of which at least two with $|\eta| < 2.5$ had to be present. The trigger efficiency of mbSpTrk was measured at $\sqrt{s} = 7$ TeV relative to several reference triggers and showed no inefficiency within the used statistics. Measurements of the selection efficiency with respect to a pure random trigger yielded at 68.3 % C.L. a lower limit of 95.0 %. A much better statistical precision is obtained when an MBTS trigger, L1_MBTS_1 or L1_MBTS_2, are used to provide the reference sample. The lower limit of the mbSpTrk trigger efficiency for events with two selected tracks is then

$$\begin{aligned} \epsilon_{\mathsf{mbSpTrk|L1\_MBTS\_1}} &\geq 99.96\ \% \\ \epsilon_{\mathsf{mbSpTrk|L1\_MBTS\_2}} &\geq 99.999\ \% \end{aligned}$$

at 68.3 % C.L. and higher for higher track multiplicities. The performance of MBTS was studied in detail in a similar way, using mbSpTrk as the reference trigger. In the same phase-space as mentioned above, the efficiency of L1_MBTS_1 was measured to

$$\epsilon_{\mathsf{L1\_MBTS\_1|mbSpTrk}} = 97.2 \pm 0.5\ (\mathrm{syst}) \pm 0.1\ (\mathrm{stat})\ \%$$

at $\sqrt{s} = 7$ TeV. The efficiency at $\sqrt{s} = 0.9$ TeV was found to be very similar. MBTS in its loosest configuration does not introduce any significant bias in p_{T} and η. A small, but still negligible bias was found in p_{T}. However, it becomes more significant as soon as more scintillator counters are required to fire. The data-driven method used for determining the trigger efficiency was a relevant part in measurements of general properties of charged particle production. Such analyses were performed emphasizing to introduce only minimal Monte Carlo model dependencies. These trigger studies were used in several ATLAS analyses, amongst them the first publication early 2010 [46]. Further measurements of inclusive charged particle spectra also use these data driven results [41, 115, 116, 124, 135].

In the second part of this thesis an analysis of charged particle multiplicities was performed. Following the strategy of introducing only minimal MC model dependencies in the analysis, four distributions were studied that characterise properties of charged particles. These were the charged particle multiplicity distribution, pseudorapidity and p_{T}-spectra and the correlation between $\langle p_{\mathrm{T}} \rangle$ and the number of charged particles. Often,

one refers to them as "Minimum Bias (MB) distributions". Two phase-space regions were considered at both centre-of-mass energies $\sqrt{s} = 0.9$ and 7 TeV, defined by the presence of at least one charged particle with $|\eta| < 0.8$ and $p_{\mathrm{T}} > 0.5$ or 1 GeV, respectively.

A typical value to compare to other measurements is the charged particle density at $\eta = 0$. For the phase-space region with $p_{\mathrm{T}} > 0.5$ GeV at $\sqrt{s} = 0.9$ TeV, this was measured to be 1.809 ± 0.006 (stat) ± 0.030 (syst). All measurements were also compared to the Monte Carlo generator PYTHIA and PHOJET and several tunes of PYTHIA. One of them is the PYTHIA tune AMBT1 that reflects already first ATLAS measurements of charged particle multiplicities and the underlying event [45]. The comparisons of measurements to Monte Carlo models show that currently none of them is able to reproduce the ensemble of MB distributions of centrally produced charged particles. Nevertheless, PYTHIA8 and AMBT1 achieve relative good agreement in certain distributions. A few problems persist however, when discrepancies surpass e.g. 50 % in the high p_{T} tails – independent of phase-space and energy.

The ATLAS, CMS and ALICE Collaboration have agreed to perform a first common analysis of charged particle multiplicities in two well-defined phase-space regions to which the results obtained in this thesis represent the ATLAS contribution. So far measurements of the charged particle multiplicity as function of pseudorapidity exist from all three experiments at both centre-of-mass energies. The comparison of these results reveal that measurements are performed with a detailed understanding of the rather complex tracking devices. All three experiments provided measurement points with a precision of around 2 to 3 % dominated by systematic effects. Overall, an excellent agreement is found between the three experiments, confirming independently the measurements of each other. It will be exciting to compare of the remaining distributions, since more complex unfolding methods are involved in the other distributions.

The presented measurements can, like previous analyses [41, 46], be used to produce new tunes of Monte Carlo generators and improve their models of soft inelastic scattering processes. Once such a model can describe the new LHC data consistently with previous measurements, such measurements may eventually lead to a more fundamental approach of the description of soft particle production.

Appendix

A. Error Calculation for Trigger Efficiencies

Statistical uncertainties of trigger efficiencies have been calculated in this thesis based on the Bayesian approach. This problem is discussed in [136, 137] and summarised here.

A.1. Binominal Errors

The usual approach to compute efficiencies and the associated statistical uncertainties is to treat n events out of a sample of N as a binominally distributed variable. The binominal probability distribution is

$$P(n|N,\epsilon) = \frac{N!}{n!(N-n)!}\epsilon^n(1-\epsilon)^{N-n} \tag{A.1}$$

with ϵ the selection efficiency which is estimated by taking the ratio of n/N. The variance associated with it is

$$\sigma_\epsilon^2 = \frac{\epsilon\,(1-\epsilon)}{N}. \tag{A.2}$$

This approach however leads to underestimated uncertainties when efficiencies are close to 0 or 1, producing for example zero uncertainty on the estimated ϵ if $n = N$. An alternative approach which avoids such drawbacks uses the Bayesian Theorem.

A.2. Bayesian Method

The Bayesian Theorem relates conditional probabilities in the following way. If P(A) is the probability of a condition A, and for condition B the probability is P(B) then the conditional probabilities, P(A|B) and P(B|A), meaning a probability of A taking place given B and vice versa respectively, relate to

$$P(A|B) = \frac{P(B|A)\cdot P(A)}{P(B)} \tag{A.3}$$

P(A) is the **prior probability distribution** signifiying a probability of A without prior assumptions, same is true for P(B). P(B|A) is a **likelihood function** interpreted as the probability that, under the assumption of A, B is observed. Their product is proportional to the **posterior probability function** P(A|B) that is the probability A is correct given B. Applying this theorem to the context of efficiency calculation one

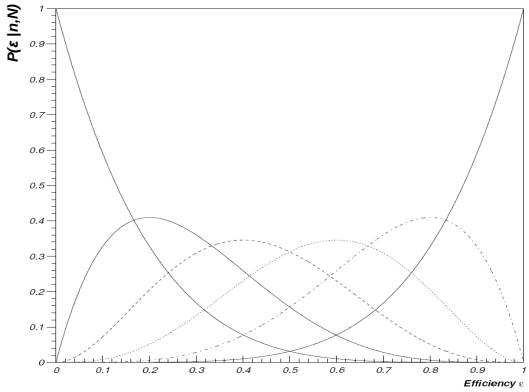

Figure A.1.: Post-data probability distribution for the efficiency ϵ, $N = 5$ and $n = 0, 1, 2, 3, 4, 5$ taken from [137].

obtains an equation for the probability of the true efficiency ϵ with Eq.(A.3) becoming

$$P(\epsilon|n, N) = \frac{P(n|N, \epsilon) \cdot P(\epsilon)}{\int P(n|N, \epsilon) \cdot P(\epsilon)\delta\epsilon} \tag{A.4}$$

The process of obtaining n out of N events selected is still an binominal process and P(n|N, ϵ) is given by Eg.(A.1). In Bayesian statistics however there is no unique prescription to determine the prior P(ϵ). For the case of the efficiency, we know the efficiency must be in the inclusive range [0,1]. No further prior knowledge is available and therefore a uniform prior between 0 an 1:

$$P(\epsilon) = \begin{cases} 1 & \text{if } 0 \leq \epsilon \leq 1, \\ 0 & \text{else.} \end{cases}$$

It remains to compute the normalisation factor in Eq.(A.4) for which one has to integrate

$$\begin{aligned} \int P(n|N, \epsilon) \cdot P(\epsilon)\, \delta\epsilon &= \frac{N!}{n!(N-n)!} \int_0^1 \epsilon^n (1-\epsilon)^{N-n} \delta\epsilon \\ &= 1. \end{aligned}$$

Using the Beta function $B(x, y) = \int_0^1 t^{x-1}(1-t)^{y-1}dt = \Gamma(x)\Gamma(y)/\Gamma(x+y)$ the result of Eq.(A.4) is

$$P(\epsilon|n, N) = \frac{\Gamma(N+2)}{\Gamma(n+1)\Gamma(N-n+1)} \epsilon^n (1-\epsilon)^{N-n} \tag{A.5}$$

The most probably value of ϵ given the data is the maximum of Eq.(A.5), illustrated for a few values of n in Fig. A.1. One can see that the uncertainties around the maxmimum will be generally asymmetric for a certain confidence interval. The definition of an associated confidence interval with a certain probability content is given by the area

below the posterior probability. Numerical solutions as used in this thesis compute the shortest interval containing 68.3 % of the probability[1]. This confidence level has a well known probability content which is the same as a "1σ" Gaussian error.

[1] This is implemented in the ROOT function `TGraphAsymmErrors::BayesDivide` [94].

B. Binning, Additional Plots and Tables for Common LHC Analysis

B.1. Binning

In order to maximise the direct comparisons of the common analysed phase-space regions it is most useful if ATLAS, CMS and ALICE apply the same binning for all distributions. First agreements were made on the pseudorapidity distributions and comparisons could directly be made. To be able to make similar comparisons with other distributions the binning in Table B.1 is suggested for the multiplicity and p_{T}-axes (their ranges may be extended if the statistics of the other experiments allow).

B.2. Additional Plots

For a better visibility, the measurements presented in Section 7.2 are shown comparing only two of the experiments: ATLAS and ALICE in Fig. B.1, ATLAS and CMS in Fig. B.2 and also ALICE and CMS in Fig. B.3.

B.3. Data Tables of $1/N_{\mathrm{ev}} \cdot \mathrm{d}N_{\mathrm{ch}}/\mathrm{d}\eta$ for ATLAS, CMS and ALICE

For a detailed view on the compared measurements, the absolute values, the statistical and systematical uncertainties of the $1/N_{\mathrm{ev}} \cdot \mathrm{d}N_{\mathrm{ch}}/\mathrm{d}\eta$ measurements of ATLAS, CMS and ALICE are given below.

Table B.1.: Common binning for LHC Analysis.

$n_{\mathrm{ch}} \geq 1$, $\lvert\eta\rvert < 0.8$, $p_{\mathrm{T}} > 0.5$ GeV		$n_{\mathrm{ch}} \geq 1$, $\lvert\eta\rvert < 0.8$, $p_{\mathrm{T}} > 1$ GeV	
bin range	bin width	bin range	bin width
multiplicity-axis at $\sqrt{s} = 0.9$ TeV			
0.5 − 14.5	1	0.5 − 10.5	1
14.5 − 20.5	2	10.5 − 12.5	2
multiplicity-axis at $\sqrt{s} = 7$ TeV			
0.5 − 26.5	1	0.5 − 10.5	1
26.5 − 34.5	2	10.5 − 14.5	2
34.5 − 42.5	4	14.5 − 22.5	4
42.5 − 50.5	8	22.5 − 30.5	8
p_{T}-axis [GeV] at $\sqrt{s} = 0.9$ TeV			
0.5 − 2.5	0.1	1 − 2.5	0.1
2.5 − 3.5	0.25	2.5 − 10	see other
3.5 − 4.0	0.5		phase-space
4.0 − 6.0	1		region
6.0 − 10	2		
p_{T}-axis [GeV] at $\sqrt{s} = 7$ TeV			
0.5 − 2.5	0.1	1.0 − 2.5	0.1
2.5 − 3.5	0.25	2.5 − 30	see other
3.5 − 4.0	0.5		phase-space
4 − 6	1		region
6 − 10	2		
10 − 20	5		
20 − 30	10		

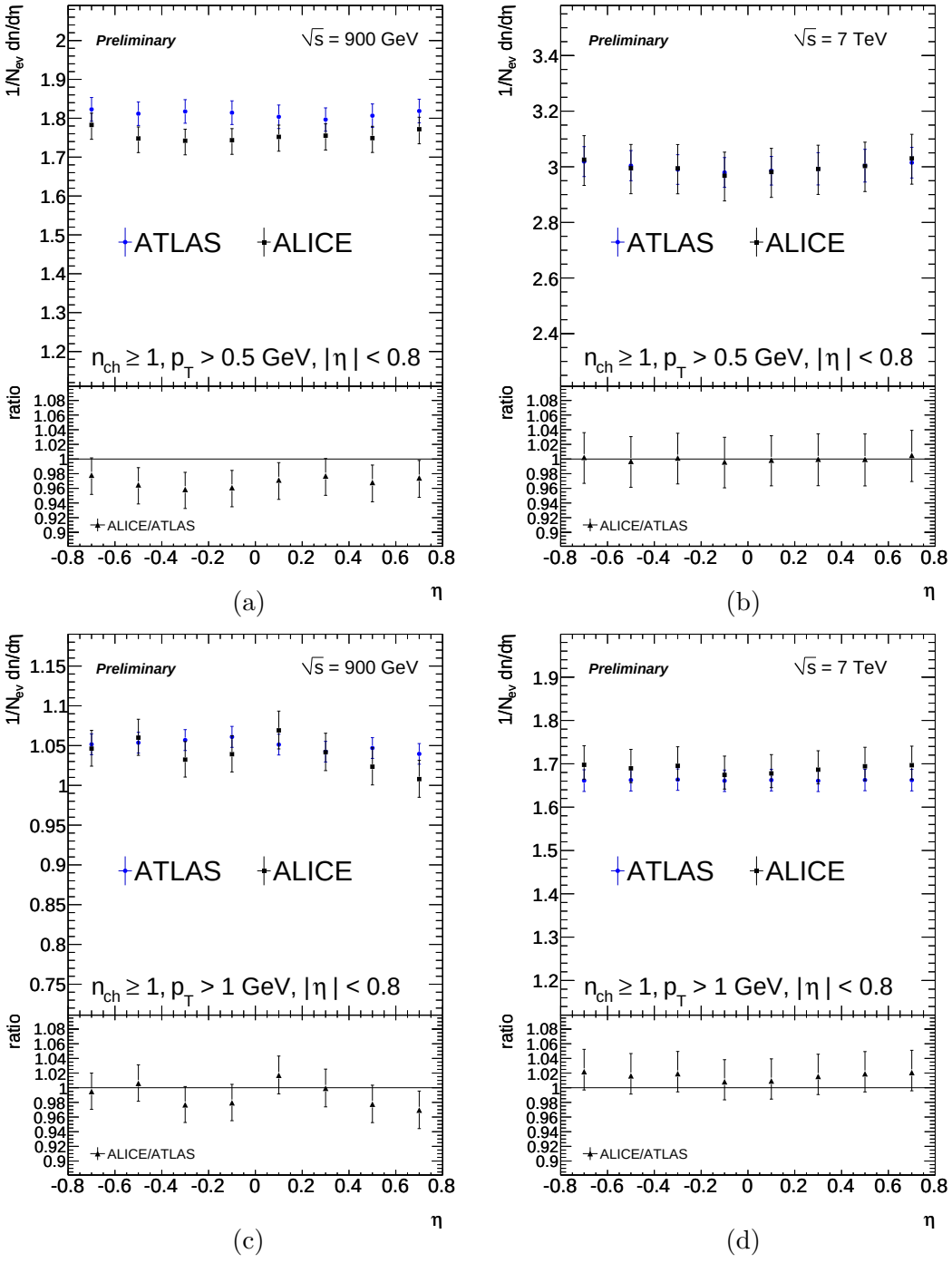

Figure B.1.: Comparisons of $1/N_{\mathrm{ev}} dN_{\mathrm{ch}}/d\eta$ measurements by ATLAS and ALICE [132] at $\sqrt{s} = 0.9$ TeV (a,c) and 7 TeV (b,d) in indicated phase-space regions. The error bars in the top pads show the total uncertainty. The bottom shows ratios with the respective uncertainties added in quadrature.

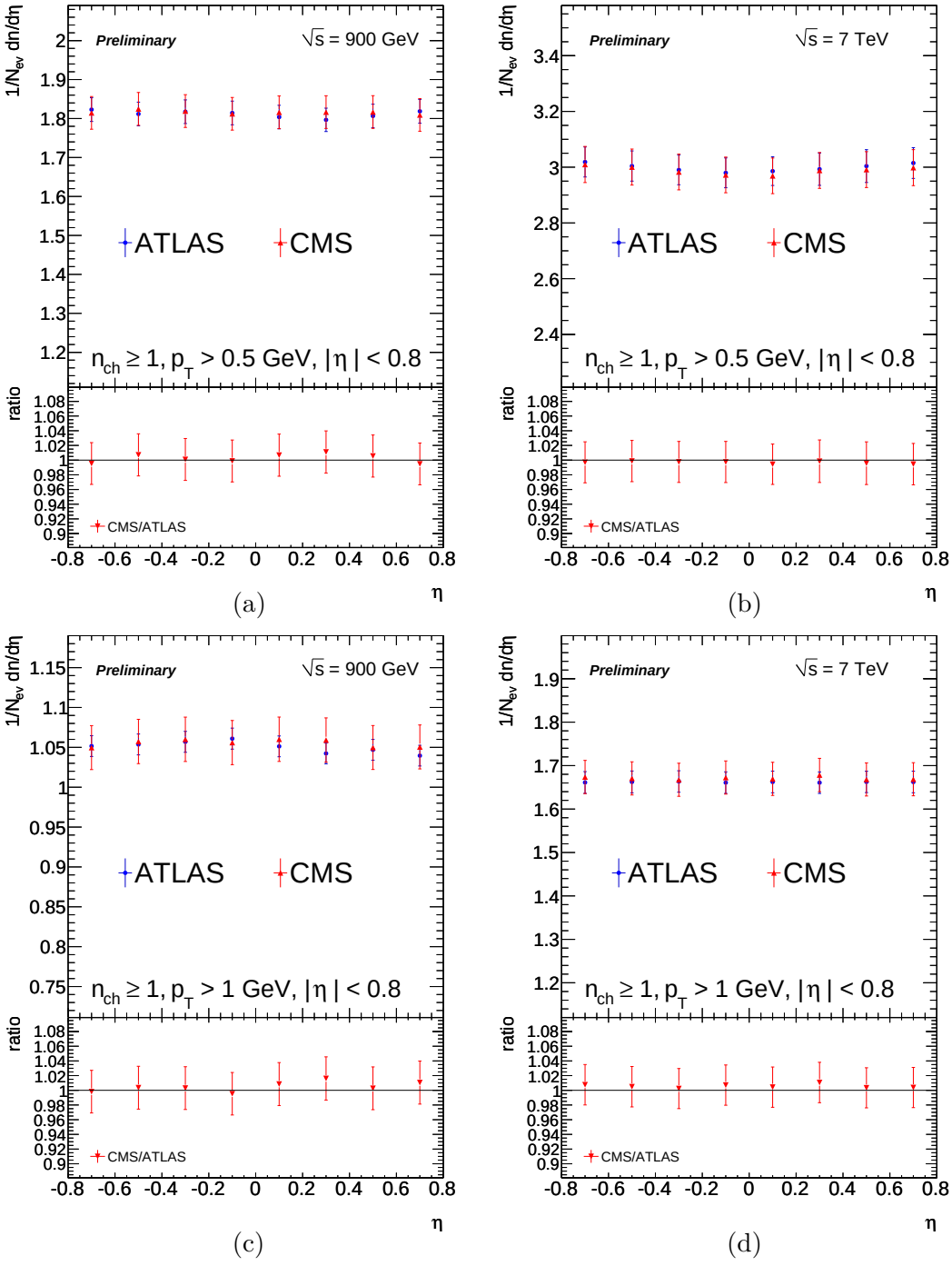

Figure B.2.: Comparisons of $1/N_{\mathrm{ev}} dN_{\mathrm{ch}}/d\eta$ measurements by ATLAS and CMS [133] at $\sqrt{s} = 0.9$ TeV (a,c) and 7 TeV (b,d) in the indicated phase-space regions. The error bars in the top pads show the total uncertainty. The bottom shows ratios with the respective uncertainties added in quadrature.

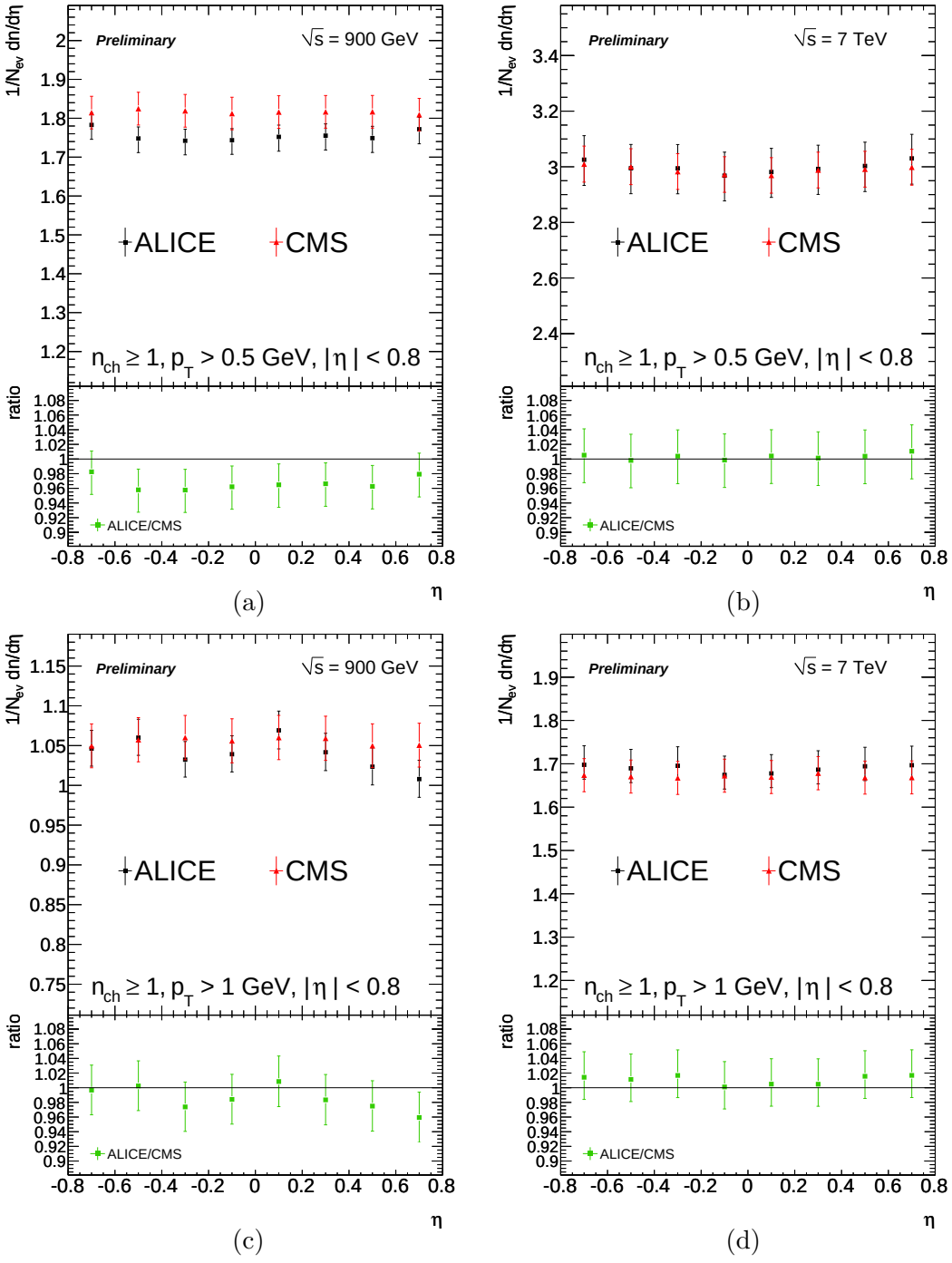

Figure B.3.: Comparisons of $1/N_{\mathrm{ev}} dN_{\mathrm{ch}}/d\eta$ measurements by ALICE [132] and CMS [133] at $\sqrt{s} = 0.9$ TeV (a,c) and 7 TeV (b,d) in the indicated phase-space regions. The error bars in the top pads show the total uncertainty. The bottom shows ratios with the respective uncertainties added in quadrature.

Table B.2.: ATLAS data of $1/N_{\mathrm{ev}} \cdot \mathrm{d}N_{\mathrm{ch}}/\mathrm{d}\eta$.

η	$1/N_{\mathrm{ev}} \cdot \mathrm{d}N_{\mathrm{ch}}/\mathrm{d}\eta$	total	stat.	syst.
ATLAS at $\sqrt{s} = 0.9$ TeV				
$n_{\mathrm{ch}} \geq 1$, $\lvert\eta\rvert < 0.8$, $p_{\mathrm{T}} > 0.5$ GeV				
-0.7	1.823	0.030	0.006	0.030
-0.5	1.812	0.030	0.006	0.030
-0.3	1.817	0.030	0.006	0.030
-0.1	1.814	0.030	0.006	0.030
0.1	1.804	0.030	0.006	0.030
0.3	1.797	0.030	0.006	0.029
0.5	1.807	0.030	0.006	0.030
0.7	1.819	0.030	0.006	0.030
ATLAS at $\sqrt{s} = 7$ TeV				
$n_{\mathrm{ch}} \geq 1$, $\lvert\eta\rvert < 0.8$, $p_{\mathrm{T}} > 0.5$ GeV				
-0.7	3.019	0.054	0.0015	0.054
-0.5	3.004	0.054	0.0015	0.054
-0.3	2.99	0.053	0.0015	0.053
-0.1	2.98	0.054	0.0015	0.053
0.1	2.986	0.051	0.0015	0.051
0.3	2.993	0.058	0.0014	0.058
0.5	3.004	0.059	0.0015	0.059
0.7	3.015	0.055	0.0015	0.055
ATLAS at $\sqrt{s} = 0.9$ TeV				
$n_{\mathrm{ch}} \geq 1$, $\lvert\eta\rvert < 0.8$, $p_{\mathrm{T}} > 1$ GeV				
-0.7	1.052	0.013	0.007	0.011
-0.5	1.054	0.013	0.007	0.011
-0.3	1.057	0.013	0.007	0.011
-0.1	1.061	0.013	0.007	0.011
0.1	1.051	0.013	0.007	0.011
0.3	1.042	0.013	0.007	0.011
0.5	1.047	0.013	0.007	0.011
0.7	1.040	0.013	0.007	0.011
ATLAS at $\sqrt{s} = 7$ TeV				
$n_{\mathrm{ch}} \geq 1$, $\lvert\eta\rvert < 0.8$, $p_{\mathrm{T}} > 1$ GeV				
-0.7	1.661	0.025	0.0014	0.025
-0.5	1.662	0.025	0.0014	0.025
-0.3	1.663	0.025	0.0014	0.025
-0.1	1.661	0.025	0.0014	0.025
0.1	1.662	0.025	0.0014	0.025
0.3	1.661	0.025	0.0014	0.025
0.5	1.663	0.025	0.0014	0.025
0.7	1.662	0.025	0.0014	0.025

Table B.3.: CMS data of $1/N_{\mathrm{ev}} \cdot \mathrm{d}N_{\mathrm{ch}}/\mathrm{d}\eta$ [133].

η	$1/N_{\mathrm{ev}} \cdot \mathrm{d}N_{\mathrm{ch}}/\mathrm{d}\eta$	total	stat.	syst.
CMS at $\sqrt{s} = 0.9$ TeV				
$n_{\mathrm{ch}} \geq 1$, $\lvert\eta\rvert < 0.8$, $p_{\mathrm{T}} > 0.5$ GeV				
-0.7	1.814	0.042	0.0020	0.042
-0.5	1.825	0.042	0.0020	0.042
-0.3	1.819	0.042	0.0020	0.042
-0.1	1.812	0.042	0.0020	0.042
0.1	1.816	0.042	0.0020	0.042
0.3	1.816	0.042	0.0020	0.042
0.5	1.817	0.042	0.0020	0.042
0.7	1.809	0.042	0.0020	0.042
CMS at $\sqrt{s} = 7$ TeV				
$n_{\mathrm{ch}} \geq 1$, $\lvert\eta\rvert < 0.8$, $p_{\mathrm{T}} > 0.5$ GeV				
-0.7	3.010	0.065	0.007	0.064
-0.5	3.000	0.065	0.007	0.064
-0.3	2.983	0.064	0.007	0.064
-0.1	2.972	0.064	0.007	0.064
0.1	2.969	0.064	0.007	0.064
0.3	2.988	0.064	0.007	0.064
0.5	2.991	0.064	0.007	0.064
0.7	2.998	0.065	0.007	0.064
CMS at $\sqrt{s} = 0.9$ TeV				
$n_{\mathrm{ch}} \geq 1$, $\lvert\eta\rvert < 0.8$, $p_{\mathrm{T}} > 1$ GeV				
-0.7	1.050	0.028	0.0021	0.027
-0.5	1.057	0.028	0.0021	0.028
-0.3	1.060	0.028	0.0021	0.028
-0.1	1.056	0.028	0.0021	0.028
0.1	1.060	0.028	0.0021	0.028
0.3	1.059	0.028	0.0021	0.028
0.5	1.050	0.028	0.0021	0.027
0.7	1.051	0.028	0.0021	0.027
CMS at $\sqrt{s} = 7$ TeV				
$n_{\mathrm{ch}} \geq 1$, $\lvert\eta\rvert < 0.8$, $p_{\mathrm{T}} > 1$ GeV				
-0.7	1.674	0.038	0.006	0.038
-0.5	1.671	0.038	0.006	0.038
-0.3	1.667	0.038	0.006	0.038
-0.1	1.673	0.038	0.006	0.038
0.1	1.670	0.038	0.006	0.038
0.3	1.678	0.038	0.006	0.038
0.5	1.668	0.038	0.006	0.038
0.7	1.669	0.038	0.006	0.038

Table B.4.: ALICE data of $1/N_{\mathrm{ev}} \cdot \mathrm{d}N_{\mathrm{ch}}/\mathrm{d}\eta$ [132].

η	$1/N_{\mathrm{ev}} \cdot \mathrm{d}N_{\mathrm{ch}}/\mathrm{d}\eta$	total	stat.	syst.
ALICE at $\sqrt{s} = 0.9$ TeV				
$n_{\mathrm{ch}} \geq 1$, $\lvert\eta\rvert < 0.8$, $p_{\mathrm{T}} >$ 0.5 GeV				
-0.7	1.783	$\pm^{0.037}_{0.030}$	0.016	$\pm^{0.033}_{0.026}$
-0.5	1.748	$\pm^{0.036}_{0.030}$	0.016	$\pm^{0.033}_{0.025}$
-0.3	1.742	$\pm^{0.036}_{0.030}$	0.016	$\pm^{0.033}_{0.025}$
-0.1	1.744	$\pm^{0.036}_{0.030}$	0.016	$\pm^{0.033}_{0.025}$
0.1	1.752	$\pm^{0.037}_{0.030}$	0.017	$\pm^{0.033}_{0.025}$
0.3	1.755	$\pm^{0.037}_{0.030}$	0.017	$\pm^{0.033}_{0.025}$
0.5	1.749	$\pm^{0.037}_{0.030}$	0.017	$\pm^{0.033}_{0.025}$
0.7	1.772	$\pm^{0.037}_{0.031}$	0.018	$\pm^{0.033}_{0.025}$
ALICE at $\sqrt{s} = 7$ TeV				
$n_{\mathrm{ch}} \geq 1$, $\lvert\eta\rvert < 0.8$, $p_{\mathrm{T}} >$ 0.5 GeV				
-0.7	3.026	$\pm^{0.086}_{0.093}$	0.004	$\pm^{0.086}_{0.092}$
-0.5	2.995	$\pm^{0.085}_{0.092}$	0.004	$\pm^{0.085}_{0.092}$
-0.3	2.994	$\pm^{0.085}_{0.092}$	0.004	$\pm^{0.085}_{0.092}$
-0.1	2.968	$\pm^{0.085}_{0.091}$	0.004	$\pm^{0.085}_{0.091}$
0.1	2.981	$\pm^{0.085}_{0.091}$	0.004	$\pm^{0.085}_{0.091}$
0.3	2.992	$\pm^{0.085}_{0.092}$	0.004	$\pm^{0.085}_{0.091}$
0.5	3.003	$\pm^{0.086}_{0.092}$	0.004	$\pm^{0.086}_{0.092}$
0.7	3.03	$\pm^{0.086}_{0.093}$	0.004	$\pm^{0.086}_{0.093}$
ALICE at $\sqrt{s} = 0.9$ TeV				
$n_{\mathrm{ch}} \geq 1$, $\lvert\eta\rvert < 0.8$, $p_{\mathrm{T}} >$ 1 GeV				
-0.7	1.046	$\pm^{0.022}_{0.023}$	0.019	$\pm^{0.012}_{0.013}$
-0.5	1.06	$\pm^{0.022}_{0.023}$	0.019	$\pm^{0.012}_{0.014}$
-0.3	1.032	$\pm^{0.022}_{0.023}$	0.018	$\pm^{0.012}_{0.013}$
-0.1	1.039	$\pm^{0.022}_{0.023}$	0.019	$\pm^{0.012}_{0.013}$
0.1	1.069	$\pm^{0.023}_{0.024}$	0.020	$\pm^{0.012}_{0.014}$
0.3	1.042	$\pm^{0.023}_{0.024}$	0.020	$\pm^{0.012}_{0.013}$
0.5	1.023	$\pm^{0.023}_{0.024}$	0.020	$\pm^{0.012}_{0.013}$
0.7	1.008	$\pm^{0.023}_{0.024}$	0.020	$\pm^{0.011}_{0.013}$
ALICE at $\sqrt{s} = 7$ TeV				
$n_{\mathrm{ch}} \geq 1$, $\lvert\eta\rvert < 0.8$, $p_{\mathrm{T}} >$ 1 GeV				
-0.7	1.698	$\pm^{0.044}_{0.033}$	0.004	$\pm^{0.044}_{0.033}$
-0.5	1.689	$\pm^{0.044}_{0.033}$	0.004	$\pm^{0.044}_{0.033}$
-0.3	1.695	$\pm^{0.044}_{0.033}$	0.004	$\pm^{0.044}_{0.033}$
-0.1	1.674	$\pm^{0.043}_{0.033}$	0.004	$\pm^{0.043}_{0.032}$
0.1	1.678	$\pm^{0.043}_{0.033}$	0.004	$\pm^{0.043}_{0.033}$
0.3	1.686	$\pm^{0.044}_{0.033}$	0.004	$\pm^{0.043}_{0.033}$
0.5	1.694	$\pm^{0.044}_{0.033}$	0.004	$\pm^{0.044}_{0.033}$
0.7	1.697	$\pm^{0.044}_{0.033}$	0.004	$\pm^{0.044}_{0.033}$

C. Data Points of ATLAS Results for Common LHC Analysis

For direct comparison with measurements performed in the same phase-space regions at the same energies, the data points of the results of this thesis are listed here. The date points of the measurements at $\sqrt{s} = 0.9$ TeV are in Table C.1 to C.8, data points at $\sqrt{s} = 7$ TeV are in Table C.2 to C.10.

Table C.1.: ATLAS data points of $1/N_{\mathrm{ev}} \cdot \mathrm{d}N_{\mathrm{ev}}/\mathrm{d}n_{\mathrm{ch}} \equiv \mathrm{Y}$ at $\sqrt{s} = 0.9$ TeV.

$n_{\mathrm{ch}} \geq 1$, $\lvert\eta\rvert < 0.8$, $p_{\mathrm{T}} > 0.5$ GeV				
n_{ch}	Y	total	stat.	syst.
1	0.3486	0.0044	0.0011	0.0043
2	0.2266	0.0014	0.0009	0.0010
3	0.1436	0.0007	0.0007	0.0001
4	0.09457	0.00085	0.00060	0.00060
5	0.06324	0.00094	0.00049	0.00080
6	0.04183	0.00092	0.00040	0.00083
7	0.02802	0.00077	0.00033	0.00070
8	0.01844	0.00058	0.00027	0.00052
9	0.01223	0.00050	0.00022	0.00045
10	0.00819	0.00043	0.00018	0.00039
11	0.00530	0.00033	0.00014	0.00030
12	0.00342	0.00024	0.00011	0.00021
13	0.00219	0.00018	0.00009	0.00015
14	0.00141	0.00013	0.00007	0.00011
14.5 - 16.5	0.000728	0.000073	0.000037	0.000063
16.6 - 18.5	0.000282	0.000036	0.000023	0.000027
18.5 - 20.5	0.000109	0.000018	0.000014	0.000011
$n_{\mathrm{ch}} \geq 1$, $\lvert\eta\rvert < 0.8$, $p_{\mathrm{T}} > 1$ GeV				
n_{ch}	Y	total	stat.	syst.
1	0.61177	0.0041	0.0021	0.0034
2	0.22510	0.0014	0.0014	0.0003
3	0.09196	0.0015	0.0009	0.0013
4	0.03963	0.0010	0.0006	0.0008
5	0.01727	0.00068	0.00038	0.00056
6	0.00784	0.00034	0.00026	0.00022
7	0.00354	0.00026	0.00017	0.00019
8	0.00149	0.00015	0.00011	0.00010
9	0.000744	0.000088	0.000079	0.000038
10	0.000354	0.000061	0.000054	0.000027
10.5 - 12.5	0.000115	0.000023	0.000022	0.000009

Table C.2.: ATLAS data points of $1/N_{\mathrm{ev}} \cdot \mathrm{d}N_{\mathrm{ev}}/\mathrm{d}n_{\mathrm{ch}} \equiv \mathsf{Y}$ at $\sqrt{s} = 7$ TeV in PS1.

$n_{\mathrm{ch}} \geq 1$, $\lvert\eta\rvert < 0.8$, $p_{\mathrm{T}} > 0.5$ GeV				
n_{ch}	Y	total	stat.	syst.
1	0.23652	0.00286	0.00016	0.00286
2	0.16722	0.00139	0.00014	0.00138
3	0.12152	0.00067	0.00012	0.00066
4	0.09235	0.00037	0.00011	0.00036
5	0.072713	+0.00014, −0.00012	0.00010	+0.00010, −0.00008
6	0.058339	+0.00018, −0.00012	0.00009	+0.00016, −0.00009
7	0.04734	+0.00028, −0.00023	0.00008	+0.00027, −0.00022
8	0.03864	+0.00037, −0.00033	0.00007	+0.00036, −0.00032
9	0.03163	+0.00042, −0.00038	0.00006	+0.00041, −0.00038
10	0.02578	+0.00044, −0.00041	0.00006	+0.00044, −0.00041
11	0.02105	+0.00044, −0.00041	0.00005	+0.00044, −0.00041
12	0.01706	+0.00043, −0.00040	0.00005	+0.00043, −0.00039
13	0.01391	+0.00042, −0.00039	0.00004	+0.00042, −0.00039
14	0.01115	+0.00039, −0.00036	0.00004	+0.00038, −0.00036
15	0.00901	+0.00035, −0.00033	0.00003	+0.00035, −0.00032
16	0.0073	+0.00032, −0.00029	0.00003	+0.00031, −0.00029
17	0.00583	+0.00028, −0.00026	0.00003	+0.00028, −0.00026
18	0.00471	+0.00025, −0.00023	0.00002	+0.00025, −0.00023
19	0.00382	+0.00022, −0.00021	0.00002	+0.00022, −0.00021
20	0.00302	+0.00019, −0.00018	0.00002	+0.00019, −0.00018
21	0.00239	+0.00017, −0.00015	0.00002	+0.00017, −0.00015
22	0.00187	+0.00014, −0.00013	0.00002	+0.00014, −0.00013
23	0.00149	+0.00012, −0.00011	0.00001	+0.00012, −0.00011
24	0.001160	+0.000097, −0.000089	0.000012	+0.000096, −0.000088
25	0.000918	+0.000082, −0.000075	0.000011	+0.000081, −0.000074
26	0.000727	+0.000068, −0.000063	0.000010	+0.000067, −0.000062
26.5 - 28.5	0.000513	+0.000052, −0.000048	0.000006	+0.000052, −0.000048
28.5 - 30.5	0.000306	+0.000035, −0.000032	0.000004	+0.000035, −0.000032
30.5 - 32.5	0.000182	+0.000023, −0.000020	0.000003	+0.000022, −0.000020
32.5 - 34.5	0.000114	+0.000016, −0.000014	0.000003	+0.000016, −0.000014
34.5 - 38.5	0.000053	+0.000008, −0.000007	0.000001	+0.000008, −0.000007
38.5 - 42.5	0.0000159	+0.0000030, −0.0000026	0.0000007	+0.0000029, −0.0000025
42.5 - 50.5	0.00000397	+0.00000087, −0.00000074	0.00000025	+0.00000084, −0.00000069

Table C.3.: ATLAS data points of $1/N_{\mathrm{ev}} \cdot \mathrm{d}N_{\mathrm{ev}}/\mathrm{d}n_{\mathrm{ch}} \equiv \mathrm{Y}$ at $\sqrt{s} = 7$ TeV in PS2.

$n_{\mathrm{ch}} \geq 1$, $\lvert\eta\rvert < 0.8$, $p_{\mathrm{T}} > 1$ GeV				
n_{ch}	Y	total	stat.	syst.
1	0.41174	0.00358	0.00027	0.00357
2	0.21565	0.00092	0.00021	0.00090
3	0.13078	0.00022	0.00016	0.00014
4	0.08325	0.00052	0.00013	0.00050
5	0.05430	0.00065	0.00010	0.00064
6	0.03562	0.00067	0.00009	0.00067
7	0.02343	0.00058	0.00007	0.00058
8	0.01532	0.00047	0.00006	0.00047
9	0.01017	0.00038	0.00005	0.00038
10	0.00673	0.00029	0.00004	0.00029
10.5 - 12.5	0.00369	0.00019	0.00002	0.00019
12.5 - 14.5	0.00159	0.00010	0.00001	0.00010
14.5 - 18.5	0.000500	0.000041	0.000005	0.000041
18.5 - 22.5	0.000095	0.000010	0.000002	0.000010
22.5 - 30.5	0.0000104	0.0000015	0.0000005	0.0000014

Table C.4.: ATLAS data points of $1/N_{\rm ev}\, 1/2\pi p_{\rm T}\, {\rm d}^2 N_{\rm ch}/{\rm d}\eta {\rm d}p_{\rm T} \equiv$ Y at $\sqrt{s} = 0.9$ TeV in PS1.

$n_{\rm ch} \geq 1$, $\lvert\eta\rvert < 0.8$, $p_{\rm T} > 0.5$ GeV				
$p_{\rm T}$ [GeV]	Y	total	stat.	syst.
0.548 (bin: 0.5 - 0.6)	1.299	0.021	0.001	0.021
0.648 (bin: 0.6 - 0.7)	0.8076	0.0133	0.0009	0.0132
0.748 (bin: 0.7 - 0.8)	0.5182	0.0085	0.0007	0.0085
0.848 (bin: 0.8 - 0.9)	0.3433	0.0056	0.0005	0.0056
0.948 (bin: 0.9 - 1.0)	0.2290	0.0038	0.0004	0.0038
1.048 (bin: 1.0 - 1.1)	0.1569	0.0026	0.0003	0.0026
1.148 (bin: 1.1 - 1.2)	0.1094	0.0018	0.0003	0.0018
1.248 (bin: 1.2 - 1.3)	0.0768	0.0013	0.0002	0.0013
1.348 (bin: 1.3 - 1.4)	0.05495	0.00092	0.00016	0.00090
1.448 (bin: 1.4 - 1.5)	0.03993	0.00067	0.00013	0.00066
1.548 (bin: 1.5 - 1.6)	0.03007	0.00052	0.00011	0.00050
1.648 (bin: 1.6 - 1.7)	0.02154	0.00038	0.000088	0.00037
1.748 (bin: 1.7 - 1.8)	0.016594	0.00028	0.000074	0.00027
1.848 (bin: 1.8 - 1.9)	0.012471	0.00022	0.000061	0.00021
1.949 (bin: 1.9 - 2.0)	0.009571	0.00017	0.000051	0.00016
2.049 (bin: 2.0 - 2.1)	0.006976	0.00013	0.000042	0.00012
2.149 (bin: 2.1 - 2.2)	0.005507	0.000098	0.000036	0.000091
2.249 (bin: 2.2 - 2.3)	0.004434	0.000080	0.000030	0.000074
2.348 (bin: 2.3 - 2.4)	0.003479	0.000064	0.000026	0.000058
2.448 (bin: 2.4 - 2.5)	0.002768	0.000051	0.000023	0.000046
2.615 (bin: 2.5 - 2.75)	0.001802	0.000033	0.000014	0.000030
2.867 (bin: 2.75 - 3.0)	0.001118	0.000021	0.000010	0.000019
3.117 (bin: 3.0 - 3.25)	0.000647	0.000013	0.000080	0.000011
3.366 (bin: 3.25 - 3.5)	0.0004128	0.0000095	0.0000056	0.0000077
3.724 (bin: 3.5 - 4.0)	0.0002126	0.0000044	0.0000026	0.0000036
4.384 (bin: 4.0 - 5.0)	0.00006204	0.0000014	0.0000009	0.0000011
5.407 (bin: 5.0 - 6.0)	0.00001564	0.00000051	0.00000044	0.00000026
6.634 (bin: 6.0 - 8.0)	0.00000286	0.00000026	0.00000012	0.00000023
8.680 (bin: 8.0 - 10.0)	0.000000608	0.000000054	0.000000042	0.000000035

Table C.5.: ATLAS data points of $1/N_{\mathrm{ev}}\, 1/2\pi p_{\mathrm{T}}\, \mathrm{d}^2 N_{\mathrm{ch}}/\mathrm{d}\eta \mathrm{d}p_{\mathrm{T}} \equiv \mathrm{Y}$ at $\sqrt{s} = 0.9$ TeV in PS2.

$n_{\mathrm{ch}} \geq 1$, $\lvert\eta\rvert < 0.8$, $p_{\mathrm{T}} > 1$ GeV				
p_{T} [GeV]	Y	total	stat.	syst.
1.048 (bin: 1.0 - 1.1)	0.3448	0.0036	0.0007	0.0035
1.148 (bin: 1.1 - 1.2)	0.2411	0.0025	0.0006	0.0025
1.248 (bin: 1.2 - 1.3)	0.1697	0.0018	0.0005	0.0017
1.348 (bin: 1.3 - 1.4)	0.1215	0.0013	0.0004	0.0012
1.448 (bin: 1.4 - 1.5)	0.08829	0.00095	0.00029	0.00091
1.548 (bin: 1.5 - 1.6)	0.06651	0.00074	0.00024	0.00070
1.648 (bin: 1.6 - 1.7)	0.04763	0.00055	0.00020	0.00051
1.748 (bin: 1.7 - 1.8)	0.03671	0.00040	0.00016	0.00037
1.848 (bin: 1.8 - 1.9)	0.02759	0.00032	0.00013	0.00029
1.949 (bin: 1.9 - 2.0)	0.02117	0.00024	0.00011	0.00021
2.049 (bin: 2.0 - 2.1)	0.01543	0.00018	0.00009	0.00016
2.149 (bin: 2.1 - 2.2)	0.01218	0.00014	0.00008	0.00012
2.249 (bin: 2.2 - 2.3)	0.00981	0.00012	0.00007	0.00010
2.348 (bin: 2.3 - 2.4)	0.00769	0.00010	0.00006	0.00008
2.448 (bin: 2.4 - 2.5)	0.006123	0.000077	0.000050	0.000059
2.615 (bin: 2.5 - 2.75)	0.003986	0.000047	0.000030	0.000037
2.867 (bin: 2.75 - 3.0)	0.002474	0.000032	0.000023	0.000023
3.117 (bin: 3.0 - 3.25)	0.001430	0.000021	0.000017	0.000012
3.367 (bin: 3.25 - 3.5)	0.0009131	0.000014	0.000012	0.000007
3.724 (bin: 3.5 - 4.0)	0.0004703	0.0000068	0.0000058	0.0000035
4.384 (bin: 4.0 - 5.0)	0.0001372	0.0000023	0.0000020	0.0000012
5.407 (bin: 5.0 - 6.0)	0.00003459	0.00000095	0.00000097	0.00000021
6.634 (bin: 6.0 - 8.0)	0.00000633	0.00000062	0.00000026	0.00000056
8.680 (bin: 8.0 - 10.0)	0.000001345	0.00000012	0.00000009	0.00000008

Table C.6.: ATLAS data points of $1/N_{\mathrm{ev}}\, 1/2\pi p_{\mathrm{T}}\, \mathrm{d}^2 N_{\mathrm{ch}}/\mathrm{d}\eta \mathrm{d}p_{\mathrm{T}} \equiv \mathsf{Y}$ at $\sqrt{s} = 7$ TeV in PS1.

$n_{\mathrm{ch}} \geq 1$, $\lvert\eta\rvert < 0.8$, $p_{\mathrm{T}} > 0.5$ GeV				
p_{T} [GeV]	Y	total	stat.	syst.
0.548 (bin: 0.5 - 0.6)	1.8026	0.0335	0.0004	0.0335
0.648 (bin: 0.6 - 0.7)	1.1770	0.0216	0.0003	0.0216
0.748 (bin: 0.7 - 0.8)	0.7885	0.0148	0.0002	0.0148
0.848 (bin: 0.8 - 0.9)	0.5444	0.0099	0.0002	0.0099
0.948 (bin: 0.9 - 1.0)	0.3844	0.0071	0.0002	0.0071
1.048 (bin: 1.0 - 1.1)	0.2763	0.0051	0.0001	0.0051
1.148 (bin: 1.1 - 1.2)	0.2015	0.0037	0.0001	0.0037
1.248 (bin: 1.2 - 1.3)	0.1489	0.0027	0.0001	0.0027
1.348 (bin: 1.3 - 1.4)	0.1118	0.0021	0.0001	0.0021
1.448 (bin: 1.4 - 1.5)	0.0846	0.0016	0.0001	0.0016
1.548 (bin: 1.5 - 1.6)	0.06472	0.00119	0.00004	0.00119
1.649 (bin: 1.6 - 1.7)	0.04994	0.00092	0.00004	0.00092
1.749 (bin: 1.7 - 1.8)	0.03892	0.00073	0.00003	0.00073
1.849 (bin: 1.8 - 1.9)	0.03059	0.00057	0.00003	0.00057
1.949 (bin: 1.9 - 2.0)	0.02412	0.00045	0.00002	0.00045
2.049 (bin: 2.0 - 2.1)	0.01917	0.00036	0.00002	0.00036
2.149 (bin: 2.1 - 2.2)	0.01542	0.00029	0.00002	0.00028
2.249 (bin: 2.2 - 2.3)	0.01234	0.00023	0.00001	0.00023
2.349 (bin: 2.3 - 2.4)	0.01002	0.00019	0.00001	0.00019
2.449 (bin: 2.4 - 2.5)	0.00821	0.00015	0.00001	0.00015
2.617 (bin: 2.5 - 2.75)	0.00579	0.00011	0.00001	0.00011
2.867 (bin: 2.75 - 3.0)	0.003634	0.000067	0.000005	0.000067
3.118 (bin: 3.0 - 3.25)	0.002331	0.000043	0.000004	0.000043
3.368 (bin: 3.25 - 3.5)	0.001526	0.000028	0.000003	0.000028
3.725 (bin: 3.5 - 4.0)	0.000862	0.000016	0.000001	0.000016
4.226 (bin: 4.0 - 4.5)	0.000420	0.000008	0.000001	0.000008
4.730 (bin: 4.5 - 5.0)	0.000219	0.000004	0.000001	0.000004
5.428 (bin: 5.0 - 6.0)	0.0000942	0.0000018	0.0000003	0.0000018
6.435 (bin: 6.0 - 7.0)	0.0000341	0.0000007	0.0000001	0.0000006
7.441 (bin: 7.0 - 8.0)	0.0000143	0.0000004	0.0000001	0.0000003
8.455 (bin: 8.0 - 9.0)	0.00000659	0.00000063	0.00000004	0.00000063
9.448 (bin: 9.0 - 10.0)	0.00000345	0.00000046	0.00000003	0.00000046
11.708 (bin: 10.0 - 15.0)	0.000000832	0.000000088	0.000000006	0.000000087
16.887 (bin: 15.0 - 20.0)	0.0000000903	0.0000000094	0.0000000013	0.0000000093
23.362 (bin: 20.0 - 30.0)	0.0000000139	0.0000000016	0.0000000003	0.0000000015

Table C.7.: ATLAS data points of $1/N_{\mathrm{ev}}\, 1/2\pi p_{\mathrm{T}}\, \mathrm{d}^2 N_{\mathrm{ch}}/\mathrm{d}\eta \mathrm{d}p_{\mathrm{T}} \equiv \mathsf{Y}$ at $\sqrt{s} = 7$ TeV in PS2.

$n_{\mathrm{ch}} \geq 1$, $\lvert\eta\rvert < 0.8$, $p_{\mathrm{T}} > 0.5$ GeV				
p_{T} [GeV]	Y	total	stat.	syst.
1.048 (bin: 1.0 - 1.1)	0.4524	0.0067	0.0002	0.0067
1.148 (bin: 1.1 - 1.2)	0.3301	0.0050	0.0002	0.0050
1.248 (bin: 1.2 - 1.3)	0.2442	0.0036	0.0001	0.0036
1.348 (bin: 1.3 - 1.4)	0.1835	0.0028	0.0001	0.0028
1.448 (bin: 1.4 - 1.5)	0.1389	0.0021	0.0001	0.0021
1.548 (bin: 1.5 - 1.6)	0.1063	0.0016	0.0001	0.0016
1.649 (bin: 1.6 - 1.7)	0.0820	0.0012	0.0001	0.0012
1.749 (bin: 1.7 - 1.8)	0.0639	0.0010	0.0001	0.0010
1.849 (bin: 1.8 - 1.9)	0.05026	0.00076	0.00004	0.00076
1.949 (bin: 1.9 - 2.0)	0.03963	0.00059	0.00004	0.00059
2.049 (bin: 2.0 - 2.1)	0.03147	0.00047	0.00003	0.00047
2.149 (bin: 2.1 - 2.2)	0.02535	0.00038	0.00003	0.00038
2.249 (bin: 2.2 - 2.3)	0.02026	0.00030	0.00002	0.00030
2.349 (bin: 2.3 - 2.4)	0.01646	0.00025	0.00002	0.00025
2.449 (bin: 2.4 - 2.5)	0.01350	0.00021	0.00002	0.00020
2.617 (bin: 2.5 - 2.75)	0.00951	0.00014	0.00001	0.00014
2.867 (bin: 2.75 - 3.0)	0.005970	0.000089	0.000008	0.000089
3.118 (bin: 3.0 - 3.25)	0.003830	0.000057	0.000006	0.000057
3.368 (bin: 3.25 - 3.5)	0.002508	0.000038	0.000005	0.000038
3.725 (bin: 3.5 - 4.0)	0.001416	0.000021	0.000002	0.000021
4.226 (bin: 4.0 - 4.5)	0.000691	0.000010	0.000001	0.000010
4.730 (bin: 4.5 - 5.0)	0.0003594	0.0000055	0.0000009	0.0000055
5.428 (bin: 5.0 - 6.0)	0.0001546	0.0000024	0.0000004	0.0000023
6.435 (bin: 6.0 - 7.0)	0.0000559	0.0000012	0.0000002	0.0000012
7.441 (bin: 7.0 - 8.0)	0.00002347	0.00000045	0.00000013	0.00000044
8.455 (bin: 8.0 - 9.0)	0.00001083	0.00000052	0.00000007	0.00000052
9.448 (bin: 9.0 - 10.0)	0.00000568	0.00000020	0.00000005	0.00000019
11.708 (bin: 10.0 - 15.0)	0.00000137	0.00000013	0.00000001	0.00000013
6.887 (bin: 15.0 - 20.0)	0.000000148	0.000000014	0.000000002	0.000000014
23.362 (bin: 20.0 - 30.0)	0.0000000231	0.0000000025	0.0000000005	0.0000000024

Table C.8.: ATLAS data points of $\langle p_{\mathrm{T}} \rangle (n_{\mathrm{ch}}) \equiv \mathrm{Y}$ at $\sqrt{s} = 0.9$ TeV.

$n_{\mathrm{ch}} \geq 1$, $\lvert\eta\rvert < 0.8$, $p_{\mathrm{T}} > 0.5$ GeV				
n_{ch}	Y	total	stat.	syst.
1	0.806	0.017	0.004	0.016
2	0.836	0.017	0.004	0.017
3	0.864	0.018	0.004	0.017
4	0.889	0.018	0.005	0.018
5	0.910	0.019	0.005	0.018
6	0.927	0.020	0.006	0.019
7	0.941	0.020	0.007	0.019
8	0.955	0.021	0.008	0.019
9	0.966	0.021	0.009	0.019
10	0.976	0.022	0.011	0.020
11	0.985	0.024	0.013	0.020
12	0.995	0.025	0.016	0.020
13	1.007	0.028	0.019	0.020
14	1.020	0.031	0.023	0.021
14.5 - 16.5	1.036	0.031	0.022	0.021
16.5 - 18.5	1.078	0.042	0.035	0.024
18.5 - 20.5	1.120	0.061	0.056	0.024
$n_{\mathrm{ch}} \geq 1$, $\lvert\eta\rvert < 0.8$, $p_{\mathrm{T}} > 1$ GeV				
n_{ch}	Y	total	stat.	syst.
1	1.406	0.029	0.008	0.028
2	1.454	0.031	0.010	0.029
3	1.493	0.033	0.013	0.030
4	1.532	0.035	0.018	0.031
5	1.556	0.040	0.025	0.031
6	1.597	0.047	0.034	0.033
7	1.623	0.058	0.048	0.033
8	1.651	0.079	0.071	0.034
9	1.704	0.104	0.097	0.039
10	1.762	0.142	0.137	0.038
10.5 - 12.5	1.827	0.176	0.170	0.042

Table C.9.: ATLAS data points of $\langle p_{\mathrm{T}} \rangle (n_{\mathrm{ch}}) \equiv \mathrm{Y}$ at $\sqrt{s} = 7$ TeV in PS1.

$n_{\mathrm{ch}} \geq 1$, $\lvert\eta\rvert < 0.8$, $p_{\mathrm{T}} > 0.5$ GeV				
n_{ch}	Y	total	stat.	syst.
1	0.824	0.017	0.001	0.017
2	0.864	0.017	0.001	0.017
3	0.901	0.018	0.001	0.018
4	0.932	0.019	0.001	0.019
5	0.957	0.019	0.001	0.019
6	0.978	0.020	0.001	0.020
7	0.995	0.020	0.001	0.020
8	1.011	0.020	0.001	0.020
9	1.025	0.021	0.001	0.021
10	1.037	0.021	0.001	0.021
11	1.048	0.021	0.001	0.021
12	1.059	0.021	0.001	0.021
13	1.069	0.022	0.001	0.022
14	1.078	0.022	0.002	0.022
15	1.087	0.022	0.002	0.022
16	1.096	0.022	0.002	0.022
17	1.104	0.022	0.002	0.022
18	1.112	0.023	0.002	0.022
19	1.120	0.023	0.002	0.023
20	1.128	0.023	0.003	0.023
21	1.135	0.023	0.003	0.023
22	1.143	0.023	0.003	0.023
23	1.150	0.024	0.004	0.023
24	1.157	0.024	0.004	0.023
25	1.164	0.024	0.004	0.024
26	1.170	0.024	0.005	0.024
26.5 - 28.5	1.180	0.024	0.004	0.024
28.5 - 30.5	1.196	0.025	0.005	0.024
30.5 - 32.5	1.212	0.026	0.007	0.025
32.5 - 34.5	1.226	0.027	0.008	0.025
34.5 - 38.5	1.247	0.027	0.008	0.026
38.5 - 42.5	1.276	0.030	0.015	0.026
42.5 - 50.5	1.339	0.048	0.024	0.041

Table C.10.: ATLAS data points of $\langle p_{\mathrm{T}} \rangle (n_{\mathrm{ch}}) \equiv \mathrm{Y}$ at $\sqrt{s} = 7$ TeV in PS2.

$n_{\mathrm{ch}} \geq 1$, $\lvert\eta\rvert < 0.8$, $p_{\mathrm{T}} > 1$ GeV				
n_{ch}	Y	total	stat.	syst.
1	1.459	0.029	0.002	0.029
2	1.520	0.031	0.002	0.030
3	1.562	0.031	0.002	0.031
4	1.595	0.032	0.002	0.032
5	1.623	0.033	0.002	0.033
6	1.648	0.033	0.003	0.033
7	1.670	0.034	0.003	0.034
8	1.690	0.034	0.004	0.034
9	1.711	0.035	0.004	0.034
10	1.732	0.035	0.005	0.035
10.5 - 12.5	1.761	0.036	0.004	0.036
12.5 - 14.5	1.803	0.037	0.006	0.037
14.5 - 18.5	1.864	0.039	0.008	0.039
18.5 - 22.5	1.988	0.047	0.017	0.044
22.5 - 30.5	2.180	0.068	0.040	0.055

Bibliography

[1] R. Kwee. Studies for the Development of a Minimum Bias Trigger at Low Luminosities in the ATLAS-Experiment at the Large Hadron Collider. Diploma Thesis at Humboldt University of Berlin, Germany, July 2007.

[2] M.E. Peskin and D.V. Schroeder. *An Introduction to Quantum Field Theory.* ABP, 1st edition, 1995.

[3] K. Nakamura et al. 2010 Review of Particle Physics. *J. Phys.*, G 37(075021), January 2010.

[4] LHC Higgs Cross section Working Group. S. Dittmaier, C. Mariotti, G. Passarino, and R. Tanaka (ed.). Handbook of LHC Higgs Cross Sections: 1. Inclusive Observables. CERN-2011-002, arXiv:1101.0593, February 2011.

[5] The ATLAS Collaboration. G. Aad et al. Higgs Boson Searches using the $H \to WW^* \to l\nu l\nu$ Decay Mode with the ATLAS Detector at $\sqrt{s} = 7$ TeV. ATLAS-CONF-2011-005, March 2011.

[6] P.W. Higgs. Broken Symmetries and the Masses of Gauge Bosons. *Phys. Rev. Lett.*, 13(16), 1964.

[7] The ALEPH, DELPHI, L3 and OPAL Collaborations and the LEP Working Group for Higgs Boson Searches. HERA results and their impact the LHC. *Phys. Lett. B*, 565:61–75, 2003.

[8] C. Berger. *Elementarteilchenphysik.* Springer, 2nd edition, 2006.

[9] The ALEPH, CDF, D0, DELPHI, L3, OPAL and SLD Collaborations, the LEP Electroweak Working Group, the Tevatron Electroweak Working Group and the SLD electroweak and heavy flavour groups. Precision Electroweak Measurements and Constraints on the Standard Model. CERN-PH-EP/2008-020, arXiv:0811.4682, November 2008.

[10] B. Kilminster for the CDF and D0 Collaborations. Higgs searches at the Tevatron. *PoS(ICHEP 2010)*, July 2010.

[11] The ATLAS Collaboration. G. Aad et al. ATLAS Sensitivity Prospects for Higgs Boson Production at the LHC Running at 7, 8 or 9 TeV. ATL-PHYS-PUB-2010-015, November 2010.

[12] P. Sphicas. LHC 2010: Summary of the Odyssey So Far and Near-Term Prospects, February 2011. CERN Academic Training Lectures.

[13] The ATLAS Collaboration. G. Aad et al. Search for stable hadronising squarks and gluinos at the ATLAS experiment at the LHC. *Phys. Lett.*, B701:1–19, March 2011. arXiv:1103.1984.

[14] The CMS Collaboration. V. Khachatryan et al. Search for Supersymmetry in pp Collisions at 7 TeV in Events with Jets and Missing Transverse Energy. *Phys. Lett.*, B698:196–218, January 2011. arXiv:1101.1628.

[15] The H1, ZEUS Collaborations. F.D. Aaron, et al. Combined Measurement and QCD Analysis of the Inclusive ep Scattering Cross Sections at HERA. *J. High Energy Phys.*, 1001(109), 2010. arXiv:0911.0884.

[16] S. Catani et al. Qcd. CERN-TH/2000-131, CERN Workshop on SM Physics (and more) at the LHC, 1999.

[17] G. Dissertori, I. Knowels, and M. Schmelling. *Quantum Chromodynamics.* Oxford Press, 2nd edition, 2003.

[18] V. Barrone and E. Predazzi. *High-Energy Particle Diffraction.* Springer, 1st edition, 2002.

[19] The ATLAS Collaboration. G. Aad et al. Measurement of the Inelastic Proton-Proton Cross-Section at $\sqrt{s} = 7$ TeV with the ATLAS Detector. *Nat. Commun.*, 2(463), 2011. arXiv:1104.0326.

[20] S. Donnachie, G. Dosch, P. Landshoff and O. Nachtmann. *Pomeron Physics and QCD.* Cambridge Monographs on Particle Physics, Nuclear Physics ans Cosmology, 1st edition, 2002.

[21] P.D.B. Collins. *An Introduction to Regge Theory and High Energy Physics.* Cambridge University Press, 1st edition, 1977.

[22] V.N.Gribov, Y.L.Dokshitzer and J.Nyiri. *Strong Interactions of Hadrons at High Energies - Gribovs Lectures on Theoretical Physics.* Cambridge Monographs on Particle Physics, Nuclear Physics ans Cosmology, 1st edition, 2009.

[23] A. Donnachie and P.V. Landshoff. Total cross sections. *Phys. Lett.*, B296(227), 1992.

[24] Bechtel, F. *The Underlying Event in Proton Proton Collisions.* PhD thesis, Hamburg Universität, 2009.

[25] Z. Koba, H. Nielsen, and P. Olesen. Scaling of multiplicity distributions in high-energy hadron collisions. *Nucl. Phys.*, B40, 1972.

[26] The UA5 Collaboration. G.J. Alner et al. Scaling Violation Favouring High Multiplicity Events at 540 GeV CMS Energy. *Phys. Lett.*, B138, 1984. CERN-EP-84-04.

[27] The UA5 Collaboration. K. Alpgard et al. Particle Multiplicities in $p\bar{p}$ interactions at $\sqrt{s} = 540$ GeV. *Phys. Lett.*, B121(2,3), 1984.

[28] The CDF Collaboration. F. Abe et al. Measurement of Double Parton Scattering in $p\bar{p}$ Collisions at $\sqrt{s} = 1.8$ TeV. *Phys. Rev. Lett.*, 79(584), 1997.

[29] The CDF Collaboration. F. Abe et al. Study of four-jet events and evidence for double parton interactions in $p\bar{p}$ collisions at $\sqrt{s} = 1.8$ TeV. *Phys. Rev.*, D47(4857), 1993.

[30] The CDF Collaboration. F. Abe et al. Double parton scattering in $\bar{p}p$ collisions at $\sqrt{s} = 1.8$ TeV. *Phys. Rev.*, D56(3811), 1997.

[31] T. Sjöstrand, S. Menna, and P. Skands. Multiple Interactions and the Structure of Beam Remnants. *J. High Energy Phys.*, 2004:053, 2004. arXiv:hep-ph/0402078v2.

[32] T. Sjöstrand and M. van Zijl. A multiple-interaction model for the event structure in hadron collisions. *Phys.Rev.D*, 36(7), 1987.

[33] T.Sjöstrand, S. Menna, and P. Skands. *PYTHIA 6.4 Physics and Manual*, 2006. arXiv:hep-ph/0603175v2.

[34] A. Buckly et al. General-purpose event generators for LHC physics. arXiv:1101.2599, 2010.

[35] R. Engel. PHOJET *Manual*, 1997.

[36] A. Capella, U. Sukhatme, C.-I. Tan, and J. Tran Thanh Van. Dual parton model. *Phys.Rep.*, 236, 1994.

[37] T. Sjöstrand. Monte Carlo Generators for the LHC, 2005. CERN Academic Training Lectures.

[38] T. Sjostrand, S. Mrenna, and P. Skands. Brief introduction to pythia 8.1. *Comput. Phys. Comm.*, 178, 2008.

[39] M. Dobbs and J.B. Hansen. The HepMC C++ Monte Carlo event record for High Energy Physics. *Comput. Phys. Commun.*, 134, 2001.

[40] The ATLAS Collaboration. G. Aad et al. ATLAS Monte Carlo Tunes for MC09. 2010. ATL-PHYS-PUB-2010-002.

[41] The ATLAS Collaboration. G. Aad et al. Charged particle multiplicities in pp interactions measured with the ATLAS detector at the LHC. *New J. Phys.*, 13 (053033), May 2011. arXiv:1012.5104v2.

[42] M. Campanelli et al. Monte Carlo Models for Minimum Bias Analysis at $\sqrt{s} =$ 0.9 TeV. Internal ATLAS Note ATL-PHYS-INT-2010-102, March 2010.

[43] A. Sherstnev and R.S. Thorne. Parton distributions for lo generators. *Eur.Phys.J.*, C55, 2008. arXiv:0711.2473v3.

[44] R. Field. Min-Bias and the Underlying Event at the Tevatron and the LHC, Oct 2002. A talk presented at the Fermilab ME/MC Tuning Workshop, Fermilab.

[45] The ATLAS Collaboration. G. Aad et al. Charged-particle multiplicities in pp interactions at $\sqrt{s} = 0.9$ TeV and 7 TeV in a diffractive limited phase space measured with the ATLAS detector at the LHC and a new pythia6 tune. ATLAS-CONF-2010-031, June 2010.

[46] The ATLAS Collaboration. Charged-particle multiplicities in pp interactions at $\sqrt{s} = 900$ GeV measured with the ATLAS detector at the LHC. *Phys. Lett.*, B688: 21–42, 2010. arXiv:1003.3124.

[47] The ATLAS Collaboration. G. Aad et al. Charged particle multiplicities in pp interactions at $\sqrt{s} = 7$ TeV measured with the ATLAS detector at the LHC. ATLAS-CONF-2010-024, April 2010.

[48] R. Engel. *Hadronic Interactions of Photons at High Energies.* PhD thesis, Universität Siegen, 1997.

[49] The ABCDHW Collaboration. G. Arnison et al. Transverse Momentum Spectra for Charged Particles at the CERN Proton anti-Proton Collider. *Phys. Lett. B*, 118, 1982.

[50] The ABCDHW Collaboration. A. Breakstone et al. Charged Multiplicity Distribution in pp Interactions at ISR Energies. *Phys. Rev. D*, 30, 1984.

[51] The UA5 Collaboration. R.E. Ansorge et al. Charged particle correlations in $p\bar{p}$ collisions at c.m. energies of 200, 546, and 900 GeV. *Z. Phys.*, C37, 1988.

[52] The UA5 Collaboration. R.E. Ansorge et al. Charged particle multiplicity distributions at 200 and 900 GeV c.m. energy. *Z. Phys.*, C43, 1989.

[53] The CDF Collaboration. F. Abe et al. Pseudorapidity distributions of charged particles produced in $\bar{p}p$ interactions at $\sqrt{s} = 630$ GeV and 1800 GeV. *Phys. Rev.D*, 41, 1990.

[54] The UA1 Collaboration. C. Albajar et al. A Study of the General Characteristics of $p\bar{p}$ Collisions at $\sqrt{s} = 0.2$ TeV to 0.9 TeV. *Nucl. Phys.B*, 335, 1990.

[55] The E735 Collaboration. T. Alexopoulos et al. Multiplicity dependence of transverse momentum spectra of centrally produced hadrons in $\bar{p}p$ collisions at 0.3, 0.54, 0.9 and 1.8 TeV center-of-mass energy. *Phys. Lett. B*, 336, 1994.

[56] The CDF Collaboration. T. Aaltonen et al. Measurement of Particle Production and Inclusive Differential Cross Sections in $p\bar{p}$ Collisions at $\sqrt{s}$ =1.96 TeV. *Phys. Rev. D*, 79, April 2009. arXiv:0904.1098.

[57] E.K.G. Sarkisyan and A.S. Sakharov. Relating multihadron production in hadronic and nuclear collisions. *Eur. Phys. J. C*, 70, 2010. arXiv:1004.4390v3.

[58] The ALICE Collaboration. Charged-particle multiplicity measurement in proton-proton collisions at $\sqrt{s} = 0.9$ and 2.36 TeV with ALICE at LHC. *Eur. Phys. J. C*, 68(1–2), 2010. arXiv:1004.3034v2.

[59] The ALICE Collaboration. Charged-particle multiplicity measurement in proton-proton collisions at $\sqrt{s} = 7$ TeV with ALICE at LHC. *Eur. Phys. J. C*, 68(3–4), 2010. arXiv:1004.3514v2.

[60] The CMS Collaboration. V. Khachatryan et al. Transverse momentum and pseudorapidity distributions of charged hadrons in pp collisions at $\sqrt{s} = 0.9$ and 2.36 TeV. *J. High Energy Phys.*, 02:041, 2010. arXiv:1002.0621.

[61] The CMS Collaboration. V. Khachatryan et al. Transverse-Momentum and Pseudorapidity Distributions of Charged Hadrons in pp Collisions at $\sqrt{s} = 7$ TeV. *Phys. Rev. Lett.*, 105, 2010. arXiv:1005.3299v2.

[62] L. Evans and P. Bryant (Ed.). The CERN Large Hadron Collider: Accelerator and Experiments. LHC Machine. *JINST*, 3 S08003, August 2008.

[63] Lari, L. *Beam-Machine Interaction studies for the Phase II LHC Collimation.* PhD thesis, École Polytechnique Fédérale de Lausanne, 2010.

[64] C. Carli, editor. *Chamonix 2009 Workshop on LHC Performance*, February 2009. CERN-ATS-2009-001.

[65] M. Ferro-Luzzi and W. Herr. LHC bunch Filling schemes for commissioning and initial luminosity optimization. Technical report, CERN and École Polytechnique Fédérale de Lausanne, June 2008. LHC Project Note 415.

[66] E. Métral. Running in 2011 – Luminosity. Slides.

[67] Bracco, C. *Commissioning Scenarios and Tests for the LHC Collimation system.* PhD thesis, École Polytechnique Fédérale de Lausanne, January 2009.

[68] A. Vogel. *Beam-Induced Backgrounds in Detectors at the ILC.* PhD thesis, Universität Hamburg, 2008.

[69] The ATLAS Collaboration. G. Aad et al. The ATLAS Experiment at the CERN Large Hadron Collider. *JINST*, 3 S08003, August 2008.

[70] The ATLAS Collaboration. G. Aad et al. ATLAS pixel detector electronics and sensors. *JINST*, 3 P07007, July 2008.

[71] P. Behara et al. Threshold Tuning of the ATLAS Pixel Detector. ATL-INDET-PUB-2010-001, August 2010.

[72] A. Andreazza for the ATLAS Collaboration. The ATLAS Pixel Detector operation and performance. *PoS(VERTEX 2010)005*, 2010.

[73] F. Campabadal et al. Design and performance of the ABCD3TA ASIC for read-out of silicon strip detectors in the ATLAS semiconductor tracker. *Nucl. Instum. Meth. Phys. Res.*, A552:292–307, 2005.

[74] The ATLAS Collaboration, September 2009. SCT Approved Plots.

[75] J. Huston. Forward scintillators in ATLAS: cryostat and MBTS, August 2005. Talk.

[76] A. Messina. Private communication, 2008.

[77] ATLAS web-page for Approved Plots, September 2008.

[78] B. Salvachua for the ATLAS Collaboration. Algorithms in the ROD DSP of the ATLAS hadronic Tile Calorimeter. In: 12th Workshop on Electronics For LHC and Future Experiments, September 2006.

[79] E. Fullana et al. Optimal Filtering in the ATLAS Hadronic Tile Calorimeter. ATL-TILECAL-2005-001, January 2005.

[80] A. Messina. Private communication, 2010.

[81] C. Ohm and T. Pauly. The ATLAS beam pick-up based timing system. arXiv:0905.3648, 2009.

[82] J. Lundberg for the ATLAS Collaboration. Performance of the ATLAS First-Level Trigger with First LHC Data. ATL-DAQ-PROC-2010-011, 2010.

[83] S. Rajagopalan for the ATLAS Collaboration. Performance of ATLAS Trigger System. ATL-DAQ-SLIDE-2011-241, June 2011.

[84] N. Garelli for the ATLAS Collaboration. Operating the ATLAS data-flow system with the first LHC collisions. ATL-DAQ-PROC-2011-003, October 2010.

[85] P. Jenni et al. ATLAS high-level trigger, data-acquisition and controls: Technical Design Report. Technical report, CERN, 2003. ATLAS-TDR-016/CERN-LHCC-2003-022.

[86] W. Wiedemann on behalf of the ATLAS Collaboration. The ATLAS online High Level Trigger framework: experience reusing offline software components in the ATLAS trigger. *J. Phys.: Conf. Ser.*, 219(022024), 2010.

[87] N. Berger et al. The ATLAS High Level Trigger Steering. *J. Phys.: Conf. Ser.*, 119(022013), 2008.

[88] S. George for the ATLAS Collaboration. The ATLAS High Level Trigger Configuration and Steering Software: Experience with 7 TeV Collisions, November 2010. ATL-DAQ-PROC-2010-053.

[89] The ATLAS Computing Group. ATLAS Computing Technical Design Report. ATLAS TDR–017/CERN-LHCC-2005-022, July 2005.

[90] J. Knobloch et al. LHC Computing Grid Technical Design Report. LCG-TDR-001/CERN-LHCC-2005-024, June 2005.

[91] K. Köneke for the ATLAS Collaboration. Distributing and storing data efficiently by means of special datasets in the ATLAS Collaboration, January 2011. ATL-SOFT-PROC-2011-036.

[92] N. Barlow for the ATLAS Collaboration. Prompt reconstruction of LHC collision data with the ATLAS reconstruction software, January 2011. ATL-SOFT-PROC-2011-019.

[93] The POOL Project. `http://pool.cern.ch`.

[94] R.Brun and F.Rademakers. Root-an object oriented data analysis framework. *Nucl. Instrum. & Meth. Phys. Res.*, A389:81–86, 1996.

[95] K. Köneke. Private communiation, 2011.

[96] The Gaudi Project. `http://proj-gaudi.web.cern.ch/proj-gaudi/`.

[97] E. Obreshkov for the ATLAS Collaboration. Software release build process and components in ATLAS offline, January 2011. ATL-SOFT-PROC-2011-012.

[98] ATLAS web-page for event displays.

[99] M. J. Costa on behalf of the ATLAS Collaboration. Commissioning of the ATLAS detector with cosmic rays and first LHC beams. *J. Phys.: Conf. Ser.*, 171(012100), 2009.

[100] The ATLAS Collaboration. Studies of the performance of the ATLAS detector using cosmic-ray muons. *Eur. Phys. J. C*, 71, 2011. arXiv:1011.6665v1.

[101] ATLAS first beam web-page.

[102] J. Baines for the ATLAS Collaboration. Performance of the ATLAS Trigger with Proton Collisions at the LHC. *PoS(ICHEP 2010)*, November 2010. ATL-DAQ-PROC-2010-052.

[103] B.A. Petersen for the ATLAS Collaboration. Commissioning of the ATLAS High Level Trigger with Proton Collisions at the LHC. *IEEE Nucl. Plas. Sci. Soc.*, July 2010. ATL-PROC-2010-001.

[104] Atlas e-News, December 2010.

[105] ATLAS public Results 2009 Page.

[106] ATLAS public Results 2010 Page.

[107] `https://twiki.cern.ch/twiki/bin/view/AtlasProtected/DataPeriods`.

[108] J. Dopke. Private communication, 2011.

[109] ATLAS internal Run Query Page.

[110] T. Cornelissen, M. Elsing, S. Fleischmann, I. Garvilenko, W. Liebig, E. Moyse, and A. Salzburger. Concepts, Design and Implementation of the ATLAS New Tracking (`NEWT`). ATL-SOFT-PUB-2007-007, 2007.

[111] A. Salzburger. Inner Detector Reconstruction Part I - Tracking. Tutorial at Artemis School on Calibration and performance of ATLAS detectors, 2008.

[112] D. Berge, M. Bona, R.C.C. Toro, R. Kwee, J. Lundberg, and A. Messina. Luminosity measurement using the ATLAS Minimum Bias Trigger Scintillator System. ATLAS Internal Note, ATL-LUM-INT-2010-004, March 2010.

[113] D. Kar for the ATLAS Collaboration. ATLAS Studies of Soft QCD Processes at 7 TeV. Conference contribution to Europhysics Conference on High-Energy Physics, June 2011.

[114] The ATLAS Collaboration. G. Aad et al. Central Charged particle multiplicities in pp-interactions measured with the ATLAS detector at the LHC. ATLAS-CONF-2010-101, December 2010.

[115] The ATLAS Collaboration. G. Aad et al. Leading charged-particle underlying event measurements in pp collisions at $\sqrt{s} = 900$ GeV and $\sqrt{s} = 7$ TeV with the ATLAS detector at the LHC. ATLAS-STDM-2010-04-001, arXiv 1012.0791v2, February 2011.

[116] The ATLAS Collaboration. G. Aad et al. Measurement of Inclusive Two-Particle Angular Correlations in pp Collisions with the ATLAS Detector at the LHC. in preparation, 2011.

[117] H. Grey, M. Limper, and A. Salzburger. Summary of the Uncertainties on the Tracking Efficiency used in the Charged Particle Multiplicity Analysis at $\sqrt{s} = 900$ GeV. Internal Note ATL-PHYS-INT-2010-096, March 2010.

[118] The ATLAS Collaboration. G. Aad et al. Charged particle multiplicities in pp interactions for track $p_T > 100$ MeV at $\sqrt{s} = 0.9$ and 7 TeV measured with the ATLAS detector at the LHC. ATL-CONF-2010-046, July 2010.

[119] The ATLAS Collaboration. Performance of the Minimum Bias Trigger in p-p Collisions at $\sqrt{s} = 7$ TeV. ATLAS-CONF-2010-068, July 2010.

[120] The ATLAS Collaboration. Performance of the Minimum Bias Trigger in p-p Collisions at $\sqrt{s} = 900$ GeV. ATLAS-CONF-2010-025, April 2010.

[121] The ATLAS Collaboration. G. Aad et al. Track Reconstruction Efficiency in $\sqrt{s} = 7$ TeV Data for Tracks with $p_T > 100$ MeV. ATL-PHYS-INT-2011-001, January 2011.

[122] ATLAS internal Non-collision background Meetings.

[123] The ATLAS Collaboration. G. Aad et al. Luminosity Determination in pp Collisions at $\sqrt{s} = 7$ TeV Using the ATLAS Detector at the LHC. *Eur. Phys. J. C*, 71: 1630, 2011. arXiv:1101.2185v1.

[124] The ATLAS Collaboration. G. Aad et al. Track-based underlying event measurements in pp collisions at $\sqrt{s} = 900$ GeV and 7 TeV with the ATLAS Detector at the LHC. ATLAS-CONF-2010-029, March 2010.

[125] U. Bintec. ATLAS Minimum Bias mailing list communication, 2010.

[126] U. Bintec. Private communication, 2010.

[127] F. Guescini et al. Beam Background Studies for the Minimum Bias Measurements from p-p Interactions at $\sqrt{s} = 0.9$ TeV. ATL-COM-PHYS-2010-037, March 2010.

[128] T. Kuhl and T. Voss. Determination of secondary tracks in the minimum bias analysis. ATL-COM-INDET-2010-011, September 2010.

[129] G. D'Agostini. A Multidimensional unfolding method based on Bayes' theorem. *Nucl. Instrum. Meth. A*, 362:487–498, 1995. doi: 10.1016/0168-9002(95)00274-X.

[130] The ATLAS Collaboration. G. Aad et al. Charged particle multiplicities in pp-interactions at $\sqrt{s} = 7$ TeV and 900 GeV measured from $p_{\mathrm{T}} > 100$ MeV: Supporting the 2nd Publication. ATL-PHYS-INT-2011-002, January 2011.

[131] The ATLAS Collaboration. G. Aad et al. Measurement of underlying event characteristics using charged particles in pp collisions at $\sqrt{s} = 900$ GeV and 7 TeV with the ATLAS detector in a limited phase space. ATLAS-CONF-2011-009, December 2011.

[132] C. Zampoli for the ALICE Collaboration. ALICE $\mathrm{d}N_{\mathrm{ch}}/\mathrm{d}\eta$ Analysis for the common plots. Talk, September 2010.

[133] The CMS Collaboration. V. Khachatryan et al. Pseudorapidity distributions of charged particles in pp collisions at $\sqrt{s} = 7$ TeV and 0.9 TeV with at least one central charged particle. CMS PAS QCD-10-024, April 2011.

[134] D. Hirschbrühl (Pixel Run Coordinator). Private communiation, 2011.

[135] The ATLAS Collaboration. G. Aad et al. Measurement of Inclusive Two-Particle Angular Correlations in Proton-Proton Collisions at $\sqrt{s}$ = 900 GeV and 7 TeV. ATLAS-CONF-2011-055, 2011.

[136] G. Cowan. Error analysis for effciency. Note, 2008.

[137] M. Paterno. Calculating Effciencies and their Uncertainties. Note, 2003.

List of Figures

List of Tables

Acknowledgements

It is a pleasure to thank all my collegues with whom I worked with. Firstly, I owe my thanks to my supervisors, Dr. Nick Ellis, Prof. Dr. Hermann Kolanoski and especially Dr. Klaus Mönig, who was also my former "Diplomavater", who all supported and encouraged me throughout my PhD-time.

I fully appreciated the highly professional work with many ATLAS collaborators. In particular the "trigger people". I collaborated with some of them right from the beginning of my thesis: William Bell, Andrea Messina, Jiri Masik, Iwona Graboska-Bold, Tomasz Bold and Emily Nurse. Also, I am indepted to Edward Sarkisyan-Grinbaum who carried on the minbias trigger validation but also for the discussion about QCD in pp and heavy ions.

During the first few minbias analyses in ATLAS, I was lucky to have collaborated with other, great people: Remi Zaidan, Alison Lister, George Aad, Oldrich Kepka, Thorsten Kuhl and Gerhard Brandt, thank you all for the discussions and explantions. In particular, special thanks to Gerhard Brandt who suggested to me the charged particle analysis within an LHC-wide effort.

I must add my full acknowledgement for the allocation of an Tier-3 Geneva account completed by uncomplicated and useful support. This was extremely useful. And certainly, I honestly appreciate the Wolfgang-Genter Programme and Michael Hauschild who granted me travels, home institute visits and a computing school... it

I am also deeply grateful to Benedikt Hegner who iterated on each chapter of this manuscript, and Gerhard Brandt, Thilo Pauly, Alison Lister, Mark Stockton, Nick Barlow and Tim Martin for their (english) corrections and comments on parts of the manuscript.

Many thanks to the Humboldt EET group, in particular to Prof. Dr. Heiko Lacker and Prof. Dr. Thomas Lohse, supporting from Berlin when ever needed.

I only mentioned a few of the great people I got to know. There were many more who made this graduation a wonderful and unique experience of particle physics!

Selbständigkeitserklärung

Ich erkläre, dass ich die vorliegende Arbeit selbständig und nur unter Verwendung der angegebenen Literatur und Hilfsmittel angefertigt habe.

Genf, den 09.09.2011 Regina Esther Kwee